Dissertation
submitted to the
Combined Faculties for the Natural Sciences and for Mathematics
of the Ruperto-Carola University of Heidelberg, Germany
for the degree of
Doctor of Natural Sciences

Put forward by
Dipl.-Phys.: Selami Yilmaz
Born in: Bayreuth

Oral examination: 01.02.2012

Retrieval of Atmospheric Aerosol and Trace Gas Vertical Profiles using Multi-Axis Differential Optical Absorption Spectroscopy

Referees: Prof. Dr. Ulrich Platt
Prof. Dr. Thomas Wagner

Bestimmung von atmosphärischen Spurengas- und Aerosolprofilen mittels Multi-Axialer Differentieller Optischer Absorptionsspektroskopie

In dieser Arbeit wurde die Multi-Axiale Differentielle Optische Absorptionsspektroskopie (MAX-DOAS) verwendet um die vertikale Verteilung von atmosphärischen Spurengasen und Aerosolen zu bestimmen. Dabei wurden verschiedene Inversionsmethoden angewandt um die Profile aus den MAX-DOAS Messungen zu bestimmen. Ein neues MAX-DOAS Instrument wurde gebaut, das speziell für die Messung von Aerosolen und Spurengasen konzipiert wurde. Im Rahmen des EUSAAR (European Supersites for Atmospheric Aerosol Research) Projektes wurden die Inversionsmethoden angewandt und weiterentwickelt. Mehrere Vergleichs-Messkampagnen wurden in Cabauw (Niederlande), Ispra (Italien) und Leipzig/Melpitz (Deutschland) durchgeführt. Aerosol Extinktions- und NO_2-Profile wurden bestimmt und mit unabhängigen In-Situ- und Fernerkundungs-Messungen verglichen. Dabei wurden sowohl für die Aerosolprofile als auch NO_2-Profile gute Übereinstimmungen mit den unabhängigen Messungen erreicht. Des weiteren wurde die verdünnte Fahne des Eyjafjallajökull Vulkans (Island) mittels MAX-DOAS SO_2 Messungen über Heidelberg im April und Mai 2010 nachgewiesen. Diese eindeutigen SO_2 Messungen sind im Einklang mit Satellitenmessungen und Modellierungen. Die in dieser Arbeit vorgestellten Fortschritte im Instrumentenbau und in der Entwicklung von Inversionsalgorithmen zeigen, dass MAX-DOAS eine leistungsfähige Methode für die Erfassung der vertikalen Verteilung der atmosphärischen Bestandteile ist. Aufgrund der Bestätigung durch unabhängige Messungen wird die Integration von MAX-DOAS Instrumenten in globale Messnetzwerke empfohlen.

Retrieval of Atmospheric Aerosol and Trace Gas Vertical Profiles using Multi-Axis Differential Optical Absorption Spectroscopy

In this thesis, the vertical distribution of atmospheric trace gases and aerosols were retrieved using Multi-Axis Differential Optical Absorption Spectroscopy (MAX-DOAS). Various inversion methods were used to retrieve the profiles from the MAX-DOAS measurements. A new MAX-DOAS instrument optimized for the measurement of aerosol and trace gas profiles was developed. The retrieval methods were tested and advanced in the scope of the EUSAAR (European Supersites for Atmospheric Aerosol Research) project. Several intercomparison campaigns were carried out in Cabauw (the Netherlands), Ispra (Italy) and Leipzig/Melpitz (Germany). Aerosol extinction and NO_2 profiles were retrieved from the MAX-DOAS measurements and compared to independent in situ and remote sensing measurements. Good agreements were achieved for both the aerosol and NO_2 profiles. Furthermore, the diluted plume of the Eyjafjallajokull volcano, Iceland, was detected by MAX-DOAS SO_2 measurements over Heidelberg in April and May 2010. These measurements showed an unambiguous detection of SO_2, and are in agreement with satellite observations and model predictions. The here presented advances in instrumental hardware and retrieval algorithms demonstrate that MAX-DOAS is a powerful tool for monitoring the vertical distribution of atmospheric constituents. Verified by independent measurements, its integration in worldwide measurement networks is recommended.

Contents

1 Introduction **1**

2 The Earth's Atmosphere **3**
2.1 Atmospheric Composition and Vertical Structure 3
2.2 Trace Species in the Troposphere 7
2.2.1 Nitrogen Dioxide 8
2.2.2 Sulfur Dioxide 11
2.3 The Oxygen Collision Complex 13
2.4 Atmospheric Aerosols 14

3 Absorption Spectroscopy **21**
3.1 The DOAS Principle 23
3.2 Experimental Implementation 25
3.3 Spectral Analysis Principle 27
3.4 Passive DOAS 29
3.4.1 Fraunhofer Lines 29
3.4.2 Ring Effect 29
3.4.3 Solar I_0 Effect 30
3.5 Multi-Axis DOAS 31
3.6 Spectral Retrieval 34
3.6.1 Dependence on the Wavelength Interval of the Retrieval . . . 36
3.6.2 Applied Retrieval Settings 45

4 Radiative Transfer in the Atmosphere **51**
4.1 Solar Radiation and the Earth-atmosphere system 52
4.2 Interaction Processes of Radiation in the Atmosphere 56
4.2.1 Absorption 56
4.2.2 Rayleigh Scattering 57
4.2.3 Raman Scattering 59
4.2.4 Mie Scattering 59
4.2.5 Aerosol Optical Properties 61
4.2.6 Radiative Transfer Equation 62
4.3 The Air Mass Factor Concept 63
4.4 Radiative Transfer Modeling 64
4.4.1 SCIATRAN 2 64
4.4.2 Model Parameter 65

5 Atmospheric Profile Retrieval **67**
5.1 Basic Inversion Principles . . . 69
5.2 Linear Inversion Case . . . 70
5.3 Non-linear Inversion Case . . . 70
5.3.1 The Gauss-Newton Method . . . 71
5.3.2 The Levenberg-Marquardt Method . . . 71
5.4 Retrieval Properties . . . 72
5.5 Retrieval Errors . . . 73
5.6 Retrieval Methods . . . 74
5.6.1 Optimal Estimation Method . . . 74
5.6.2 Regularization Method . . . 75
5.7 Iteration Strategy . . . 76
5.8 State and Measurement Vectors . . . 77
5.9 State Vector Transformations . . . 79
5.10 Retrieval Implementation . . . 81

6 Application of the Retrieval Methods **83**
6.1 Application of the Optimal Estimation Method . . . 84
6.1.1 Retrieval of the Aerosol Extinction Profile and AOD . . . 85
6.1.2 Retrieval of Further Aerosol Optical Properties . . . 98
6.1.3 Parameterized Retrieval of the Aerosol Profile . . . 98
6.1.4 Retrieval of the Trace Gas Profile . . . 101
6.2 Application of the Regularization Method . . . 105
6.2.1 Retrieval of the Aerosol Extinction Profile and AOD . . . 105
6.2.2 Retrieval of the Trace Gas Profile . . . 109

7 Instrumentation **111**
7.1 MAX-DOAS Instrument . . . 111
7.1.1 Instrumental Concept . . . 112
7.1.2 Instrument Characteristics . . . 117
7.2 Complementary Dataset . . . 122
7.2.1 Remote Sensing of Aerosols from the Ground . . . 122
7.2.2 Ground Based In Situ Measurements . . . 125
7.2.3 Satellite Trace Gas Observations . . . 128
7.2.4 Total Sky Imager . . . 129
7.2.5 Transport Model FLEXPART . . . 129

8 Field Campaigns **131**
8.1 Measurement Sites and Instrumentation . . . 132
8.2 Cabauw 2008 . . . 133
8.2.1 Comparison of the O_4 and Intensity Measurements to Simulations Using Independent Aerosol Data . . . 135
8.2.2 Retrieval of Aerosol Extinction Profiles and Optical Depths . . . 140
8.2.3 Retrieval of NO_2 Profiles . . . 162
8.3 Melpitz 2008 . . . 172
8.4 Ispra 2009 . . . 174
8.5 Leipzig 2009 . . . 177

8.6 CINDI 2009 . . . 180
8.6.1 Retrieval of Aerosol Extinction Profiles and Optical Depths . . 181
8.6.2 Retrieval of NO_2 Profiles . . . 185
8.7 Cabauw 2009 and 2010 . . . 187
8.7.1 Retrieval of Aerosol Extinction Profiles and Optical Depths . . 187
8.7.2 Retrieval of NO_2 Profiles . . . 188
8.8 Heidelberg 2010 . . . 190
8.8.1 Detection of the Volcanic Plume of Eyjafjallajokull by SO_2 Measurements . . . 191
8.8.2 Retrieval of Aerosol Extinction Profiles and Optical Depths . 194
8.8.3 Retrieval of SO_2 and NO_2 Profiles . . . 197

9 Conclusions and Outlook **199**

A Sensitivity Studies **205**

B Construction Plans **213**

List of Figures **217**

List of Tables **231**

Bibliography **233**

Acknowledgements **253**

Chapter 1

Introduction

Aerosols and trace gases are key components of physical and chemical processes in the Earth's atmosphere, and have numerous impacts on maritime and continental ecosystems as well as human health. Aerosols significantly impact the atmospheric energy budget via direct and indirect effects on the radiation balance. E.g., their influence on cloud formation processes leads to a modification of the appearance and optical properties of clouds. Furthermore, aerosols can serve as catalysts and influence chemical reactions in the atmosphere. High pollution levels in the atmosphere, caused by aerosols and trace gases, can directly affect human health, especially the respiratory system.

The physical and chemical processes in the atmosphere are still not completely understood. In particular, the knowledge on atmospheric aerosols is subject to large uncertainties (IPCC, 2007). To improve the scientific understanding of these complex and variable processes, observations of atmospheric constituents over long time periods and with large areal coverage are of crucial importance. They are further required for the improvement of numerical models used for the prediction of future atmospheric composition and climate. Therefore, novel measurement techniques are desirable, which allow for automated comprehensive observations with remote sensing capabilities, integrated in worldwide measurement networks.

A variety of established techniques for the measurement of aerosol optical properties are currently integrated in monitoring networks. In situ measurement techniques, like nephelometers, provide information on aerosol properties at the instrument's location. Usually only optical properties of dried aerosol particles are determined, and the optical properties of the ambient aerosol needs to be extrapolated. Sun photometers provide extensive information on aerosol optical and microphysical properties measured by passive remote sensing. The information is restricted to the total vertical column and vertically resolved information is not available. The requirements on the calibration and stability of Sun photometers are very high, since they rely on measurements of the absolute solar radiation. Lidar instruments are well suited to measure altitude resolved scattering properties of aerosols using artificial light sources. However, quantitative estimates of the aerosol extinction and scattering are complicated, since the exact knowledge of the backscatter-to-extinction ratio is nec-

essary. A more sophisticated approach is used by the so-called Raman lidar systems, which can directly relate the measurements to aerosol extinction. However, these systems require powerful light sources for a reliable detection. Otherwise, quantitative extinction measurements by Raman lidar systems are restricted to night time.

In the recent years, remarkable advances in the application of the Multi-Axis Differential Optical Absorption Spectroscopy (MAX-DOAS) technique for the retrieval of atmospheric aerosol and trace gas profiles have been made. Using MAX-DOAS measurements of trace gases with a known vertical profile, like O_4, it is possible to retrieve information on atmospheric aerosols. The approach of combining MAX-DOAS trace gas measurements with advanced numerical inversion methods allows for the height resolved determination of the constituents in the lower troposphere. In contrast to the established techniques for the measurement of aerosol optical properties, the MAX-DOAS technique has the advantage of being capable to retrieve trace gas as well as aerosol profiles from the same measurements. Lidar instruments can not measure aerosols in surface near altitudes where the MAX-DOAS measurements provide high sensitivity.

In this work, a novel type of MAX-DOAS instrument optimized for the measurement of aerosol and trace gas profiles was developed. Various inversion algorithms were developed and applied on the MAX-DOAS measurements. In the scope of a joint research activity of the European Supersites for Atmospheric Aerosol Research (EUSAAR) project, several intercomparison campaigns were carried out at different sites in Europe. The aim of these campaigns was the comparison of the aerosol profiles retrieved from MAX-DOAS to measurements with the established in situ and remote sensing techniques. Furthermore, NO_2 profiles were retrieved from MAX-DOAS measurements and compared to in situ and satellite measurements.
In addition to the tasks related to the EUSAAR project, MAX-DOAS measurements were performed in Heidelberg in 2010. During these measurements, the highly diluted plume of the Eyjafjallajokull volcano in Iceland was observed by the detection of volcanic SO_2.

This work is structured as follows. Chapter 2 gives an overview on the structure of the Earth's atmosphere and its constituents relevant for the measurements in the scope of this work. The principles and details of the applied MAX-DOAS technique are addressed in Chapter 3, while the radiative transfer in the atmosphere is content of Chapter 4. The theoretical principles of the aerosol and trace gas profile retrievals are discussed in detail in Chapter 5. The application of these methods is presented in Chapter 6 using synthetic measurements to explore the retrieval sensitivities and capabilities. The newly developed MAX-DOAS instrument is described in the first part of Chapter 7, while the second part addresses the different instruments, to which the MAX-DOAS measurements were compared. Chapter 8 contains the results from the different intercomparison campaigns as well as the measurements in Heidelberg. Chapter 9 completes this work with a conclusion and gives an outlook for future studies based on the findings of this work.

Chapter 2

The Earth's Atmosphere

The life on Earth would not be possible without a protecting atmosphere. Although its vertical extend corresponds to roughly 1 % of the Earth's radius, its importance for all types of living creatures on Earth is immense. This thin layer, in relation to global dimensions, determines the amount and type of incomming and outgoing radiation. It supplies oxygen to animals and carbon dioxide to plants. Besides the most abundant gaseous constituents of atmospheric air, trace substances are also present with nevertheless major importance for the atmospheric chemistry and climate.
This Chapter presents an overview on the composition and vertical structure of the atmosphere in Section 2.1. The atmospheric compounds measured within the scope of this work are introduced in the subsequent sections. The observed gaseous trace constituents are described in Section 2.2, while Section 2.3 deals with the oxygen collision complex O_4. Finally, the physical properties of atmospheric aerosols are discussed in Section 2.4.

2.1 Atmospheric Composition and Vertical Structure

The atmosphere is characterized by several distinct layers (Figure 2.1). According to the underlying physical processes, the division of the different layers can be related to molecular motion mechanism, the degree of ionization, and the thermal structure. These processes also determine the atmospheric composition with altitude.

Composition

With respect to its major components, the atmospheric composition is fairly constant up to about 100 km altitude. Molecular nitrogen, oxygen and the noble gas argon are the most abundant species, which constitute more than 99.9 % of dry air. Together with further species, these major components of the atmosphere are listed in Table 2.1. In addition to the different noble gases, the atmosphere contains water vapour with volume mixing ratios between 10^{-6} and a few %. Furthermore, the greenhouse gases carbon dioxide and methane have obtained a prominent position. The latter are refered to as trace gases since the abundance of these species is much

Table 2.1: *The main constituents of the unpolluted dry atmosphere*

Gas	Chemical formula	Mixing ratio by volume [%]
Nitrogen	N_2	78.08
Oxygen	O_2	20.95
Argon	Ar	0.93
Carbon dioxide	CO_2	0.037
Neon	Ne	0.0018
Helium	He	0.00052
Methane	CH_4	0.00017
Krypton	Kr	0.00011
Xenon	Xe	0.00009
Hydrogen	H_2	0.00005
Dinitrogen oxide	N_2O	0.00003

lower. Including molecular hydrogen and nitrous oxide, the atmosphere contains a multitude of other trace gas species. Section 2.2 addresses such trace gases, which were observed with measurements performed within this work. Excluding water vapour, carbon dioxide, methane and dinitrogen oxide, the species listed in Table 2.1 have atmospheric residence times exceeding 1000 years. Thus, these constituents are referred to as permanent. 99 % of all atmospheric gases are confined to altitude regions below 32 km. This region, i.e. troposphere and a part of stratosphere (see Figure 2.1), is the main focus of atmospheric research.
In addition to the gaseous compounds, the atmosphere also contains aerosols. These are small particles of liquid or solid matter dispersed and suspended in air, with sizes ranging from a few nanometers to tens of micrometers. Typical examples are droplets of water or acid, dust or soot particles. Atmospheric aerosols are discussed in detail in Section 2.4.

Vertical Structure

The vertical structure of the atmosphere is frequently characterized by its temperature profile. It determines the division of the atmosphere in several layers with distinct boundaries, called pauses (see Figure 2.1). The lowermost layer is the **troposphere**, where the temperature profile is dominated by adiabatic expansion and compression of rising and sinking air masses, respectively, which is driven by solar radiation. When the surface is heated during the day, warm air ascends and cools down by expansion resulting in a temperature decrease of 5–10 K per 1 km altitude. This leads to a first temperature minimum, which defines the tropopause region. In the upper troposphere, an additional radiative cooling effect occurs, which is caused by the emission of radiation in the infrared wavelength range by water vapour. Thus, the upper limit of the troposphere is influenced by its water vapor content, that in turn depends on the surface temperature. The tropopause altitude ranges between 17–18 km in the tropics and between 9–13 km at higher latitudes. The

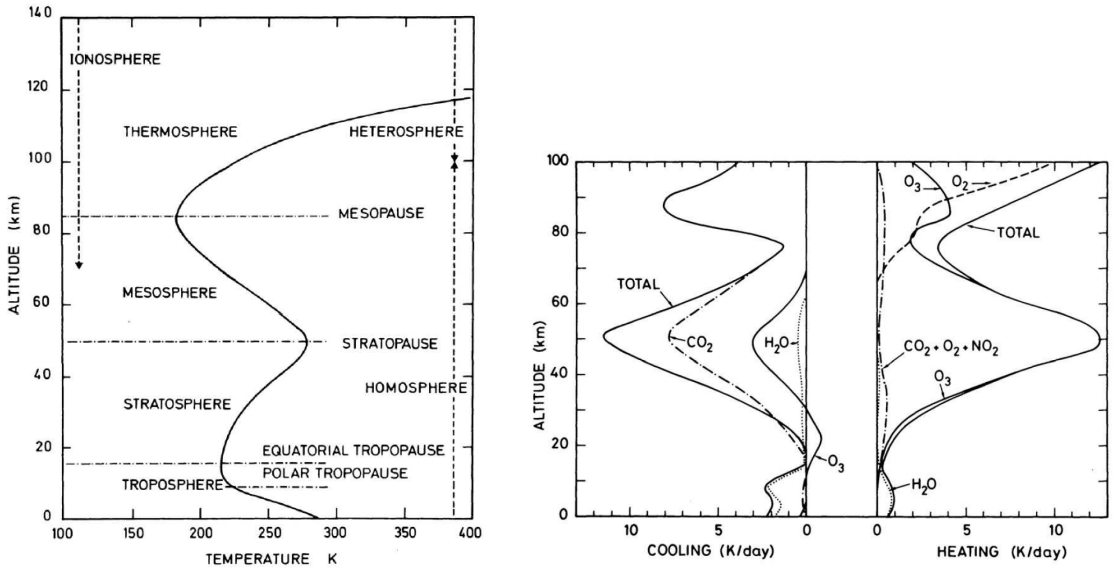

Figure 2.1: *Left panel: thermal structure of the Earth's atmosphere. Adapted from Brasseur and Solomon (1986). Right panel: vertical distribution of solar short wave heating rates by O_3, O_2, NO_2, H_2O, CO_2, and of terrestrial long wave cooling rates by CO_2, O_3, and H_2O. Adapted from London (1980).*

lowest tropopause heights occur at polar winter latitudes. Due to the convection processes accompanied with the generation of the temperature profile, the troposphere is relatively well mixed.

The troposphere can be further subdivided into the atmospheric boundary layer and the free troposphere. The boundary layer, also referred to as mixing layer, roughly covers the lowest 1–3 km of the atmosphere, while the free troposphere extends from the top of the boundary layer to the tropopause. Air movement and mixing in the boundary layer are influenced by friction on the Earth's surface.

The thermal conditions in the **stratosphere** are opposite to the troposphere. The upper stratosphere is heated by the absorption of solar radiation by ozone, while the lower stratosphere is cooled by the infrared emission of water vapor in the upper troposphere and tropopause. Thus, the temperature increases with altitude in the stratosphere, which leads to very little convection and mixing. In contrast to the troposphere, the temperature profile in the stratosphere is mainly determined by absorption of solar radiation and emission of infrared radiation, which results in a maximum at roughly 50 km altitude defining the stratopause region.

The **mesosphere** is localized between the stratopause and the mesopause. The latter is located at around 85 km and is the coldest point of the atmosphere. In the mesosphere, the temperature decreases again with the altitude due to similar processes as in the troposphere. Above the mesopause is the **thermosphere**, where the temperature increases up to values of 1200–1500 K due to absorption of solar ultra-violet radiation mainly by oxygen.

At altitudes above 100 km, atmospheric constituents start to separate, according to their mass. This region is therefore referred to as the **heterosphere**. In contrast to

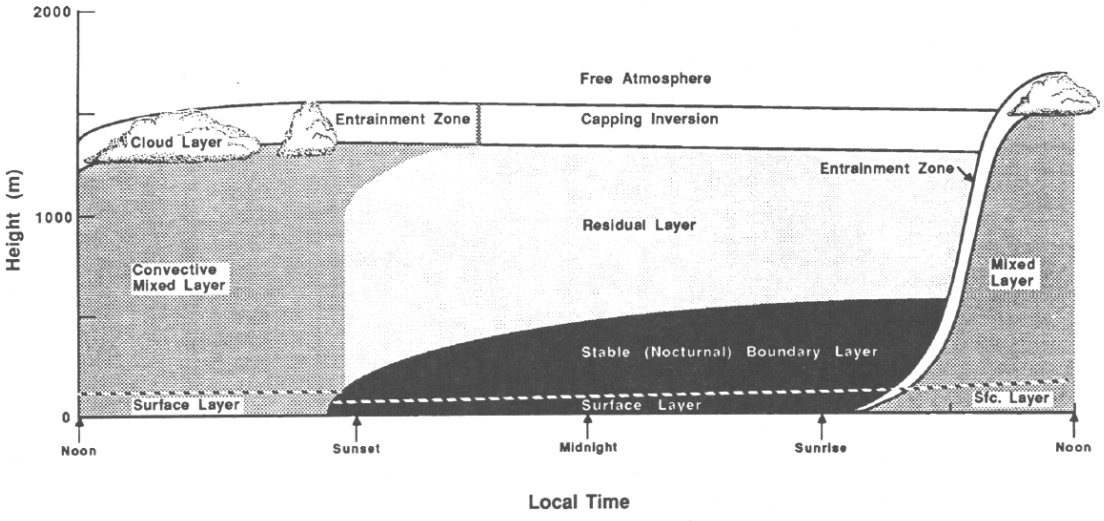

Figure 2.2: *The typical diurnal development of the atmospheric boundary layer. Adapted from Stull (1988).*

the **homosphere** below, where the atmospheric constituents are mixed by turbulent fluid motions, the molecular diffusion plays a dominating role in the heterosphere due to the increased mean free path between collisions.
The degree of ionization allows a further division of the atmosphere. The **ionosphere** is located above approximately 65 km of altitude. Here, the atmospheric constituents are increasingly ionized by solar radiation, in contrast to the **neutrosphere** below.

Atmospheric Boundary Layer

The atmospheric boundary layer (BL) is the layer of the atmosphere which is directly affected by friction and the exchange of momentum between atmosphere and surface. It is of particular interest when studying the effects of emissions, since most emission sources are ground-based, but also due to the simple fact that we live in it. The BL can be further subdivided in different layers. The lowermost millimeters form the molecular viscous layer, where the dynamics are dominated by molecular diffusion. The following layer ranging up to 20–200 m forms the Prandtl layer or surface layer where the dynamics are dominated by turbulent diffusion and the impact of surface friction is strongest. The subsequent layer is the Ekman layer and extends to the top of the BL. The wind directions in this layer change continuously from the ground wind directions to the direction of the geostrophic winds of the free troposphere, which are isobaric wind streams induced by an equilibrium state between the forcing of pressure gradient and Coriolis force.
The typical diurnal development of the BL is depicted in Figure 2.2. At the sunset, a stable (nocturnal) BL is created by the deep surface cooling. Above this layer, there is a residual layer, which is basically the leftover part of the daytime mixing layer. The stable BL is characterized by statically stable air with weaker turbulence,

and can also be formed during the day in situations, where the underlying surface is colder than the air. The beginning and increasing heating of the surface shortly after the sunrise causes turbulence, which produces a well mixed layer near the ground. The vertical extent of this layer increases to a maximum in the late morning. Usually, a stable inversion layer, where the temperature increases with altitude, is located at the top of the mixing layer and prevents the development of deep convection. However, in cases with sufficient surface heating and humidity, convection can break through. In contrast to the day time mixing layer with a clearly defined top, the stable nocturnal BL smoothly blends into the residual layer.

2.2 Trace Species in the Troposphere

Atmospheric trace gases are constituents with much lower abundances than the main compounds of the atmosphere, and originate either from direct emissions, being natural or anthropogenic, or production in different chemical reaction pathways. Although their concentration is very small, the chemical processes in the atmosphere are predominately influenced by these trace species. Thus, their impact on the atmosphere is very noticeable, despite their low concentrations. Furthermore, most trace species have a direct negative impact on human health, especially on the respiratory tract. The chemistry in the troposphere is dominated by ozone (O_3) and other oxidants, i.e. hydroxyl/peroxy radicals, nitrogen oxides, and volatile organic carbons. The chemistry of these species is closely linked with many various reaction pathways.
O_3 is a key compound in the chemistry of the atmosphere. It determines the oxidation capacity. Approximately 90 % of the atmospheric O_3 is located in the stratospheric ozone layer, which absorbs the major fraction of the solar ultra-violet radiation. In the troposphere, O_3 is formed by chemical reactions involving nitrogen dioxide (NO_2), nitric oxide (NO), CH_4 and other reactive hydrocarbons (Fishman and Crutzen, 1978), as well as reactions with carbon monoxide (CO) and Volatile Organic Compounds (VOC). The nitrogen compounds NO_2 and NO, which are often referred to as NO_x, are among the most important trace gases. Both are radicals and thus highly reactive. Since NO_2 was measured within this work, a description of the reaction pathways involving NO_2 are dicussed in Section 2.2.1.
Formaldehyde (HCHO) also has an influence on the oxidation capacity of the atmosphere. It is involved in reaction cycles that can lead to the formation of the hydroxyl radical (OH). The oxidation of VOCs generate as a secondary product HCHO, which is the predominant source (Altshuller, 1993). The typical mixing ratios of HCHO in polluted urban areas range from 1 to 20 parts per billion (ppb) (Finlayson-Pitts and Pitts jr., 2000). However, HCHO is also emitted as a primary product by biomass burning and fossil fuel combustion. Furthermore, vegetation is known to emit HCHO directly.
A further trace species that can lead to the formation of OH is nitrous acid (HONO) altering the oxidation capacity of the atmosphere (Platt and Perner, 1980). The direct emission of HONO from combustion sources was observed, but are too small to explain the measured concentrations of HONO in the atmosphere (Platt, 1986). Although several sources and reaction pathways including heterogeneous reactions

Table 2.2: *Tropospheric sources of NO_x emissions (Lee et al., 1997). The source strength is given in million tons of fixed nitrogen [Tg N] per year.*

Source	Emission [Tg N y^{-1}]	Uncertainty range [Tg N y^{-1}]
Fossil fuel combustion	22	13-31
Biomass burning	7.9	3-15
Soil emissions	7.0	4-12
Thunderstorms	5.0	2-20
Aircraft emissions	0.9	-

on surfaces are already identified, the formation processes of HONO are still not well known.
The oxidation of numerous VOCs generates glyoxal (CHOCHO). Furthermore, the reactions of aromatics with OH are the predominant sources for CHOCHO in urban air (Volkamer et al., 2010). CHOCHO is also emitted by biomass burning and recent studies reported significant concentrations over oceans (Sinreich et al., 2010).
Another trace gas originating from natural and anthropogenic emissions, is sulfur dioxide (SO_2). It is a key compound in the formation of acid rain and strongly influences the regional air quality. Furthermore, reaction products of SO_2 in the atmosphere can serve as cloud condensation nuclei enabling the formation of clouds with a higher albedo, which influence the radiative budget of the atmosphere and thus the climate. SO_2 was also detected in measurements of urban air and a highly diluted volcanic plume in the scope of this work and is addressed in Section 2.2.2.

2.2.1 Nitrogen Dioxide

NO_2 is of large importance for the atmospheric chemistry, since it affects the oxidation capacity of the atmosphere by influencing the abundance and partitioning of hydroxyl and peroxy radicals. While in the troposphere, NO_2 enables the formation of O_3, the degradation of the stratospheric ozone layer is enhanced by NO_2.
NO_2 and NO are strongly linked, since both are converted rapidly to each other, and thus referred to as NO_x. The main source of NO_x emissions is the anthropogenic fossil fuel combustion, mainly by industrial activities as well as traffic. Biomass burning, due either to natural or man made ignition, is a further source of NO_x generation. Furthermore, intensive agriculture leads to an enrichment of nitrogen compounds in the soil, which then enhances the natural emission of NO_x from the soil. In contrast to these mainly ground based emissions, air traffic and thunderstorms are additional sources, which contribute to the NO_x budget in higher altitudes. The most important sources are listed in Table 2.2 with the according amounts and uncertainties (Lee et al., 1997).
While naturally emitted NO_x is distributed more uniformly over the globe, anthropogenic sources are concentrated to relative small areas. The mean global distribution of the tropospheric NO_2 vertical column density retrieved from satellite measurements for the period of 2003 to 2010 is shown in Figure 2.3. Large cities

as well as areas with high industrial activities can be identified due to remarkably increased NO_2 column densities. The removal of NO_x from the atmosphere is carried out in form of acid rain containing nitric acid (HNO_3). The effective lifetime of NO_2, ranging from 33 hours in winter and 12 hours in summer, is determined by the solar radiation (Beirle et al., 2003).
NO_x is primarily emitted in form of NO, which is subsequently oxidized by ozone to NO_2. Whenever air is heated to temperatures higher than 2000 K, the thermal energy is sufficient for the dissociation of O_2. The atomic oxygen reacts then with N_2 to form NO:

$$O + N_2 \longrightarrow NO + N \tag{2.1}$$

The produced NO is rapidly oxidized by ozone to form NO_2:

$$NO + O_3 \longrightarrow NO_2 + O_2 \tag{2.2}$$

Ultra-violet solar radiation of wavelengths below 420 nm can result in the photolysis of the produced NO_2:

$$NO_2 \xrightarrow{h\nu\ (\lambda<420\ nm)} NO + O(^3P) \tag{2.3}$$

During noon with direct Sun radiation, this photolysis reaction can occur quickly, so that the lifetime of NO_2 is restricted to several minutes. $O(^3P)$ reacts rapidly with O_2 to form ozone under the involvement of a collision partner M (e.g. N_2 or O_2), which is necessary to conserve energy and spin momentum:

$$O(^3P) + O_2 + M \longrightarrow O_3 + M \tag{2.4}$$

Thus, from each NO_2 molecule, one O_3 and NO molecule is generated, which both can form an NO_2 molecule again according to reaction (2.2). This results in a partitioning of NO and NO_2 during daytime which is controlled by ozone and described by the Leighton ratio L (Leighton, 1961):

$$L = \frac{[NO]}{[NO_2]} = \frac{j_{NO_2}}{k_{NO} \cdot [O_3]} \tag{2.5}$$

where j_{NO_2} is the photolysis frequency of NO_2 and k_{NO} is the rate constant of the reaction of ozone with NO (reaction (2.2)). While the photolysis frequency j_{NO_2} changes with the solar radiation in the course of the day, the rate constant k_{NO} depends on the temperature with a value of $1.8 \cdot 10^{-14}$ cm^3 molec^{-1} s^{-1} at 298 K (Atkinson et al., 2004).
Typical Leighton ratios in the lower troposphere range from 0.5 to 1, depending on the ozone concentration and daytime. With increasing altitude, the Leighton ratio is shifted towards NO due to the temperature dependency of k_{NO} and the increasing NO_2 photolysis frequency.
In the photochemical equilibrium, the reactions (2.2) - (2.4) result in no net ozone production. This situation changes, when sufficient amounts of NO_x is abundant to

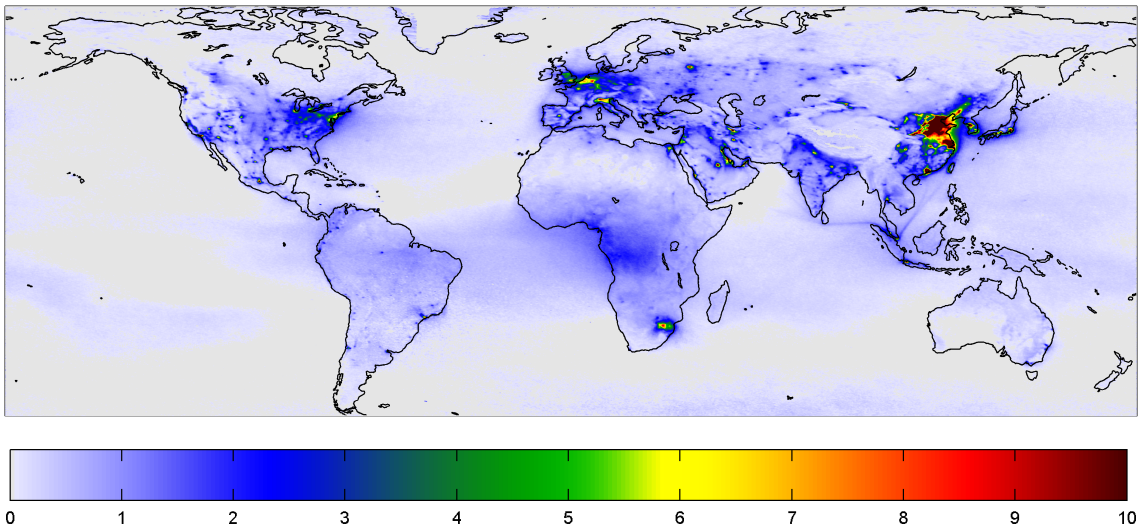

Figure 2.3: *Mean global distribution of the tropospheric NO_2 vertical column density in 10^{15} molecules/cm_2 retrieved from SCIAMACHY satellite measurements for cloud free conditions during 2003–2010 (Steffen Beirle, MPI Mainz, personal communication).*

react with peroxy radicals, HO_2 and RO_2:

$$NO + HO_2 + \longrightarrow NO_2 + HO \tag{2.6a}$$
$$NO + RO_2 + \longrightarrow NO_2 + RO \tag{2.6b}$$

Thus, more ozone is produced by reaction (2.3) and (2.4) than degraded by NO, leading to the so-called photosmog containing large amounts of ozone, oxidized VOCs and organic aerosols.
During night time, the missing NO_2 photolysis results in a shift of the Leighton ratio towards NO_2. Then, ozone oxidizes NO_2 to NO_3:

$$NO_2 + O_3 \longrightarrow NO_3 + O_2 \tag{2.7}$$

During the day NO_3 is photolyzed rapidly, but during night time it builds the reservoir species N_2O_5 by the reaction with NO_2:

$$NO_2 + NO_3 \longrightarrow N_2O_5 \tag{2.8}$$

The decomposition of N_2O_5 is collisional or due to photolysis during day time:

$$N_2O_5 + M \longrightarrow NO_3 + NO_2 + M \tag{2.9a}$$
$$N_2O_5 \xrightarrow{h\nu\ (\lambda \leq 1252\ \mathrm{nm})} NO_2 + NO + O_2 \tag{2.9b}$$

The sink of NO_2 is the reaction with OH which generates HNO_3:

$$NO_2 + OH_3 \longrightarrow HNO_3 \tag{2.10}$$

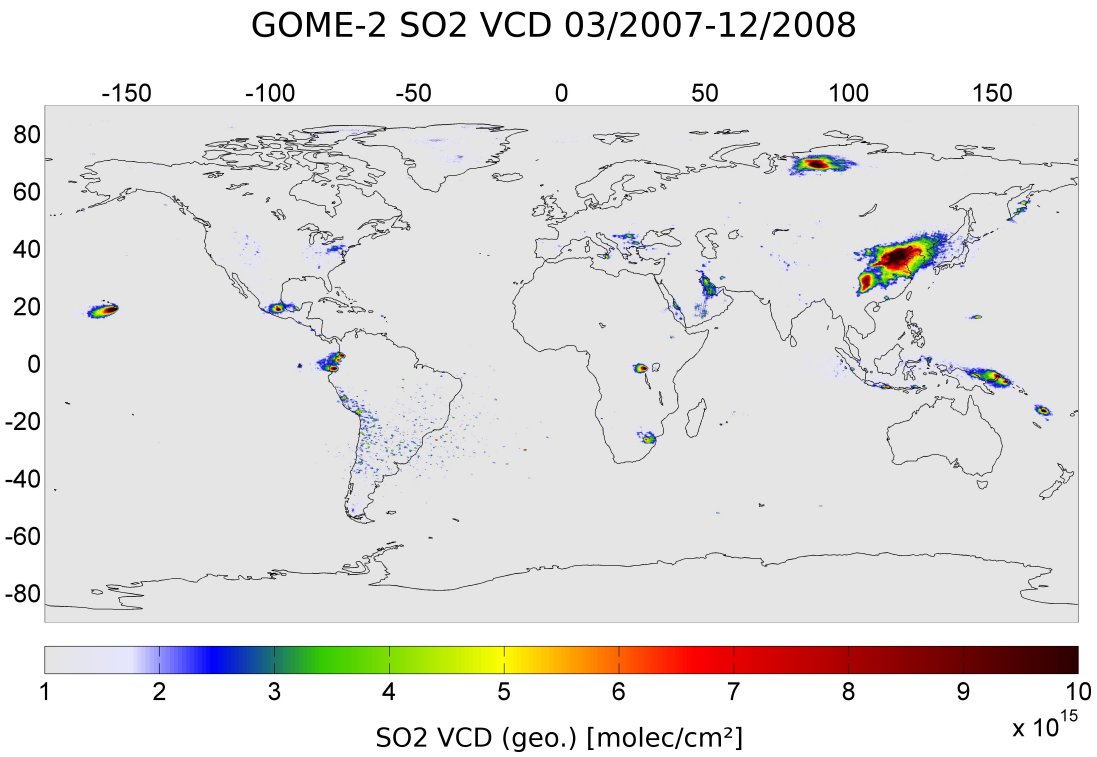

Figure 2.4: *Mean global distribution of the atmospheric SO_2 vertical column density retrieved from GOME-2 satellite measurements (Christoph Hörmann, IUP Heidelberg, personal communication).*

which is usually removed from the atmosphere by precipitation. This reaction is also a sink for OH and describes how NO_2 degrades the concentration of the hydroxyl radical.

2.2.2 Sulfur Dioxide

The majority of SO_2 emissions originate from anthropogenic sources (Brasseur et al., 1999). The combustion of fossil fuel containing sulfur emits SO_2. It is converted to sulfuric acid (H_2SO_4) which causes acid rain. One consequence of the negative effects connected to acid rain is the endeavor to increase the usage of desulfurized fuel. Several branches of industry generate SO_2 in their applied processes, like e.g. in the metal, smelting industry and in oil refineries. Furthermore, biomass burning, ignited either naturally or due to agricultural activity, also produces SO_2. The most important natural source of sulfur compounds are volcanoes. Besides water vapor and CO_2, volcanic emissions contain, in the order of descending magnitude, SO_2, hydrogen sulphide (H_2S), carbonyl sulphide (COS) and carbon disulphide (CS_2) (Textor et al., 2004). All further natural sources emit sulfur compounds in a reduced form, which are rapidly oxidized by OH in the atmosphere and generate SO_2. H_2S is a by-product of the degradation of proteins and is present in the atmosphere with mixing ratios up to 300 ppb. It smells like rotten eggs. COS is emitted by

organic species near the surface layer of the ocean (Ulshöfer and Andreae, 1997) or from soils and marshes (Ulshöfer, 1995). CS_2 is naturally released by the ocean, marshes and forests, but also from industrial activities (Watts, 2000). Furthermore, dimethyl sulphide (DMS, CH_3SCH_3) is produced by biological processes in the ocean (Andreae et al., 1985).
The mean global distribution of the atmospheric SO_2 vertical column density retrieved from satellite measurements is shown in Figure 2.4. The SO_2 column densities are remarkably increased especially above China due to industrial activity. Several individual volcanoes emitting large amounts of SO_2 can be identified as isolated sources, like e.g. in Hawaii and Indonesia.
The removal of approximately 30–50 % of the total SO_2 from the atmosphere takes place by dry deposition (see Section 2.4) on the gound. The most important gas-phase reaction of SO_2 is oxidation, which is initiated by OH addition (Stockwell and Calvert, 1983):

$$SO_2 + OH + M \longrightarrow HSO_3 + M \tag{2.11a}$$
$$HSO_3 + O_2 \longrightarrow SO_3 + HO_2 \tag{2.11b}$$
$$SO_3 + H_2O + M \longrightarrow H_2SO_4 + M \tag{2.11c}$$

where about 30 % of the total SO_2 is degraded. During these reactions, the oxidation capacity of the atmosphere does not change. Due to its relatively high solubility in water, SO_2 reacts with liquid water. Thus, an equilibrium of SO_2 in gas phase and SO_3^{2-} in liquid phase occurs, e.g. in clouds. The involved reactions are:

$$SO_{2\,(g)} + H_2O_{(liq)} \longleftrightarrow H_2SO_{3\,(liq)} \tag{2.12a}$$
$$H_2SO_{3\,(liq)} \longleftrightarrow HSO^-_{3\,(liq)} + H^+_{(liq)} \tag{2.12b}$$
$$HSO^-_{3\,(liq)} \longleftrightarrow SO^{2-}_{3\,(liq)} + H^+_{(liq)} \tag{2.12c}$$

H_2SO_3 and SO_3^{2-} in liquid phase can be further oxidized to H_2SO_4 and sulphate (SO_4^{2-}), for example by hydrogen peroxide (H_2O_2). The sulphate formed is eventually transported to the ground together with the cloud or fog droplets, thus contributing to acid rain or acid haze.
H_2SO_4 will quickly condense after its formation in the gas phase, due to its low vapor pressure. Thus, small particles are formed, which can act as cloud condensation nuclei (CCN) and therefore impact cloud formation. Then, the formed clouds consist of more and smaller cloud droplets, since the available water in the atmosphere is distributed to more droplets. This process results in an increase of the cloud albedo compared to clouds consisting of less and larger droplets. In addition to this indirect aerosol cooling effect on the Earth's radiative budget, a direct aerosol effect occurs due to sulphate particles. Volcanic emissions of SO_2 are known to be transported to the stratosphere, where the formed sulfate particles have a cooling effect since the solar radiation is scattered back to space.

2.3 The Oxygen Collision Complex

The interaction of pairs of O_2 molecules result in different bonded molecules, i.e. the weakly bonded van der Waals dimer O_4 and the collisionally induced complex $(O_2)_2$. In contrast to the discrete structured ro-vibrational bands of the electronic transition of O_2 and the structured bands of the dimer O_4, $(O_2)_2$ also has broad unstructured absorption bands (see, e.g., Greenblatt et al., 1990; Solomon et al., 1998; Wagner et al., 2002). While absorption features due to $(O_2)_2$ were already known for solid, liquid and high pressure oxygen, the first atmospheric observation was carried out by Perner and Platt (1980). The bands in the region from 300–1300 nm belong to transitions between dimers of ground state oxygen molecules and electronically exited states of $(O_2)_2$. The weak temperature dependence of the $(O_2)_2$ absorption under atmospheric conditions indicate that they are related to the collision complex rather than to the bonded dimer (Greenblatt et al., 1990). It should be noted, that ab initio studies determined that the most stable form of covalently bonded O_4 lies higher in energy than molecular O_2 (Adamantides et al., 1980; Adamantides, 1980). Thus, the contribution of covalently bonded O_4 is negligible under atmospheric conditions.
The atmospheric concentration profile of $(O_2)_2$ is well known, since it is proportional to the square of the O_2 concentration:

$$c_{(O_2)_2}(z) = k_{eq} \cdot (0.21 \cdot c_{air}(z))^2 \tag{2.13}$$

where $c_{air}(z)$ denotes the air density at the altitude z and k_{eq} is the equilibrium constant. k_{eq} is not well known, but since the literature absorption cross section of $(O_2)_2$ used for absorption spectroscopy measurements includes this equilibrium constant, the retrieved optical densities are not affected (see Section 3.5). The profile of $(O_2)_2$ is fairly constant in time and depends only on the small changes of the air density due to the temperature and barometric pressure. The scale height of $(O_2)_2$ corresponds roughly to 4 km.
While the collision complexes of two ground state oxygen molecules are probably not significant for atmospheric chemistry, the exited electronic states of $(O_2)_2$ may be of importance (Perner and Platt, 1980). However, investigations and observations concerning such capabilities where not reported yet.
The absorptions of $(O_2)_2$ are generally used as an indicator for the changes in the radiative transfer in the atmosphere, since the profile of $(O_2)_2$ is known (equation (2.13)). Therefore, the observed changes in the absorption are due to the according light path. In combination with radiative transfer simulations and numerical inversion methods, the information on the light path can be gained from $(O_2)_2$ absorption measurements. This approach is also applied in this work (see Section 3.5 and Chapter 5).
The oxygen collision complex $(O_2)_2$ will be referred to as O_4 in the following, since this term is conventionally used in the Differential Optical Absorption Spectroscopy literature.

Table 2.3: *Global emission estimates for major aerosol classes (Seinfeld and Pandis, 2006, and references therein).*

Source	Estimated flux [Tg y^{-1}]
Natural primary	
Mineral dust	1490
Seasalt	10100
Volcanic dust	30
Biological debris	50
Natural secondary	
Sulfates from DMS	12.4
Sulfates from volcanic SO_2	20
Organic aerosol from biogenic VOC	11.2
Anthropogenic primary	
Industrial dust (except black carbon)	100
Black carbon	12 (Tg C)
Organic aerosol	81 (Tg C)
Anthropogenic secondary	
Sulfates from SO_2	48.6 (Tg S)
Nitrates from NO_x	21.3 (Tg NO_3^-)

2.4 Atmospheric Aerosols

An aerosol is defined as a suspension of fine solid or liquid particles in a gas. However, the general usage of the term aerosol refers to the particulate component only. Aerosols in the atmosphere originate from natural as well as anthropogenic sources. Thereby, a distinction is made between primary aerosols, which are emitted directly, and secondary aerosols, which are formed in the atmosphere by the conversion of gas to particles in various processes. Several chemical and physical processes can change the size and composition of aerosols once they are suspended in the atmosphere. The sizes of the particles range from a few nanometers to tens of micrometers in the diameter, while particles smaller than 1 μm diameter usually have atmospheric concentrations in the range from roughly ten to several thousand per cm^3 and those exceeding 1 μm diameter generally have concentrations less than 1 per cm^3.

Table 2.3 presents a range of emission estimates of particles generated from natural and anthropogenic sources, on a global basis. Natural emissions are mainly driven by dispersion due to wind. The highest natural direct emissions result from sea spray, which produce sea salt aerosols when air bubbles burst in the crest of a wave. Sea salt aerosols contain mainly sodium chloride (NaCl), calcium sulfate ($CaSO_4$) and magnesium chloride ($MgCl_2$). Further natural sources for direct aerosol emissions are soil and rock debris as well as dust. These particles consist mainly of minerals and are therefore referred as mineral dust. Especially in very dry desert regions, strong winds can disperse large amounts of dust, which can be transported over

Table 2.4: *Concentrations of selected elements found in atmospheric aerosols and the corresponding particle size ranges (Schroeder et al., 1987).*

Element	Aerosol mode (Fine, Coarse)	Concentration [ng m^{-3}]		
		Remote	Rural	Urban
Fe	F and C	0.6-4200	55-14500	130-13800
Pb	F	0.01-65	2-1700	30-90000
Zn	F	0.03-450	10-400	15-8000
Cd	F	0.01-1	0.4-1000	0.2-7000
As	F	0.01-2	1-28	2-2500
V	F and C	0.01-15	3-100	1-1500
Cu	F and C	0.03-15	3-300	3-5000
Mn	F and C	0.01-15	4-100	4-500
Hg	-	0.01-1	0.05-160	1-500
Ni	F and C	0.01-60	1-80	1-300
Sb	F	0-1	0.5-7	0.5-150
Cr	F and C	0.01-10	1-50	2-150
Co	F and C	0-1	0.1-10	0.2-100
Se	F and C	0.01-0.2	0.01-30	0.2-30

long distances and subsequently serve as fertilizer for oceanic plankton. Volcanic eruptions emit both directly dust and SO_2, which generates sulfate particles (see Section 2.2.2). Furthermore, the emission of pollen by vegetation and the direct and indirect aerosol production by biomass burning contribute to the natural emissions. Anthropogenic emissions of particulate matter arise primarily from fuel combustion, industrial processes and any kind of traffic. These source categories emit primary aerosols mainly consisting of carbonaceous compounds, which can be divided into black carbon and organic aerosols. While the latter can be produced also from atmospheric reactions involving emitted gaseous organic precursors, black carbon aerosols can be produced only in a combustion process and is therefore solely primary. Black carbon aerosols are also referred to as soot, which is used to refer to any light-absorbing, combustion-generated carbonaceous material. Additionally, the anthropogenic NO_2 and SO_2 emissions result in the generation of secondary nitrate and sulfate particles, respectively (see Section 2.2.1 and 2.2.2), and the emission of primary aerosols due to wind erosion of cropland can be attributed to as anthropogenic.

The geographic distribution of the aerosol sources is inhomogeneous, and there are large variations on a global scale. An additional reason for this is the removal processes for aerosols. On the one hand, the dry deposition of mainly larger particles at the Earth's surface, and on the other hand, the incorporation into cloud droplets during the formation of precipitation. The latter is referred to as wet deposition, and includes the acting of smaller particles as cloud condensation nuclei as well as the washing out of particles of any size by precipitation. In contrast to atmospheric trace gases, which have lifetimes ranging from less than a second to a century or more, tropospheric aerosols exhibit residence times varying only from a few days to

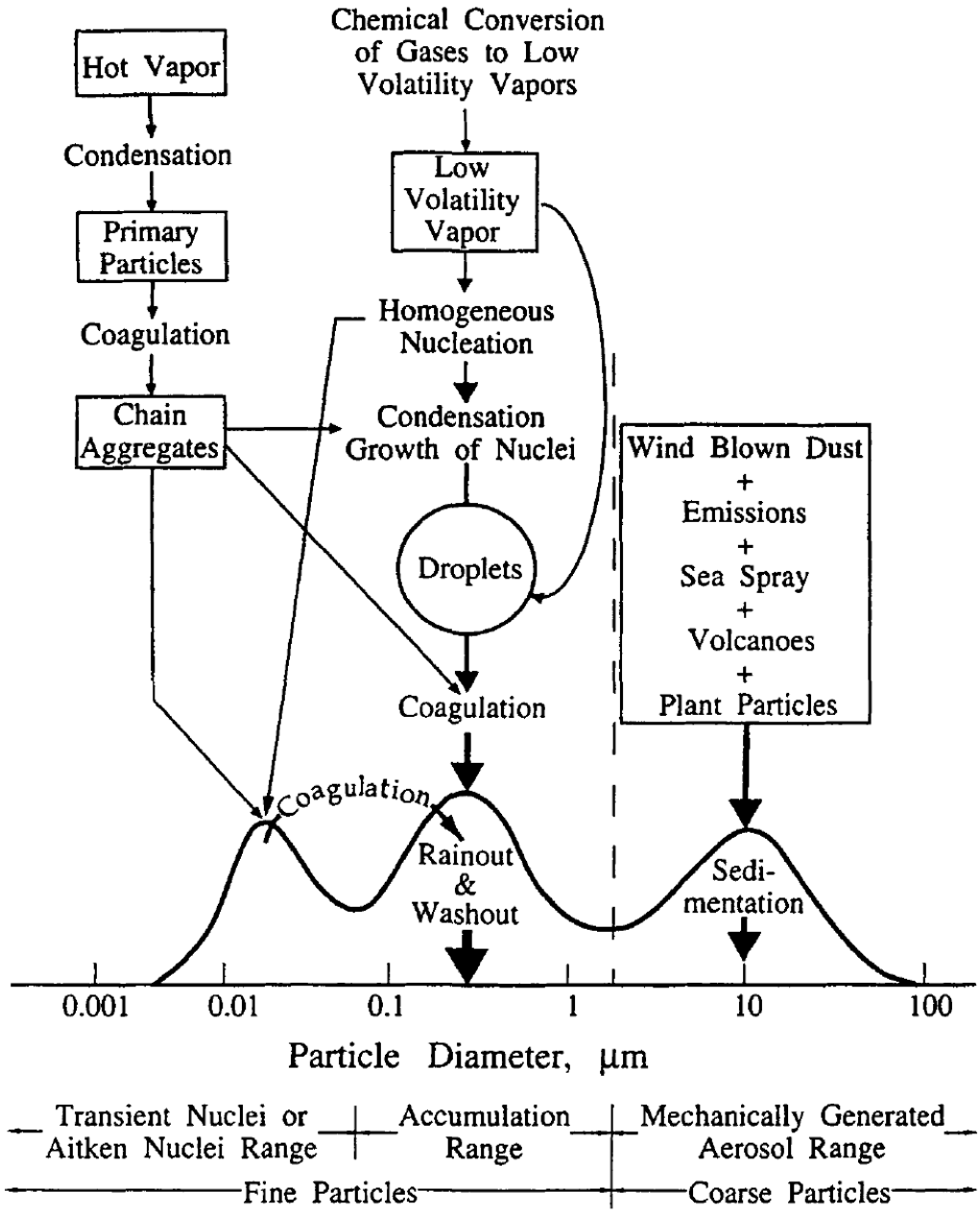

Figure 2.5: *Idealized schematic of the distribution of particle surface area of an atmospheric aerosol. Principal modes, sources, and particle formation and removal mechanisms are indicated. Adapted from (Seinfeld and Pandis, 2006).*

a few weeks.

Table 2.4 gives an overview of the concentrations of selected elements found in atmospheric aerosols depending on the region. The size mode of the according particles are also given. For similar pollution levels, the concentration of these elements vary over a large range, indicating the strong influence of local sources on the chemical composition of the particles.

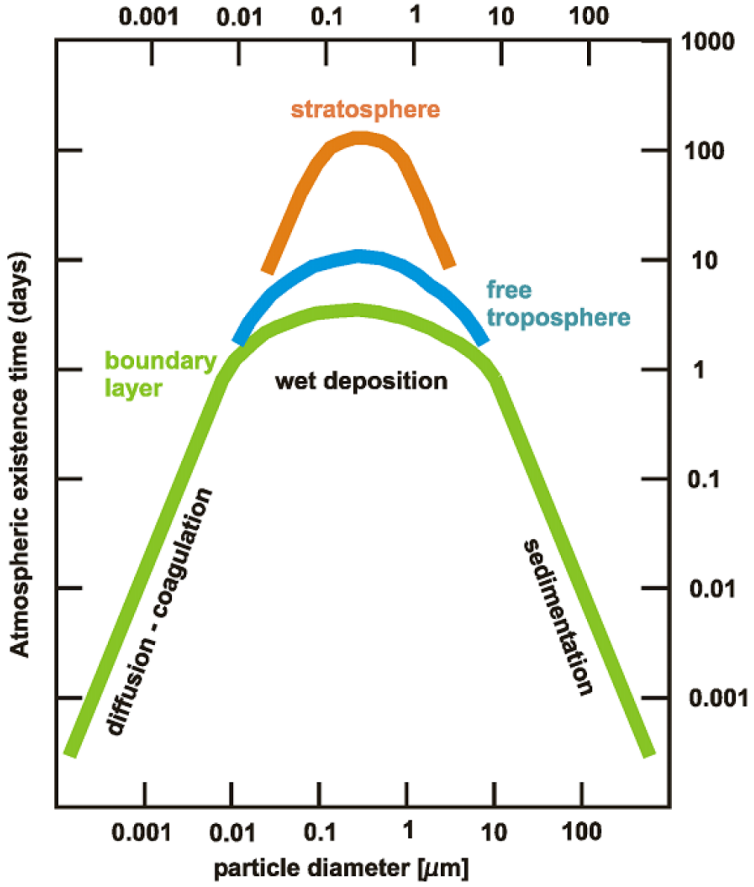

Figure 2.6: *Atmospheric resistance time as a function of particle diameter for the different atmospheric layers. The predominant removal mechanisms are indicated. Adapted from (Jaenicke, 1978).*

In the stratosphere, globally distributed background aerosols are present. It is composed of an aqueous sulfuric acid solution, which is generated from COS originating from the Earth's surface. Due to its long tropospheric life time, COS diffuses into the stratosphere where it is dissociated by solar ultra-violet radiation and forms sulfuric acid. In addition, frequent volcanic eruptions inject remarkable amounts of SO_2 directly into the stratosphere (e.g., Brasseur and Granier, 1992). Here, the aerosol residence times are much longer (≈ 1 year) than in the troposphere, since the efficiencies of the deposition mechanisms are strongly reduced.

Once the particles are in the atmosphere, their size and composition can change due to evaporation, coagulation, chemical reactions, or activation in conditions with supersaturated water to form fog and cloud droplets. Furthermore, the particles can serve as catalysts, since chemical reactions proceed faster at surfaces than in gaseous phase. The processes influencing the particle sizes are shown in an idealized schematic in Figure 2.5. In addition, the typical distribution of surface area of atmospheric aerosols is shown. The lower and upper limit for the size range of atmospheric aerosols can be localized by considering two general phenomena. The

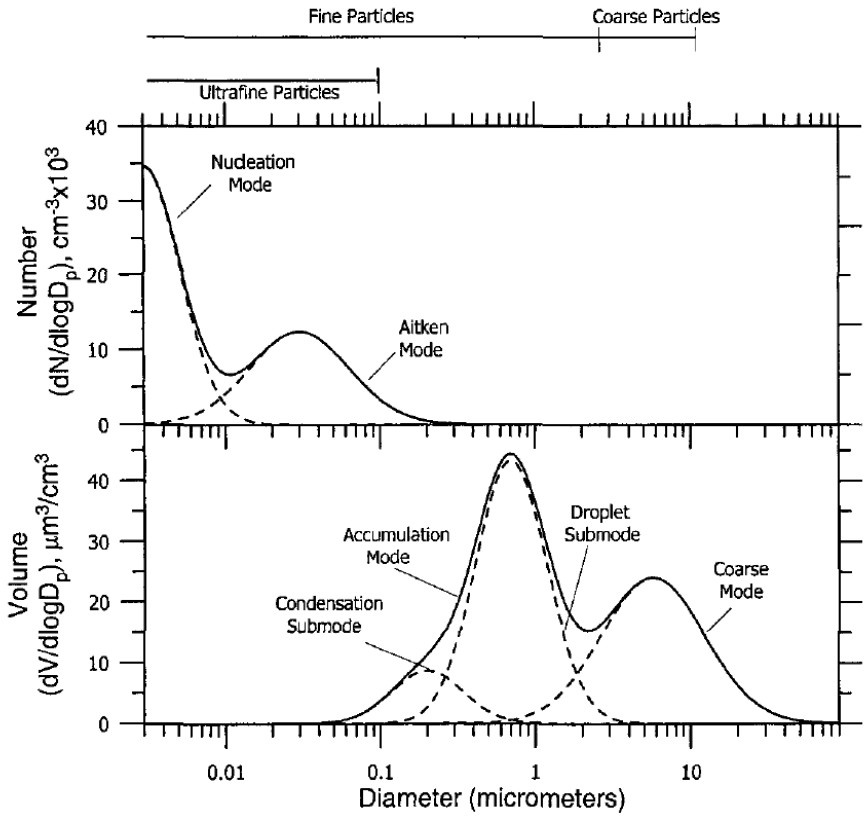

Figure 2.7: *Typical number and volume distributions of atmospheric particles with the different modes. Adapted from (John et al., 1990; Seinfeld and Pandis, 2006).*

upper limit is determined by the settling velocity of large particles, which causes sedimentation. Since the settling velocity varies approximately with the square of the particle radius, larger particles have smaller atmospheric residence times and are removed rapidly by sedimentation. At the lower size range limit, particles originating from nucleation can repeatedly evaporate and condense again before they reach a critical size of a stable state. The critical size is not uniquely defined, since it depends on atmospheric conditions. It is determined by the temperature, relative humidity and, e.g., the oxidation rate of SO_2, which yields the condensable sulphuric acid molecules.

The atmospheric particles can be divided in different modes as depicted in Figure 2.5. Particles with diameters up to about 10 nm compose the nucleation (or nuclei) mode, while the Aitken mode comprises particles with diameters ranging from about 10 nm to 100 nm. These two modes account for the dominance of particles by number, while their total mass rarely account for more than a few percent due to their small size. The nucleation mode contains particles, which are formed during combustion processes by the condensation of hot vapors as well as by nucleation of atmospheric species. The coagulation with larger particles causes the depopulation of this size regime. Usually, most of the aerosol surface area and a considerable part of the aerosol mass is comprised by the accumulation mode, which ranges from 0.1 to about 2.5 μm in particle diameter. The particles in this mode originate from co-

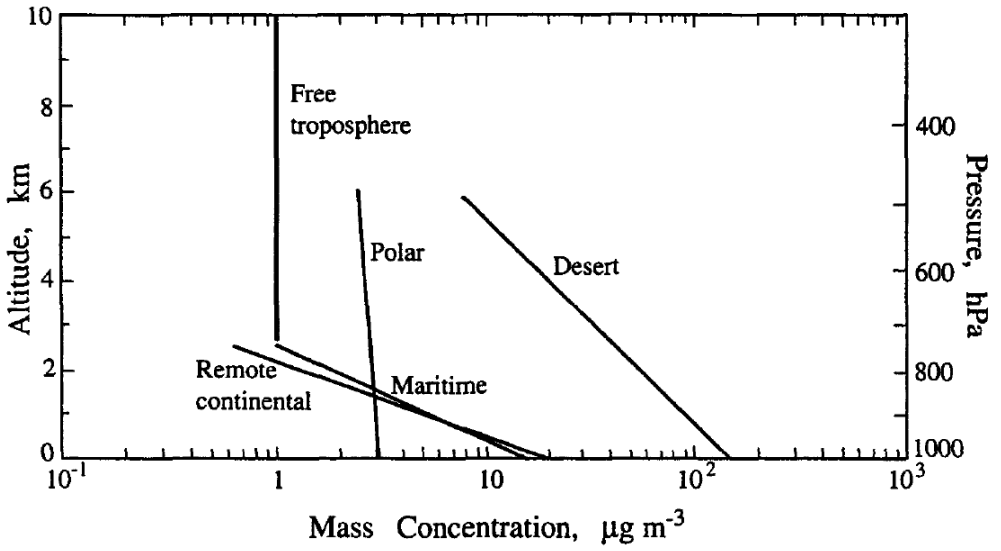

Figure 2.8: *Representative vertical distribution of aerosol mass concentration. Adapted from (Jaenicke, 1993).*

agulation of particles in the nucleation mode and from condensation of vapors onto existing particles, resulting in the growth into this size range. The adjacent size range of particle with diameters larger than 2.5 μm depicts the coarse mode, containing aerosols generated by mechanical processes like natural and anthropogenic dust particles.

Since the particle removal mechanisms are efficient at the small and large particle extremes of the size spectrum, the particles accumulate in the accumulation mode size range. Here, the removal mechanisms are inefficient and result in longer atmospheric residence times than those in either the nucleation or coarse mode. Figure 2.6 shows the atmospheric resistance time as a function of particle diameter for the different atmospheric layers. Also the predominant removal mechanisms are indicated.

The above mentioned differences in the contributions of the individual modes to the total number and mass of atmospheric aerosols is accounted for by using different representations of the aerosol size distribution. For this purpose, the size distributions are generally described with respect to the aerosol number and volume. The according distribution functions are then represented by $n_N(\log D_p) = \mathrm{d}N/\mathrm{d}\log D_p$ and $n_V(\log D_p) = \mathrm{d}V/\mathrm{d}\log D_p$ for the number N and volume V, respectively. Since the particle diameter size range spans over several orders of magnitude, the logarithm of the diameter D_p normalized with 1 μm is used. Thus, the size distributions for the number and volume of aerosols are given in units of cm^{-3} and $\mu\mathrm{m}^3/\mathrm{cm}^3$, respectively. The relation between both distributions is described by:

$$n_V(\log D_p) = \frac{\pi}{6} D_p^3 \cdot n_N(\log D_p) \tag{2.14}$$

For the mathematical description of these size distributions, the lognormal distribution is used in atmospheric applications, which is the logarithm version of the normal distribution.
Figure 2.7 shows typical number and volume distributions of atmospheric particles. It also contains the lognormal size distributions of the individual modes, which are depicted by the dashed lines. The number distribution is dominated by the nucleation and Aitken mode (Figure 2.7, upper panel). In contrast, the accumulation and coarse mode dominate the volume distribution and contribute practically all the aerosol mass (Figure 2.7, lower panel). Furthermore, the accumulation mode often consists of two overlapping submodes, which are the condensation mode and the droplet mode (John et al., 1990).
The typical vertical distribution of mass concentrations of different aerosol types is shown in Figure 2.8. These profiles are rough representations of long-term averages (Jaenicke, 1993), while large local variations occur especially in urban areas depending on the emission sources. The mass concentration profiles of the different aerosol types typically decrease exponentially with altitude in the lower troposphere, wheres the back ground profile in the free troposphere remains constant with altitude.
The impact of atmospheric aerosols on the global radiative budget occurs directly and indirectly (see Section 2.2.2). Fine particles can serve as CCN and increase the cloud albedo due to the formation of smaller and more cloud droplets. Then, the indirect aerosol cooling effect occurs due to the larger fraction of solar radiation reflected back to space. Furthermore, since aerosols scatter radiation rather than absorb, the direct cooling effect results from the shielding of solar radiation. The knowledge on these effects of atmospheric aerosols is subject to large uncertainties (IPCC, 2007).

Chapter 3

Differential Optical Absorption Spectroscopy

Since its introduction by Platt et al. (1979), Differential Optical Absorption Spectroscopy (DOAS) became more and more an indispensable and powerful remote sounding technique for the determination of atmospheric constituent concentrations. It has been applied for three decades to measure a wide variety of gaseous species relevant to atmospheric chemistry. Several trace gas species were detected the first time by DOAS, e.g. OH by Perner et al. (1976), HONO by Perner and Platt (1979), NO_3 by Platt and Perner (1980), BrO by Sanders et al. (1989) and Hausmann and Platt (1994), IO by Alicke et al. (1999) and CHOCHO by Volkamer et al. (2005a). Also several other trace gases like e.g. O_3, NO_2, SO_2, HCHO, H_2O, NH_3, ClO, OClO and CS_2 can be detected due to their individual absorption cross sections in the ultra-violet and visible wavelength region (Platt, 1994; Platt and Stutz, 2008). Also CH_4, CO and CO_2, absorbing in the near-infrared wavelength region, can be detected by DOAS (e.g., Frankenberg et al., 2005).

DOAS is based on the spectral analysis of light, which has undergone characteristic absorption by the constituents of a certain air mass. The individual absorption cross section of each trace gas allows for the unambiguous identification and determination of the corresponding concentrations contained in the probed air mass simultaneously. Due to the contact free nature of the DOAS technique, highly reactive species can be detected under ambient conditions without uncertainties due to interactions within the measurement process.

Depending on the origin of the collected light to be analyzed by the DOAS technique, it can be distinguished between passive and active DOAS. While passive DOAS instruments case utilize natural extraterrestrial light sources like the Sun or the Moon, and can be further divided into direct and scattered light DOAS, active DOAS applications are based on artificial light sources like e.g. high pressure Xe-arc lamps or light emitting diodes.

A large number of different passive and active applications were developed since the first introduction of DOAS. While the first passive DOAS instruments collected scattered sunlight only from the zenith viewing direction, which allows for the investigation of trace gases in the stratosphere, the introduction of the Multi-Axis-DOAS (MAX-DOAS) technique enabled to derive information on the vertical distribution

of trace gases in the troposphere (e.g., Hönninger and Platt, 2002; Hönninger et al., 2004). Thereby, the viewing direction is varied subsequently, whereby the height information is gained.
MAX-DOAS instruments are generally simple, robust and cost-effective with moderate maintenance demands, and therefore highly suited for longterm measurements and the integration in worldwide atmospheric monitoring networks. Several networks of MAX-DOAS instruments have been instituted in the recent past. The Network for the Detection of Atmospheric Composition Change (NDACC), a major contributor to the worldwide atmospheric research effort, includes several stations equipped with DOAS instrumentation (e.g., Brinksma et al., 2008; Roscoe et al., 2010). The Network of Observation of Volcanic and Atmospheric Change (NOVAC) is monitoring volcanic SO_2 emissions with more than 50 MAX-DOAS instruments at over 20 volcanoes, mainly in Latin America (Galle et al., 2010). The Institute of Environmental Physics of the University of Heidelberg runs a MAX-DOAS network with instruments set up at measurement sites ranging from mid-latitudes to Polar Regions (e.g., Frieß et al., 2010). The Institute of Environmental Physics of the University of Bremen runs an equivalent MAX-DOAS network BEDROM (Bremen DOAS Network for Atmospheric Measurements; e.g., Wittrock et al., 2004). The Anhui Institute of Optics and Fine Mechanics of the Chinese Academy of Sciences in Hefei is about to built up a MAX-DOAS network in China.
The compact construction of MAX-DOAS instruments allow for the installation on a large number of different platforms, such as cars (e.g., Ibrahim et al., 2010; Wagner et al., 2010), vessels (e.g., Martin et al., 2009), airplanes (e.g., Dix et al., 2009; Heue et al., 2010) and research balloons, whereas the latter are even able to rise up into the stratosphere (e.g., Kritten et al., 2010).
The basic active DOAS application is long path DOAS, where artificial light is emitted by the telescope, reflected at retro-reflectors in several kilometers distance and finally received again. The measurements are limited to the lowermost atmosphere, but in contrast to passive DOAS, continuous night-time measurements are possible (e.g., Sihler et al., 2009; Kern et al., 2009; Poehler et al., 2010; Frieß et al., 2011). By combining several intersecting light paths, tomographic DOAS measurements can provide information on the spatial trace gas distribution in the surface near atmospheric layer. Multiple reflection cells (White Cells) increase the light path through a defined small air sample and thus enable in-situ DOAS measurements. Similar is possible with Cavity Enhanced Absorption Spectroscopy, which implements the light path increase by an optical cavity system (e.g., Platt et al., 2009, 2010).
Passive DOAS instruments installed aboard satellites enable an unique and objective view on the global distribution of atmospheric trace gases, which is independent from national political interests (Wagner, 2007). Beginning in 1996, several research satellites with DOAS instruments were launched into the Earth's orbit: the Global Ozone Monitoring Experiment (GOME, e.g., Beirle et al., 2003) aboard the satellite ERS-2, the Scanning Imaging Absorption Spectrometer for Atmospheric Chartography (SCIAMACHY, e.g., Kuehl et al., 2008) aboard Envisat, the Ozone Monitoring Instrument (OMI, e.g., Beirle et al., 2011) aboard NASA/EOS-Aura and GOME-2 (e.g., Heue et al., 2010) aboard MetOp. Several successor satellites are already planed to continue the observations from space.

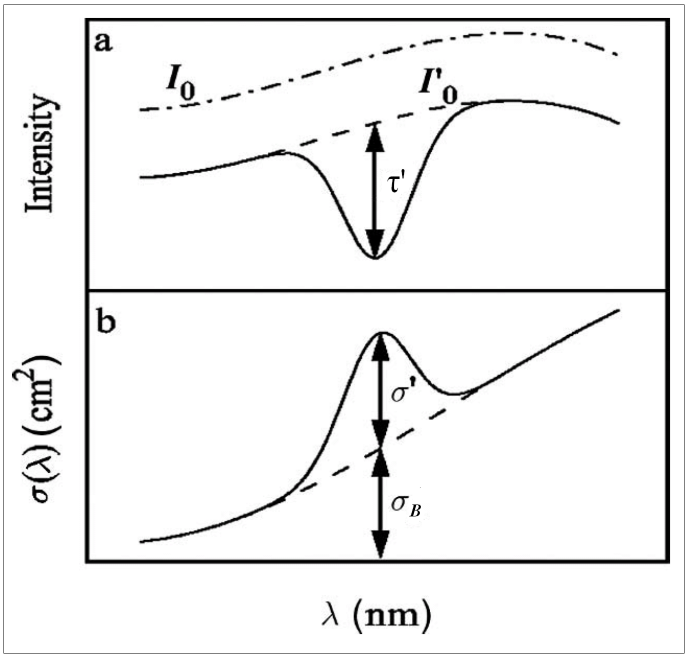

Figure 3.1: *Basic principle of DOAS: I_0 and σ are separated by an adequate filtering procedure into a narrow (τ' and σ') and broad band part (I'_0 and σ_B). Adapted from Platt and Stutz (2008)*

Two-dimensional images color coded with the trace gas spatial distribution can be retrieved from imaging DOAS measurements, which is especially suited for monitoring power plants or volcanic plumes (Heue et al., 2008).
Since this work is based on MAX-DOAS measurements, only the basics and concepts relevant to MAX-DOAS will be introduced in the following. After the explanation of the general DOAS principle in Section 3.1, the experimental implementation and spectral analysis principle are discussed in Section 3.2 and 3.3, respectively. The additional effects to be considered in the framework of passive DOAS measurements are discussed in Section 3.4. The principle of MAX-DOAS is explained in Section 3.5, followed by the summary of the spectral retrieval settings in Section 3.6 for trace gases measured in line with this work.
The interested reader is referred to the book "Differential Optical Absorption Spectroscopy" written by Platt and Stutz (2008), where all basics, principles, concepts and applications are discussed in detail.

3.1 The DOAS Principle

DOAS is based on the Lambert-Beer Law, which describes the relationship between an incident intensity, the extinction capacity of the traversed matter and the remaining intensity:

$$I(\lambda, L) = I_0(\lambda) \cdot e^{-\sigma(\lambda) \cdot c \cdot L} \,, \tag{3.1}$$

with the wavelength dependent incident and remaining intensity $I_0(\lambda)$ and $I(\lambda, L)$, respectively. $\sigma(\lambda)$ is the wavelength dependent absorption cross section of the material and L denotes the light path length in the material. In passive DOAS measurements, the Sun serves as light source and the traversed material is the Earths's atmosphere with several absorbers, so that equation (3.1) can be extended to:

$$I(\lambda, L) = I_0(\lambda) \cdot e^{-\int_0^L \left[\sum_{j=1}^{n} \sigma_j(\lambda,p,T)\cdot c_j(l)+\epsilon_R(\lambda,l)+\epsilon_M(\lambda,l)\right] \mathrm{d}l} . \tag{3.2}$$

Now, the extinction is described by the absorption cross sections $\sigma_j(\lambda, p, T)$ of the trace gas j in units of $[\frac{\mathrm{cm}^2}{\mathrm{molec}}]$, which depend on the wavelength λ, the temperature T and the pressure p, and the according concentrations $c_j(l)$ along the light path. Rayleigh and Mie scattering (see Section 4.2) are included by the extinction coefficients $\epsilon_R(\lambda, l)$ and $\epsilon_M(\lambda, l)$, respectively.
The optical density $\tau(\lambda, L)$ is defined as:

$$\tau(\lambda, L) := \ln\left(\frac{I_0(\lambda)}{I(\lambda, L)}\right) . \tag{3.3}$$

The determination of $\tau(\lambda, L)$ from ground based passive DOAS measurements requires the knowledge on I_0. It is, in this case, the solar radiation before entering the Earth's atmosphere, which is not always available for obvious reasons. Additionally, the retrieval of the optical density due to absorption by trace gases would require the exact knowledge of the overlaid scattering processes in equation (3.2), which is also not possible without further effort. These restrictions can be overcome by the basic concept of the DOAS technique, which is the separation of the absorption cross section $\sigma(\lambda, p, T)$ according to:

$$\sigma(\lambda, p, T) := \sigma'(\lambda, p, T) + \sigma_B(\lambda, p, T) , \tag{3.4}$$

with the differential (narrow band) and broad band part of the absorption cross section $\sigma'(\lambda, p, T)$ and $\sigma_B(\lambda, p, T)$, respectively. In practice, this separation can be done by high pass filtering. Inserting equation (3.4) into equation (3.2) and subsequent rearrangement results in:

$$\begin{aligned} I(\lambda, L) &= I_0(\lambda) \cdot e^{-\int_0^L \left\{\sum_{j=1}^{n} \left[\sigma'_j(\lambda,p,T)+\sigma_{B,j}(\lambda,p,T)\right]\cdot c_j(l)+\epsilon_R(\lambda,l)+\epsilon_M(\lambda,l)\right\} \mathrm{d}l} \\ &= I'_0(\lambda, L) \cdot e^{-\int_0^L \left[\sum_{j=1}^{n} \sigma'_j(\lambda,p,T)\cdot c_j(l)\right] \mathrm{d}l} , \end{aligned} \tag{3.5}$$

where $I'_0(\lambda, L)$ includes $I_0(\lambda)$ and the broad band structured part of the extinction, which consists of the broad band part of the trace gas absorption cross section as well as the Mie and Rayleigh extinction coefficients. In analogy to equation (3.3) and using equation (3.5), the differential optical density $\tau'(\lambda, L)$ is defined as:

$$\tau'(\lambda, L) = \ln\left(\frac{I'_0(\lambda)}{I(\lambda, L)}\right) . \tag{3.6}$$

This relationship is illustrated in Figure 3.1. The slant column density (SCD) S is defined as:

$$S = \int_0^L c(l)\ \mathrm{d}l\ , \tag{3.7}$$

and is the integrated concentration $c(l)$ of the trace gas along the light path l given in units of $[\frac{\mathrm{molec}}{\mathrm{cm}^2}]$. This is the basic quantity measured by DOAS and can also be described by inserting equation (3.7) in equation (3.5) and comparing with equation (3.6) as:

$$S = \frac{\tau'(\lambda, L)}{\sigma'(\lambda, p, T)}\ . \tag{3.8}$$

Since passive DOAS measurements utilize a reference spectrum $I'_0(\lambda)$ which also contains absorption by trace gases, the determined SCD is a differential SCD, namely the difference between the actual SCD and the SCD contained in the employed reference spectrum for the calculation of the intensity ratio in equation (3.6).

3.2 Experimental Implementation

The typical setup of a DOAS measurement is sketched in Figure 3.2. The intensity $I_0(\lambda)$ emitted by the light source traverses the air mass of the atmosphere to be probed and contains the individual trace gas absorption structures afterwards. The intensity $I(\lambda, L)$, which has a high spectral resolution and contains in this case only the absorption of formaldehyde (HCHO), enters the entrance slit of a grating spectrograph (Figure 3.2a). The optical properties of the spectrograph, namely the grating properties and the entrance slit, cause a spectral degradation of $I(\lambda, L)$ (Figure 3.2b). This $I^*(\lambda, L)$ is imaged on the detector and can be described by the convolution of $I(\lambda, L)$ with the instrument function H:

$$I^*(\lambda, L) = H * I(\lambda, L) = \int I(\lambda') \cdot H(\lambda - \lambda')\ \mathrm{d}\lambda'\ . \tag{3.9}$$

The detector consists of discrete pixels, whereby the intensity $I^*(\lambda, L)$ mapped on a single pixel i is integrated within the according wavelength interval λ_i and λ_{i+1} (Figure 3.2c):

$$I'(i) = \int_{\lambda_i}^{\lambda_{i+1}} I^*(\lambda', L)\ \mathrm{d}\lambda'\ . \tag{3.10}$$

In most cases, the wavelength mapping can be approximated by a polynomial:

$$\lambda(i) = \sum_{k=0}^{q} \beta_k \cdot i^k\ , \tag{3.11}$$

which describes the relationship between the pixel i and the wavelength $\lambda(i)$. Usually, a polynomial of order two suits best for this wavelength calibration. Thereby, a spectral shift and squeeze or stretch is scaled by the zeroth and first order coefficient, respectively. The second and eventually higher order coefficients scale possible spectral distortion, due to unequal spectral pixel widths. The wavelength calibra-

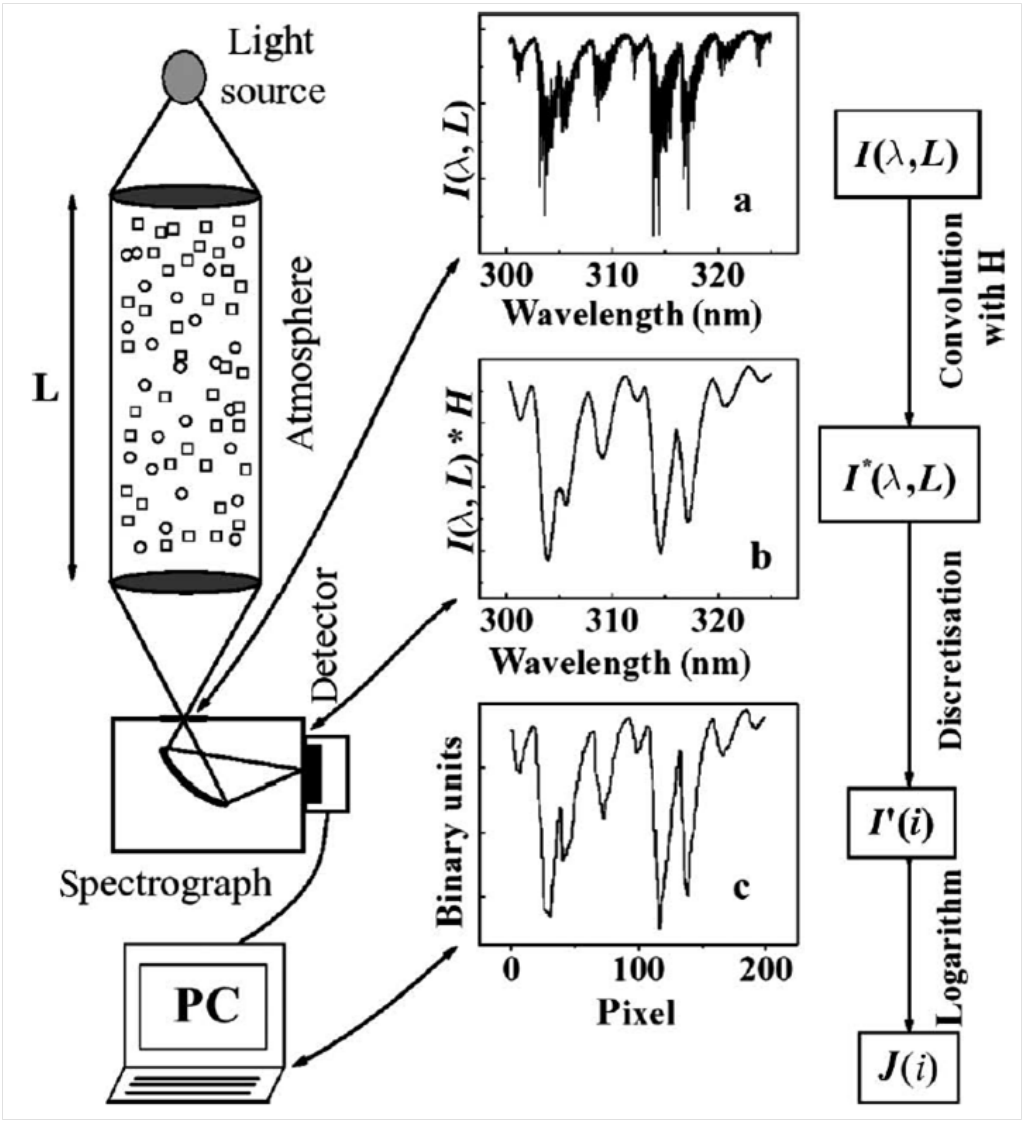

Figure 3.2: *Schematic view of a DOAS instrument used to measure trace-gas concentrations. Collimated light undergoes absorption processes on its way through the atmosphere. In (a), an example of this light entering the spectrograph is given when HCHO is assumed to be the only absorber. (b), the same spectrum convolved with the spectrograph's instrumental function reaches the detector. In the detector the wavelength is mapped to discrete pixels. This spectrum, (c), is then stored in the computer and can be analyzed numerically. Adapted from Stutz and Platt (1996)*

tion strongly depends on the spectrometer temperature (see Section 7.1.2). Thus, the changes in the optical properties of the spectrometer due to its temperature has to be taken into account thoroughly.
Usually, differential trace gas absorption cross sections $\sigma(\lambda, T, p)$ measured in the laboratory with high spectral resolution instruments are used for the DOAS analysis procedure. Therefore, the instrument dependent wavelength calibration from equation (3.11) has to be applied. Furthermore, the consideration of the spectral

resolution by convolution with the instrument function H is necessary:

$$\sigma^*(\lambda, T, p) = H * \sigma(\lambda, T, p) = \int \sigma(\lambda', T, p) \cdot H(\lambda - \lambda') \, \mathrm{d}\lambda' \,, \tag{3.12}$$

yielding the absorption cross section $\sigma^*(\lambda, T, p)$ with appropriate spectral properties.

3.3 Spectral Analysis Principle

As described in Section 3.1, the trace gas SCD is the basic quantity retrieved from DOAS measurements. The logarithm of equation (3.2) is:

$$\ln(I(\lambda, L)) = \ln(I_0(\lambda)) - \int_0^L \left\{ \sum_{j=1}^{n} \left[\sigma'_j(\lambda, p, T) + \sigma_{B,j}(\lambda, p, T) \right] \cdot c_j(l) + \epsilon_R(\lambda, l) + \epsilon_M(\lambda, l) \right\} \mathrm{d}l \,. \tag{3.13}$$

The broad band part of the trace gas absorption cross section $\sigma_{B,j}(\lambda, p, T)$, the Rayleigh scattering $\epsilon_R(\lambda, l)$ and Mie $\epsilon_M(\lambda, l)$ scattering can be merged into one polynomial (Platt et al., 1979):

$$\ln(I(\lambda, L)) = \ln(I_0(\lambda)) - \int_0^L \left(\sum_{j=1}^{n} \sigma'_j(\lambda, p, T) \cdot c_j(l) + \sum_{m=0}^{p} \mu_m \cdot \lambda^m \right) \mathrm{d}l \,. \tag{3.14}$$

The order and the coefficients of the polynomial has to be chosen according the shape of the total broad band structure in the respective wavelength range. Assuming constant pressure and temperature in the probed air mass and considering that the differential absorption cross section $\sigma'_j(\lambda, p, T)$ as well as the polynomial do not depend on the light path, equation (3.14) can be rearranged and combined with equation (3.7):

$$\begin{aligned} \ln(I(\lambda, L)) &= \ln(I_0(\lambda)) - \left(\sum_{j=1}^{n} \sigma'_j(\lambda, p, T) \cdot \int_0^L c_j(l) \, \mathrm{d}l + \sum_{m=0}^{p} \mu_m \cdot \lambda^m \right) \\ &= \ln(I_0(\lambda)) - \left(\sum_{j=1}^{n} \sigma'_j(\lambda, p, T) \cdot S_j + \sum_{m=0}^{p} \mu_m \cdot \lambda^m \right) \,. \end{aligned} \tag{3.15}$$

The aim of the DOAS retrieval is to find the best S_j and μ_m that reproduce the measured $I(\lambda, L)$ and $I_0(\lambda)$. These quantities can be derived by applying a least squares fit (Gomer et al., 1993; Stutz and Platt, 1996). Then, the basic condition

to be fulfilled is the minimization of χ^2, which is defined as:

$$\chi^2 = \int_{\lambda_1}^{\lambda_2} \left(\ln(I(\lambda, L)) - \ln(I_0(\lambda)) + \sum_{j=1}^{n} \sigma'_j(\lambda, p, T) \cdot S_j + \sum_{m=0}^{p} \mu_m \cdot \lambda^m \right)^2 \mathrm{d}\lambda \xrightarrow{!} \min, \tag{3.16}$$

where λ_1 and λ_2 denote the limits of the spectral window to be considered, and $\sigma'_j(\lambda, p, T)$, n and p are fix parameters. The minimum can be retrieved using linear least squares fitting (Albritton et al., 1976; Bevington, 1969). Considering the discrete pixel mapping from equation (3.10), the least squares condition to be minimized becomes:

$$\chi^2 = \sum_{k=k_{\lambda_1}}^{k_{\lambda_2}} \left(\ln(I(k, L)) - \ln(I_0(k)) + \sum_{j=1}^{n} \sigma'_j(k, p, T) \cdot S_j + \sum_{m=0}^{p} \mu'_m \cdot k^m \right)^2 \xrightarrow{!} \min, \tag{3.17}$$

where the integral over the according wavelength range is replaced by the sum over the pixels covering the spectral window of interest. This window should include strong differential absorption features of the trace gas of interest to ensure its unambiguous identification. At the same time, strong absorption structures of other trace gases and significant Fraunhofer structures should be avoided in this spectral window (see Section 3.6.1). Due to photon and electronic noise (see Section 7.1.2), a residual R remains, although the best fit parameters are found within the fitting procedure:

$$R(k) = \ln(I(k, L)) - \ln(I_0(k)) + \sum_{j=1}^{n} \sigma'_j(k, p, T) \cdot S_j + \sum_{m=0}^{p} \mu'_m \cdot k^m, \tag{3.18}$$

whose root mean square (RMS) χ serves as an indication for the quality of the spectral fit. While in an ideal case, when the residual contains only noise and therefore no spectral structure, several reasons can cause systematic residual structures. For instance, an inaccurate wavelength calibration or absorption cross section as well as not considered absorbers are possible reasons for structured residuals.
In typical DOAS measurements, slight changes in the wavelength to pixel mapping of the spectrometer can occur, mainly due to temperature instabilities, resulting in systematic structures in the residual since an adequate spectral fitting is strongly affected thereby. This effect can be accounted for by introducing a new wavelength grid described by a polynomial, which allows for the adjustment of the initial wavelength calibration:

$$I(\lambda_k) \rightarrow I(\lambda'_k) \qquad \text{with} \qquad \lambda'_k = \lambda_k + s_0 + s_1(\lambda_k - \lambda_c) + s_2(\lambda_k - \lambda_c)^2, \tag{3.19}$$

with the center wavelength λ_c of the investigated wavelength interval from equation (3.17). Now, the appropriate parameter s_0 describes the necessary wavelength shift, while s_1 and s_2 account for the wavelength squeezing or stretching.
Another effect, appearing in the experimental implementation of the DOAS technique, is the possible occurrence of stray light in the housing of the spectrometer.

This can result in an additional broad banded signal overlaid to the actual measured intensities. This artificial signal can be compensated by adding a polynomial to the intensity:

$$I(\lambda) \rightarrow I_{add}(\lambda) = I(\lambda) + P_{add} \, . \tag{3.20}$$

The additional polynomial P_{add} should not be confused with the polynomial from equation (3.14).
The latter two non-linear effects are integrated in the spectral fitting procedure using the Levenberg-Marquardt method (Levenberg, 1944; Marquardt, 1963). Thus the best shift, squeeze/stretch and additional polynomial parameters are determined, so that the fit of equation (3.17) results in the optimal solution.

3.4 Passive DOAS

In passive DOAS measurements, where scattered sunlight serves as light source, several effects occur, which have to be considered in the spectral analysis procedure.

3.4.1 Fraunhofer Lines

The sunlight arriving at the top of the Earth's atmosphere exhibits a highly structured spectral signature, due to discrete absorption and re-emission of radiation in the photosphere of the Sun. The optical densities of these Fraunhofer lines are typically two to three orders of magnitude higher than the optical densities of the trace gases in the Earth's atmosphere. Therefore, the Fraunhofer lines have to be considered in the spectral retrieval to avoid the falsification of the results. This consideration is achived by including a Fraunhofer reference spectrum (FRS), which also serves as the I_0 spectrum. For obvious reasons, the FRS is taken from the same instrument instead of one measured from space including no absorptions in the Earth's atmosphere. Thus, care has to be taken in the adequate choice of the FRS and the interpretation of the retrieved trace gas slant column densities (see Section 3.5).

3.4.2 Ring Effect

Grainger and Ring (1962) first observed that the optical density of the Fraunhofer lines in scattered sunlight spectra are reduced compared to direct sunlight measurements. This "filling in" of the Fraunhofer lines is caused by inelastic Raman scattering (see Section 4.2.3) of photons by air molecules (Bussemer, 1993; Fish and Jones, 1995; Burrows et al., 1996), which changes the wavelength of the scattered photon (Brinkmann, 1968). Since the intensities in the Fraunhofer lines are less than in the bordering wavelength regions, the probability for photons to be scattered inelastically into the Fraunhofer lines is greater than vice versa. This effect has to be accounted for in the passive DOAS spectral retrieval, since the optical densities of the Ring effect can be, depending on the light path, up to one to two orders of magnitude higher than the optical densities of the trace gases. Therefore, a so called Ring spectrum is included in the spectral retrieval. The scattered sunlight intensity

I_{meas} measured by passive DOAS instruments can be described as:

$$I_{meas} = I_{Rayleigh} + I_{Mie} + I_{Raman} = I_{elastic} + I_{Raman} \,, \tag{3.21}$$

with $I_{Rayleigh}$, I_{Mie} and I_{Raman} denoting the intensities originating form elastic Rayleigh, Mie and inelastic Raman scattering processes, respectively. Taking the logarithm results in:

$$\begin{aligned} \ln(I_{meas}) &= \ln(I_{elastic} + I_{Raman}) \\ &= \ln(I_{elastic}) + \ln\left(1 + \frac{I_{Raman}}{I_{elastic}}\right) \\ &\approx \ln(I_{elastic}) + \frac{I_{Raman}}{I_{elastic}} = \ln(I_{elastic}) + I_{Ring} \end{aligned} \tag{3.22}$$

The Ring spectrum I_{Ring} can be determined by conducting polarization sensitive intensity measurements, since Rayleigh and Raman scattered light exhibit different degrees of polarization (Solomon et al., 1987). However, for the undisturbed Ring spectrum measurement, the contribution of Mie scattering with weak wavelength dependence caused by aerosols would have to be omitted, which is usually not possible for obvious reasons. Additionally, the dependence of the light path on the polarization can result in atmospheric absorption structures in the measured Ring spectrum, which would affect the spectral trace gas retrieval (Wagner, 1999). These limitations can be overcome by using a modeled Ring spectrum. Since the main constituents of the atmosphere are nitrogen and oxygen with known rotational states, the spectrum of inelastically scattered light can be modeled (Bussemer, 1993; Fish and Jones, 1995; Chance and Spurr, 1997) to a degree of accuracy, which compares very good to high resolution atmospheric observations (Aben et al., 2001).
For this work, Ring spectra calculated from the high resolution solar spectrum (Kurucz et al., 1984) are used. The calculations were performed using the WinDOAS software (Fayt and Van Roozendael, 2001), which applies the method described in Chance and Spurr (1997).

3.4.3 Solar I_0 Effect

As described in Section 3.4.1, the solar spectrum contains highly structured Fraunhofer lines, which cannot be resolved by typical DOAS instruments with spectral resolutions ranging from tenths of a nanometer to several nanometers. As a result, the detected absorption structures from the spectral fit can differ slightly from the utilized trace gas absorption cross sections, which where recorded under laboratory conditions with unstructured light sources. However, this so called solar I_0 effect (Platt et al., 1997; Richter, 1997) has to be considered for strongly absorbing trace gases, but can be neglected for weak absorbers. Following Johnston (1996), the absorption cross sections can be corrected for the I_0 effect, leading to $\sigma_{I_0}(\lambda, S)$:

$$\sigma_{I_0}(\lambda, S) = -\ln\left(\frac{I^*(\lambda)}{I_0^*(\lambda)}\right) \cdot \frac{1}{S} \,, \tag{3.23}$$

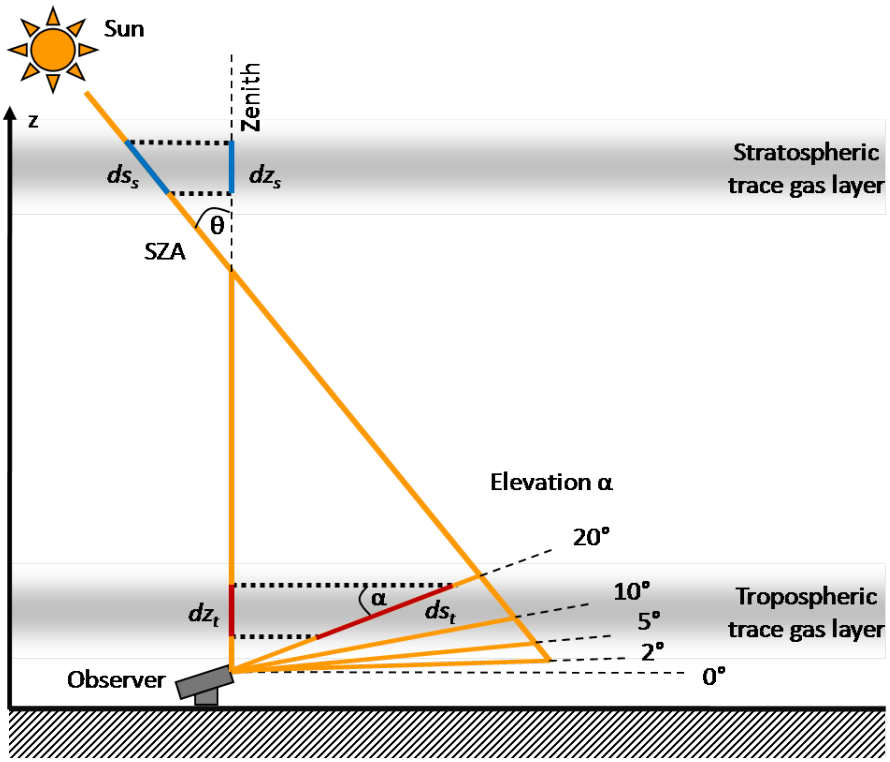

Figure 3.3: *Simplified schematic view of a MAX-DOAS measurement. The telescope collects scattered sunlight from viewing directions with different elevation angles. The yellow lines indicate the light paths.*

with the high resolution solar spectrum convolved with the instrument function H:

$$I_0^*(\lambda) = H * I_0(\lambda)\,, \tag{3.24}$$

and the synthetic spectrum, which contains absorption of the concerning trace gas with a typical slant column density S:

$$I^*(\lambda) = H * \left[I_0(\lambda) \cdot e^{-\sigma(\lambda)\cdot S}\right]\,. \tag{3.25}$$

The slant column densities used for the I_0 corrections in this work are summarized in Section 3.6.2.

3.5 Multi-Axis DOAS

A simplified sketch of a typical Multi-Axis DOAS (MAX-DOAS) measurement geometry is illustrated in Figure 3.3. The instrument is located at the ground and collects scattered sunlight from different viewing directions with varying elevation angles α, which is defined relative to the horizon. The position of the Sun relative to the viewing direction of the instrument is determined by the solar zenith angle (SZA) θ, which is defined relative to the zenith, and the angle spanned by the projection of the viewing direction and the direction of the sun relative to the instrument

onto the horizontal plane, namely the relative solar azimuth angle ϕ. While zenith sky measurements are mainly sensitive for stratospheric absorbers, the light path through the atmospheric layer near the surface is strongly increased for viewing directions with small elevation angles, along with an increase in the sensitivity for absorbers in this layer (Hönninger, 2002; Hönninger and Platt, 2002; Leser et al., 2003; van Roozendael et al., 2003; Hönninger et al., 2004; Wagner et al., 2004; Wittrock et al., 2004; v. Friedeburg et al., 2005; Heckel et al., 2005; Sinreich et al., 2005; Frieß et al., 2006; Sinreich et al., 2007; Sinreich, 2008). The light paths indicated in Figure 3.3 describe the situations when only one scattering event occurs along the total light path. Thus, the following assumptions considering the interpretation of the retrieved slant column densities S depending on the choice of the FRS can be made. On the one hand, the reference spectrum can be chosen with respect to the SZA θ_{ref} and elevation angle α_{ref} to be the lowest and highest, respectively, with relatively low absorption included. This applies to a zenith measurement around noon time. Then, the retrieved SCD is:

$$dS(\theta, \alpha) = S(\theta, \alpha) - S(\theta_{ref}, \alpha_{ref}) \, . \tag{3.26}$$

On the other hand, the zenith measurement of the current elevation scan sequence can be chosen as reference spectrum. The retrieved SCD is then:

$$\Delta S(\theta, \alpha) = S(\theta, \alpha) - S(\theta, 90^\circ) \, . \tag{3.27}$$

In this case, both spectra are recorded approximately at the same SZA but differ in the elevation angle. Since the SCD can be separated into a tropospheric and stratospheric part, equation (3.27) can be written as:

$$\Delta S(\theta, \alpha) = [S_{trop}(\theta, \alpha) + S_{strat}(\theta, \alpha)] - [S_{trop}(\theta, 90^\circ) + S_{strat}(\theta, 90^\circ)] \ , \tag{3.28}$$

and since the condition $S_{strat}(\theta, \alpha) \approx S_{strat}(\theta, 90^\circ)$ is fulfilled for a fixed SZA, the approximation:

$$\Delta S(\theta, \alpha) \approx S_{trop}(\theta, \alpha) - S_{trop}(\theta, 90^\circ) \tag{3.29}$$

can be made, showing the high sensitivity of MAX-DOAS to tropospheric absorbers. In the experimental practice, the different elevation angles are scanned subsequently, so that the SZA of the individual measurements differ slightly. However, this resulting difference in the stratospheric part caused by not exactly equal SZA can be neglected, since the time differences are usually very small. Significant effects can appear during periods with high and rapidly changing SZA, namely in the morning and evening hours. The increased light paths in the stratosphere result in higher absorption by ozone and NO_2 in the ultra-violet wavelength range. For any other conditions, the spectral retrieval of ΔS is always less affected by temporally unstable spectrometer properties compared to the retrieval of dS, resulting in smaller residuals.

The SCD depends on the light path and is therefore not well suited for quantitative implications on the trace gas concentrations. In contrast, the vertical column density (VCD) V, which is the integrated concentration $c(z)$ along the height z, does

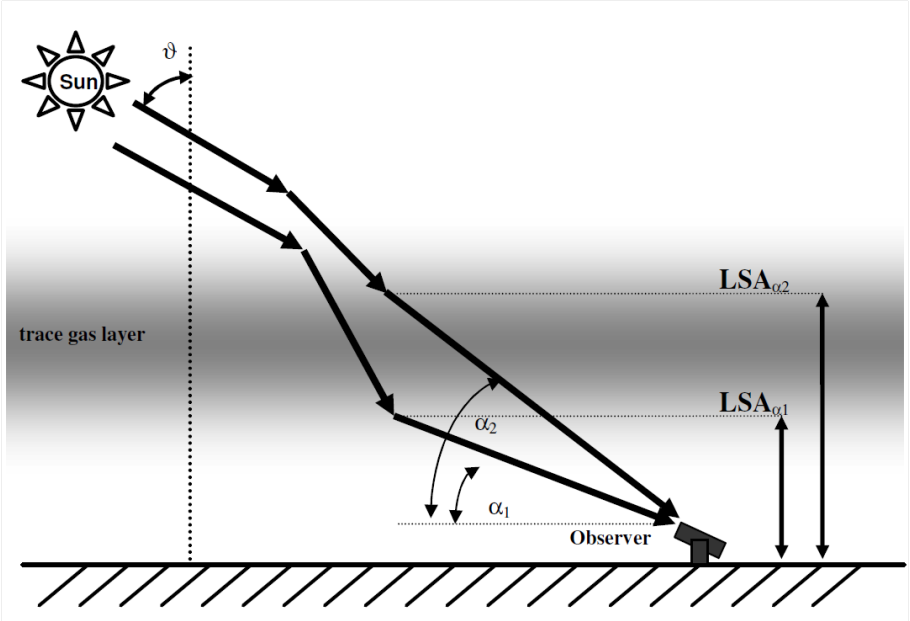

Figure 3.4: *The Last Scattering Altitude LSA: for low elevation angles, the mean free path in the viewing direction is shorter due to higher density and/or aerosol load. This can result in the slant path through absorbing layers at higher altitudes being shorter for lower elevation angles than for higher ones. Adapted from Hönninger et al. (2004)*

not depend on light path and wavelength:

$$V = \int c(z)\, dz\,, \tag{3.30}$$

and allows for direct comparisons of the results from different measurement techniques. As depicted in Figure 3.3, the following approximations for the VCD can be made using a geometrical approach:

$$V_{trop} \approx \sin(\alpha) \cdot S_{trop}(\alpha) \qquad \text{and} \qquad V_{strat} \approx \cos(\theta) \cdot S_{strat}(\theta)\,, \tag{3.31}$$

for the VCD of a tropospheric and stratospheric absorber V_{trop} and V_{strat}, respectively. The combination of both results in:

$$S(\theta, \alpha) \approx \left[\frac{V_{trop}}{\sin(\alpha)} + \frac{V_{strat}}{\cos(\theta)}\right]\,. \tag{3.32}$$

Attention has to be paid for conditions with elevation angles smaller than about 20° and solar zenith angles larger then about 70°, due to the inapplicability of the geometrical approximation and possible scattering within the trace gas layer. For such cases, radiative transfer models have to be utilized to determine the relationship between the SCD and VCD, which is discussed in detail in Chapter 4. Furthermore, atmospheric aerosols have a tremendous influence on the light path due to the increase in scattering probability, and therefore make the usage of radiative transfer

models indispensable. In conditions with high aerosol load, multiple scattering can occur and the geometrical light path approximation is thus not valid anymore. This situation is illustrated in Figure 3.4. The multiple scattering events can result in more vertical light paths through an elevated absorber layer for lower elevation viewing directions than for higher ones, which is in contrast to what would be expected from the geometrical approach. Similar considerations are valid for decreased light paths of low elevation viewing directions through absorber layers located directly above the surface.
Hönninger et al. (2004) verified in an intensive radiative transfer modeling study the potential for the retrieval of trace gas vertical profiles from MAX-DOAS measurements. Such a retrieval can be implemented using inverse modeling methods, which combine forward radiative transfer models and iterative Levenberg-Marquardt algorithms to determine the trace gas profile from the measured slant column densities. In this work, profiles of nitrogen dioxide and selected other trace gases are retrieved and compared to independent datasets from other measurement techniques. The utilized retrieval method is described and discussed in detail in Chapter 5.
Since aerosols strongly influence the light path in MAX-DAOS measurements, the detailed knowledge on their vertical distribution and optical properties is of crucial importance for the trace gas profile retrieval to succeed. Here, the elegance of the MAX-DOAS technique comes to light once more. Wagner et al. (2004) explored the information on aerosols contained in MAX-DOAS measurements of the oxygen collision complex O_4. Since the vertical distribution of O_4 is proportional to the square of the oxygen concentration and therefore depends on pressure, it is nearly constant in time and well known (see Section 2.3). The O_4 slant column densities derived from MAX-DOAS measurements cannot be referred to O_4 since the equilibrium constant between O_4 and $(O_2)_2$ is not known. Therefore, the O_4 SCD is referred to the integrated quadratic O_2 concentration and includes the equilibrium constant (Greenblatt et al., 1990). In contrast to the other absorbers, the O_4 SCD is then given in units of $[\frac{molec^2}{cm^5}]$. Any changes in the observed slant column densities is therefore due to the characteristic light path caused by aerosols. Thus, the aerosol profile can be extracted from the O_4 measurements by inverse modeling methods. Frieß et al. (2006) investigated the retrieval of aerosol profiles and optical properties from simulated MAX-DOAS O_4 measurements using the optimal estimation method, concluding its applicability. Based on the approach of Frieß et al. (2006), the retrieval method for aerosol profiles was modified and extended within the scope of this work and applied to MAX-DOAS measurements. It is described and discussed in detail in Chapter 5. The retrieved aerosol profiles were then used as input for the trace gas profile retrieval.

3.6 Spectral Retrieval

The spectral trace gas retrieval within this work was performed using the WinDOAS program package, developed at the Belgium Institute for Space Aeronomy (IASB, Fayt and Van Roozendael, 2001). The WinDOAS program does not provide an internal option to perform the spectral analysis for the retrieval of slant column densities with respect to the current zenith measurement from the accord-

Table 3.1: *Trace gas absorption cross sections utilized in this work.*

No.	Molecule (Temperature)	Reference
1	O_4 (298 K)	Hermans (2002)
2	O_3 (223 K)	Bogumil et al. (2003)
3	O_3 (243 K)	Bogumil et al. (2003)
4	O_2 (294 K)	Rothman et al. (2009)
5	H_2O (294 K)	Rothman et al. (2009)
6	NO_2 (220 K)	Vandaele et al. (1998)
7	NO_2 (294 K)	Vandaele et al. (1998)
8	SO_2 (293 K)	Bogumil et al. (2003)
9	HCHO (298 K)	Meller and Moortgat (2000)
10	HONO (298 K)	Stutz et al. (2000)
11	CHOCHO (296 K)	Volkamer et al. (2005b)

ing elevation scan sequence (ΔSCD, see Section 3.5). Therefore, a program was written, which selects the spectra of one complete elevation scan sequence, identifies the zenith measurement to be used as FRS and runs the WinDOAS program after processing the controlling files. This program offers also the possibility to select the noon zenith measurement from the according day to be set as the FRS (dSCD, see Section 3.5), if required. Such a flexible handling of the FRS choice is especially desirable, when the analyzed data covers a long time period of several months.
The total measurement error consists of statistical and potential systematic errors. The statistical error arises due to photon and instrumental noise, and is the limiting factor for the detection limit of the spectral retrieval (see Section 7.1.2). During day time, the instrumental noise, consisting of the electronic offset and dark current noise, is negligible compared to the photon noise. For the retrieved slant column densities, the WinDOAS program provides the statistical errors. These 1σ errors are calculated from the standard deviations of the linear and non-linear fit algorithms, weighted by the fit χ^2 and number of degrees of freedom, which is the number of channels in the spectral window minus the number of linear and non-linear parameters to fit (Fayt and Van Roozendael, 2001). They compare also very well to fit errors derived, when applying the method proposed by Stutz and Platt (1996)(Heue, 2005).

The sources for systematic errors are diverse. In cases where absorbers are not considered in the fitting procedure due to the missing knowledge on their absorption cross section or the unexpected occurrence during a measurement, the uncertainties of the spectral fit can increase. The available cross sections, measured under laboratory conditions with well defined temperatures and pressures, include uncertainties in the absolute values of up to 5 %. Due to the temperature dependence of the cross sections, additional systematic errors arise, since the different temperatures at which the trace gases are probed in the atmosphere can not be accounted for exactly. Furthermore, the spectral retrieval in wavelength regions with strong H_2O and O_2 absorptions are affected by errors in the respective cross sections. In general, these cross sections are extracted from the HITRAN database (Rothman et al., 2009). Since the database contains laboratory-measured as well as modeled

Table 3.2: *Fit scenarios and according optical densities used for the wavelength mapping with artificial spectra.*

	Optical density in fit scenario [$\cdot 10^{-2}$]						
	O_4				NO_2		SO_2
Absorber	360 nm	477 nm	577 nm	630 nm	vis	UV	
O_4	2	5	11	7	5	2	-
O_3	0.5	0.2	1	1	0.2	1	60
O_2	-	-	-	4	-	-	-
H_2O	-	0.3	8	6	0.3	-	-
NO_2	8	8	3	0.6	8	8	5
SO_2	-	-	-	-	-	0.05	10
HCHO	0.3	-	-	-	-	0.3	0.4
HONO	-	-	-	-	-	0.9	0.6
CHOCHO	-	-	-	-	0.4	-	-
Ring	-3	-0.7	-0.3	-0.2	-0.7	-3	-5

absorption lines, the absorption structures observed in atmospheric measurements can differ significantly.

Another source for systematic errors is an inaccurate wavelength to pixel mapping. Since this mapping depends on the spectrometer temperature, the calibration of each spectrum has to be done thoroughly to account for possible shifts in the spectrometer optical properties in the course of time. The instrument function is also affected by this effect and is furthermore wavelength dependent, especially for miniaturized spectrometers. When this dependency is neglected in the convolution procedure, the spectral retrieval will not be able to identify the absorbers accurately, resulting in additional systematic errors.

Also correlations between cross sections included in the spectral fit, which have similar differential structures in the according wavelength range, can result in distorted results. For example, O_3 and SO_2 show correlations, and when the order of the polynomial is selected to high, correlations with O_4 can occur.

Furthermore, instrumental stray light and possible detector non-linearities can result in spectral structures distorting the fit.

3.6.1 Dependence on the Wavelength Interval of the Retrieval

The appropriate choice of the wavelength interval for the spectral retrieval is of crucial importance. Within this interval, the trace gas of interest should have strong differential absorption structures to ensure its unambiguous identification. However, wavelength regions with overlapping strong differential absorption features of other trace gases involved in the fit scenario should be avoided, as well as regions with strong Fraunhofer structures.

A well suited tool for the determination of the optimal wavelength interval is the plot of the retrieval results as function of the lower and upper interval limit, as proposed and investigated by Vogel (2011) for SO_2 and bromine monoxide (BrO). Therefore,

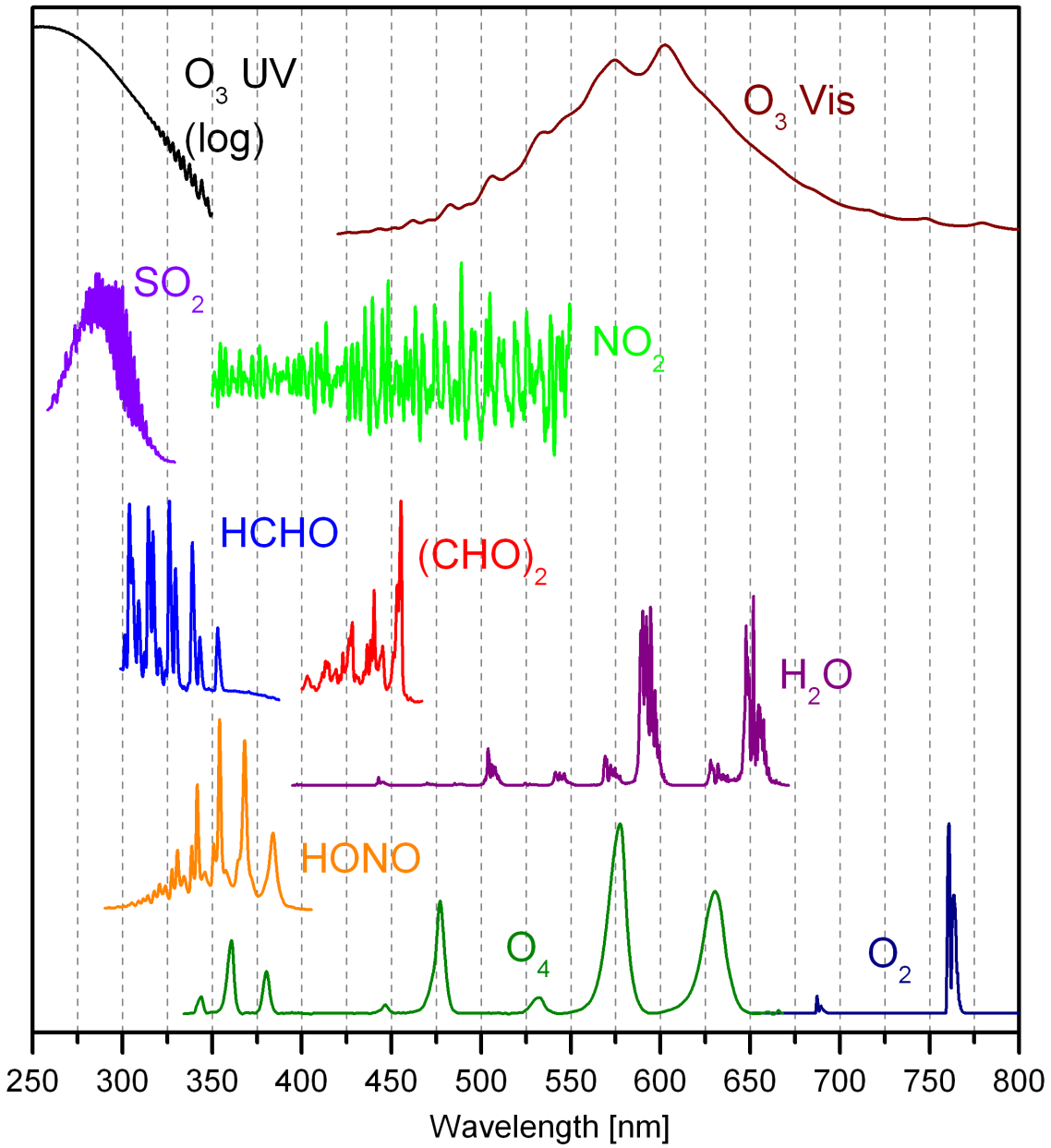

Figure 3.5: *Overview of the literature absorption cross sections in the wavelength range from 250–800 nm listed in Table 3.1.*

examples for the wavelength mapping applied on the trace gases and wavelength regions analyzed in the context of this work are given here.
For this purpose, artificial spectra were simulated and spectral retrievals were performed using the WinDOAS program, which was combined with an extra program, written for the handling of the output and adjustment of the wavelength interval. The high resolution solar spectrum (Kurucz et al., 1984) was utilized as I_0 spectrum. To calculate the artificial spectrum I containing the trace gas absorptions, the high resolution absorption cross sections listed in Table 3.1 were scaled with typically observed slant column densities and applied on the I_0 spectrum according to equation

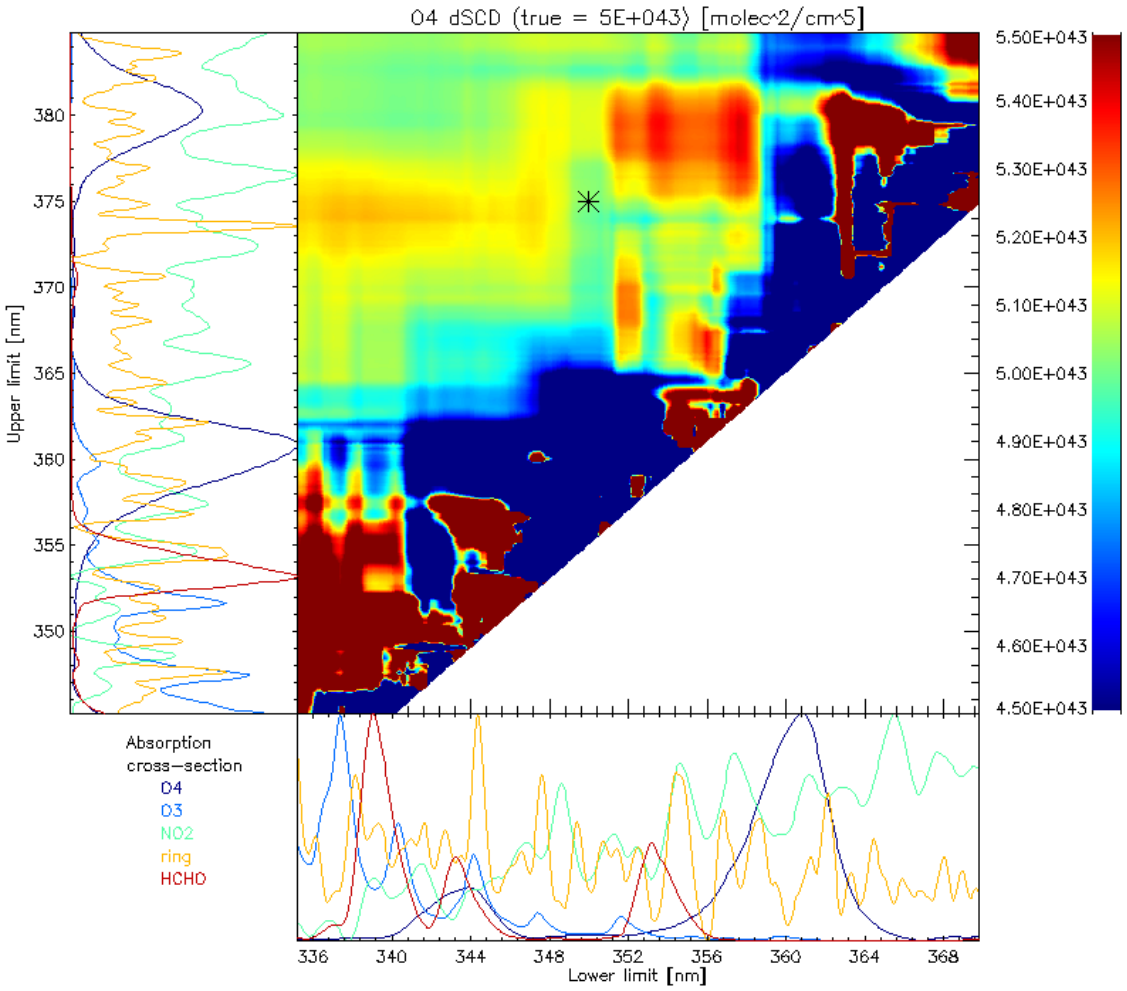

Figure 3.6: *Wavelength range plot for the spectral retrieval of the O_4 absorption at 360 nm. The plot shows the retrieved O_4 dSCD depending on the lower and upper limit of the wavelength range used in the fit. The color code indicates the dSCDs. The left and bottom panels show the considered absorption cross sections.*

(3.15), together with a polynomial to simulate the broad banded extinction. The included trace gases and the according optical densities are summarized in Table 3.2. An overview of the absorption cross sections from Table 3.1 is given in Figure 3.5. A Ring spectrum, calculated from the high resolution solar spectrum, was also included and treated as an additional absorber. Depending on the investigated trace gas and wavelength region, only absorbers with relevant differential absorptions structures in the corresponding wavelength interval were included. The resulting I spectra as well as the I_0 spectra and the cross sections were then convolved with wavelength dependent instrument functions and interpolated on wavelength grids, which both are typical for the spectrometers utilized within this work (see Section 7.1.2). This procedure was performed using a program, written by Udo Frieß (see Section 3.6.2). After the convolution, Gaussian distributed noise with a standard deviation of $5 \cdot 10^{-4}$, which is in the order of typical residual RMS values achieved

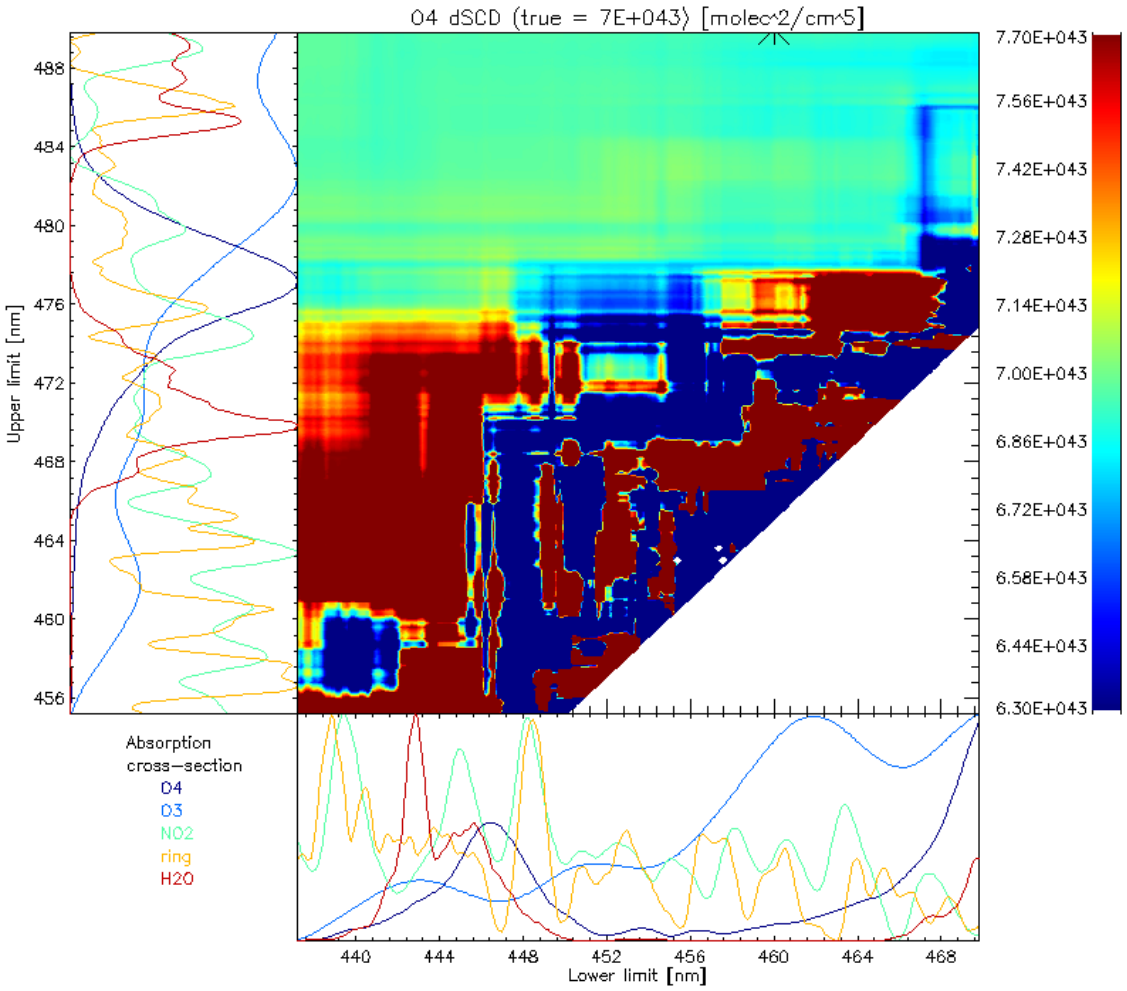

Figure 3.7: *Same as Figure 3.6 but for the spectral retrieval of the O_4 absorption at 477 nm.*

in retrievals from spectra measured within this work, were added to the artificial spectra. It should be noted, that the retrievals using these artificial spectra are aimed to visualize the effect of including or avoiding individual absorption bands of the involved trace gases rather than investigate statistical effects on the retrieval result. Furthermore, the calculation of the artificial spectra includes the simplifications, that the wavelength dependent radiative transfer was not considered, and thus the Ring spectrum was treated as an absorber.

Figures 3.6 - 3.12 illustrate the wavelength mapping for O_4, NO_2 and SO_2 in different wavelength regions. These Figures are structured in such a way that the investigated trace gas is listed on top of the plot together with the SCD value used for the artificial spectra calculation. The centered contour plot shows the retrieved SCD depending on the lower and upper wavelength limit of the spectral retrieval. The scale of the color code is limited to values of $\pm 10\,\%$ of the true SCD. The adjacent panels on the left and at the bottom display the cross sections of the included

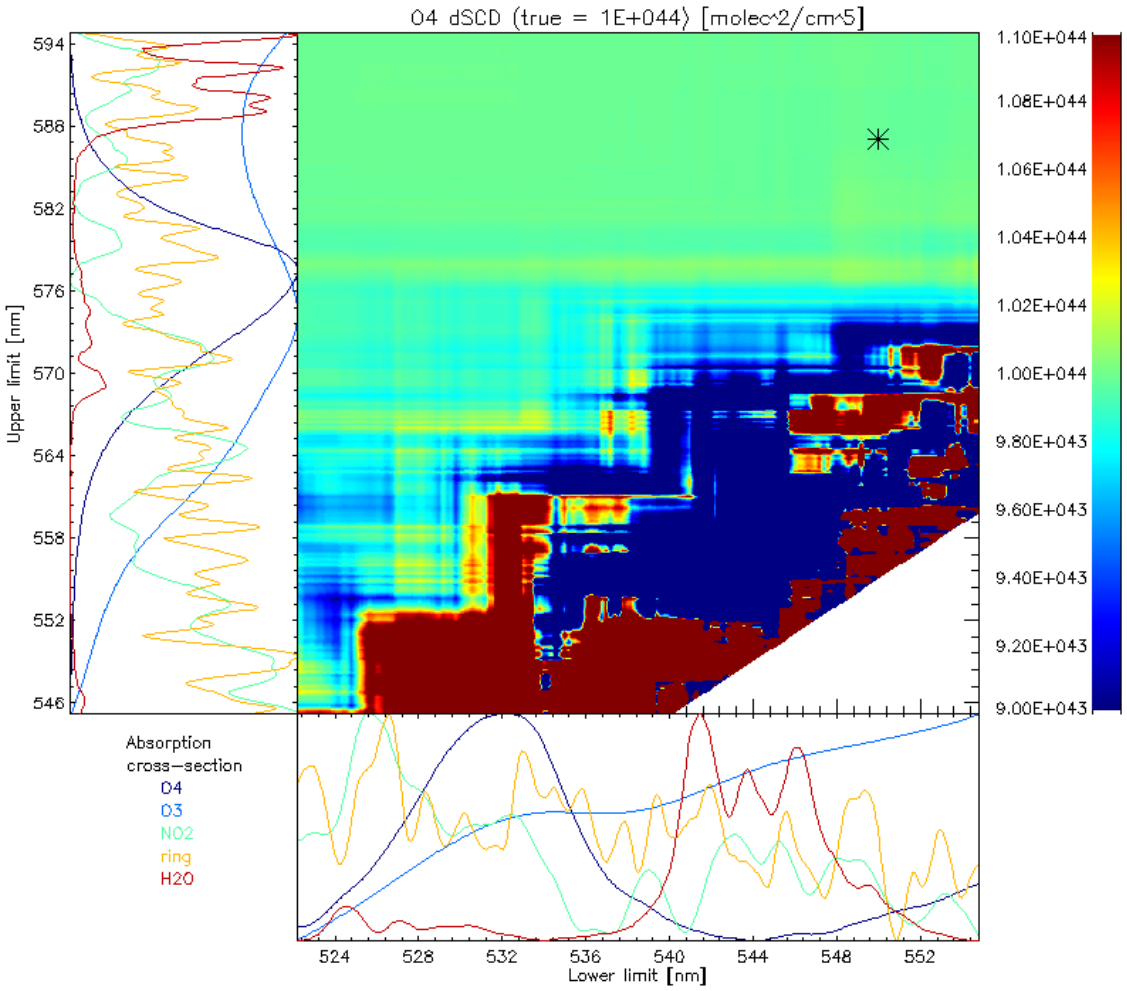

Figure 3.8: *Wavelength range plot for the spectral retrieval of the O_4 absorption at 577 nm. The plot shows the retrieved O_4 dSCD depending on the lower and upper limit of the wavelength range used in the fit. The color code indicates the dSCDs. The left and bottom panels show the considered absorption cross sections.*

absorbers. Furthermore, the wavelength range, used in the spectral retrievals of measured spectra in this work are indicated by the black asterisk symbol in the individual Figures.

The wavelength mapping for the spectral retrieval of the O_4 absorption band around 360 nm is shown in Figure 3.6. In contrast to the spectral retrieval from measured spectra (see Table 3.3), O_3 and NO_2 cross sections of only one temperature were included. Two areas can be identified, where initial and retrieved O_4 dSCDs agree. One of which is enclosed by lower limits for the wavelength window below approximately 346 nm and above approximately 377 nm for the upper limits, while the other one is enclosed by the lower limits of approximately 349 to 352 nm and 367 to 377 nm for the upper limits. These areas mark combinations of the upper and lower limit of the retrieval wavelength interval with stable results in good agreement with the true SCD. The first area implies the coverages of the O_4 absorption bands centered

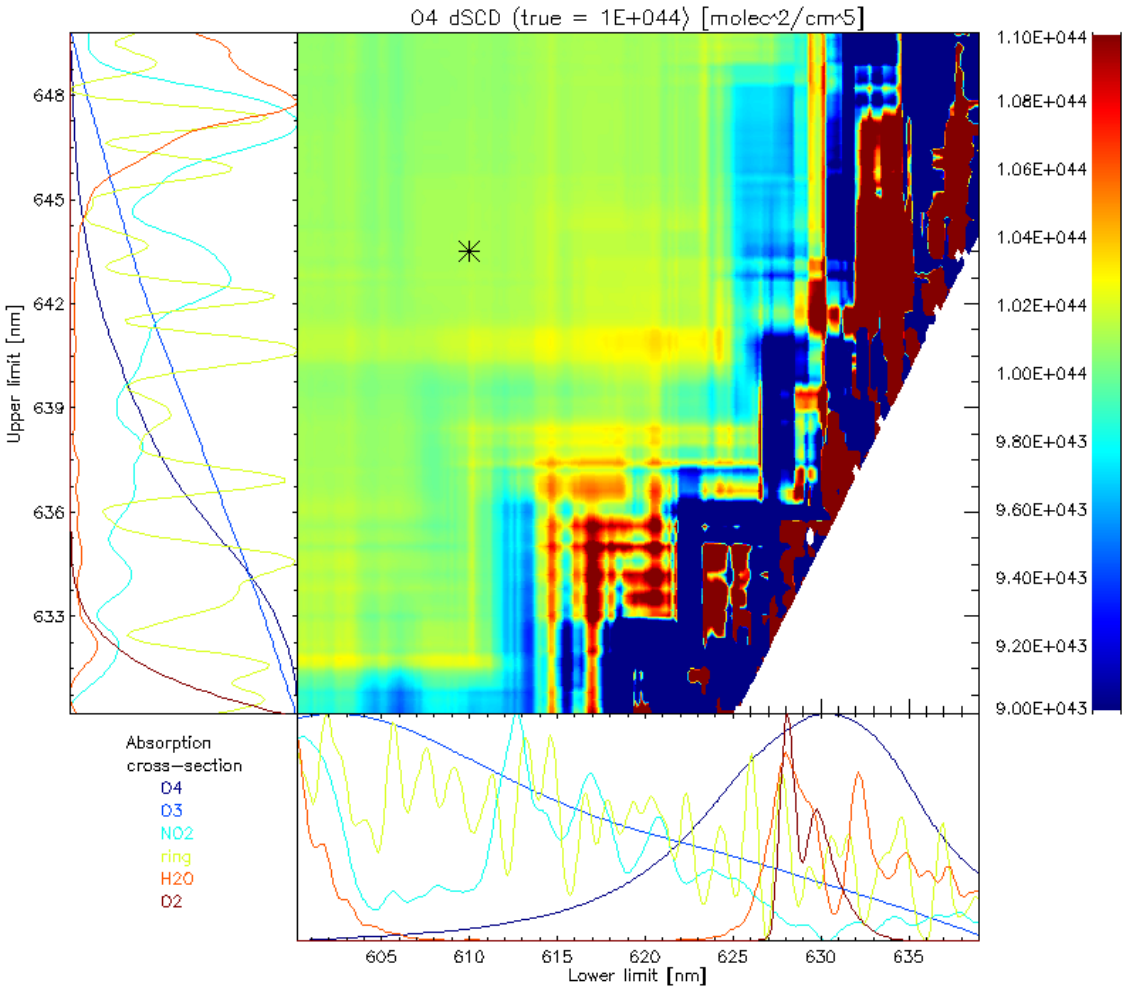

Figure 3.9: *Same as Figure 3.8 but for the spectral retrieval of the O_4 absorption at 630 nm.*

around 343, 360 and 380 nm simultaneously by the retrieval wavelength window. Also the case covering the bands at 360 and 380 nm is possible within this area. The second area covers the O_4 absorption band centered around 360 nm only. However, retrieval wavelength intervals covering only the bands centered around 343 or 380 nm are not suitable for the O_4 retrieval since the results for the according combinations of the lower and upper limit differ significantly from the true SCD. The optical density of the O_4 343 nm band is less than one third of the 360 nm band and therefore the isolated retrieval is affected by O_3, HCHO, NO_2 and Ring absorptions. When the lower and upper limit of the wavelength interval for the spectral retrieval is set to values covering only the O_4 380 nm band, the similar NO_2 differential structures in this region disturb the unambiguous allocation of the O_4 absorption. Too large wavelength intervals in spectral retrievals from measured spectra should be avoided, since the light path in the atmosphere is wavelength dependent and is not accounted for in the normal DOAS fit. This would imply a wavelength dependent SCD to be used in the fit (see Equation (3.15)). Furthermore, the requirement for spectrom-

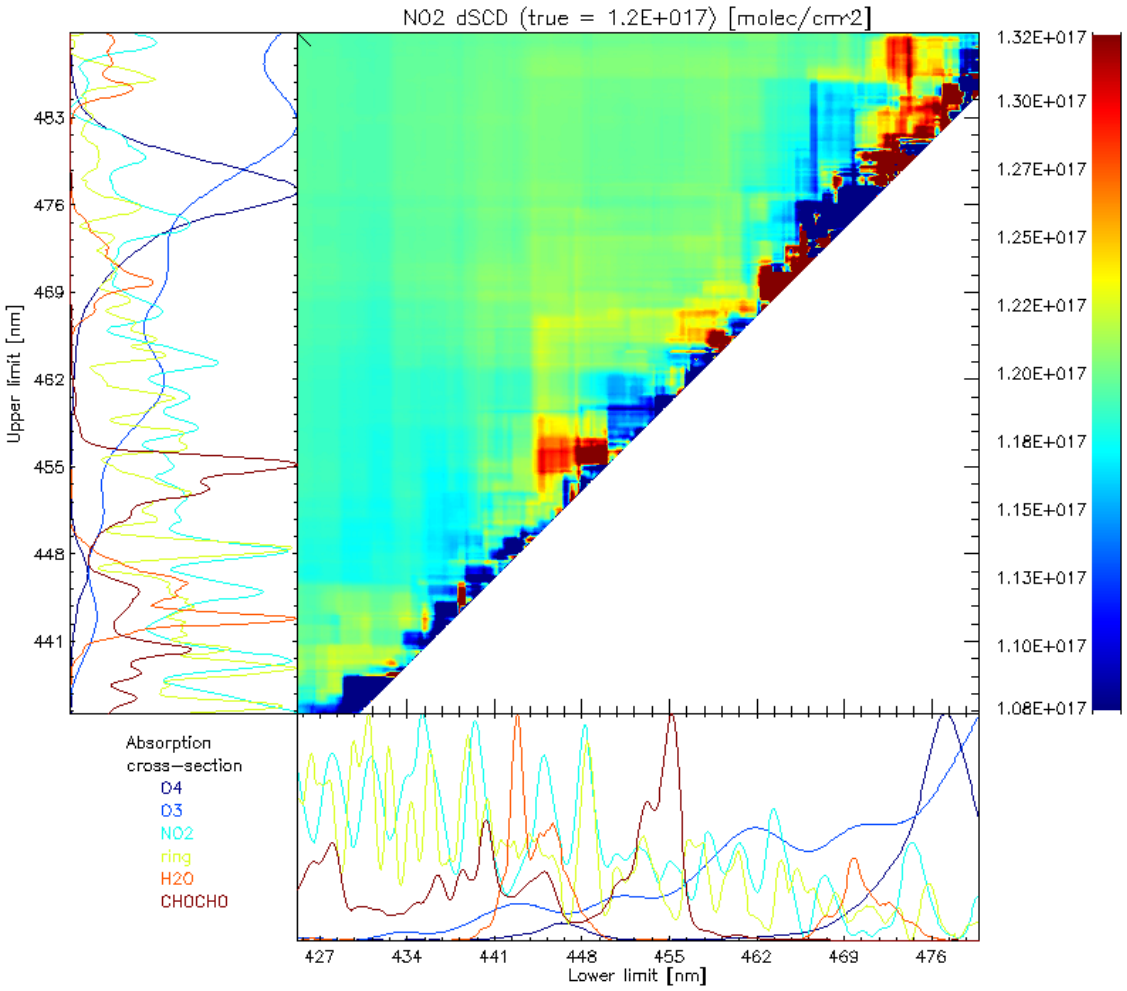

Figure 3.10: *Wavelength range plot for the spectral retrieval of the NO_2 absorption in the visible wavelength range. The plot shows the retrieved NO_2 dSCD depending on the lower and upper limit of the wavelength range used in the fit. The color code indicates the dSCDs. The left and bottom panels show the considered absorption cross sections.*

eter stability would increase to assure the quality of the spectral fits. Therefore, the wavelength interval used within this work for the spectral retrieval of O_4 in the ultra-violet is set to 350–375 nm, which is indicated by the asterisk in Figure 3.6. Thus, possible effects arising from the wavelength dependence of the light path is minimized. This is of special relevance since the measured O_4 optical densities are compared to values calculated with radiative transfer models (see Section 4.4), which utilize discrete wavelength values.

The situation for the retrieval of the O_4 absorption band centered around 477 nm is shown in Figure 3.7. Now, the areas and their classification of stable and instable differ from the case in the ultra-violet. The spectral retrieval tends to be independent of the lower wavelength limit and slant column densities in good agreement with the true value, as long as the 477 nm absorption band is included. The very small band

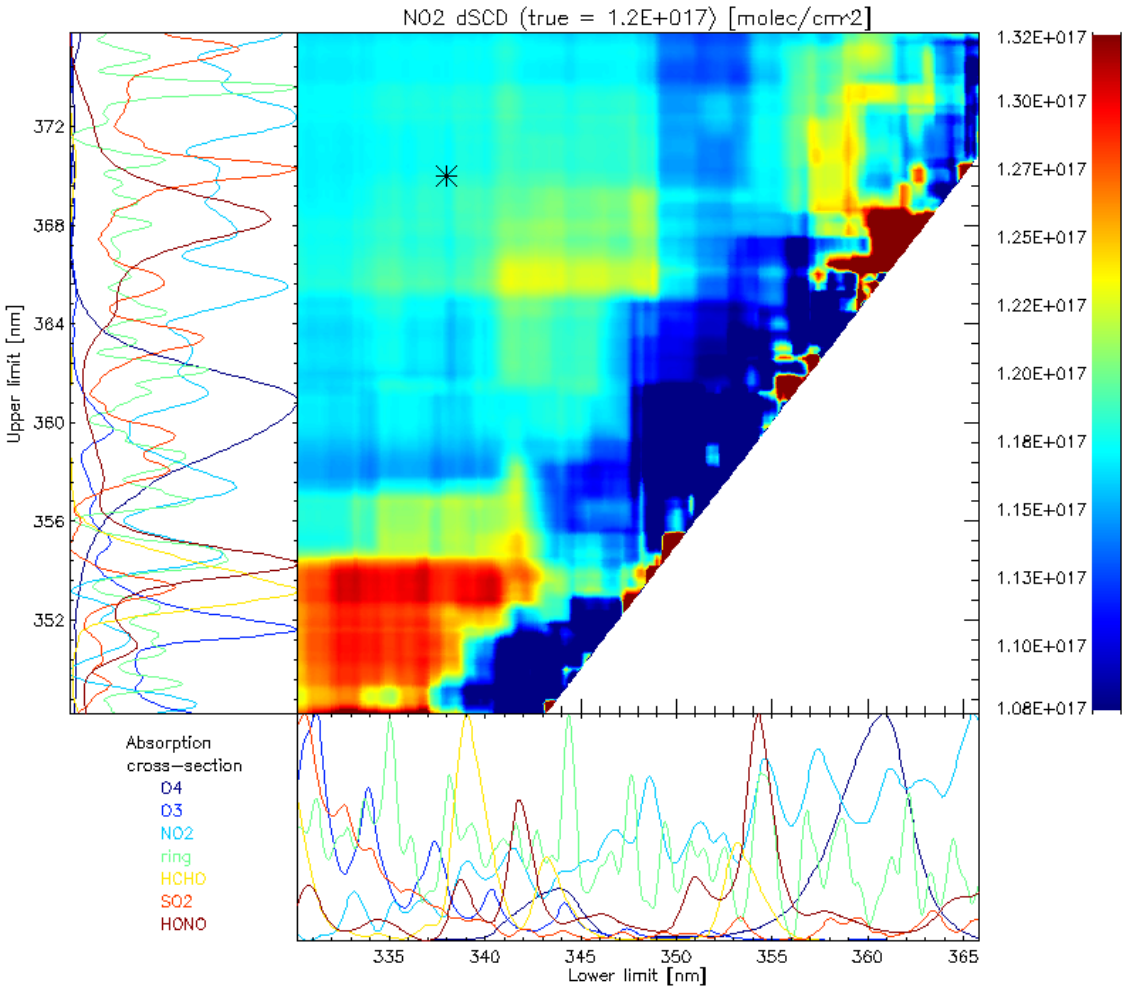

Figure 3.11: *Same as Figure 3.10 but for the spectral retrieval of the NO_2 absorption in the ultra-violet wavelength range.*

at around 446 nm, with an optical density of less then one tenth of the 477 nm band, is superimposed by strong absorption bands of H_2O, so that a retrieval covering only this small band is not suitable. The retrieval of the O_4 477 nm band is quite robust, since the variation of the lower and upper limit result in values which vary about $\pm 2\,\%$ around the true value. The asterisk at the top edge of the spectral map indicates the interval of 460–490 nm, used in this work for the retrieval of the O_4 477 nm band. It covers only the 477 nm band for the above mentioned reasons.
The wavelength mapping for the O_4 577 nm band is shown in Figure 3.8. The situation is similar to the case for the 477 nm band. The spectral retrieval is robust when covering the absorption band centered around 577 nm along with no dependency on the lower limit. The slant optical densities retrieved in this area, beginning for upper limit values greater then 577 nm, vary about less then $\pm 1\,\%$ around the true value. To avoid a negative impact of the strong H_2O absorptions on the retrieval, the interval of 550–587 nm covering only the 577 nm band was applied in this work for the investigation of the O_4 absorption in this wavelength region. The band at

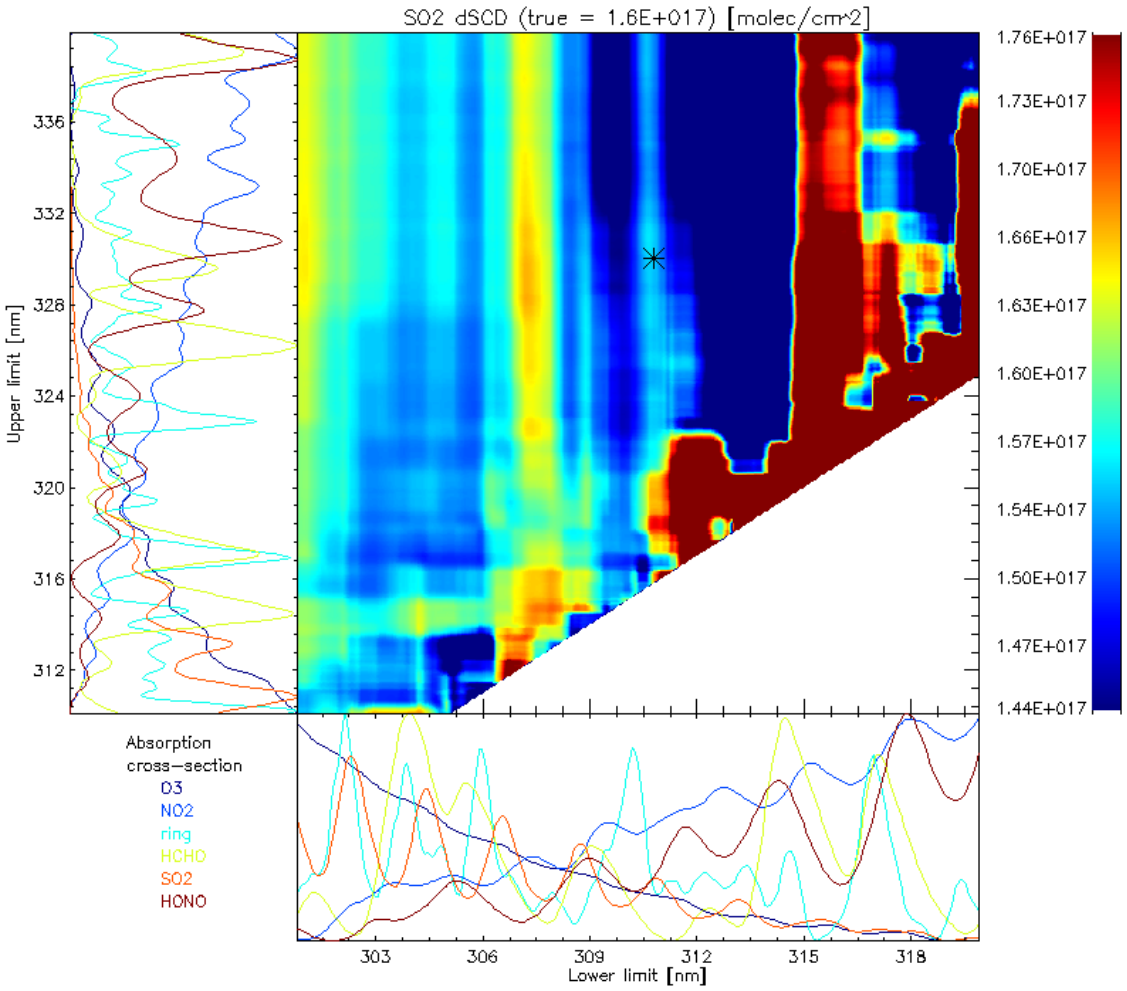

Figure 3.12: *Wavelength range plot for the spectral retrieval of the SO_2 absorption. The plot shows the retrieved SO_2 dSCD depending on the lower and upper limit of the wavelength range used in the fit. The color code indicates the dSCDs. The left and bottom panels show the considered absorption cross sections.*

around 532 nm, with an optical density of less then one tenth of the 577 nm band, can be retrieved in a seperate wavelength window but the results vary between −6 and +10 % around the true value.
Figure 3.9 shows the wavelength mapping for the O_4 630 nm band. Retrievals with wavelength intervals covering the complete 630 nm band, which is broader then the other O_4 bands, result in overestimations of up to 3 % compared to the true value. The interval of 610–643.5 nm was applied in this work for measured spectra to avoid the strong H_2O absorptions centered around 648 nm. As mentioned above, the H_2O and O_2 absorptions overlayed with the O_4 630 nm band are difficult to remove from measured spectra and cause systematic structures in the residual (see Section 3.6.2). The dependency of the NO_2 retrieval on the interval in the visible wavelength range was investigated from 425–490 nm. The wavelength mapping shown in Figure 3.10, illustrates that the NO_2 retrieval is more stable over a wide range of lower and up-

per limits of the wavelength interval, which is due to the well defined differential absorption structures of NO_2 making the allocation of the according optical density unambiguously. The applied wavelength interval for the measurements of this work was 425–490 nm. Although this interval is quite large, it was chosen to be in agreement with the common setting during the CINDI campaign (see Section 8.6), where NO_2 and O_4 slant column densities retrieved from MAX-DOAS-measurements of several different research groups were inter-compared (Roscoe et al., 2010; Piters et al., 2011).
The wavelength mapping for the retrieval of NO_2 in the ultra-violet wavelength range is shown in Figure 3.11. An area enclosed by lower limits less than 347 nm and upper limits greater than 359 nm can be identified with retrieval results varying about ± 3 % around the true value, beeing the most stable area for the NO_2 results within the map. In this example, the influence of well defined differential absorption structures of different involved trace gas species overlayed in certain wavelength regions is illustrated clearly. Depending on the edges of the intervall, the influence on the NO_2 retrieval varies with the inclusion or exclusion of individual absorption peaks of different absorbers. This effect is particularly obviuos here, since a large number of absorbers were included in the retrieval. The NO_2 interval for retrievals in the ultra-violet wavelength range was 338–370 nm in this work, which was also used as common setting during the CINDI campaign.
Figure 3.12 shows the wavelength mapping for the SO_2 retrieval. The spectral retrieval results for SO_2 depend to a high degree on the choice of the lower limit of the wavelength interval, which is due to the increasingly strong absorption of SO_2 below approximately 305 nm. Depending on how many SO_2 absorption bands are included in the spectral window, the retrieved slant column densities show a large variation around the true value. This effect is mainly driven and affected by the dominating strong absorptions by O_3. Within this work, the wavelength interval of 310.8–330 nm was used and is indicated by the asterisk in Figure 3.12. The reason for applying this interval, although the wavelength map suggests more suitable combinations of the lower and upper limit with less deviations from the true value, is discussed in Section 3.6.2.

3.6.2 Applied Retrieval Settings

The spectra measured with the MAX-DOAS instrument (Section 7.1) were corrected for the offset and dark current signal (Section 7.1.2), prior to the DOAS retrieval. The measurement program (Section 7.1.1) was set to record offset and dark current spectra every night, to allow for the consideration of possible temporal changes in these signals.

The instrument functions H of the different spectrometers were determined using emission line spectra of mercury and neon vapor lamps. These instrument functions are wavelength dependent (Section 7.1.2). Therefore, a convolution program developed by Udo Frieß was used, that accounts for the wavelength dependency of the instrument function $H(\lambda)$. For that purpose, several instrument functions at different wavelengths are provided to the program, which then interpolates the signature of the functions between the supplied wavelength values. The thus deter-

Table 3.3: *Spectral retrieval settings.*

Analysis	Interval [nm]	Molecules (No. from Table 3.1)
O_4 - 360 nm	350 - 375	(1), (2), (3), (6), (7), (9)
O_4 - 477 nm	460 - 490	(1), (2), (5), (6), (7)
O_4 - 577 nm	550 - 587	(1), (2), (5), (6), (7)
O_4 - 630 nm	610 - 643.5	(1), (2), (4), (5), (6), (7)
NO_2 - UV	338 - 370	(1), (2), (3), (6), (7), (9)
NO_2 - Vis	425 - 490	(1), (2), (5), (6), (7)
SO_2	310.8 - 330	(2), (3), (7), (8), (9)

mined relationship between the wavelength and the instrument function is used for the convolution. Using this procedure, the high resolution trace gas cross sections (Table 3.1) were convolved and interpolated on the wavelength grid of the utilized spectrometers. Also the I_0 correction (Section 3.4.3) was applied using the convolution program with SCD values of $1 \cdot 10^{20}$, $5 \cdot 10^{24}$, $1 \cdot 10^{17}$ and $1 \cdot 10^{23}$ for O_3, O_2, NO_2 and H_2O, respectively. In the case of the O_4 cross section, a wavelength interpolation instead of a convolution was sufficient due to the relatively broad absorption bands.
An initial wavelength calibration was created using the emission lines of mercury and neon. The wavelength-to-pixel mapping of the spectrometers is described by a polynomial of order two. Since the number of emission lines in the wavelength ranges of the different spectrometers is not sufficient for the determination of an exact calibration, a further procedure was applied. Using the WinDOAS analysis program, the initial wavelength calibration was adjusted using the Fraunhofer structures of a high resolution solar spectrum (Kurucz et al., 1984). This was achieved by fitting the measured spectrum with the initial calibration to the solar spectrum, which was previously convolved with $H(\lambda)$. The fit was performed within several sub-windows, delivering a wavelength shift to adjust the initial calibration to the calibration of the solar spectrum. A higher order polynomial fitted to the individual shift values of the according sub-windows determines the exact calibration. This calibration was then used instead for the FRS and the spectrum to be analysed.
In addition to the cross sections listed in Table 3.3, a third order polynomial was included in the spectral retrieval to account for the broad banded spectral structures. The Ring spectrum utilized for the fits was calculated with the WinDOAS program from the high resolution solar spectrum (Kurucz et al., 1984).

Since the main focus of this work is the retrieval of aerosol profiles from MAX-DOAS O_4 measurements, the slant column densities of the individual absorption bands around 360, 477, 577 and 630 nm were retrieved. NO_2 slant column densities were retrieved in the ultra-violet and visible wavelength range. Furthermore, the detection of a highly diluted volcanic plume was achieve by the retrieval of SO_2 slant column densities. The according spectral retrieval settings are listed in Table 3.3. In cases where cross sections of two different temperatures were included to account for the temperature dependence of the cross sections and the occurrence of the

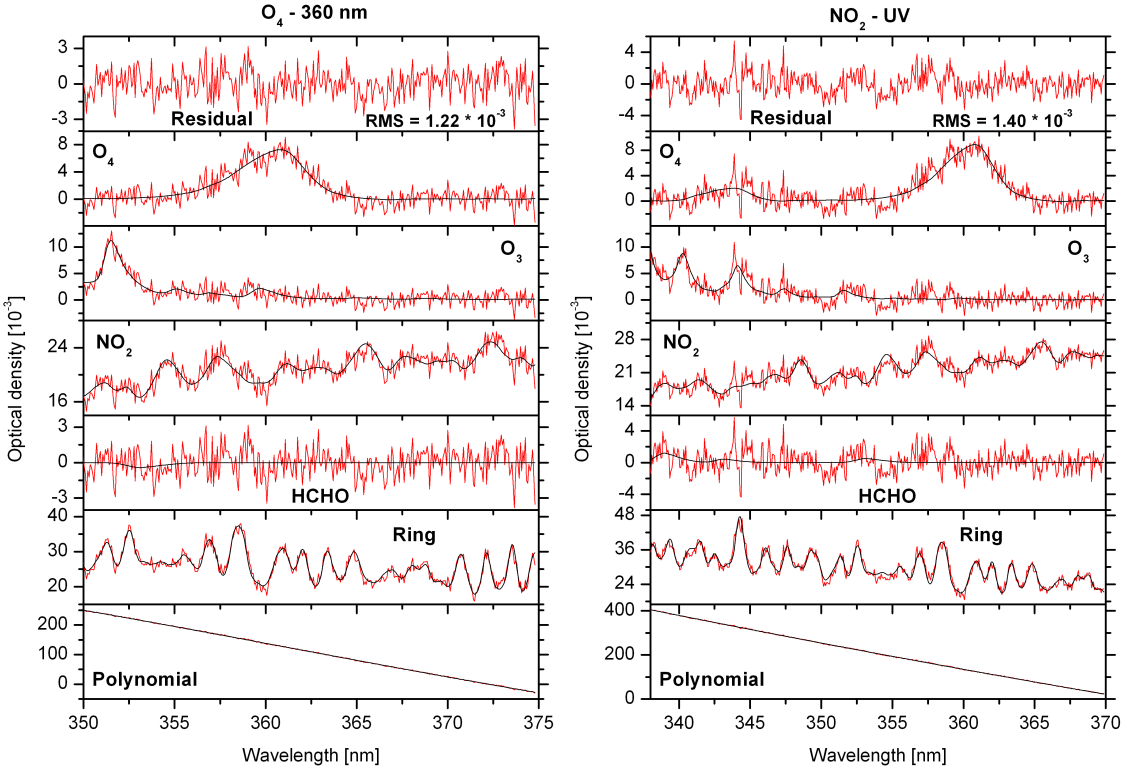

Figure 3.13: *Example for the spectral retrieval of the 360 nm band of O_4 (left panel) and NO_2 (right panel) in the ultra-violet wavelength range. The spectrum was recorded in Cabauw on 10 May 2008 for a SZA of 56° and an elevation angle of 2°. The zenith measurement from the same elevation sequence was taken as FRS. The retrieved spectral signatures are indicated in red and the fitted cross sections in black.*

according species at different temperatures in the atmosphere, an orthogonalization between both cross sections was applied. Thus, both cross sections became linearly independent, which reduced the correlation due to quite similar structures.
In Figures 3.13 - 3.15, examples for the spectral retrievals performed in this work are given. These Figures show the retrieved spectral signatures in red and the fitted optical densities in black as a function of the wavelength. The different components of the fit are indicated within the individual plots.

An example for the spectral retrieval of the 360 nm O_4 absorption band is given in the left panel of Figure 3.13. The retrieved O_4 ΔSCD is $(1.72 \pm 0.09) \cdot 10^{43} \frac{\text{molec}^2}{\text{cm}^5}$ and the RMS of the residual is $1.22 \cdot 10^{-3}$. An example for the NO_2 spectral retrieval in the ultra-violet applied on the same spectrum is shown in the right panel of Figure 3.13. The retrieved NO_2 ΔSCD is $(4.46 \pm 0.45) \cdot 10^{16} \frac{\text{molec}}{\text{cm}^2}$ and the RMS of the residual is $1.40 \cdot 10^{-3}$. The MAX-DOAS instrument utilizes three miniature spectrometers covering in total the wavelength range of 290 to 789 nm, while the individual intervals per spectrometer are approximately 290–425, 400–607 and 600–789 nm (Section 7.1.1). During operation, the recording of the spectra with the different spectrometer is synchronized, and the total integration time was chosen to ensure an appropriate temporal resolution of the measurement as well as a sufficient

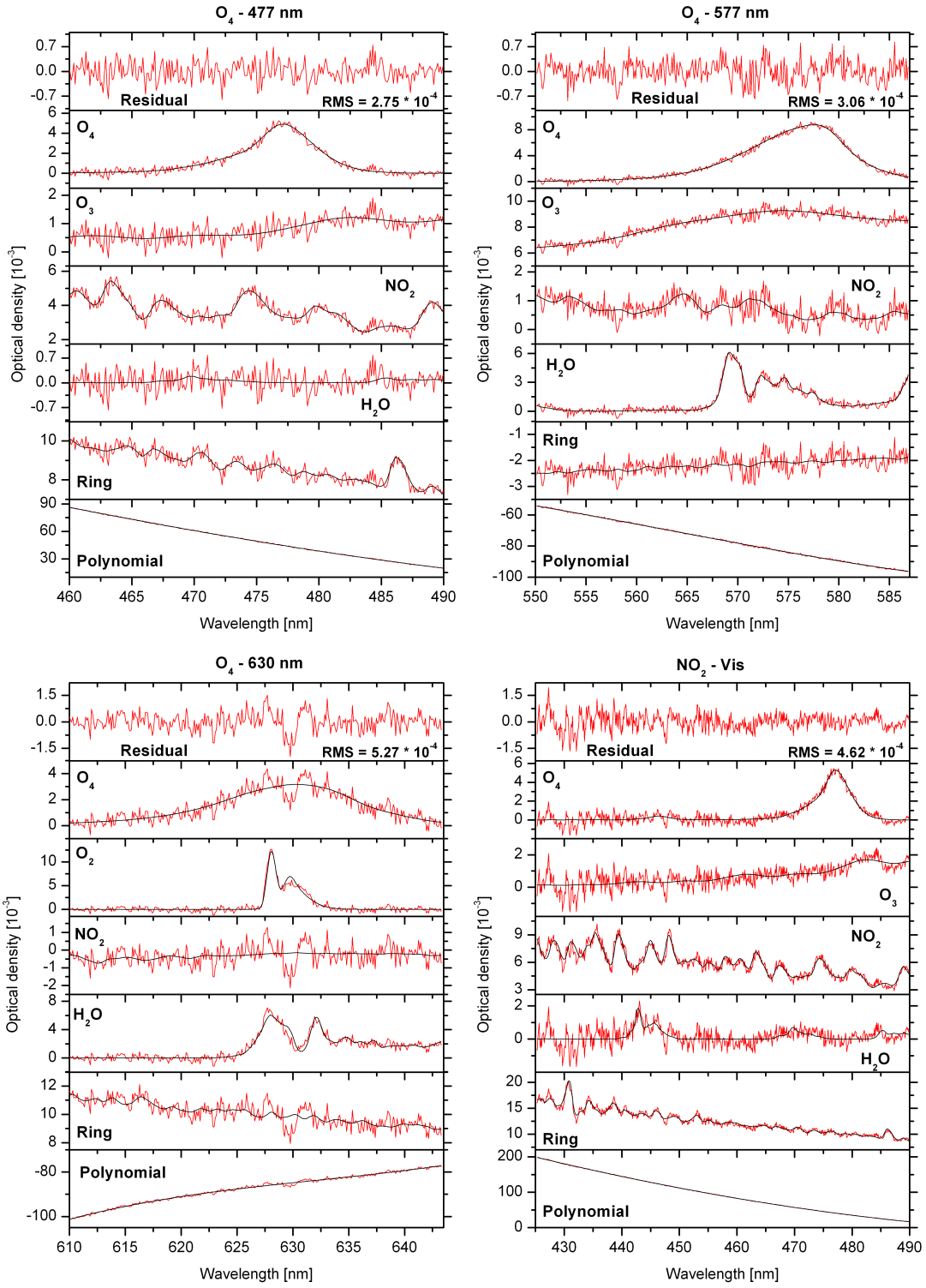

Figure 3.14: *Example for the spectral retrieval of the different O_4 absorption bands and NO_2 in the visible wavelength range. The spectra were recorded in Cabauw on 10 May 2008 for a SZA of 55° and an elevation angle of 20°. The zenith measurement from the same elevation sequence was taken as FRS. The retrieved spectral signatures are indicated in red and the fitted cross sections in black.*

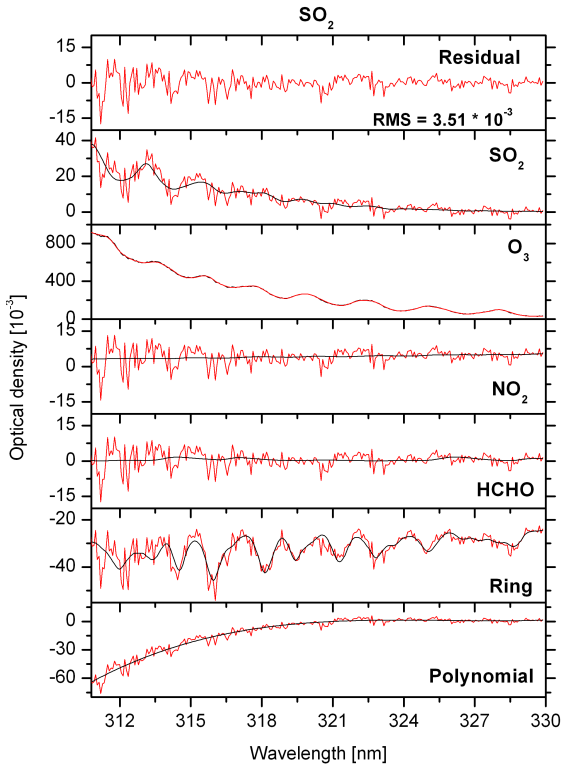

Figure 3.15: *Example for the spectral retrieval of SO_2. The spectrum was recorded in Heidelberg on 18 May 2010 for a SZA of 61° and an elevation angle of 1°. The zenith measurement from noon of the same day for a SZA of 30° was taken as FRS. The retrieved spectral signatures are indicated in red and the fitted cross sections in black.*

signal-to-noise ratio. The ultra-violet fraction of scattered sunlight intensity is less than the visible (see Chapter 4). Furthermore, the detectors in the spectrometers have a low sensitivity in the ultra-violet. These factors cause the low quality of the ultra-violet spectra and the comparably high RMS of the residual. However, the fit errors of 5 % and 10 % indicate that the unambigious detection of O_4 and NO_2, respectively, is possible, although the ΔSCD of NO_2 is comparably small in this example.

Examples for the retrieval in the visible are shown in Figure 3.14. The fit results for the 477 nm O_4 absorption band are shown in the upper left panel. The retrieved O_4 ΔSCD is $(7.67 \pm 0.21) \cdot 10^{42}$ $\frac{\text{molec}^2}{\text{cm}^5}$ and the RMS of the residual is $2.75 \cdot 10^{-4}$. In the example for the 577 nm O_4 absorption band shown in the upper right panel, the retrieved O_4 ΔSCD is $(7.98 \pm 0.15) \cdot 10^{42}$ $\frac{\text{molec}^2}{\text{cm}^5}$ and the RMS of the residual is $3.06 \cdot 10^{-4}$. In both cases, the RMS is smaller by nearly one order of magnitude compared to the O_4 retrieval in the ultra-violet. An example for the NO_2 spectral retrieval in the visible applied on the same spectrum is shown in the lower right panel of Figure 3.14. The retrieved NO_2 ΔSCD is $(1.38 \pm 0.09) \cdot 10^{16}$ $\frac{\text{molec}}{\text{cm}^2}$ and the RMS of the residual is $4.62 \cdot 10^{-4}$.

The retrieval of the 630 nm O_4 absorption band from a spectrum recorded with the third spectrometer is shown in an example in the lower right panel of Figure 3.14. The retrieved O_4 ΔSCD is $(4.49 \pm 0.75) \cdot 10^{42}$ $\frac{\text{molec}^2}{\text{cm}^5}$ and the RMS of the residual is

$5.27 \cdot 10^{-4}$. Significant structures remain in the residual at wavelengths connected to strong absorption by O_2 and H_2O. The reference spectra were extracted from the HITRAN database (Rothman et al., 2009). Since this database contains absorption lines which are modeled and measured in the laboratory, the absorption signatures in the atmospheric spectrum is possibly not reproduced accurately by the O_2 and H_2O reference spectra, which is clearly visible in the according graphs of the example. The comparably large relative O_4 error of 17 % is also due to the influence of the O_2 and H_2O reference spectra.
The spectral retrieval of SO_2 is shown in Figure 3.15. The intensity of scattered sunlight in the wavelength range relevant for SO_2 absorption decreases rapidly for wavelengths smaller than approximately 310 nm due to the strong O_3 absorption. Therefore, the wavelength range of 310.8 to 330 nm was used for the SO_2 retrieval. Since in this region the measured intensities are comparably low, the signal to noise ratio decreases due to lower signal saturation levels. To overcome this problem to some degree and to increase the quality of the retrieval, three subsequent spectra of equal viewing directions were added prior the spectral retrieval. Furthermore, in contrast to the other examples, the SO_2 retrieval was performed using a zenith measurement at noon time of the same day as FRS. This was necessary, since the detected volcanic plume was located in or above water clouds. Thus, the light path within the volcanic plume is the same for the zenith and off-axis viewing direction, so that the retrieval using the zenith measurement from the same elevation sequence as FRS results in no detection. The determined SO_2 dSCD is $(1.35 \pm 0.14) \cdot 10^{17} \frac{\text{molec}}{\text{cm}^2}$ and the RMS of the residual is $3.51 \cdot 10^{-3}$. The increasing noise toward smaller wavelengths in the residual and the high optical density of O_3 can be clearly identified. However, the relative SO_2 dSCD error of 10 % indicates the unambigious detection (Stutz and Platt, 1996).

Chapter 4

Radiative Transfer in the Atmosphere

The Sun is the primary source of energy for the Earth System. The solar radiation, once penetrated into the Earth's atmosphere, interacts in several different physical and chemical processes with the atmospheric compounds, like e.g. scattering and absorption by gaseous and particulate constituents. These processes, together with the interactions of radiation absorbed and emitted by the Earth's surface, are almost totally responsible for the terrestrial climate and weather on both global and local scales. In fact, the atmosphere controls the amount of solar radiation that actually reaches the Earth's surface, as well as the amount of terrestrial radiation that is emitted into space.
The quantification of the individual processes requires the knowledge of the vertical and horizontal distribution of the involved atmospheric constituents. As described in Section 3.5, MAX-DOAS measurements contain information on the vertical distribution of atmospheric trace gases and aerosols. The appropriate interpretation of the basic quantity of MAX-DOAS measurements, namely the slant column densities of the according trace species, is only possible, when the corresponding atmospheric light paths are known.
The atmospheric light paths are mainly determined by the occurring scattering processes, caused by the interaction of the solar radiation with air molecules and aerosols. This Chapter summarizes the atmospheric radiative transfer and describes the individual processes influencing the propagation of radiation. After the introduction of the basic quantities related to radiation transport, the approximation of the radiative budget in the atmosphere is described using a simple two-stream model in Section 4.1. The different interaction processes of radiation in the atmosphere and the resulting radiative transfer equation is addressed in Section 4.2. The air mass concept mentioned in Section 3.5 is discussed in detail in Section 4.3. Finally, Section 4.4 deals with the radiative transfer models, which are necessary to simulate the MAX-DOAS measurements and to calculate weighting functions for the trace gas and aerosol profile inversion methods.

4.1 Solar Radiation and the Earth-atmosphere system

The understanding of the processes involved in the radiative transfer in the atmosphere requires the knowledge of some basic radiometric quantities.
The radiant flux Φ is defined as radiation energy per unit time, regardless of the direction of its emission:

$$\Phi = \frac{\mathrm{d}E}{\mathrm{d}t} \qquad \left[\frac{Ws}{s} = W\right] . \tag{4.1}$$

The irradiance B is defined as the radiant flux Φ received by an (illuminated) area A_e:

$$B = \frac{\Phi}{A_e} \qquad \left[\frac{W}{m^2}\right] . \tag{4.2}$$

The radiation intensity F is the radiation flux Φ per solid angle Ω:

$$F = \frac{\Phi}{\Omega} \qquad \left[\frac{W}{sr}\right] . \tag{4.3}$$

The radiance I, also referred to as intensity, is the radiation intensity per area A_s:

$$I = \frac{\Phi}{\Omega \cdot A_s} \qquad \left[\frac{W}{sr\ m^2}\right] . \tag{4.4}$$

The involved areas A_e and A_s are assumed to be oriented perpendicular to the propagation direction of the radiation. Furthermore, the radiation quantities are often given as wavelength or frequency dependent quantities i.e. the specific radiance $I(\lambda)\,\mathrm{d}\lambda$.

The spectral irradiance of the Sun can be approximated by a blackbody at a temperature of 6000 K, with a maximum in the visible spectrum at about 500 nm and thus referred to as shortwave radiation. The solar irradiance spectrum contains Fraunhofer lines due to absorptions in the photosphere and chromosphere of the Sun. Furthermore, due to absorptions in the Earth's atmosphere by molecular oxygen, water vapor, ozone and carbon dioxide, the spectral irradiance reaching the Earth's surface is altered (see Figure 4.1). The solar irradiance, integrated over all wavelengths, on a surface oriented perpendicular to the solar beam at the Earth's orbit is about 1368 $\mathrm{W/m^{-2}}$ and is referred to as the solar constant S_0. Considering the cross-sectional area of the Earth that intercepts the solar beam and the surface area of the Earth that receives the radiation, the fraction of the solar constant received is 1/4 and thus about 342 $\mathrm{W/m^{-2}}$, if the Earth would be uniformly illuminated.

The Earth has a mean surface temperature of about 288 K. The corresponding irradiance spectrum of a blackbody has its maximum in the thermal infrared range and is referred to as longwave radiation with an irradiance of roughly 390 $\mathrm{W/m^{-2}}$ (see Figure 4.2).

The estimate for the Earth's annual and global mean energy balance is illustrated in Figure 4.3. Roughly 30 % of the incomming solar short wave radiation is reflected

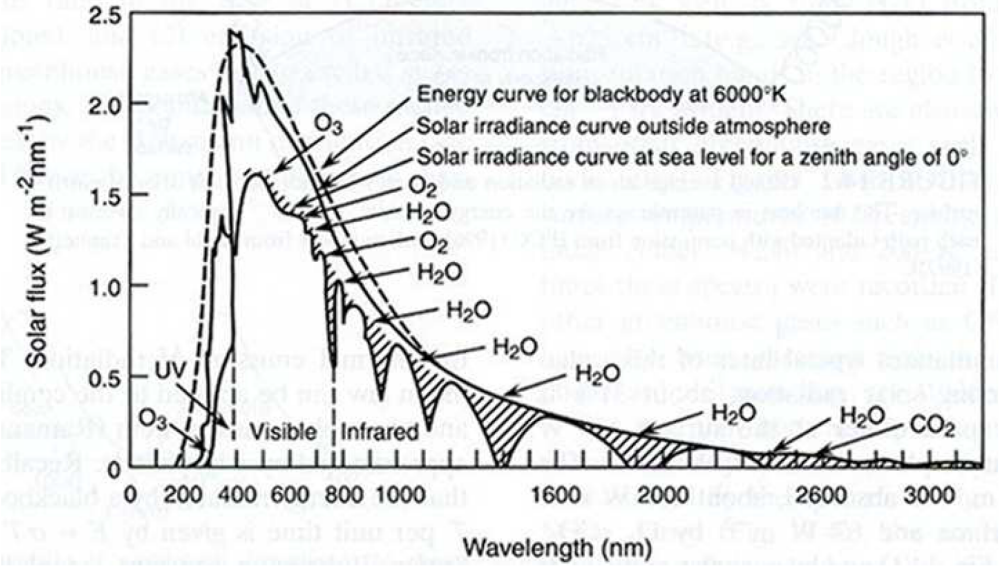

Figure 4.1: *Solar irradiance spectrum at the top of the Earth's atmosphere and at the surface. The solar irradiance spectrum is reshaped by the absorption of atmospheric constituents, such as molecular oxygen, water vapor, ozone and carbon dioxide. Adapted from Finlayson-Pitts and Pitts jr. (2000).*

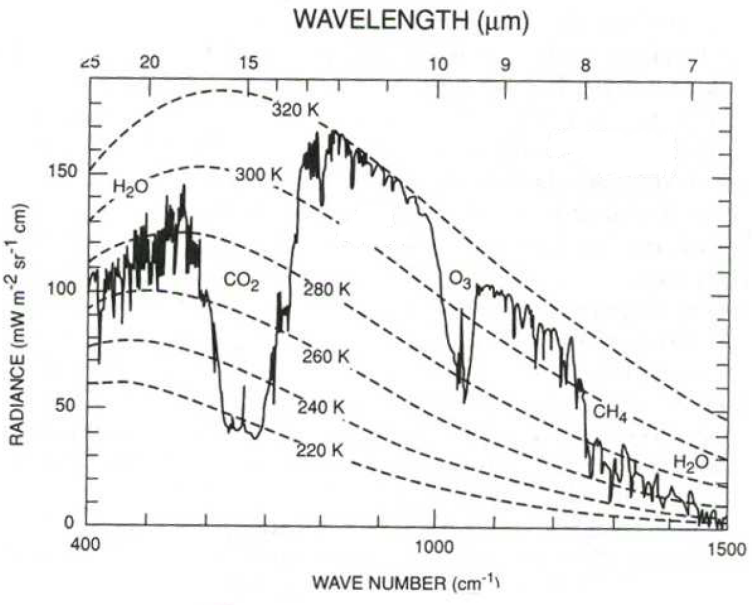

Figure 4.2: *Terrestrial radiance spectrum for cloud free conditions including the absorptions by water vapor, carbon dioxide, ozone and methane. Adapted from Brasseur et al. (1999).*

by clouds, air molecules, aerosol particles and the surface back to space, according to a mean planetary albedo $R_p \approx 0.3$. The major fraction is absorbed by the Earth's

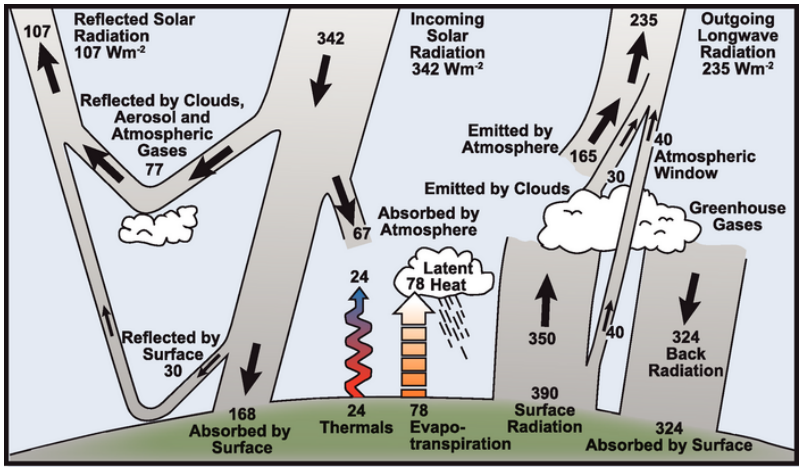

Figure 4.3: *The Earth's annual and global mean energy balance. Adapted from Solomon et al. (2007).*

surface and the remaining part is absorbed in the atmosphere. The amount of absorbed incoming short wave radiation is balanced by the release of the same amount of outgoing longwave radiation from the Earth and atmosphere over the long term. The absorbed energy by the surface is transferred to the atmosphere by warming the air in contact with the surface (thermals) and by evapotranspiration of plants. Furthermore, the surface emitts the energy by longwave radiation that is absorbed by clouds and greenhouse gases, like e.g. water vapor, carbon dioxide, ozone and methane, and emitted back to Earth as well as out to space.
An estimation of the equilibrium temperature of the Earth can be calculated using a simple model, which equates the incoming short wave and outgoing longwave radiation. The incoming solar energy at the Earth's surface is:

$$F_S = \frac{S_0}{4}(1 - R_p)\,. \tag{4.5}$$

For an average global temperature of the Earth-atmosphere system T_e, the longwave blackbody radiation is given by $F_L = \sigma T_e^4$, with the Stefan-Boltzmann constant $\sigma = 5.671 \cdot 10^{-8}\,\mathrm{Wm^{-2}K^{-4}}$. Equating F_S and F_L yields for T_e:

$$T_e = \left(\frac{(1 - R_p)S_0}{4\,\sigma}\right)^{\frac{1}{4}} \approx 255\,\mathrm{K}\,, \tag{4.6}$$

corresponding to the temperature of a blackbody with an irradiance of $235\,\mathrm{Wm^{-2}}$. As mentioned above, the Earth's surface emission corresponds to a blackbody temperature of 288 K. Thus, the surface temperature is about 33°C warmer than it would be if the atmosphere was completely transparent and the planetary albedo was still 0.3.

In an equilibrium state, the net radiative energy input, $F_{net} = F_S - F_L$, is zero. The change in net energy input due to perturbations in the shortwave and longwave components is given by $\Delta F_{net} = \Delta F_S - \Delta F_L$. Then, a temperature change

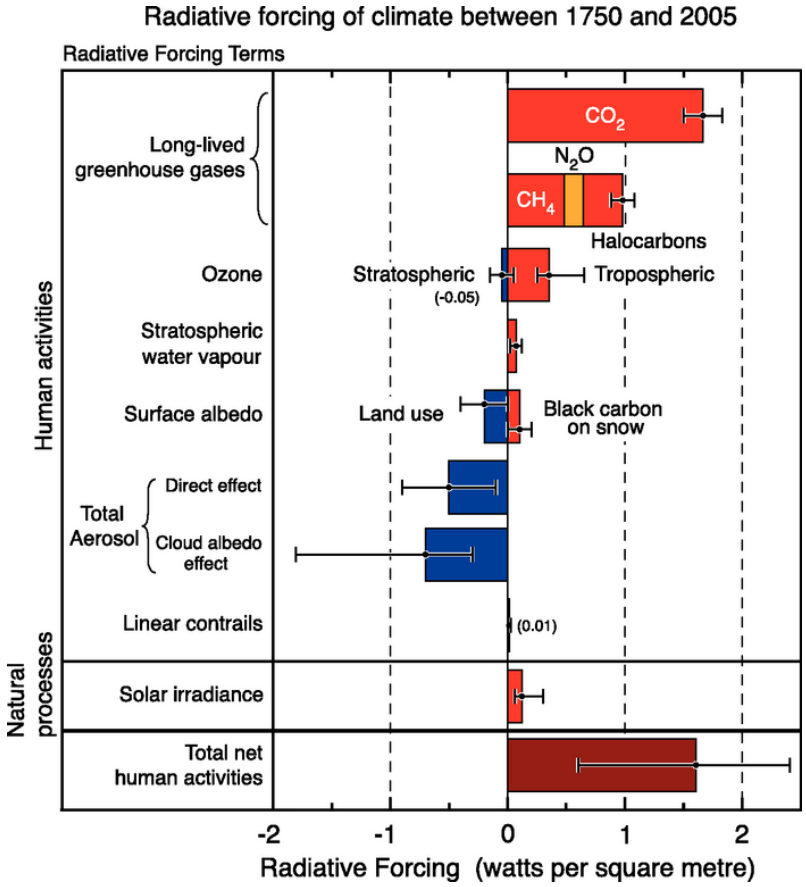

Figure 4.4: *The principal components and corresponding uncertainties of the radiative forcing of climate change. The values represent the forcings in 2005 relative to the start of the industrial era (about 1750). Adapted from Solomon et al. (2007).*

ΔT_e results to reestablish equilibrium. It can be related linearly to ΔF_{net} by a parameter λ_0, resulting in the relation $\Delta T_e = \lambda_0 \Delta F_{net}$. The parameter λ_0 is the climate sensitivity parameter (e.g., Solomon et al., 2007). ΔF_{net} is referred to as radiative forcing. Figure 4.4 summarizes the principal components of the radiative forcing of climate change. The individual radiative forcings of the according components result from different factors affecting climate and are associated with human activities or natural processes. Positive forcings lead to warming of climate and negative forcings lead to a cooling. The major fraction of the total radiative forcing is due to human activities, which cause significant changes in the abundance of long-lived gases, ozone, water vapour, surface albedo and aerosols. While the forcings attributable to gaseous species is positve, aerosols contribute to negative forcings. However, the large uncertainties of the aerosol forcing components indicate the low level of scientific understanding, and requires more and intensive observations and studies connected to atmospheric aerosols.

The considerations so far are only applicable to global average radiation budgets. The atmospheric radiation transfer on a local scale, occurring during and thus relevant to MAX-DOAS observations (Section 3.5), requires the detailed consideration of the interaction processes of radiation with the atmospheric constituents. These

processes are subject of the following Section.

4.2 Interaction Processes of Radiation in the Atmosphere

Radiation traversing the atmosphere can interact in a variety of processes with air molecules or aerosol particles. **Absorption** results in a removal of the radiation from the radiation field and a conversion into some other form of energy, e.g. heat. **Elastic scattering**, by air molecules (Rayleigh scattering) or atmospheric aerosol particles (Mie scattering), changes the direction of propagation of an individual photon, but not its energy. In contrast, **inelastic scattering** additionally changes the photon energy beside the propagation direction. Inelastic scattering by molecules is called Raman scattering, where the photon energy can be reduced (Stokes scattering) or increased (anti-Stokes scattering). The **thermal emission** from air molecules and aerosol particles in the infrared wavelength range are negligible for MAX-DOAS measurements in the ultra-violet and visible.

4.2.1 Absorption

The absorption of photons change the energetic states of molecules due to different phenomena. During these interactions, electronic, vibrational and rotational transitions occur.
For small atoms, the energy level E_n of an electronic state n is in good approximation given by the Rydberg formula $E_n = -R_{Ry}/n^2$, where R_{Ry} denotes the Rydberg constant for the particular atom. Thus, the absorption of a photon in the ultraviolet/visible wavelength range results in the redistribution of the electronic shell according to $\Delta E_{el} = E_{n_1} - E_{n_2} = h\nu$, where n_1 and n_2 denote the lower and upper state of the atom, respectively, and ν the frequency of the photon.
In contrast to atoms, molecules have electronic states of different energy and additional excitation schemes. The rotation of the entire molecule according to the angular momentum $\vec{J}$ and quantum number J, can be changed by the absorption of photons with wavelengths in the sub-mm or microwave range. The allowed rotational energy levels in a molecule are given by $E_j = BJ(J+1)$, where $B = \frac{\hbar}{2\Theta}$ denotes the rotational constant of the particular molecule and rotation axis with the moment of inertia Θ with respect to this axis. The energy difference of two consecutive states is $\Delta E_j = 2B(J+1)$. Transitions between states with different J are constrained by the selection rule, and comprise different branches depending on the angular momentum difference between the initial and final state, namely the O, P, Q, R and S-branches with $\Delta J = -2, -1, 0, +1$ and $+2$, respectively.

The vibration of molecules can be approximated by a harmonic oscillator with energy levels $E_\nu = (\nu + 1/2)\hbar\omega_0$, quantized by the vibrational quantum number ν and the zero-point energy of the molecular oscillator $\frac{1}{2}\hbar\omega_0$. Energies of vibrational transitions correspond to wavelengths in the infrared spectral range. Since the molecules are also excited rotationally, each vibrational transition splits into a series of rotational lines.

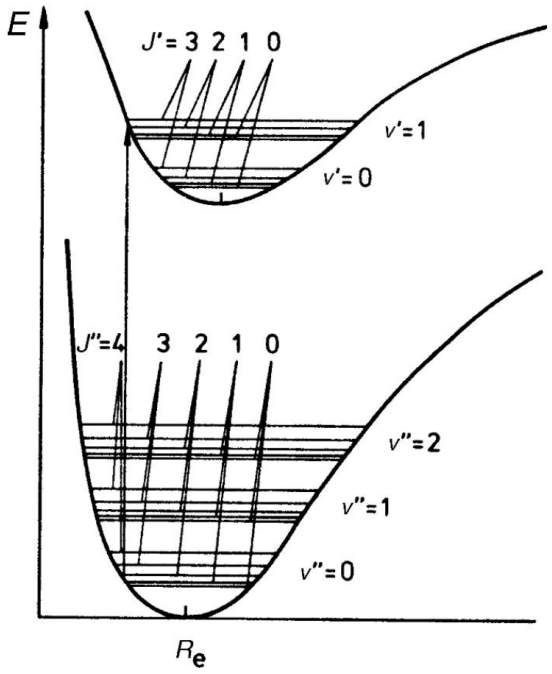

Figure 4.5: *Sketch of ro-vibrational energy levels of two electronic states of a (diatomic) molecule. The electronic energies are given as a function of the distance between the nuclei of the atoms within the molecule and are minimal at R_e, which usually depends on electronic state. The equidistant, horizontal groups of lines denote the lowest rotational levels of the vibrational states.*

As a consequence of the different excitation schemes, the energy levels of the molecular electronic shell are split into a set of vibrational and rotational levels (Figure 4.5). Thus, the absorption spectra of molecules have differential structures in the ultra-violet and visible range, which enable the application of the DOAS method (see Chapter 3).

4.2.2 Rayleigh Scattering

The scattering process, changing the propagation direction of a photon without changing its energy, induced by dielectric particles, which are small compared to the wavelength of the scattered photon (e.g. air molecules), is denoted as Rayleigh scattering. The physical process can be described by the excitation of an oscillating dipole in a polarizable air molecule induced by the incident radiation (e.g., Van de Hulst, 1981). The Rayleigh scattering cross section σ_R in cm^2 is given by:

$$\sigma_R \approx \frac{8\,\pi^3}{3\,\lambda^4 N_{air}^2} \cdot \left(n_0(\lambda)^2 - 1\right)^2 \cdot F_{\mathrm{K}}(\lambda)\,, \tag{4.7}$$

where λ denotes the wavelength in cm, $n_0(\lambda)$ is the wavelength-dependent index of refraction of air, N_{air}^2 is the number density of air, and $F_{\mathrm{K}}(\lambda) \approx 1.061$ is a correction for anisotropy, namely the polarisability of air molecules. The Rayleigh extinction

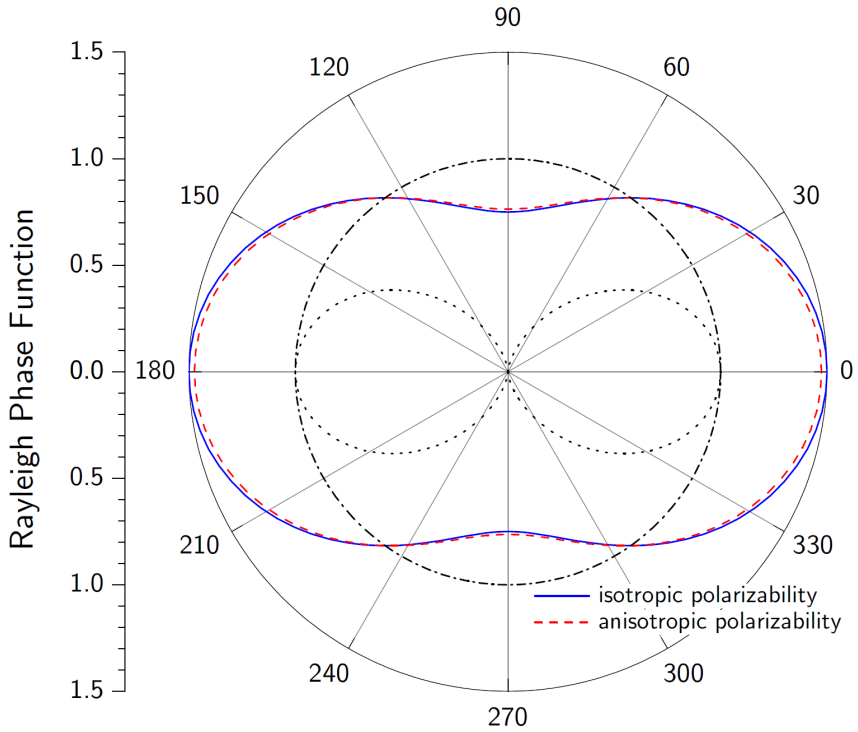

Figure 4.6: *Polar diagram of the Rayleigh scattering phase function $\Phi_R(\theta)$ for unpolarized incident light (see text). Adapted from Hönninger (2002).*

coefficient ϵ_R is then given by $\epsilon_R = N_{air} \cdot \sigma_R$.
Figure 4.6 shows a polar diagram of the Rayleigh scattering phase function $\Phi_R(\theta)$ for unpolarized incident light. It illustrates the relative intensity of the scattered light in dependence of the scattering angle θ between the incident propagation direction and the direction after the scattering event. The contribution of light polarized parallel to the scattering plane is depicted by the dotted black line, and indicates the $\propto \sin^2\theta'$ dependence of a Hertz dipole, with $\theta' = \frac{\pi}{2} - \theta$ being the angle between dipole axis and the Poynting vector. The contribution of light polarized perpendicular to the scattering plane is depicted by the dash dotted line, and shows no dependence on θ. The superposition of both contributions is indicated by the blue line. The Rayleigh scattering phase function is given by:

$$\Phi_R(\cos\theta) = \frac{3}{4}\left(1 + \cos^2\theta\right) \ , \tag{4.8}$$

Taking the anisotropy of the polarisability into account, equation (4.8) becomes (Penndorf, 1957):

$$\Phi_R(\cos\theta) = 0.7629\left(0.9324 + \cos^2\theta\right) \ , \tag{4.9}$$

which is depicted by the red line in Figure 4.6.

4.2.3 Raman Scattering

Raman scattering specifies the inelastic scattering of photons by air molecules. The energy of the scattering photon is changed in addition to the change of its propagation direction. During this interaction process, the photon either transfers part of its energy to the molecule (Stokes, $\Delta J = +2$, S-branch), or takes over part of the molecule's excitation energy (Anti-Stokes, $\Delta J = -2$, O-branch). When only the rotational excitation is affected ($\Delta\nu = 0$), the term rotational Raman scattering (RRS) is used. The term rotational-vibrational Raman scattering (RVRS) is used, if also the vibrational state changes during the scattering process ($\Delta\nu = \pm 1$). Only discrete amounts of energy given by the difference between the discrete excitation levels can be transferred between the photon and the molecule. For air molecules (oxygen and nitrogen) RRS frequency shifts of up to $\pm 200\ \mathrm{cm}^{-1}$ occur, which corresponds to several nanometers in the ultra-violet/visible wavelength range. In case of RVRS a vibrational shift of $\pm 2331\,\mathrm{cm}^{-1}$ for nitrogen and $\pm 1555\,\mathrm{cm}^{-1}$ for oxygen has to be added. Since the RRS is one order of magnitude stronger then the RVRS, it dominates the Raman scattering and the RVRS can be neglected for the calculation of the Ring spectrum (see Section 3.4.2). Further details on the Raman scattering can be found in the literature (Burrows et al., 1996; Haug, 1996; Sioris and Evans, 1999).

4.2.4 Mie Scattering

When the dimensions of the scattering particle becomes comparable to the wavelength of the incident light, the interaction is described by Mie scattering. The involved physical process can be regarded as the radiation resulting from a large number of coherently excited elementary emitters in a particle. Thereby, interference effects occur due to comparable linear dimension of the particle and the wavelength of the incident light. Since the shape and size of aerosols differ strongly, the calculation of the particle scattering cross section can be very complicated. However, the well developed Mie theory is implemented in a number of numerical models allowing the calculation of scattering phase functions and extinction coefficients for given aerosol types and particle size distributions (Van de Hulst, 1981; Wiscombe, 1980). Mie scattering refers to spherical aerosols and the non-spherical cases are approximated by the spherical description.

The scattering phase function in the Mie case depends in general on the ratio between the radius r of the particle and the wavelength λ of the scattered light, which is referred to by the aerosol size parameter x:

$$x := \frac{2\,\pi\,r}{\lambda}\,. \tag{4.10}$$

Figure 4.7 shows the Mie scattering phase functions $\Phi_M(\theta)$ for water droplets of three different $x = 1, 3$ and 10 calculated for $\lambda = 550\,\mathrm{nm}$ (Sanghavi, 2003). The fraction of forward scattering increases with increasing particle size.
In the atmosphere, however, aerosols are present in different sizes, shapes and chemical compositions. Within the Mie theory the bulk scattering properties are therefore described by integrating the single scattering properties of aerosols over their en-

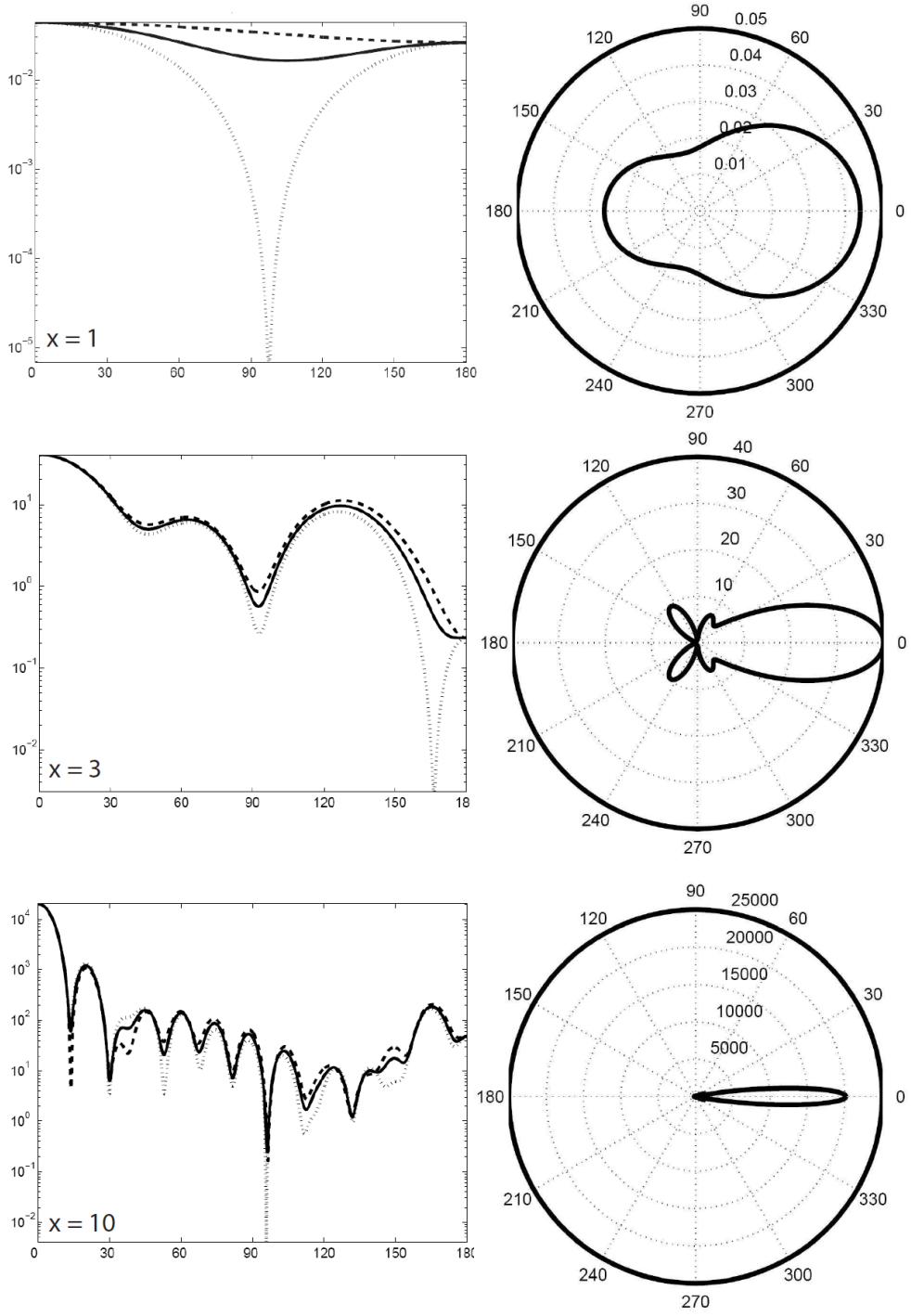

Figure 4.7: *Mie scattering phase functions at 550 nm for water droplets with aerosol size parameters $x = 1, 3$ and 10. Left column: Phase function on logarithmic scale; Right column: Polar diagrams of the same phase functions on linear scale. It becomes apparent that forward scattering dominates with increasing particle size. Adapted from Sanghavi (2003).*

tire size distribution. The computational effort in these calculations is remarkably reduced by the usage of an analytical expression for the scattering phase function, depending only on a few observable parameters. Most common is the Henyey-Greenstein parametrization (Henyey and Greenstein, 1941):

$$\Phi_{HG}(\cos\theta) = \frac{1-g^2}{4\,\pi\cdot(1+g^2-2\,g\cos\theta)^{\frac{3}{2}}}\,, \tag{4.11}$$

where g is the average cosine of the scattering function $g = \langle\cos\theta\rangle$ referred to as the asymmetry parameter. A value of 0 indicates an isotropic scattering behavior, while the value of 1 indicates a complete forward scattering. Typical values for tropospheric aerosols are $g \approx 0.6$–0.7.

4.2.5 Aerosol Optical Properties

In addition to their scattering nature, atmospheric aerosols may also absorb radiation depending on their chemical composition. Besides the scattering phase function, aerosols are characterized by the extinction coefficient ϵ_M, given in units of inverse length, and the dimensionless single scattering albedo (SSA) ω_0. The SSA quantifies the relation between the extinctions due to scattering and absorption:

$$\omega_0(\lambda) = \frac{\epsilon_s(\lambda)}{\epsilon_s(\lambda)+\epsilon_a(\lambda)} \qquad \text{and} \qquad \epsilon_M(\lambda) = \epsilon_s(\lambda)+\epsilon_a(\lambda)\,, \tag{4.12}$$

where $\epsilon_s(\lambda)$ and $\epsilon_a(\lambda)$ denotes the wavelength dependent aerosol scattering and absorption coefficient, respectively. A value of 1 for the SSA describes only scattering aerosol, while completely absorbing aerosols have a SSA of 0. The wavelength dependence of $\epsilon_M(\lambda)$ is described by the Ångström exponent for extinction α_M:

$$\epsilon_M(\lambda) = \epsilon_M(\lambda_0)\cdot\left(\frac{\lambda}{\lambda_0}\right)^{-\alpha_M}\,, \tag{4.13}$$

where $\epsilon_M(\lambda_0)$ is the extinction coefficient at the reference wavelength λ_0. The Ångström exponent for extinction is inversely related to the mean aerosol particle radius. Typically $\epsilon_M(\lambda)$ is found in the range 0.5–2.5, with an 'average' value of ≈ 1.3 (Angström, 1930). Thus, the wavelength dependence is weaker compared to Rayleigh scattering. Generally, the wavelength dependence of the scattering and absorption coefficients differ and are depicted by the Ångström exponent for scattering α_s and absorption α_a, respectively, in a similar manner as in equation (4.13). The integrated aerosol extinction profile along the height is referred to as the aerosol vertical optical depth (AOD) τ_M:

$$\tau_M(\lambda) = \int \epsilon_M(\lambda, z)\,\mathrm{d}z\,. \tag{4.14}$$

One practical application is the rough approximation of the aerosol extinction based on visibility. Since aerosols cause a reduction in the visibility, and the human eye may distinguish intensity differences as small as 2 % (Rödel, 2000), the simple estimation

described by:

$$L_{vis} = \frac{3.9}{\epsilon_M(\lambda_{eye})} \tag{4.15}$$

can be made for the visibility distance L_{vis}. λ_{eye} denotes the wavelength at which the human eye has its highest sensitivity and is approximately 500 nm.

4.2.6 Radiative Transfer Equation

The radiative transfer equation (RTE) integrates changes of the radiance $I(\lambda)$ at a given wavelength while passing through the atmosphere. $I(\lambda)$ is reduced by the amount $\mathrm{d}I_a(\lambda)$ after traversing an absorbing layer of the thickness $\mathrm{d}s$:

$$\mathrm{d}I_a(\lambda) = -I(\lambda) \cdot \epsilon_a(\lambda)\,\mathrm{d}s = -I(\lambda) \cdot \sigma_a(\lambda) \cdot N\,\mathrm{d}s\,, \tag{4.16}$$

where ϵ_a is the absorption coefficient, σ_a and N are the absorption cross-section and number per unit volume of the absorber, respectively. The integration of equation (4.16) over the thickness of the absorbing layer L yields the well known Lambert-Beer's law including the initial radiance $I_0(\lambda)$ (see Section 3.1).
The extinction of $I(\lambda)$ due to scattering is described, in analogy to the absorption, by:

$$\mathrm{d}I_s(\lambda) = -I(\lambda) \cdot \epsilon_s(\lambda)\,\mathrm{d}s = -I(\lambda) \cdot \frac{\mathrm{d}\sigma_s(\lambda)}{\mathrm{d}\Omega} \cdot N\,\mathrm{d}\Omega\mathrm{d}s\,, \tag{4.17}$$

where ϵ_s is the scattering coefficient, σ_s and N are the scattering cross-section and number per unit volume of the scattering centers, respectively. $\mathrm{d}\sigma_s(\lambda)/\mathrm{d}\Omega$ denotes the differential scattering cross-section, which depends on the scattering angle θ and polar angle ϕ. The total scattering cross-section is thus given by:

$$\sigma_s(\lambda) = \int_{4\pi} \frac{\mathrm{d}\sigma_s(\lambda)}{\mathrm{d}\Omega}\,\mathrm{d}\Omega\,. \tag{4.18}$$

Frequently, a dimensionless scattering function is useful:

$$S(\theta,\phi) = \frac{4\pi}{\sigma_s(\lambda)} \cdot \frac{\mathrm{d}\sigma_s(\lambda)}{\mathrm{d}\Omega}\,. \tag{4.19}$$

In the ultra-violet and visible wavelength region, contributions to the radiance due to thermal emission can be neglected. Thus, the RTE is described by:

$$\frac{\mathrm{d}I(\lambda)}{\mathrm{d}s} = \underbrace{-\left[\epsilon_a(\lambda) + \epsilon_s(\lambda)\right] \cdot I(\lambda)}_{1} \underbrace{+\epsilon_s(\lambda) \int_0^{\pi}\int_0^{2\pi} I(\lambda,\theta,\phi) \cdot \frac{S(\theta,\phi)}{4\pi}\,\mathrm{d}\phi \cdot \sin\theta\,\mathrm{d}\theta}_{2}\,. \tag{4.20}$$

The first term on the right hand side denoted by '1' describes the extinction due to absorption and scattering processes, while second term '2' describes the radiance added to the direction of propagation by scattering.

4.3 The Air Mass Factor Concept

The MAX-DOAS technique measures slant column densities, which are integrated concentrations of trace gases along the light path (see Chapter 3). Thereby, the slant column densities depend on the light paths occurring during the particular viewing geometries at which the MAX-DOAS measurements are conducted. These light paths depend also on the wavelength. The quantitative interpretation and comparison to measurements obtained by other techniques require the conversion of the slant column density into the vertical column density, which is the integrated concentration along the height. Thus, the vertical column density is independent from the wavelength and measurement geometry. The connection between the slant (S) and vertical column density (V) is obtained by the Air Mass Factor (AMF) A (Noxon et al., 1979; Solomon et al., 1987; Marquard et al., 2000):

$$A(\lambda, \theta, \alpha, \phi) = \frac{S(\lambda, \theta, \alpha, \phi)}{V} \,, \tag{4.21}$$

with the wavelength λ, solar zenith angle θ, elevation angle of the instrument line of sight α and the relative solar azimuth angle ϕ (see Section 3.5).
The AMF can be approximated geometrically for absorber layers in the stratosphere and troposphere. However, the geometrical approximation is not appropriate for elevation angles smaller than 20° and solar zenith angles larger than 70°. Furthermore, the assumption that the light is scattered only once into the line of sight of according elevation angle has to be fulfilled. In the case of tropospheric absorbers, this scattering event should occur above the absorber layer and, in the case of stratospheric absorbers, scattering should occur below the absorber layer (see Section 3.5.
Since the geometrical approximation assumes the occurrence of single scattering events, its applicability is generally limited to specific atmospheric conditions. Atmospheric aerosols significantly influence the light path by increasing the scattering probability. Thus, in the presence of high aerosol loads and clouds, multiple scattering may occur. Furthermore, the surface albedo and the absorption by strong absorbers have an impact on the light path and the AMF. To account for these effects, the height dependent radiation field in the atmosphere has to be considered including the vertical distribution of the light path determining quantities. Since the necessary calculations are complex, radiative transfer models are used to simulate the radiation field in the atmosphere (Section 4.4). These models allow for the calculation of Box Air Mass Factors (Box-AMF), which are height resolved AMFs. Thereby, the atmosphere is discretized along its vertical axis into layers of height h_i, called boxes. The Box-AMF A_i is the air mass factor for box i defined by:

$$A_i := \frac{\mathrm{d}S}{\mathrm{d}V_i} \,, \tag{4.22}$$

where V_i is the vertical column density in the box i. The Box-AMF quantifies how the measured slant column density changes with an alteration of the vertical column density in a certain box. Box-AMFs can be utilized in the retrieval of trace gas vertical profiles (see Section 5.8). In the case of weak absorbers, the inversion problem of the profile retrieval is linear, since the Box-AMFs do not depend on the

according trace gas profile. In contrast, strong absorbers influence the Box-AMFs, causing the inversion problem to become non-linear.
The total AMF can be calculated from the Box-AMFs and the respective trace gas profile by adding the Box-AMFs over the whole atmosphere, weighted with the partial trace gas vertical columns:

$$A = \frac{\sum_i A_i \cdot V_i}{\sum_i V_i} , \tag{4.23}$$

and can be used for the conversion of the measured slant column density.

4.4 Radiative Transfer Modeling

The calculation of air mass factors requires the simulation of the radiation field in the atmosphere. In addition, the sensitivity of MAX-DOAS O_4 and radiance measurements to perturbations in the aerosol profile has to be determined for the aerosol profile retrieval (see Section 5.8). It is quantified by the according weighting function, which also requires the vertically resolved simulation of the radiation field in the atmosphere.
Radiative transfer simulations in the atmosphere require the solution of the RTE (equation (4.20)). The RTE has no analytical solution, and radiative transfer models (RTM) are therefore utilized. In general, two different numerical approaches are commonly applied in RTMs. On the one hand, numerical methods, e.g. the Discrete Ordinate Method, which applies a discretization for the ordinates and directions, are implemented for the calculation of the resulting radiation field. On the other hand, the paths of an ensemble of individual photons, with randomly chosen parameters, through the atmosphere are calculated in a statistical approach using e.g. Monte Carlo Methods. Examples for the former approach are DISORT (Stamnes et al., 1988) and SCIATRAN 2 (Rozanov et al., 2005). The latter approach is utilized e.g. by TRACY (von Friedeburg, 2003) and McArtim (Deutschmann et al., 2011). Both approaches have in common, that several simplifications and approximations have to be introduced to reduce the complexity of the RTE solution. SCIATRAN 2 was utilized for the calculations performed within this work.

4.4.1 SCIATRAN 2

The radiative transfer model SCIATRAN 2 applies the Discrete Ordinate Method to solve numerically the RTE for monochromatic unpolarized radiation in a spherical atmosphere (Rozanov et al., 2005). Thereby, the term denoted by '2' in equation (4.20) is separated in a part, contributing due to one scattering event, and a part for the contribution due to multiple scattering. The resulting combined differential-integral equations are then solved using the Finite Difference Method and the Picard iterative approximation for the multiple scattering term (Rozanov et al., 2000, 2001). Furthermore, both the azimuthal dependence of the radiation field and the scattering phase function are developed in Fourier series in combination with Legendre

polynomials. The solar zenith angle dependency is discretized and the according integrals are replaced by Gaussian quadratures. Also the height coordinate is discretized. Finally, the approximations and discretization result in a set of equations, which are solved by matrix inversion for each harmonic of the Fourier expansion separately.

4.4.2 Model Parameter

SCIATRAN 2 provides the calculation of radiances, total AMFs and Box-AMFs for an arbitrary output altitude. The atmosphere is subdivided in layers defined by the altitude grid. Atmospheric properties are assumed to be homogeneous within these layers. The temperature and pressure profile can either be provided by the user, e.g. radiosonde measurements, or adapted from a climatological data base. The climatology data included in SCIATRAN 2 has been obtained using a two dimensional chemo-dynamical model developed at the Max Planck Institute for Chemistry in Mainz (Brühl and Crutzen, 1993). The same applies for the trace gas profiles. The trace gas absorption cross sections are provided by the user and consist of several cross sections at different temperatures to account for the temperature dependence. The optical properties of aerosols are quantified by the vertical distribution of the extinction coefficient, single scattering albedo and asymmetry parameter of the Henyey-Greenstein parametrization of the phase function. The provided profiles are interpolated on the altitude grid using Akima interpolation (Akima, 1970). Furthermore, the surface albedo and the wavelength for the calculations are selected by the user. SCIATRAN 2 allows for the consideration of several viewing geometries in one program run. Each viewing geometry is determined by the solar zenith and relative azimuth angle, and the elevation angle of the observer line of sight.

Chapter 5

Retrieval of Atmospheric Trace Gas and Aerosol Profiles by Inverse Modeling

The inversion of the vertical distribution of atmospheric constituents from indirect measurements is a widespread technique in atmospheric sciences. For example, the vertical distribution of O_3 was retrieved from nadir observations of backscattered light carried out by the satellite instrument of the Global Ozone Monitoring Experiment (GOME) using the optimal estimation method (Munro et al., 1998; Hoogen et al., 1999). This method is also applied to ground based MAX-DOAS observations. The retrieval of bromine oxide (BrO) and aerosol profiles in the boundary layer from MAX-DOAS measurements in the Arctic is presented in Frieß et al. (2011). Furthermore, NO_2 and O_3 profiles in the stratosphere were retrieved from balloon-borne DOAS measurements using a modified version of the optimal estimation method (Kritten et al., 2010). Using the regularization method, Prados-Roman et al. (2011) retrieved tropospheric BrO profiles from DOAS measurements in limb geometry aboard an aircraft during the ascent and descent.

In this work, trace gas and aerosol profiles are retrieved from slant column densities and intensities measured by MAX-DOAS. As described in Section 3.5, the information on atmospheric aerosols can be derived from MAX-DOAS O_4 measurements. Since the vertical profile of O_4 is known and nearly constant in time, the obtained slant column densities and thus the light paths are mainly determined by the vertical distribution and optical properties of aerosols. These are in detail the aerosol extinction, single scattering albedo, phase function and Ångström exponent (see Section 4.2). These parameters are used by radiative transfer models (RTM) and include all information necessary for the simulation of the impact of aerosols on the radiative transfer. When the results of MAX-DOAS O_4 measurements are compared to simulations from the RTM, the aerosol parameters can be adjusted iteratively until agreement between model and measured values is achieved. Then, the aerosol scenario used for the model is in agreement with the atmospheric aerosol scenario during the real measurement. The iterative adjustment process can be performed using well established mathematical approaches. In this work, the optimal estimation method (Rodgers, 1976, 1990, 2000) is used for the retrieval of aerosol

extinction profiles at 360, 477, 577 and 630 *nm* using the individual absorption bands of O_4. Furthermore, the regularization method (Phillips, 1962; Tikhonov, 1963; Hasekamp and Landgraf, 2001; Steck, 2002) is also applied for the retrieval of aerosol profiles. The determined aerosol profiles are used for the retrieval of NO_2 and SO_2 profiles from MAX-DOAS measurements also using the optimal estimation and regularization method.
Since the first studies of Hönninger and Platt (2002), Hönninger et al. (2004) and Wagner et al. (2004) on the capability of MAX-DOAS measurements to provide profile informations on trace gases and aerosols, and the intensive modeling study of Frieß et al. (2006) on the application of the optimal estimation method for the retrieval of aerosol profiles from MAX-DOAS O_4 measurements, a growing number of groups within the worldwide DOAS community focused their work on this topic. Irie et al. (2008) utilized an approach, which uses the optimal estimation method and a parametrization of the aerosol profile. The lower troposphere is divided into three layers of 1 *km* extent and the aerosol profile is described by the fractions of the total aerosol optical depth (AOD) attributed to the individual layers. This method using the O_4 477 *nm* band was then extended to use also the 360 *nm* band (Irie et al., 2009). In a next study, the retrieval method was also applied to determine profiles of several trace gas species (Irie et al., 2011).
A parameterized description of the aerosol profile was also used by Li et al. (2010) for the aerosol retrieval using MAX-DOAS O_4 measurements. In this study, a simple least squares method using a lookup table was applied as an alternative for the optimal estimation method. The parameters for the aerosol profile were used to scale the AOD, the height of the box-shaped boundary layer and the fraction attributed to the exponential decreasing part of the profile above the boundary layer. The retrieval approach used by Wagner et al. (2011) for the determination of aerosol, HCHO and NO_2 profiles is base on the method from Li et al. (2010), but extended by further parameters allowing for a more flexible description of the profile shape. In contrast to the studies mentioned so far, Clémer et al. (2010) applied the optimal estimation method in combination with a complete profile, namely the aerosol extinction as a function of altitude, as proposed by Frieß et al. (2006). The profiles were retrieved for 360, 477, 577 and 630 *nm* using the MAX-DOAS O_4 measurements.

The retrieval approach used in this work is based on the method explored in Frieß et al. (2006), but utilizes the RTM SCIATRAN Version 2 (see Section 4.4.1, Rozanov et al., 2005) instead of Version 1 (Rozanov et al., 2002). The main advantage of this change is the direct parameterization of the aerosol optical properties instead of the usage of the OPAC database (Hess et al., 1998). The aerosol single scattering albedo and the asymmetry parameter for the Henyey-Greenstein parameterization of the phase function (Section 4.2.5) can be adjusted directly in SCIATRAN 2, while in SCIATRAN 1 the setting of these parameters is controlled by the adjustable mixture of predefined aerosol types, whose optical properties is then looked up in the OPAC database. The latter method limits the possibilities of to RTM usage in combination with MAX-DOAS measurements, and can additionally imply uncertainties due to errors in the database values.
In contrast to the studies mentioned above, the aerosol profile retrieval utilized here can also include the intensities measured by the MAX-DOAS instrument, which

increases especially the sensitivity for the AOD.
In the following, the nomenclature used by Rodgers (2000) is addapted. In Section 5.1, the basics of the inversion method is introduced, followed by the description of the linear and non-linear case in Section 5.2 and 5.3, respectively. The different properties of the retrieval method are pointed out in Section 5.4 and the errors are discussed in Section 5.5. The difference of the optimal estimation and regularization method is clarified in Section 5.6, while the common iteration strategy is described in Section 5.7. The description of the different state and measurement vectors, depending on whether the aerosol or trace gas quantities are retrieved, is given in Section 5.8. The method applied to avoid physically meaningless values in the retrieved profiles in explained in Section 5.9, followed by Section 5.10 describing the implementation of the retrieval.
The application of the retrieval methods and detailed retrieval sensitivity studies on simulated MAX-DOAS measurements are subject of Chapter 6.

5.1 Basic Inversion Principles

In-situ measurement techniques are generally applied for the direct quantification of atmospheric constituents. These measurements are only representative for small air parcels located in the near surrounding of the instrument. The determination of the atmospheric state over a large horizontal and vertical extent is only possible with remote sensing techniques. In general, the atmosphere is probed indirectly by remote sensing measurements. This applies also to MAX-DOAS measurements. The quantities of interest, namely the trace gas and aerosol vertical distribution, are determined by inverse methods using the measured slant column densities. For this purpose, a model function is necessary, which describes the physical processes in the atmosphere. Since there is no analytical solution of the radiative transfer equation, radiative transfer models are used, which approximate the light path in the atmosphere for a given state using different methods (see Section 4.4).
In the following, the measured quantities are referred to as the measurement vector and the atmospheric state, i.e. the according profile, as the state vector. The RTM is referred to as the model function.
The basic aim of the inversion is to minimize the error weighted difference between measurement and modeled values from the model function as well as the error weighted difference between the state and an a priori guess for the state, which can be derived, e.g., from climatological databases. This is expressed by the so called cost function $\chi^2(\mathbf{x})$:

$$\chi^2(\mathbf{x}) = \sum_{m=0}^{M} \left(\frac{F_m(\mathbf{x}) - y_m}{\sigma_{\epsilon,m}} \right)^2 + \sum_{n=0}^{N} \left(\frac{x_n - x_{a,n}}{\sigma_{a,n}} \right)^2 , \tag{5.1}$$

where $\mathbf{x}$ is the state vector consisting of the N-element trace gas or aerosol profile. y_m is the element of the measurement vector $\mathbf{y}$ consisting of the M trace gas slant column densities in the case of the trace gas profile retrieval. The measurement vector contains the O_4 slant column densities and optionally the intensities measured at the appropriate wavelength in the case of the aerosol profile retrieval. These

elements are measurements with different viewing directions according to the elevation angles in MAX-DOAS observations. $F_m(\mathbf{x})$ denotes the corresponding modeled value calculated using the model function F for the state $\mathbf{x}$. $x_{a,n}$ is the n^{th} element of the a priori state vector. The errors of the measurement and a priori state vector are denoted by $\sigma_{\epsilon,m}$ and $\sigma_{a,n}$, respectively. The more general form of $\chi^2(\mathbf{x})$ using vector and matrix notation is:

$$\chi^2(\mathbf{x}) = [\mathbf{F}(\mathbf{x}) - \mathbf{y}]^T \mathbf{S}_\epsilon^{-1} [\mathbf{F}(\mathbf{x}) - \mathbf{y}] + [\mathbf{x} - \mathbf{x}_a]^T \mathbf{S}_a^{-1} [\mathbf{x} - \mathbf{x}_a] \,, \tag{5.2}$$

where $\mathbf{S}_\epsilon$ denotes the diagonal measurement covariance matrix containing the square of the measurement errors $\sigma_{\epsilon,m}$. $\mathbf{S}_a$ is the a priori covariance matrix consisting of the squared a priori state errors as the diagonal elements. It can also contain non-zero non-diagonal elements, which constrain the smoothness of the state vector. The minimization of the cost function is analogous to finding a solution for the equation:

$$\nabla_{\mathbf{x}} \chi^2(\hat{\mathbf{x}}) = 0 \;\longrightarrow\; \nabla_{\mathbf{x}} \mathbf{F}(\hat{\mathbf{x}})^T \mathbf{S}_\epsilon^{-1} [\mathbf{K}\hat{\mathbf{x}} - \mathbf{y}] + \mathbf{S}_a^{-1} [\hat{\mathbf{x}} - \mathbf{x}_a] = 0 \,, \tag{5.3}$$

with the optimal state $\hat{\mathbf{x}}$. Depending on the state vector and the model function, the inversion problem and the solution of the equation (5.3) is a linear or non-linear case.

5.2 Linear Inversion Case

In the linear case, the model function $\mathbf{F}$ is linear in $\mathbf{x}$ and the modeled vector can be expressed by:

$$\mathbf{F}(\mathbf{x}) = \mathbf{K}\mathbf{x} \;\longrightarrow\; \nabla_{\mathbf{x}} \mathbf{F}(\mathbf{x}) = \mathbf{K} \,. \tag{5.4}$$

The weighting function matrix $\mathbf{K}$ does not depend on the state vector. Each element of $\mathbf{K}$ is the partial derivative of the model function element with respect to the state vector element, i.e. $K_{ij} = \partial F_i(\mathbf{x}) / \partial x_j$. Thus, the minimization equation (5.3) can be written as:

$$\mathbf{K}^T \mathbf{S}_\epsilon^{-1} [\mathbf{K}\hat{\mathbf{x}} - \mathbf{y}] + \mathbf{S}_a^{-1} (\hat{\mathbf{x}} - \mathbf{x}_a) = 0 \,, \tag{5.5}$$

which is solved by:

$$\hat{\mathbf{x}} = \left(\mathbf{S}_a^{-1} + \mathbf{K}^T \mathbf{S}_\epsilon^{-1} \mathbf{K}\right)^{-1} \left(\mathbf{K}^T \mathbf{S}_\epsilon^{-1} \mathbf{y} + \mathbf{S}_a^{-1} \mathbf{x}_a\right) \,. \tag{5.6}$$

5.3 Non-linear Inversion Case

When the weighting function matrix $\mathbf{K}$ depends on the state vector, the inversion problem is non-linear. The replacement from equation (5.5) cannot be applied and the state $\hat{\mathbf{x}}$, which fulfills equation (5.3), has to be determined iteratively using numerical approaches.

5.3.1 The Gauss-Newton Method

The Gauss-Newton method is based on the following relationship between a variable x, a scalar-valued function g and its gradient $dg(x)/dx$:

$$g(x) = y \;\longrightarrow\; x_{i+1} = x_i - \left[\frac{dg(x_i)}{dx_i}\right]^{-1} y_i \,, \tag{5.7}$$

where the index i refers to a certain point defined by x_i and y_i. This iterative relationship can be adopted to the vector-valued case and utilized to find the minimum of the cost function in the non-linear case. Then, it is applied on the gradient of the cost function $\mathbf{g}(\mathbf{x})$:

$$\mathbf{g}(\mathbf{x}) = \frac{1}{2}\nabla_{\mathbf{x}}\chi^2(\mathbf{x}) \;\longrightarrow\; \mathbf{g}(\mathbf{x}) = \mathbf{K}^T\mathbf{S}_\epsilon^{-1}[\mathbf{F}(\mathbf{x}) - \mathbf{y}] + \mathbf{S}_a^{-1}(\mathbf{x} - \mathbf{x}_a) \,, \tag{5.8}$$

resulting in the iteration scheme in vector notation:

$$\mathbf{x}_{i+1} = \mathbf{x}_i - \left[\nabla_{\mathbf{x}}\mathbf{g}(\mathbf{x}_i)\right]^{-1}\mathbf{g}(\mathbf{x}_i) \,. \tag{5.9}$$

In this case, the gradient of $\mathbf{g}(\mathbf{x})$ is:

$$\mathbf{H} = \nabla_{\mathbf{x}}\mathbf{g}(\mathbf{x}) = \nabla_{\mathbf{x}}\mathbf{K}^T\mathbf{S}_\epsilon^{-1}[\mathbf{F}(\mathbf{x}) - \mathbf{y}] + \mathbf{K}^T\mathbf{S}_\epsilon^{-1}\mathbf{K} + \mathbf{S}_a^{-1} \,. \tag{5.10}$$

The first term on the right-hand side of this equation can be omitted in high dimensional problems, since its contribution becomes very small near the optimal solution and can be neglected. Additionally, its calculation is computationally expensive since it is a tensor of third order. Instead, the so called Pseudo-Hessian $\mathbf{H}_p$ is used as an approximation:

$$\mathbf{H} \approx \mathbf{H}_p = \mathbf{K}^T\mathbf{S}_\epsilon^{-1}\mathbf{K} + \mathbf{S}_a^{-1} \,. \tag{5.11}$$

The resulting iteration equation for the Gauss-Newton method is then:

$$\mathbf{x}_{i+1} = \mathbf{x}_i + \left(\mathbf{S}_a^{-1} + \mathbf{K}_i^T\mathbf{S}_\epsilon^{-1}\mathbf{K}_i\right)^{-1}\left[\mathbf{K}_i^T\mathbf{S}_\epsilon^{-1}\left(\mathbf{y} - \mathbf{F}(\mathbf{x}_i)\right) - \mathbf{S}_a^{-1}\left(\mathbf{x}_i - \mathbf{x}_a\right)\right] \,, \tag{5.12}$$

with $\mathbf{K}_i = \mathbf{K}(\mathbf{x}_i)$.

5.3.2 The Levenberg-Marquardt Method

The Gauss-Newton method converges rapidly to the optimal solution when the cost function is quadratic or nearly quadratic in the state vector. However, if the true solution is far from the current iteration point, it is possible that the convergence is slow or that the iteration diverges. To deal with this problem, the iteration scheme in equation (5.12) is modified following the suggestions of Levenberg and Marquardt (Levenberg, 1944; Marquardt, 1963) by replacing the approximated Hessian matrix by $\mathbf{H}_{LM}$, which is defined as:

$$\mathbf{H}_{LM} = \mathbf{H}_p + \gamma\mathbf{S}_a^{-1} = (1+\gamma)\,\mathbf{S}_a^{-1} + \mathbf{K}^T\mathbf{S}_\epsilon^{-1}\mathbf{K} \,. \tag{5.13}$$

The iteration scheme of the Levenberg-Marquardt method is then given by:

$$\mathbf{x}_{i+1} = \mathbf{x}_i + \left[(1+\gamma_i)\,\mathbf{S}_a^{-1} + \mathbf{K}_i^T\mathbf{S}_\epsilon^{-1}\mathbf{K}_i\right]^{-1} \left\{\mathbf{K}_i^T\mathbf{S}_\epsilon^{-1}\left[\mathbf{y} - \mathbf{F}(\mathbf{x}_i)\right] - \mathbf{S}_a^{-1}\left[\mathbf{x}_i - \mathbf{x}_a\right]\right\} , \tag{5.14}$$

where γ_i is chosen at each step to minimize the cost function. For small values of γ_i, the iteration step tends to Gauss-Newton, whereas for large γ_i, the iteration step direction tends to steepest descent.

5.4 Retrieval Properties

The properties of the retrieval are mainly determined by the weighting function matrix $\mathbf{K}$ and the measurement and a priori covariance matrix $\mathbf{S}_\epsilon$ and $\mathbf{S}_a$, respectively. The quantities, which describe the retrieval properties, are summarized in the following.
The retrieval gain function matrix $\mathbf{G}$ describes the sensitivity of the retrieval to the measurement and is calculated according to:

$$\mathbf{G} = \frac{\partial\hat{\mathbf{x}}}{\partial\mathbf{y}} = \left(\mathbf{S}_a^{-1} + \mathbf{K}^T\mathbf{S}_\epsilon^{-1}\mathbf{K}\right)^{-1}\mathbf{K}^T\mathbf{S}_\epsilon^{-1} . \tag{5.15}$$

An important quantity of the retrieval is the averaging kernel matrix $\mathbf{A}$, which describes the sensitivity of the retrieved state $\hat{\mathbf{x}}$ to the true state $\mathbf{x}_t$:

$$\mathbf{A} = \frac{\partial\hat{\mathbf{x}}}{\partial\mathbf{x}_t} = \mathbf{G}\mathbf{K} = \left(\mathbf{S}_a^{-1} + \mathbf{K}^T\mathbf{S}_\epsilon^{-1}\mathbf{K}\right)^{-1}\mathbf{K}^T\mathbf{S}_\epsilon^{-1}\mathbf{K} . \tag{5.16}$$

For a noise free measurement, the retrieved state vector describes a smoothed version of the true state vector according the vertical resolution and sensitivity of the retrieval at particular altitudes:

$$\hat{\mathbf{x}} = \mathbf{x}_a + \mathbf{A}(\mathbf{x}_t - \mathbf{x}_a) . \tag{5.17}$$

Thus, the averaging kernel matrix of an ideal retrieval would be the identity matrix ($\mathbf{A} = \mathbf{I}$), yielding ($\hat{\mathbf{x}} = \mathbf{x}_t$).
The degrees of freedom for signal d_s quantify the number of independent pieces of information that can be measured:

$$d_s = tr(\mathbf{A}) . \tag{5.18}$$

The vertical resolution of the retrieval can be quantified using the spread function. There are several possibilities to define the spread function. Following the definition by Backus and Gilbert (1970), the spread function is quantified by:

$$s(z) = 12\,\frac{\int (z-z')^2 A^2(z,z')\,\mathrm{d}z'}{\left(\int A(z,z')\,\mathrm{d}z'\right)^2} . \tag{5.19}$$

It provides an estimate of the width of the averaging kernel at altitude z (Rodgers,

2000).

5.5 Retrieval Errors

Imperfect prior knowledge on the state can be quantified as a probability density function (*pdf*) over the state space. Due to experimental error, the measurement can also be quantified as a *pdf* over the measurement space. The calculation of the retrieval errors is based on Bayes' theorem, which provides a formalism for the mapping of a measurement *pdf* into the state space in combination with the prior knowledge. The following functions are scalar valued and defined as (Rodgers, 2000):

$P(\mathbf{x})$ as the prior *pdf* of the state $\mathbf{x}$. This means that the quantity $P(\mathbf{x})\,\mathrm{d}\mathbf{x}$ is the probability that $\mathbf{x}$ lies in the multidimensional volume $(\mathbf{x},\, \mathbf{x}+\mathrm{d}\mathbf{x})$ before the measurement has been made, expressing quantitatively the knowledge of $\mathbf{x}$ before the measurement. It is normalized so that $\int P(\mathbf{x})\, d\mathbf{x} = 1$.

$P(\mathbf{y})$ as the prior *pdf* of the measurement $\mathbf{y}$, with a similar meaning. This is the *pdf* of the measurement before it is made.

$P(\mathbf{x},\mathbf{y})$ as the joint prior *pdf* of $\mathbf{x}$ and $\mathbf{y}$, meaning that $P(\mathbf{x},\mathbf{y})\,\mathrm{d}\mathbf{x}\,\mathrm{d}\mathbf{y}$ is the probability that $\mathbf{x}$ lies in $(\mathbf{x},\, \mathbf{x}+\mathrm{d}\mathbf{x})$ and $\mathbf{y}$ lies in $(\mathbf{y},\, \mathbf{y}+\mathrm{d}\mathbf{y})$.

$P(\mathbf{y}|\mathbf{x})$ as the conditional *pdf* of $\mathbf{y}$ given $\mathbf{x}$, meaning that $P(\mathbf{y}|\mathbf{x})\,\mathrm{d}\mathbf{y}$ is the probability that $\mathbf{y}$ lies in $(\mathbf{y},\, \mathbf{y}+\mathrm{d}\mathbf{y})$ when $\mathbf{x}$ has a given value.

$P(\mathbf{x}|\mathbf{y})$ as the conditional *pdf* of $\mathbf{x}$ given $\mathbf{y}$, meaning that $P(\mathbf{x}|\mathbf{y})\,\mathrm{d}\mathbf{x}$ is the probability that $\mathbf{x}$ lies in $(\mathbf{x},\, \mathbf{x}+\mathrm{d}\mathbf{x})$ when $\mathbf{y}$ has a given value. This is the quantity that is of interest for solving the inverse problem.

Then Bayes' theorem, which is the relationship between conditional probability density functions, allows for the calculation of $P(\mathbf{x}|\mathbf{y})$, which is necessary to update the prior knowledge $P(\mathbf{x})$:

$$P(\mathbf{x}|\mathbf{y}) = \frac{P(\mathbf{y}|\mathbf{x})P(\mathbf{x})}{P(\mathbf{y})}\,. \tag{5.20}$$

Assuming that the measurement error can be described by a Gaussian *pdf*, which is an eligible assumption for atmospheric measurements, and that the a priori information on the state vector follows a Gaussian *pdf*, which is less realistic but convenient, the total retrieval covariance matrix $\hat{\mathbf{S}}$ results from the formalism of Equation (5.20). It is the sum of the smoothing error $\mathbf{S}_s$ and the retrieval noise $\mathbf{S}_m$:

$$\hat{\mathbf{S}} = \mathbf{S}^s + \mathbf{S}_m\,. \tag{5.21}$$

The detailed description given in Rodgers (2000) shows that the covariance matrix of the smoothing error is quantified by

$$\mathbf{S}_s = (\mathbf{A} - \mathbf{I}_n)\,\mathbf{S}_a\,(\mathbf{A} - \mathbf{I}_n)^T\,, \tag{5.22}$$

or on substituting Equation (5.16):

$$\mathbf{S}_s = \left(\mathbf{K}^T\mathbf{S}_\epsilon^{-1}\mathbf{K} + \mathbf{S}_a^{-1}\right)^{-1}\mathbf{S}_a^{-1}\left(\mathbf{K}^T\mathbf{S}_\epsilon^{-1}\mathbf{K} + \mathbf{S}_a^{-1}\right)^{-1} . \tag{5.23}$$

For the interpretation of the smoothing error, two cases can be distinguished. The retrieval can either be regarded as an estimate of a state smoothed by the averaging kernel rather than an estimate of the true state, or as an estimate of the true state, but with an error contribution due to smoothing. Since the true state is normally not known, the actual smoothing error $(\mathbf{A} - \mathbf{I}_n)(\mathbf{x}_t - \mathbf{x}_a)$ cannot be estimated. Therefore, the retrieval should be considered as an estimation of a smoothed version of the state, rather than an estimate of the complete state. Another error pattern is the covariance matrix of the retrieval noise, which is quantified by:

$$\mathbf{S}_m = \mathbf{G}\mathbf{S}_\epsilon\mathbf{G}^T , \tag{5.24}$$

or on substituting Equation (5.15):

$$\mathbf{S}_m = \left(\mathbf{K}^T\mathbf{S}_\epsilon^{-1}\mathbf{K} + \mathbf{S}_a^{-1}\right)^{-1}\mathbf{K}^T\mathbf{S}_\epsilon^{-1}\mathbf{K}\left(\mathbf{K}^T\mathbf{S}_\epsilon^{-1}\mathbf{K} + \mathbf{S}_a^{-1}\right)^{-1} . \tag{5.25}$$

This error component describes the error of the retrieved state vector due to measurement error. The sum of Equation (5.23) and (5.25) is:

$$\hat{\mathbf{S}} = \left(\mathbf{K}^T\mathbf{S}_\epsilon^{-1}\mathbf{K} + \mathbf{S}_a^{-1}\right)^{-1} , \tag{5.26}$$

which is identical with Equation (5.21). The visualization of covariance matrices as a description of the error of a retrieved state is not easy, but the simplest error component is the variance, i.e. the diagonal elements of the covariance matrix. This component will be utilized as the error of the retrieved quantities. The retrieval covariance from Equation (5.26) does not include forward model errors and model parameter errors. The contribution of these error components will be discussed in Chapter 6.

5.6 Retrieval Methods

The inversion using the Levenberg-Marquardt method can be implemented by different approaches. The differences in these approaches are mainly due to the definition of the χ^2 condition as formulated in Equation (5.2) and the utilization of the a priori knowledge. In addition, the state vector in the retrieval can either be the profile itself or some parameters which are used to describe the profile to be retrieved by a certain function or parametrization.

5.6.1 Optimal Estimation Method

The formalism described in Section 5.3.2 seeks the maximum a posteriori (MAP) solution. It is the statistically most likely solution for the given measurement with its error and the a priori knowledge, consisting of the a priori profile and its covariance matrix.

The usage of a priori information is necessary due to the limited information content of the measurement. Therefore, the solution is found by using the a priori state as the starting linearization point for the iteration, and the retrieved information from the measurement is the difference to the a priori state.
At best, the a priori information should be taken from climatological databases. But for some atmospheric constituents, this information is not available and therefore an experienced guess has to serve as a priori information. However, in both cases, the assumption that the a priori covariance follows a Gaussian probability density function is not necessarily fulfilled.
To deal with the limitation of the information which can be extracted from the measurement, it is possible to use a parametrization of the profile of interest by a number of parameters which is in the range of the degrees of freedom for signal of the retrieval, and to retrieve these parameters rather than using the profile itself as the state vector. However, using a parametrization with a small number of state vector elements it is not guaranteed that all possible states are represented by the model.

5.6.2 Regularization Method

The cost function to be minimized for the Phillips-Tikhonov regularization (Phillips, 1962; Tikhonov, 1963) has much in common with the cost function of the optimal estimation method and is described by:

$$\chi^2(\mathbf{x}) = [\mathbf{F}(\mathbf{x}) - \mathbf{y}]^T \mathbf{S}_\epsilon^{-1} [\mathbf{F}(\mathbf{x}) - \mathbf{y}] + [\mathbf{x} - \mathbf{x}_a]^T \mathbf{R} [\mathbf{x} - \mathbf{x}_a] \,. \tag{5.27}$$

Instead of the inverse a priori covariance matrix, as in the optimal estimation case, a regularization matrix $\mathbf{R}$ is utilized. Now, this second term of the cost function is a constraining term, which does not represent the error weighted difference to the a priori state, but the shape of the difference to the a priori state. This constraint can be implemented differently depending on the choice of the regularization matrix. Here, it is defined as :

$$\mathbf{R} = \rho \mathbf{L}^T \mathbf{L} \,, \tag{5.28}$$

where ρ is the regularization parameter which controls the strength of the constraint and $\mathbf{L}$ is the constraint operator. To achieve a constraint on the smoothness of the state vector, the diagonal identity matrix ($\mathbf{I}$), the discrete first- or second-derivative operator can be chosen as constraint operator. An example for the discrete first-derivative operator for a regular height grid of 200 m vertical resolution is:

$$\mathbf{L}_1 = \begin{pmatrix} -5 & 5 & 0 & \cdots & 0 \\ 0 & -5 & 5 & \ddots & \vdots \\ \vdots & \ddots & \ddots & \ddots & 0 \\ 0 & \cdots & 0 & -5 & 5 \end{pmatrix} \,, \tag{5.29}$$

and for the discrete second-derivative operator:

$$\mathbf{L}_2 = \begin{pmatrix} 25 & -50 & 25 & 0 & \cdots & 0 \\ 0 & 25 & -50 & 25 & \ddots & \vdots \\ \vdots & \ddots & \ddots & \ddots & \ddots & 0 \\ 0 & \cdots & 0 & 25 & -50 & 25 \end{pmatrix} . \tag{5.30}$$

In the cases of the discrete first- or second-derivative operators, only the shape of the state is constrained but not the absolute value. However, the strength of the constraint, namely the regularization parameter has to be chosen appropriately. This can be done iteratively, while the identification of the appropriate value depends on the criterion to be optimized. A commonly used approach is the L-curve method (e.g., Hasekamp and Landgraf, 2001), which will be discussed in Section 6.2. For the error analysis, the formalism described in Section 5.5 can be applied by replacing $\mathbf{S}_a^{-1}$ by $\mathbf{R}$ (Steck, 2002).
The difference of the Phillips-Tikhonov regularization and the optimal estimation method mainly arises by the way the least squares conditions in the cost function are balanced. In the optimal estimation method, the inverse of the a priori covariance matrix plays a similar role as the regularization matrix. This becomes obvious when considering a diagonal a priori covariance matrix of the form $\mathbf{S}_a = \sigma_a^2\mathbf{I}$, with σ_a^2 as the a priori variance. The comparison of Equation (5.2) and (5.27) makes clear that a small σ_a corresponds to a large ρ and vice versa.
In the regularization method, the L-curve method delivers a criterion for ρ to filter out contributions from the effective null-space, which is the part of the state space on which no information can be gained from the measurement (see Rodgers (2000) for details). In the optimal estimation method, this filtering is determined by the a priori covariance matrix and cannot be regularized. This means that in certain situations, the solution of the optimal estimation method can contain noise-determined components from the effective null-space or can be over-constrained, which means the loss of information.

5.7 Iteration Strategy

The iteration procedure described in Section 5.3.2 is applied for the optimal estimation and regularization method. The scaling factor γ in Equation (5.14) plays an important role in the convergence behavior of the iteration process. Therefore, an adequate choice of γ is essential and is managed as follows (Press et al., 2007):

1. For the first iteration step, start at the a priori state and choose a γ which does not cause a too large step, since then the probability of leaving the approximate linear region is very high. Since this starting γ value also depends on the a priori covariance or the regularization matrix, respectively, and is different for the specific inversion problem, it is a matter of experience to determine the appropriate value. χ^2 is calculated for the starting point of the iteration according to Equation (5.2).

2. According to Equation (5.14), $\mathbf{x}_{i+1} = \mathbf{x}_{next}$ is calculated.

3. χ^2_{next} is calculated for this new $\mathbf{x}_{next}$ and compared to the initial χ^2 value. Afterwards, χ^2 and χ^2_{next} are compared and the further approach depends on the change $\Delta\chi^2 = \chi^2_{next} - \chi^2$:

   - When $\Delta\chi^2$ is negative, a further determination is necessary:
     - When $\Delta\chi^2$ is less than the threshold value, the iteration can be stopped since the optimal state is found
     - When $\Delta\chi^2$ is greater than the threshold value, γ is adjusted, $\mathbf{x}_{next}$ is set as the initial state and the iteration is continued at (2.).
   - When $\Delta\chi^2$ is positive, γ is adjusted and a further determination is necessary:
     - When the new γ value is greater than the threshold value, the iteration can be stopped since no improvement can be expected
     - When the new γ value is less than the threshold value, the iteration is continued at (3.).

The adjustment of γ in the case where $\Delta\chi^2$ is positive is carried out by multiplying γ with a factor between 2 and 10. In the case where $\Delta\chi^2$ is negative, γ is divided by a factor between 2 and 10. The optimal values for the increase and reduction of γ are also a matter of experiment since they strongly depend on the specific inversion problem. Also the maximum number of iteration steps to be evaluated has to be chosen appropriately. Insufficient iteration steps will result in not 'reaching' the optimal solution, whereas too many steps cause only computational load but no remarkable improvement in the solution.

5.8 State and Measurement Vectors

As described at the beginning of this chapter, there are numerous inversion problems in the field of atmospheric sounding by remote sensing techniques. From MAX-DOAS O_4 and intensity measurements, the retrieval of the atmospheric aerosol extinction profile $\boldsymbol{\epsilon}_M(z, \lambda)$ and in certain cases the optical properties, namely the single scattering albedo $\omega_0(\lambda)$, the asymmetry parameter $g(\lambda)$ for the Henvey-Greenstein parametrization of the phase function and the Ångström exponent α_M is possible. Then, the state vector $\mathbf{x}$ consists of the aerosol extinction profile and optionally the optical properties:

$$\mathbf{x} = \left[\boldsymbol{\epsilon}_M(z, \lambda_{ref}),\ \ \omega_0(\lambda_1),\ \ \cdots,\ \ \omega_0(\lambda_l),\ \ g(\lambda_1),\ \ \cdots,\ \ g(\lambda_l),\ \ \alpha_M\right]^T, \quad (5.31)$$

where λ_{ref} denotes the reference wavelength for which the extinction profile is given. λ_l refer to the wavelengths of the l individual O_4 absorption bands, which are considered within the retrieval. When several bands are used simultaneously, the aerosol extinction profile is converted to the according wavelength using α_M. In the case

of a retrieval using only one O_4 absorption band, the state vector to be retrieved contains the following extinction profile and optional optical properties:

$$\mathbf{x} = \left[\boldsymbol{\epsilon}_M(z,\lambda), \quad \omega_0(\lambda), \quad g(\lambda)\right]^T . \tag{5.32}$$

The measurement vector contains the O_4 slant columns densities of the considered wavelengths and optionally the according intensities:

$$\begin{aligned}\mathbf{y} &= \left(\mathbf{y}_{S_{O_4}}, \quad \mathbf{y}_I\right)^T \\ &= \Big\{ \left[S_{O_4}(\lambda_1,\boldsymbol{\Omega}_1), \quad \cdots, \quad S_{O_4}(\lambda_1,\boldsymbol{\Omega}_e), \quad S_{O_4}(\lambda_l,\boldsymbol{\Omega}_1), \quad \cdots, \quad S_{O_4}(\lambda_l,\boldsymbol{\Omega}_e)\right]^T, \\ &\qquad \left[I(\lambda_1,\boldsymbol{\Omega}_1), \quad \cdots, \quad I(\lambda_1,\boldsymbol{\Omega}_e), \quad I(\lambda_l,\boldsymbol{\Omega}_1), \quad \cdots, \quad I(\lambda_l,\boldsymbol{\Omega}_e)\right]^T \Big\} . \end{aligned} \tag{5.33}$$

$\boldsymbol{\Omega}_e$ represents the viewing direction of each measurement, which is determined by the elevation, solar zenith and relative solar azimuth angle. The radiative transfer model calculation provide absolute slant column densities, whereas the measured slant column densities are retrieved relative to a reference spectrum. For the comparison of the measured and simulated slant column densities, a normalization relative to the zenith measurement is applied according to:

$$\Delta S_{O_4}(\lambda,\boldsymbol{\Omega}_e) = S_{O_4}(\lambda,\boldsymbol{\Omega}_e) - S_{O_4}(\lambda,\boldsymbol{\Omega}_{90^\circ}) . \tag{5.34}$$

Since the measured and modeled intensities have different units, again a normalization is necessary which is in this case:

$$\tilde{I}(\lambda,\boldsymbol{\Omega}_e) = \frac{I(\lambda,\boldsymbol{\Omega}_e)}{I(\lambda,\boldsymbol{\Omega}_{90^\circ})} . \tag{5.35}$$

The weighting function of this inversion problem is calculated numerically with the radiative transfer model (see Section 5.10). The normalization of the measurement vector has to be accounted for in the weighting function calculation, which results in the following relationship:

$$\begin{aligned}\mathbf{K}_{S_{O_4},e} &= \frac{\partial y_{S_{O_4}}(\lambda,\boldsymbol{\Omega}_e)}{\partial \mathbf{x}} \\ \rightarrow \Delta\mathbf{K}_{S_{O_4},e} &= \frac{\partial y_{S_{O_4}}(\lambda,\boldsymbol{\Omega}_e)}{\partial \mathbf{x}} - \frac{\partial y_{S_{O_4}}(\lambda,\boldsymbol{\Omega}_{90^\circ})}{\partial \mathbf{x}} ,\end{aligned} \tag{5.36}$$

and for the intensity weighting function:

$$\begin{aligned}\mathbf{K}_{I,e} &= \frac{\partial y_I(\lambda,\boldsymbol{\Omega}_e)}{\partial \mathbf{x}} \\ \rightarrow \tilde{\mathbf{K}}_{I,e} &= \frac{\partial y_I(\lambda,\boldsymbol{\Omega}_e)}{\partial \mathbf{x}} \cdot \frac{1}{y_I(\lambda,\boldsymbol{\Omega}_{90^\circ})} - \frac{\partial y_I(\lambda,\boldsymbol{\Omega}_{90^\circ})}{\partial \mathbf{x}} \cdot \frac{y_I(\lambda,\boldsymbol{\Omega}_e)}{y_I(\lambda,\boldsymbol{\Omega}_{90^\circ})^2} .\end{aligned} \tag{5.37}$$

For the retrieval of trace gas profiles, the measurement vector contains the trace gas slant column densities and is normalized according equation (5.34). The box air mass factors $A_{box}(\lambda, \mathbf{\Omega}, z)$ introduced in Section 4.3, are the height resolved sensitivities of the measured slant column density to changes in the partial vertical column densities $\Delta V(z)$ of the according altitude z. They are defined as:

$$A_{box}(\lambda, \mathbf{\Omega}, z) = \frac{\partial S(\lambda, \mathbf{\Omega})}{\partial \Delta V(z)} \,. \tag{5.38}$$

The box air mass factors quantify the weighting functions of the trace gas profile retrieval. The state vector consists of the profile of partial vertical column densities $\Delta V(z)$:

$$\mathbf{x} = \left[\Delta V(z_0), \;\; \cdots, \;\; \Delta V(z_q)\right]^T \quad \text{with} \quad \Delta V(z) = \int\limits_{z-\frac{\Delta z}{2}}^{z+\frac{\Delta z}{2}} c(z') \, \mathrm{d}z' \,, \tag{5.39}$$

where $c(z')$ is the trace gas number density at the according altitude and Δz denotes the altitude range referred to. The state vector can be converted to mass concentration, number density or volume mixing ratio profiles using appropriate temperature and pressure profiles. The normalization of the measurement vector has to be accounted for in the weighting function, and is done similar to equation (5.36).
The inversion of aerosol profiles from MAX-DOAS O_4 measurements is a non-linear problem since the weighting function depends on the aerosol profile (see Section 5.3). The inversion of trace gas profiles from MAX DOAS measurements is a linear problem since the box air mass factors depend only on the aerosol profile but not on the trace gas profile. This situation changes for strongly absorbing trace gases, since the light path is then also influenced by the trace gas itself. This results in a non-linear relationship between trace gas profile and observed slant column density. The transformation of the state vector, which is necessary to avoid physically invalid values in the retrieval is described in Section 5.9. The linear problem of the weakly absorbing trace gas profile inversion becomes non-linear. Therefore, the methods from Section 5.3 are utilized instead of the method from Section 5.2 for the inversion.

5.9 State Vector Transformations

During the individual iteration steps, negative state vector values can occur. Since negative values are physically invalid in connection with trace gas profiles or aerosol optical properties and profiles, and the forward models usually cannot deal with negative values, their occurrence in the inversion must be avoided. This can be achieved using an appropriate transformation of the state vector. The transformation to be applied depends on the according element of the state vector. When the state vector consists of the aerosol extinction or trace gas partial column density profile, the physically valid range for the values would be the positive half-space. On the other hand, the retrieval of the aerosol single scatting albedo and the asymmetry param-

eter of the Henvey-Greenstein parametrization of the aerosol phase function results in a restriction of the state vector elements to values between 0 and 1. A similar situation is given for the aerosol Ångström exponent, with values ranging from 0 the Rayleigh limit of 4 (see Seciton 4.2.5). The transformation of the state vector part consisting of the aerosol profile components ϵ_M to x_{ϵ_M} using the transformation function t is described by:

$$\epsilon_M \rightarrow x_{\epsilon_M} \qquad \text{with} \qquad x_{\epsilon_M} = t(\epsilon_M) = \ln(\epsilon_M)\,, \tag{5.40}$$

with the derivative :

$$\frac{\partial t(\epsilon_M)}{\partial \epsilon_M} = \frac{1}{\epsilon_M}\,. \tag{5.41}$$

Then the according transformation of the weighting function $\mathbf{K}$ yielding $\mathbf{T}$ is given by:

$$K_{ij} = \frac{\partial y_i}{\partial \epsilon_{M,j}} \qquad \rightarrow \qquad T_{ij} = \frac{\partial y_i}{\partial x_{\epsilon_M,j}} = \frac{\partial \epsilon_{M,j}}{\partial x_{\epsilon_M,j}} \cdot \frac{\partial y_i}{\partial \epsilon_{M,j}} = \epsilon_{M,j} \cdot K_{ij}\,. \tag{5.42}$$

The error of the profiles $\mathrm{d}\epsilon_M$ are transformed using:

$$\mathrm{d}\epsilon_M \rightarrow \mathrm{d}x_{\epsilon_M} \qquad \text{with} \qquad \mathrm{d}x_{\epsilon_M} = \frac{\partial x_{\epsilon_M}}{\partial \epsilon_M} \cdot \mathrm{d}\epsilon_M = \frac{1}{\epsilon_M} \cdot \mathrm{d}\epsilon_M\,. \tag{5.43}$$

The transformations and relationships from the equation (5.40) - (5.43) can also be applied in the trace gas profile retrieval. The suitable transformation for the single scattering albedo ω_0 and asymmetry parameter g is described by:

$$g \rightarrow x_g \qquad \text{with} \qquad x_g = t(g) = a \cdot \ln\left(\frac{g}{1-g}\right)\,, \tag{5.44}$$

which is the inverse of a scaled Boltzmann distribution, where a is a parameter scaling the shape of the function and has to be chosen appropriately. The slightly modified version for the Ångström exponent α_M is:

$$\alpha_M \rightarrow x_{\alpha_M} \qquad \text{with} \qquad x_{\alpha_M} = t(\alpha_M) = a \cdot \ln\left(\frac{\alpha_M}{4-\alpha_M}\right)\,. \tag{5.45}$$

The according transformations of the weighting function and the error for the single scattering albedo $\mathrm{d}\omega_0$ and asymmetry parameter $\mathrm{d}g$ are:

$$K_i = \frac{\partial y_i}{\partial g} \qquad \rightarrow \qquad T_i = \frac{\partial y_i}{\partial x_g} = \frac{\partial g}{\partial x_g} \cdot \frac{\partial y_i}{\partial g} = \frac{g-g^2}{a} \cdot K_i \tag{5.46}$$

$$\mathrm{d}g \rightarrow \mathrm{d}x_g \qquad \text{with} \qquad \mathrm{d}x_g = \frac{\partial x_g}{\partial g} \cdot \mathrm{d}g = \frac{a}{g-g^2} \cdot \mathrm{d}g\,, \tag{5.47}$$

and in the case of the Ångström exponent, the relationships are given by:

$$K_i = \frac{\partial y_i}{\partial \alpha_M} \qquad \rightarrow \qquad T_i = \frac{\partial y_i}{\partial x_{\alpha_M}} = \frac{\partial \alpha_M}{\partial x_{\alpha_M}} \cdot \frac{\partial y_i}{\partial \alpha_M} = \frac{4\alpha_M - \alpha_M^2}{4a} \cdot K_i \tag{5.48}$$

$$\mathrm{d}\alpha_M \rightarrow \mathrm{d}x_{\alpha_M} \qquad \text{with} \qquad \mathrm{d}x_{\alpha_M} = \frac{\partial x_{\alpha_M}}{\partial \alpha_M} \cdot \mathrm{d}\alpha_M = \frac{4a}{4\alpha_M - \alpha_M^2} \cdot \mathrm{d}\alpha_M \,. \tag{5.49}$$

When the optimal solution is found, a back-transformation has to be applied. In the optimal estimation method, the retrieved state vector, the a priori covariance matrix and the weighting function can be transformed back and the retrieval properties and errors can be calculated according to equations (5.15) - (5.26). In the regularization method, the utilized regularization matrices (see equations (5.29) and (5.30)) are not invertible. Therefore, the gain function **G** (see equation(5.15)) is calculated in the transformed state, and the back-transformed gain function **U** is subsequently calculated using the relationship:

$$G_{ji} = \frac{\partial \hat{\epsilon}_{M,j}}{\partial y_i} \rightarrow U_{ji} = \frac{\partial \hat{x}_{\hat{\epsilon}_M,j}}{\partial y_i} = \frac{\partial \hat{x}_{\hat{\epsilon}_M,j}}{\partial \hat{\epsilon}_{M,j}} \cdot \frac{\partial \hat{\epsilon}_{M,j}}{\partial y_i} = \frac{1}{\hat{\epsilon}_{M,j}} \cdot G_{ji} \,, \tag{5.50}$$

for the part of the state vector containing the profile. The calculation for the other state vector components is similar. The retrieval errors are then calculated using the back-transformed weighting and gain function.

5.10 Retrieval Implementation

The retrieval algorithms described so far have to be implemented using a platform which:

- Reads in the data retrieved from the MAX-DOAS measurements
- Creates the necessary numerical quantities, namely the state and measurement vectors, the corresponding covariance matrices and so on
- Calls the radiative transfer model, reads in the simulated quantities and creates the simulated measurement vector $\mathbf{F(x)}$ and the weighting function matrix $\mathbf{K}$
- Performs the matrix calculations for the iteration procedure and calculates the relevant quantities and results
- Stores the retrieval results and properties

The platform used for the retrievals in this work is the program IDL from ITT Visual Information Solutions (former Research Systems, Inc.).

Chapter 6

Application of the Retrieval Methods and Sensitivity Studies

The practical application of the theoretical inversion concepts introduced in the previous chapter consists of several individual steps. The approach in connection with MAX-DOAS measurements is depicted by a flowchart in Figure 6.1. The measured spectra are analyzed using the DOAS technique (Chapter 3). The retrieved O_4 slant column densities and relative intensities serve as the measurement vector and the according errors quantify the measurement covariance matrix. The aerosol extinction profiles and optionally further optical properties are retrieved using an appropriate inversion method, which is based on radiative transfer simulations. In this work, the radiative transfer model SCIATRAN 2 (Section 4.4.1) is used. The retrieval properties, which are determined by the used a priori profile and covariance matrix, the measurement covariance matrix and the according weighting functions, quantify the retrieval covariance. The retrieved aerosol profiles serve as input parameters for the radiative transfer simulations in the trace gas profile retrieval, where the according slant column densities and errors from MAX-DOAS measurements serve as the measurement vector and covariance matrix, respectively.
In this Chapter, the application of the inversion methods are presented and the sensitivity of the retrieval to several parameters is explored. MAX-DOAS measurements were simulated for different measurement and atmospheric conditions. The first part of this chapter addresses the optimal estimation method (Section 6.1), while the regularization method is content of the second part (Section 6.2).
The retrieval of aerosol profiles from simulated MAX-DOAS O_4 and intensity measurements using optimal estimation is introduced in detail at the beginning of Section 6.1.1. The subsequent part of this Section contains the sensitivity studies with respect to the calculation of the weighting functions, the transformation of the state vector, the knowledge on the a priori state, and the influence of the true aerosol scenario. Furthermore, the influence of statistical errors in the measurement and systematic errors caused by uncertainties in the assumed atmospheric parameters or introduced by the measurement are addressed. The dependence of the retrieval properties on the measurement vector components are also content of Section 6.1.1.
The retrieval of further aerosol optical properties, namely the aerosol single scattering albedo, the asymmetry parameter of the Henyey-Greenstein phase function

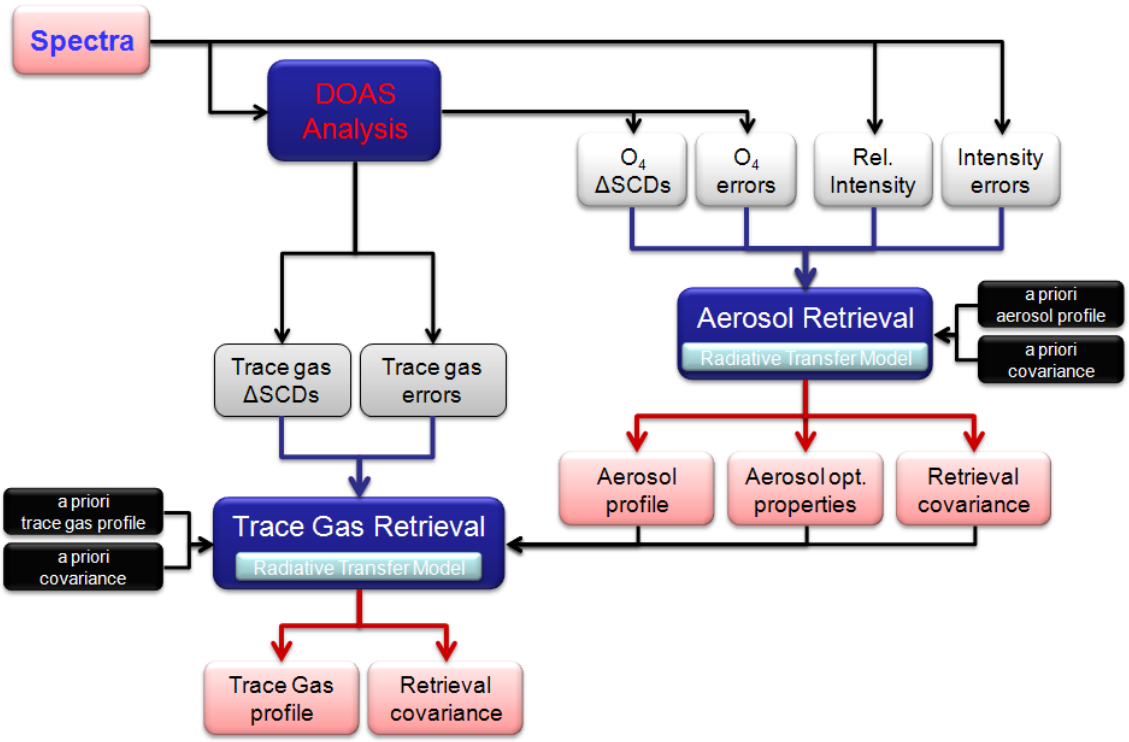

Figure 6.1: *Flowchart of the aerosol and trace gas profile retrieval procedure using MAX-DOAS measurements.*

parametrization and the Ångström exponent, from MAX-DOAS O_4 and intensity measurements is demonstrated in Section 6.1.2.
In Section 6.1.3, a parametrization of the aerosol profile by appropriate functions using either two or three parameters is presented. These parameters are retrieved instead of the profile itself. The influence of different true aerosol profile shapes on the performance of the parameterized retrieval is determined.
The retrieval of trace gas profiles from MAX-DOAS measurements using optimal estimation is discussed in Section 6.1.4, and the influence of the aerosol and trace gas profile on the retrieval properties is explored.
The regularization method is applied for the retrieval of aerosol and trace gas profiles in Section 6.2.1 and 6.2.2, respectively.

6.1 Application of the Optimal Estimation Method

The profiles of atmospheric aerosols and trace gases are generally characterized by a smooth shape in the boundary layer, since the constituents are well mixed and strong gradients are rather untypical. The elements of the aerosol and trace gas profiles are therefore correlated. A constraint on the smoothness of profiles to be retrieved can be introduced by including non-diagonal elements in the a priori covariance matrix $\mathbf{S}_a$ (Section 5.1). It contains the squared a priori state errors σ_a as diagonal elements and non-diagonal elements for the according altitude, which can be chosen

as follows:

$$\mathbf{S}_{a\,ij} = \sigma^2_{a\,i} \cdot e^{-\frac{|z_i - z_j|}{\eta}} \,. \tag{6.1}$$

The correlation length η quantifies the strength of the smoothness (Barret et al., 2002; Frieß et al., 2006). It has been set to 0.5 km in the retrievals preformed in this work.

The averaging kernel matrix $\mathbf{A}$ quantifies the sensitivity of the retrieval to particular altitude levels as well as the height dependent vertical resolution of the retrieval (Section 5.4). In the case of ground based MAX-DOAS measurements, the sensitivity and vertical resolution decrease with altitude. Therefore, the comparison of aerosol or trace gas profiles retrieved from MAX-DOAS to independent measurements, e.g. from lidar instruments, requires the consideration of the different height resolution of both techniques. Aerosol extinction profiles measured by lidar are generally sampled on an altitude grid with a typical resolution of 15–40 m. In contrast, the aerosol retrieval from MAX-DOAS exhibits height resolutions ranging from $\approx$200 m in the lower altitudes up to $\approx$700 m in the higher altitudes. Furthermore, the height dependent sensitivity of the retrieval from MAX-DOAS causes a reshape of the true aerosol profile, since extinction contributions in higher altitudes are attributed to in lower altitudes by the retrieval. Thus, a realistic comparison between both instruments requires that the lidar profiles with a much higher vertical resolution are degraded to the vertical resolution of the MAX-DOAS (Rodgers and Connor, 2003; Vigouroux et al., 2009). This is achieved by applying the MAX-DOAS averaging kernel to the high resolution profile $\mathbf{x}_h$:

$$\mathbf{x}_s = \mathbf{x}_a + \mathbf{A}(\mathbf{x}_h - \mathbf{x}_a) \,, \tag{6.2}$$

where $\mathbf{x}_s$ is a smoothed version of the high resolution profile. In particular, $\mathbf{x}_s$ is the profile that the MAX-DOAS instrument would have measured if the true profile would have been the high resolution profile $\mathbf{x}_h$.

The information content of the retrieval can be interpreted by considering the concept of linear vector spaces, namely the state space and the measurement space. The act of measurement can be considered as a mapping from the state space into the measurement space. The inverse problem is that of finding an appropriate inverse mapping from the measurement space back into the state space. Depending on the inversion properties, the state space may contain components, which are not accessible by the measurement. This subspace of the state space is the null space of the mapping. Furthermore, additional components of the state space may become unmeasurable due to measurement errors, resulting in an effective null space. The inversion problem in connection with ground based MAX-DOAS measurements is generally under-determined, and a constraint on the atmospheric state is therefore introduced by the a priori state vector (Rodgers, 2000).

6.1.1 Retrieval of the Aerosol Extinction Profile and Optical Depth

To investigate the capability of the MAX-DOAS O_4 optical density and intensity measurements to retrieve aerosol extinction profiles using the optimal estimation

method, retrievals based on synthetic measurements for different viewing geometries and atmospheric conditions were performed. The dependence on retrieval parameters and settings, different aerosol loads and profile shapes, and different measurement viewing geometries as well as the influence of retrieval parameter uncertainties are identified by relating the consequential changes to the results of a retrieval using standard settings.
The retrieval with the settings referred to as standard was performed using a synthetic MAX-DOAS measurement consisting of the O_4 optical densities and intensities at 477 nm for elevation angles of 1°, 2°, 4°, 8°, 14°, 30° and 90°, a solar zenith angle of 60° and a relative azimuth angle of 30°. Thus, the measurement vector consists of the differential O_4 optical densities (ΔOD) and relative intensities calculated according equation (5.34) and (5.35), respectively (Section 5.8). To identify the effects attributable to the retrieval settings, parameters and performance, the O_4 ΔOD and relative intensity errors were set to $5 \cdot 10^{-4}$ and $5 \cdot 10^{-3}$ in the measurement covariance matrix, respectively, without adding random noise to the synthetic measurements. The aerosol extinction profile was described on a height grid with a resolution of 200 m from the surface up to the altitude of 4 km.
The results of the profile retrieval are shown Figure 6.2. The true profile used for the calculation of the synthetic measurement is indicated in black in Figure 6.2a, and describes a smoothed box-shaped distribution. The a priori and retrieved profile are indicated in dashed red and solid red, respectively. The profile resulting from the application of the averaging kernel according to Equation (6.2) on the true profile is shown in green in Figure 6.2a. The true profile is very well reproduced by the retrieval with respect to the absolute extinction values as well as the vertical extent of the aerosol layer. The good agreement between the retrieved and smoothed true profile indicates the correct performance of the retrieval. The retrieved aerosol optical depth (AOD) of 0.20 ± 0.02 matches the true value of 0.2. The deviation of the retrieved extinction from the true and convolved true profile are depicted in Fig-

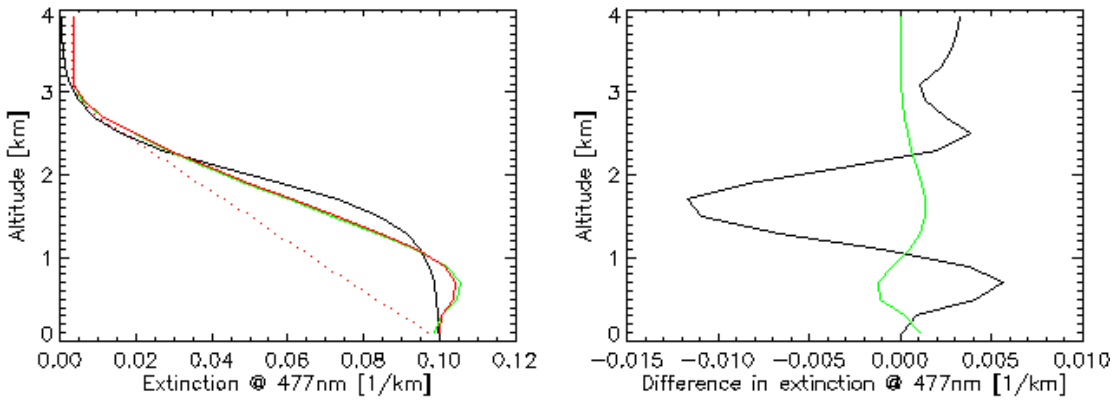

(a) **(b)**

Figure 6.2: *Retrieval of the aerosol extinction profile: the (a) a priori (red, dotted), retrieved (red, solid), true (black) and convolved true (green) profile; (b) deviation of the retrieved extinction from the true (black) and convolved true (green) profile.*

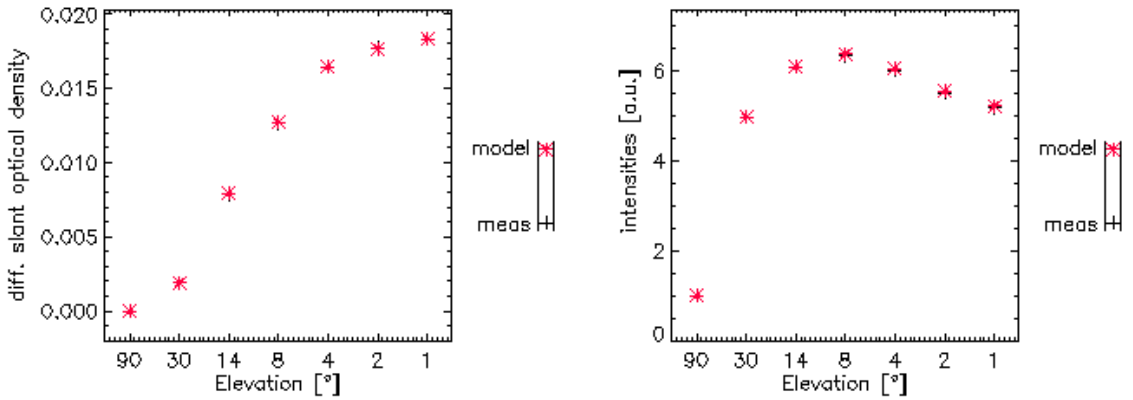

(a) (b)

Figure 6.3: *The true (black cross) and retrieved (red asterisk) differential (a) O_4 optical densities and (b) relative intensities as a function of the elevation angle.*

ure 6.2b in black and green, respectively. The characteristic vertical resolution and sensitivity of the retrieval result in structured deviations between the retrieved and true profile, while the differences between the retrieved and convolved true profile are very small. The true and retrieved O_4 ΔODs and relative intensities are shown in Figure 6.3a and 6.3b, respectively, and lie on top of each other.
The sensitivity of the measurement to perturbations of the aerosol extinction at different altitudes is quantified by the weighting functions, which are shown in Figure 6.4a and 6.4b with respect to the O_4 ΔODs and relative intensities, respectively. The different colors indicate the elevation angles of the measurements. These weighting functions represent the partial derivatives of the O_4 ΔOD and relative intensity with respect to the aerosol extinction at the according altitude, and were calculated

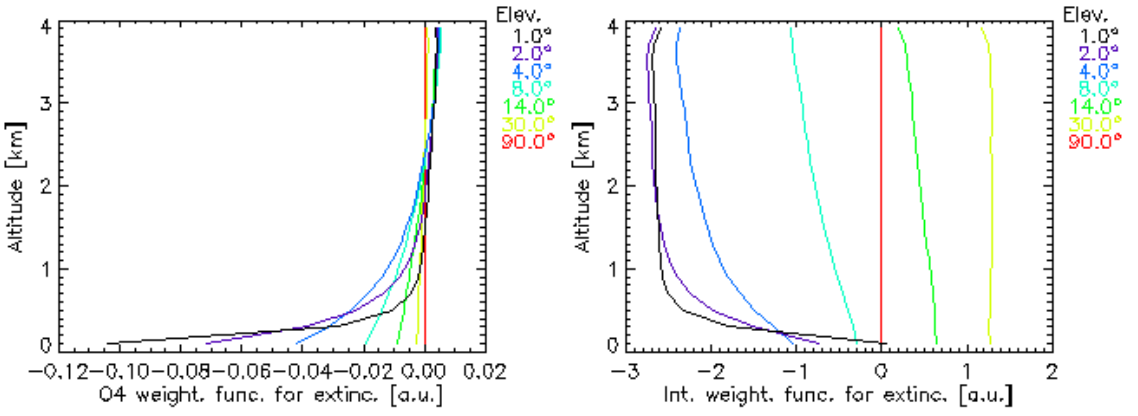

(a) (b)

Figure 6.4: *The weighting functions of the aerosol extinction profile retrieval with respect to (a) the differential O_4 optical density and (b) relative intensity. The elevation angles of the measurements are indicated by the different colors.*

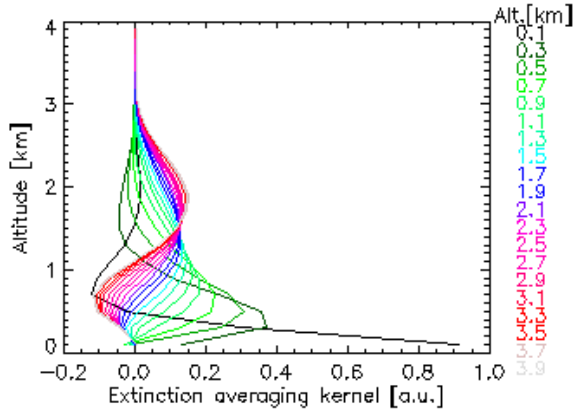

Figure 6.5: *Averaging kernels of the aerosol extinction profile retrieval. The corresponding altitudes are indicated by the different colors.*

numerically with the radiative transfer model for changes of $+0.1\,\mathrm{km}^{-1}$ in the extinction at altitudes between 0 and 4 km. The weighting functions depend on the aerosol profile itself and therefore vary with the according profile. In general, the weighting functions of the O_4 ΔOD are characterized by a peak at the surface and a rapid decrease with altitude. This indicates a high sensitivity for aerosols in the lowermost altitude ranges. Furthermore, the sensitivity for aerosols near the ground are highest at small elevation angles due to the increased light paths through the lowermost atmospheric layers. In contrast to O_4, the weighting functions for the relative intensity generally show less variation with altitude, and therefore provide less information on the altitude distribution of aerosols. However, in this case, rapid changes occur in lower altitudes for the smallest two elevation angles. Furthermore, the relative intensities provide a strong constraint for the AOD. The numerical calculation of the weighting functions requires high computational effort and is therefore time consuming. Thus, the weighting functions for the retrievals performed in this work are calculated only for the starting point of the iteration sequence and kept unchanged during the individual iteration steps.

The averaging kernels for the aerosol profile retrieval, which quantify the sensitivity of the retrieved to the true aerosol extinction, are depicted in Figure 6.5. The averaging kernels show distinct peaks for altitude layers below ≈ 2 km, while the averaging kernels for the lowermost ≈ 1.8 km peak at around their nominal altitudes. The averaging kernels for altitudes above ≈ 2 km are characterized by negative and positive peaks around ≈ 500–700 m and ≈ 1.7–1.9 km, respectively. The negative values indicate the opposite sensitivity which means that higher aerosol loads result in smaller retrieved extinctions at the according altitudes. Similar to the retrieval sensitivity, the vertical resolution decreases with altitude and ranges from ≈ 300 m at the surface to ≈ 1.1 km at 1.7 km altitude. The degrees of freedom for signal of the retrieval, which determines the number of independent pieces of information (equation (5.18)), is 2.9, while the measurement vector contains 12 elements. Thus, the measurements are far from independent.

In the following sections, the above mentioned influences of the retrieval parameters and their uncertainties on the retrieval performance and results are explored. The

Figures in these Sections apply similar colors and line styles for the graphs showing the a priori (dotted red), retrieved (solid red), true (black) and convolved true (green) profiles as depicted in Figure 6.2a. The graphs containing the averaging kernels also apply similar color codes for the different altitudes as in Figure 6.5.

6.1.1.1 Dependence on Weighting Function Calculation

The dependence of the retrieval performance and results on the weighting function calculation is determined by the comparison of three different approaches. In addition to the retrieval using a constant weighting function, which is not recalculated in each iteration step, a retrieval was performed, in which two subsequent iteration sequences were carried out. The retrieved profile from the first iteration sequence was used as the starting point for the second iteration sequence and the weighting function was recalculated for this profile. In the third approach, the weighting function was recalculated in each iteration step, which is the actual iteration strategy of the Levenberg-Marquardt method (equation (5.14)).
Figure 6.6 shows the results and averaging kernels for the retrieval of a smoothed box-shaped profile using the three different approaches. The weighting functions for the linear decreasing a priori profile and the retrieved profile with a smoothed box-shaped distribution are quite similar, due to an approximately linear dependence for these extinction values and their vertical distributions. Therefore, the resulting profiles and averaging kernels do not show remarkable differences for the different retrieval approaches.

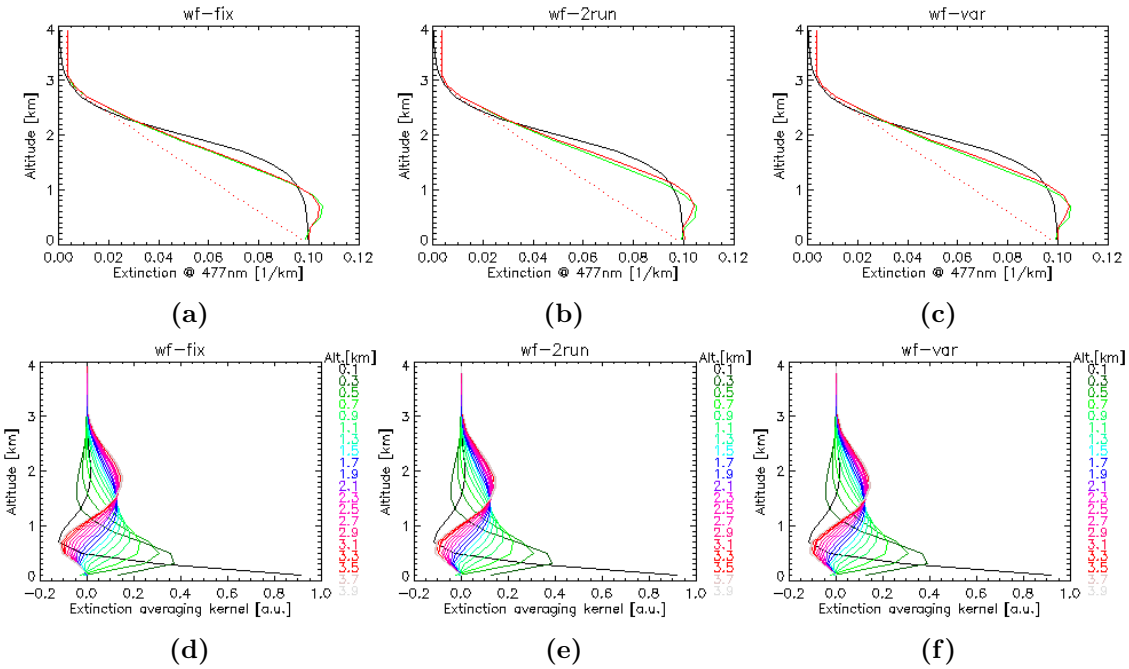

Figure 6.6: *Retrieval of a smoothed box-shaped profile and corresponding averaging kernels with (a,d) a constant weighting function, (b,e) two subsequent iteration sequences with a recalculated weighting function in the second sequence and (c,f) a recalculated weighting function in each iteration step.*

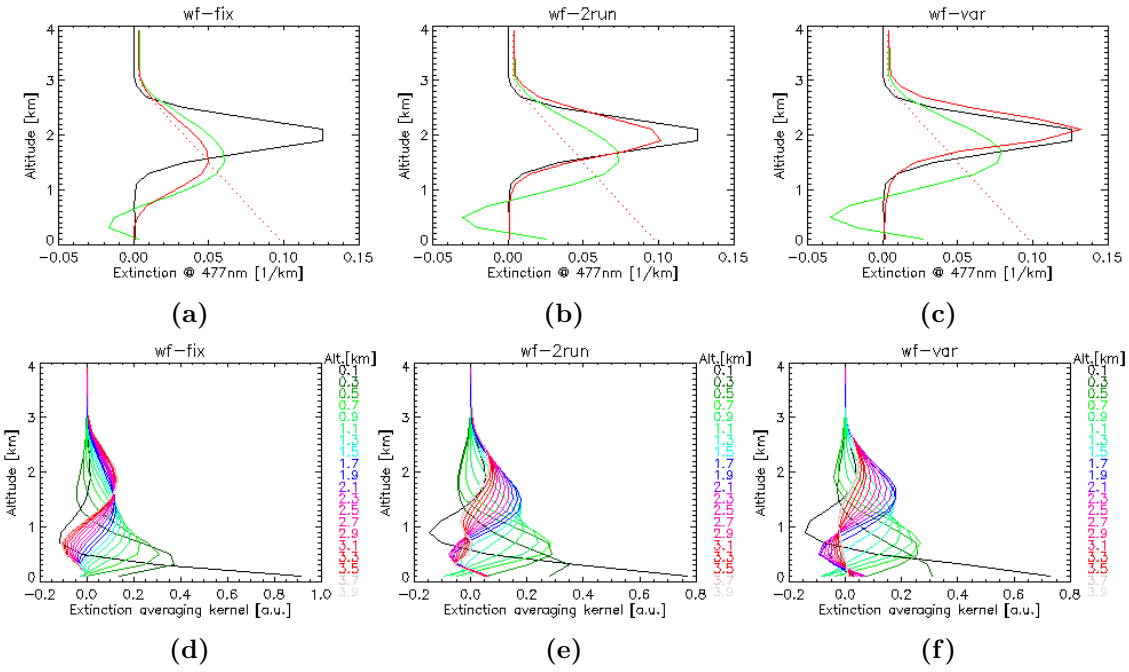

Figure 6.7: *Same as Figure 6.6, but for the retrieval of an elevated aerosol layer centered around 2 km.*

In contrast to this situation, the retrievals of an elevated aerosol layer centered around 2 km altitude using the different approaches show significant differences. Such retrievals were performed using the same a priori profile as in the box-shaped profile case, and the results and averaging kernels are shown in Figure 6.7. The retrieval using a constant weighting function, which is the same as in the box-shaped profile case, reproduces an elevated layer that is smoothed according the vertical resolution and sensitivity determined by the averaging kernel and thus centered around lower altitudes. The degrees of freedom for signal is 2.8 and the AOD of 0.07 ± 0.02 is smaller than the true value of 0.1. The non-linearity of the inversion problem is indicated by the changes in the averaging kernels in Figure 6.7e compared to the constant weighting function case. The recalculation of the weighting function after the first iteration sequence accounts for the significant changes in the aerosol distribution and the resulting changes in the retrieval sensitivity. The lower aerosol load near the surface results in a decrease in sensitivity and the increased aerosol load at the higher altitudes leads to higher sensitivities at the according altitude ranges. Furthermore, the vertical resolution at higher altitudes is improved. Similar changes are present in the case where the weighting function is calculated for each iteration step. For both cases, the degrees of freedom for signal slightly increases to 3.0. While the AOD of 0.10 ± 0.01 in the two iteration sequences case matches the true value, the approach using iterative weighting function calculation results in a slightly overestimated AOD of 0.11 ± 0.01. These examples illustrate the importance of a recalculation of the weighting functions in the presence of elevated aerosol layers, due to the remarkable changes in the retrieval properties. However, the comparison of the retrieved and convolved true profiles in Figure 6.7b and 6.7c indicate that contributions from the effective null space occur within the iteration

steps, since the retrieved profiles feature higher resolved distributions than determined by the according averaging kernels. Strategies for avoiding such contributions are discussed in Section 6.2 in the context of the regularization method.

6.1.1.2 Influence of the State Vector Transformation

The introduced state vector transformation and the accompanied conversion of affected retrieval quantities (Section 5.9) were tested for possible influences on the retrieval results and properties by performing retrievals using and omitting the transformation. Figure 6.8 shows examples for both cases. It can be identified, that the state vector transformation does not influence the retrieval, and the results and averaging kernels are almost identical.

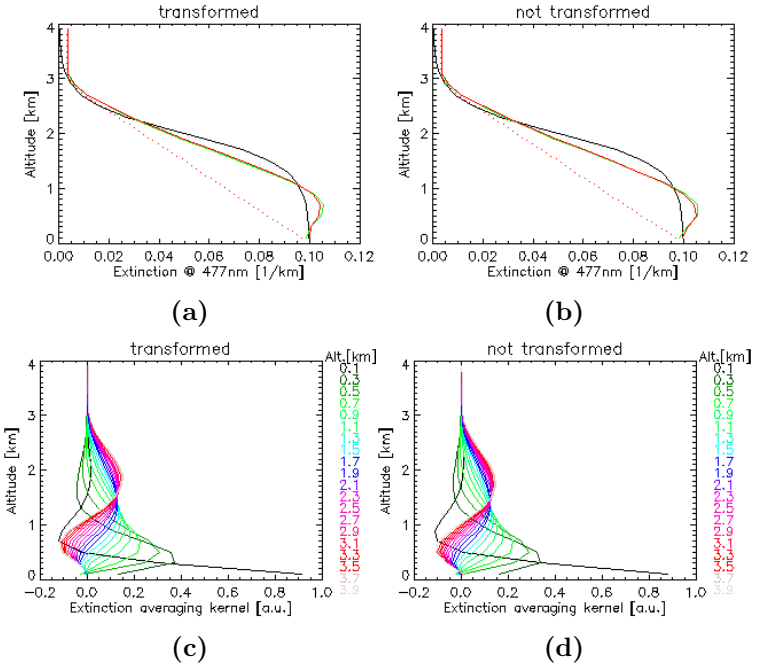

Figure 6.8: *Resulting profiles and corresponding averaging kernels for retrievals (a,c) using and (b,d) omitting a state vector transformation.*

6.1.1.3 Influence of the A Priori Profile

The retrievals were performed using different a priori profiles, to identify the influence of the a priori profile. Since the a priori errors are proportional to the a priori extinctions, the constraints on the retrieval changes with altitude for different a priori profiles. As in the standard example, linear decreasing profiles were used, but with different total aerosol loads and profile shapes. The resulting profiles and averaging kernels for a retrieval using an a priori profile which is more constrained to lower altitudes than in the standard example is depicted in Figure 6.9a and 6.9d, respectively. Due to the missing sensitivity of the retrieval at altitudes above $\approx 2\,\mathrm{km}$ and the constraint of the a priori profile, the retrieved profile underestimates the height of the true profile and attributes the aerosol extinction of higher altitudes to

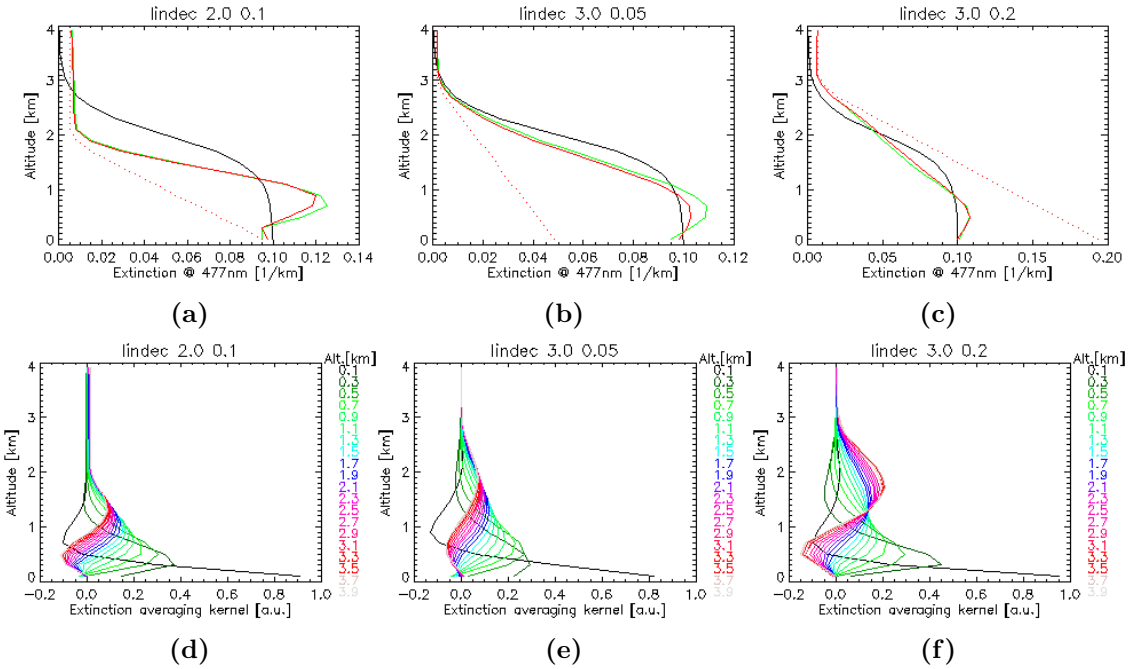

Figure 6.9: *Resulting profiles and corresponding averaging kernels for retrievals using a linear decreasing a priori profile with (a,d) a surface value of 0.1 km^{-1} and a height of 2.0 km, (b,e) 0.05 km^{-1} and 3.0 km, and (c,f) 0.2 km^{-1} and 3.0 km, respectively.*

lower ones. Retrievals using an a priori profile with a similar shape as in the standard case but with a lower and higher AOD are shown in Figure 6.9b and 6.9c. The retrieved profiles indicate, that the iteration direction, namely from smaller to larger extinction values and vice versa, does not affect the retrieval results significantly.

6.1.1.4 Influence of the True Aerosol Profile

In addition to the true aerosol scenarios considered in Section 6.1.1.1, retrievals were performed assuming an elevated aerosol layer centered around 1 km with an AOD of 0.1 and a smoothed box-shaped profile with an AOD of 0.1 and a height of 1.0 km to determine the influence of true profile shapes covering the altitude range, where the retrieval has distinct sensitivity features. The used a priori profile is the same as in the standard example and the retrieved profiles are shown in Figure 6.10. In the case of the elevated aerosol layer centered around 1 km, the retrieved profile is a smoothed version of a lofted layer, centered around the correct altitudes. Thus, the retrieved peak aerosol extinction is less than in the true profile. Furthermore, the retrieved profile resembles rather the a priori profile at altitudes above ≈ 1.7 km than the true profile, due to the limited sensitivity at these altitude ranges. The retrieved AOD of 0.13 ± 0.02 is therefore overestimated compared to the true value of 0.1. Similar results are achieved in the case of the smoothed box-shaped profile with respect to the retrieved aerosol extinctions above ≈ 1.7 km. An overestimation of the AOD of 0.12 ± 0.02 occurs, compared to the true value of 0.1.
The examples in Figure 6.9 and 6.10 illustrate the importance of applying an ad-

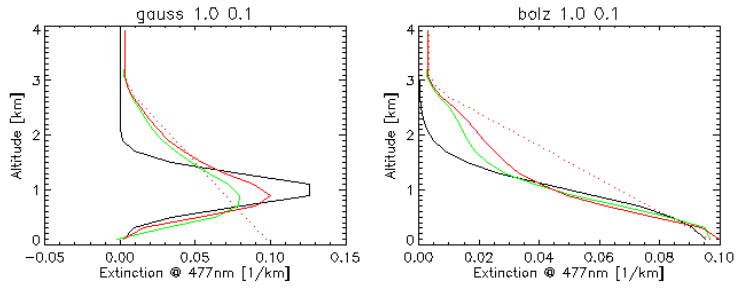

Figure 6.10: *Retrieval of (a) an elevated aerosol layer centered around 1 km with an AOD of 0.1 and (b) a smoothed box-shaped profile with an AOD of 0.1 and a height of 1.0 km.*

equate a priori profile. The a priori profile should not excessively constrain the retrieval, but at the same time, it should not introduce extinction features at altitudes where the retrieval is less sensitive.

6.1.1.5 Influence of the Measurement Vector Components

The choice of the measurement vector components strongly influences the retrieval. Retrievals were performed using measurement vectors consisting of different components to identify the resulting effects. Retrievals using only the O_4 ΔODs at 477 nm, the O_4 ΔODs at 360, 477, 577 and 630 nm and the O_4 ΔODs and relative intensities

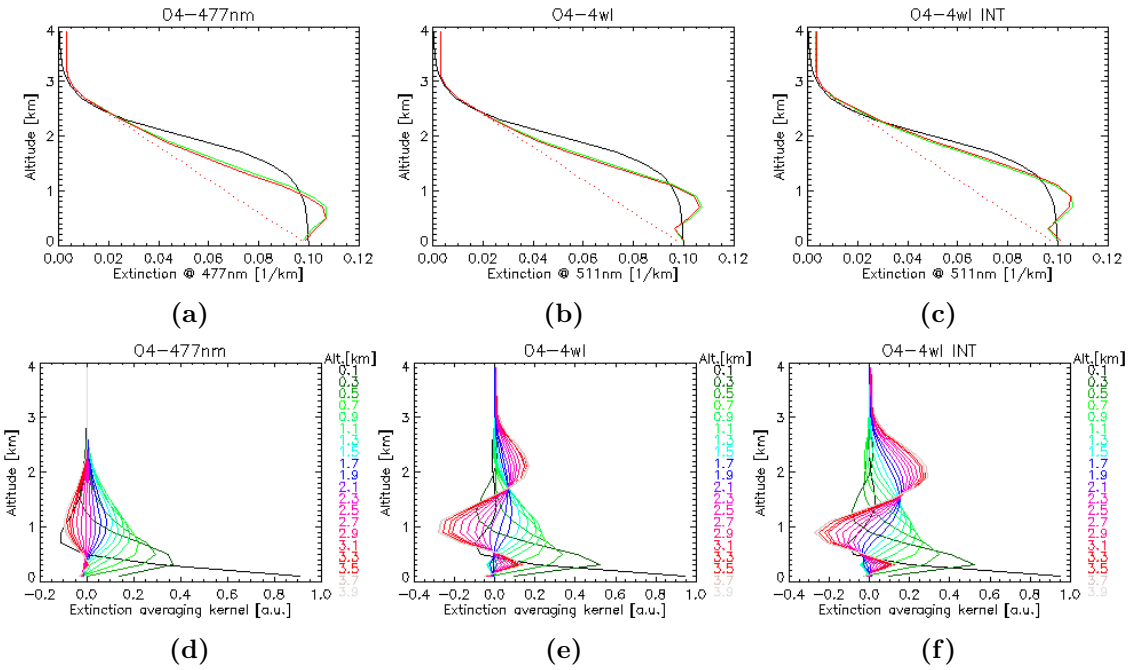

Figure 6.11: *Resulting profiles and corresponding averaging kernels for retrievals using (a,d) only the O_4 ΔOD at 477 nm, (b,e) the O_4 ΔODs at four wavelengths and (c,f) the O_4 ΔODs and relative intensities at four wavelengths.*

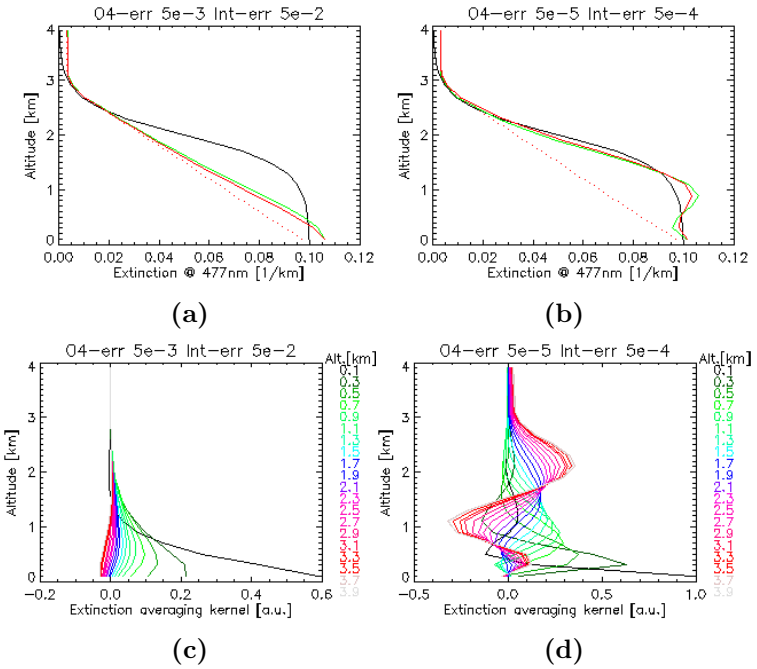

Figure 6.12: *Resulting profiles and corresponding averaging kernels for retrievals using (a,c) O_4 ΔODs with errors of $5 \cdot 10^{-3}$ and relative intensities with errors of $5 \cdot 10^{-2}$ and (b,d) $5 \cdot 10^{-5}$ and $5 \cdot 10^{-4}$, respectively.*

at these four wavelengths were performed and are aimed for a comparison to the retrieval using the O_4 ΔODs and relative intensities at 477 nm from the standard example in Figures 6.2 and 6.5.
The profiles and the corresponding averaging kernels of the retrieval using only the O_4 ΔODs at one wavelength are shown in Figure 6.11a and 6.11d, respectively. The vertical resolution and sensitivity for altitudes below 1 km are similar to values achieved by the retrieval from the standard example. In contrast, the sensitivities for altitudes above 1 km rapidly decrease, so that no information on the aerosol extinction above ≈ 1.7 km can be gained from measurement vectors consisting of the O_4 ΔODs at one wavelength only. The according degrees of freedom for signal is 2.4 and smaller compared to the retrieval using additionally the relative intensity at 477 nm. Similar sensitivities with respect to the altitude ranges are achieved in a retrieval using the O_4 ΔODs at four different wavelengths simultaneously in the measurement vector. (Figure 6.11b and 6.11e). However, the vertical resolutions and the absolute sensitivities in the lower altitudes are improved due to the wavelength dependent light path in the atmosphere. The resulting degrees of freedom for signal of 3.2 is higher than in the retrieval of the standard example. The best retrieval performance with respect to vertical resolution and sensitivity is achieved by simultaneously considering the O_4 ΔODs and relative intensities at four wavelengths in the measurement vector (Figure 6.11c and 6.11f). Thereby, the retrieval sensitivity increases for higher altitudes and the averaging kernels for more altitudes peak at their nominal height. The degrees of freedom for signal reaches a value of 3.7.
Another important factor limiting the retrieval capabilities with respect to sensitiv-

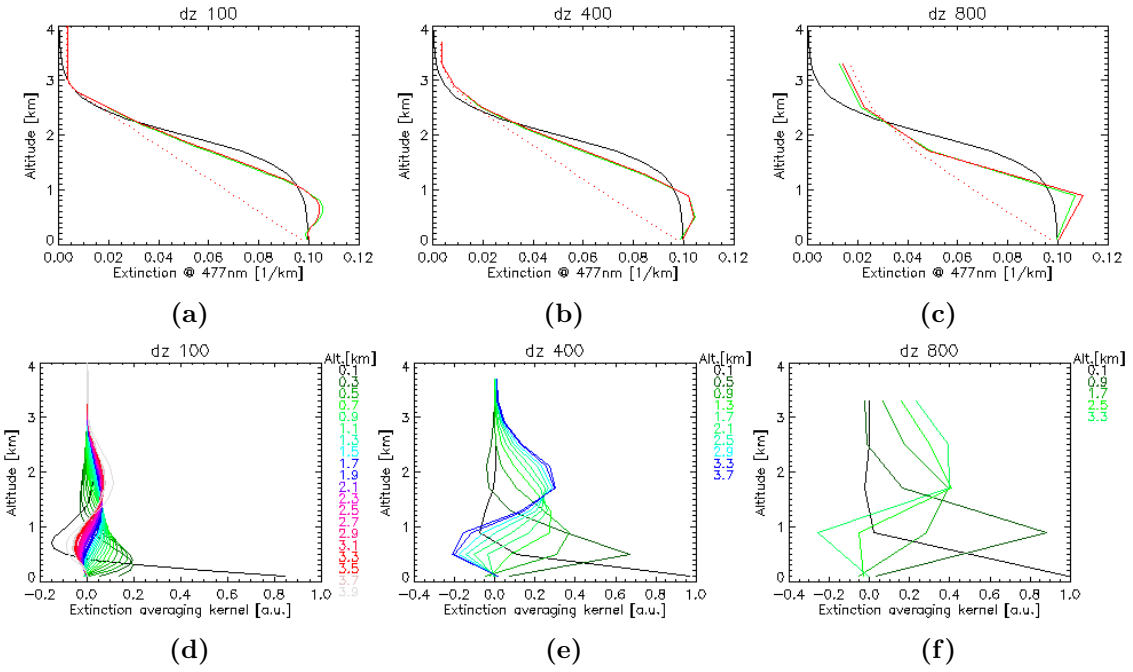

Figure 6.13: *Resulting profiles and corresponding averaging kernels for retrievals using (a,d) a height grid with 100 m, (b,e) 400 m and (c,f) 800 m resolution.*

ity and vertical resolution is the measurement error. It determines to which degree information is gained from the measurement or the a priori knowledge. While the retrieval of the standard example was performed using an error of $5 \cdot 10^{-4}$ for the O_4 ΔODs and $5 \cdot 10^{-3}$ for the relative intensity, two further retrievals were performed with smaller and larger assumed measurement errors. Figure 6.12a and 6.12c show the retrieved profiles and averaging kernels for an assumed error of $5 \cdot 10^{-3}$ for the O_4 ΔODs and $5 \cdot 10^{-2}$ for the relative intensity. The retrieved profile resembles rather the a priori than the true profile. The corresponding averaging kernels indicate the significant loss in sensitivity due to the larger measurement errors. The vertical resolution is degraded, and distinct peaks occur only for the lowermost altitudes mainly not centered around the nominal altitude. The degrees of freedom for signal of 1.2 is clearly reduced compared to the standard example case. In contrast, the assumption of an error of $5 \cdot 10^{-5}$ for the O_4 ΔODs and $5 \cdot 10^{-4}$ for the relative intensity results in remarkable improvements of the retrieval results and properties with respect to vertical resolution and sensitivity for the aerosol profile as depicted in Figure 6.12b and 6.12d. Compared to the retrieval of the standard example, the averaging kernels show distinct peaks for altitudes below 2.2 km which are centered around their nominal height. Furthermore, the sensitivity and the vertical resolution is improved, and the degrees of freedom for signal is increased to 4.2.

6.1.1.6 Influence of the Height Grid Resolution

The influence of the height grid on the retrrieval is depicted in Figure 6.13 for height grids with 100, 400 and 800 m resolution. The degrees of freedom for signal is not affected by the different representations of the profile height grid. While

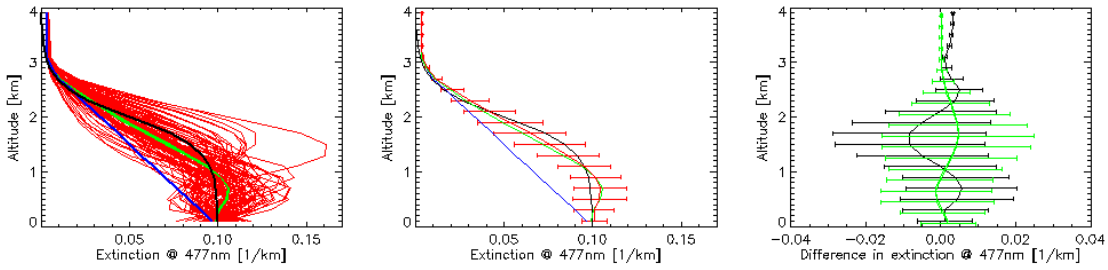

Figure 6.14: *(a) The a priori (blue), retrieved (red), true (black) and convolved true (green) profiles from 100 retrieval repetitions with random measurement noise. (b) The average and the standard deviations of the retrieved profiles are shown in red instead of the individual profiles. (c) The difference of the retrieved average to the true (black) and convolved true (green) profile with the standard deviations.*

the true profile is well reproduced by the retrievals using 100 and 400 m height grid resolutions, the height of the box-shaped true profile is underestimated in the case using the 800 m resolution, due to the rough sampling of the profile and the decreasing sensitivity at altitudes above ≈ 2 km.

6.1.1.7 Uncertainties Owing to Statistical and Systematic Errors

The uncertainties in the retrieved profiles due to measurement error were simulated by adding normally distributed random noise with a standard deviation of $5 \cdot 10^{-4}$ and $5 \cdot 10^{-3}$ to the synthetic O_4 ΔODs and relative intensities, respectively. Figure 6.14a shows the retrieved profiles of 100 retrieval runs. The average of these retrieved profiles is shown in Figure 6.14b with the standard deviation as error bars. The resulting difference of the retrieved average profile to the true and convolved true profile is depicted in Figure 6.14c together with the standard deviations. The retrieval results from the standard example (Figure 6.2), which were retrieved without measurement noise, are shown Figure 6.15 together with the total retrieval,

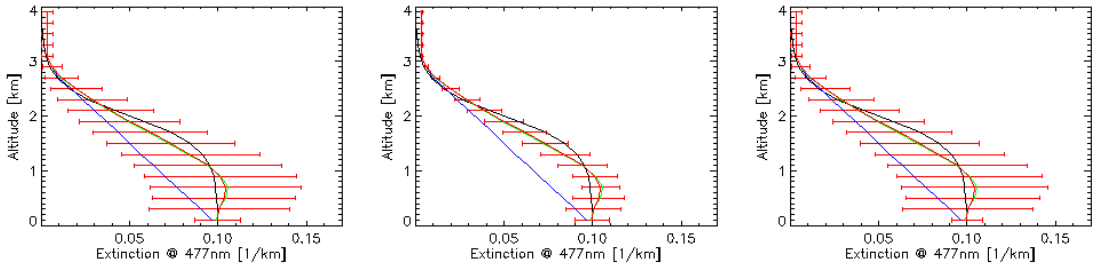

Figure 6.15: *The a priori (blue), retrieved (red), true (black) and convolved true (green) profile from a retrieval without random measurement noise. The retrieved profile is shown with the (a) total retrieval error, (b) retrieval noise error and (c) smoothing error.*

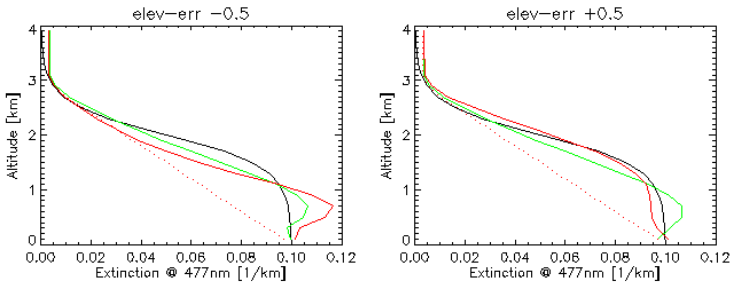

(a) **(b)**

Figure 6.16: *Resulting profiles for retrievals with an error in the elevation angles of (a) - 0.5° and (b) + 0.5°.*

retrieval noise and smoothing error (see Section 5.5). The major fraction of the total retrieval error is attributable to the smoothing error. The uncertainties caused by the measurement error are accounted for by the retrieval noise error, which is a smaller portion of total retrieval error. The comparison of Figure 6.14b and 6.15b indicates the accurate consideration of the measurement error by the retrieval.
The effect of systematic uncertainties in the elevation angle (i.e., a misalignment of the telescope) on the retrieved profile is shown in Figure 6.16 for differences between the true and assumed elevation angles of - 0.5 and + 0.5. Remarkable differences in the shape of the retrieved profiles can be identified in comparison with the retrieval of the standard example. The profile height is underestimated if the telescope points higher than assumed and vice versa.
The influences of possible uncertainties in the O_4 absorption cross section are shown in Figure 6.17 for cases of underestimated and overestimated absolute values of the cross section. The retrievals were performed assuming an O_4 absorption cross section, which was scaled by a factor of 0.75 and 1.25. The underestimation of the absorption cross section results in an overestimation of the aerosol profile height and vice versa. Furthermore, the retrieved AOD of 0.17 ± 0.02 in the case of the underestimated absorption cross section is smaller than the true value of 0.2. In contrast, a larger AOD of 0.23 ± 0.02 was retrieved when the absorption cross section was overestimated.

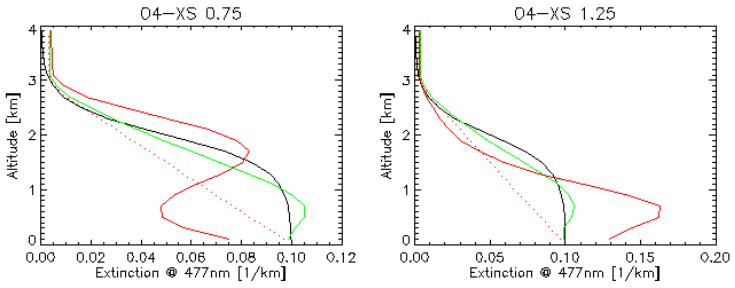

(a) **(b)**

Figure 6.17: *Resulting profiles for retrievals with (a) an underestimation of the O_4 absorption cross-section of 25 % and (b) overestimation of 25 %.*

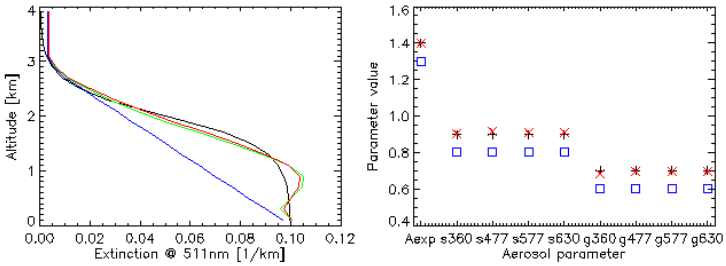

(a) **(b)**

Figure 6.18: *Simultaneous retrieval of the aerosol extinction profile, Ångström exponent, single scattering albedo and asymmetry parameter using the O_4 ΔODs and relative intensities at 360, 477, 577 and 630 nm. (a) The a priori (blue), retrieved (red), true (black) and convolved true (green) profile. (b) The a priori (blue, square), true (black, plus) and retrieved (red, cross) optical parameters.*

6.1.2 Retrieval of Further Aerosol Optical Properties

MAX-DOAS O_4 and intensity measurements are sensitive not only to the aerosol extinction but also to further aerosol optical properties, when additional measurements at different azimuth angles are considered besides the measurements at different elevation angles (Wagner et al., 2004; Frieß et al., 2006). In particular, the combined O_4 ΔOD and relative intensity measurement at several wavelengths as a function of azimuth angle contains significant information on the aerosol phase function, single scattering albedo and Ångström exponent. Synthetic MAX-DOAS measurements of the O_4 ΔOD and relative intensity at 360, 477, 577 and 630 nm were calculated for a solar zenith angle of 60°, an elevation angle sequence of 1°, 2°, 4°, 8°, 14°, 30° and 90° at a fixed azimuth angle of 30° as well as an azimuth angle sequence of $\pm$5°, $\pm$6°, $\pm$8°, $\pm$10°, $\pm$15°, $\pm$20°, $\pm$30°, $\pm$45°, $\pm$60°, $\pm$75°, $\pm$90°, $\pm$100°, $\pm$120°, $\pm$150° and 180° at a fixed elevation angle of 25°, while the aerosol optical parameters, except the extinction, were assumed to be constant with altitude. The resulting profile is shown in Figure 6.18a, while Figure 6.18b shows the a priori, retrieved and true aerosol optical parameters, namely the Ångström exponent, single scattering albedo and asymmetry parameter for the Henyey-Greenstein parameterization of the phase function. All aerosol optical properties are very well reproduced by the retrieval using the optimal estimation method. The degrees of freedom for signal of 12.5 indicate that the information for a complete description of the aerosol optical properties can be gained from MAX-DOAS measurements. Furthermore, the application of model calculations based on Mie theory should enable the retrieval of the aerosol complex refractive index and size distribution from the optical parameters retrieved from MAX-DOAS similar to Sun photometer retrievals (Dubovik et al., 2000; Dubovik and King, 2000).

6.1.3 Parameterized Retrieval of the Aerosol Profile

The information content of ground based MAX-DOAS measurements is limited with respect to the aerosol extinction profile. The retrieval in the standard example in

Section 6.1.1 using the complete aerosol profile as state vector determines a degree of freedom for signal of 2.9 when the O_4 ΔODs and relative intensities at 477 nm serve as measurement vector. This suggests the strategy of describing the aerosol extinction profile by two or three parameters and appropriate functions. The capabilities of such parameterized retrievals using the optimal estimation method are assessed in the following Sections.

6.1.3.1 Aerosol Profile Description by Two Parameters

The aerosol profile can be described by two parameters using a box-shaped distribution, which can be quantified by the height of the box and the total AOD. A function similar to the Boltzmann distribution can be used to avoid large gradients in the profile shape, since aerosol distributions in the atmosphere are rather smoothed than constrained by sharp edges. Thus, the aerosol profile can be described by two parameters using the relationship:

$$\epsilon_M(z) = \frac{\epsilon_M(0)}{1 + \exp\left(\frac{z - \frac{\tau_M}{\epsilon_M(0)}}{0.3}\right)}, \tag{6.3}$$

where $\epsilon_M(0)$ denotes the extinction coefficient at the surface and τ_M is the AOD. The usage of $\epsilon_M(0)$ rather than the height of the box has the advantage, that both parameters are in the same order of magnitude.
The resulting profiles for retrievals using the O_4 ΔODs and relative intensities at 477 nm as measurement vector and the two parameter description from equation (6.3) are shown in Figure 6.19. The true profiles are a smoothed box-shaped profile with an AOD of 0.2 and a height of 2 km, a linear decreasing profile with an AOD of 0.1 and a height of 2 km and an elevated aerosol layer centered around 2 km with an AOD of 0.1. While the box-shaped profile is reproduced perfectly by the parameterized retrieval, the extinction at the surface is underestimated in the linear decreasing profile case, which is due to the nature of the profile parametrization. However, the retrieval is not able to reproduce the elevated aerosol layer, which is also due to the limitation of the profile parametrization.

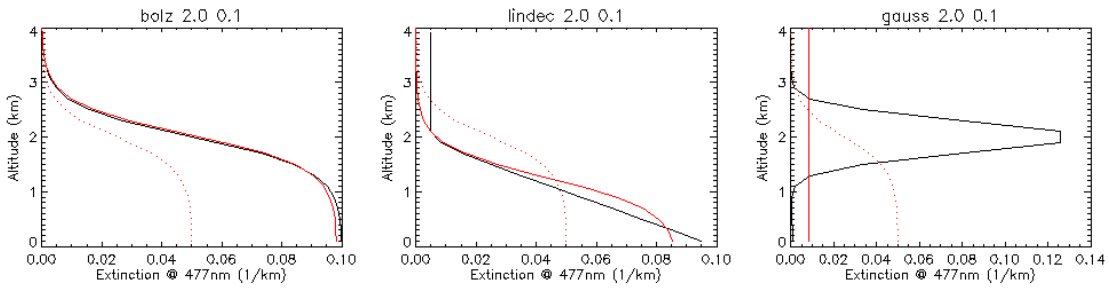

Figure 6.19: *Results of the two parameter retrievals of a (a) smoothed box-shaped profile, (b) linearly decreasing profile and (c) elevated aerosol layer. The a priori (red, dotted), retrieved (red) and true (black) profiles are shown in each panel.*

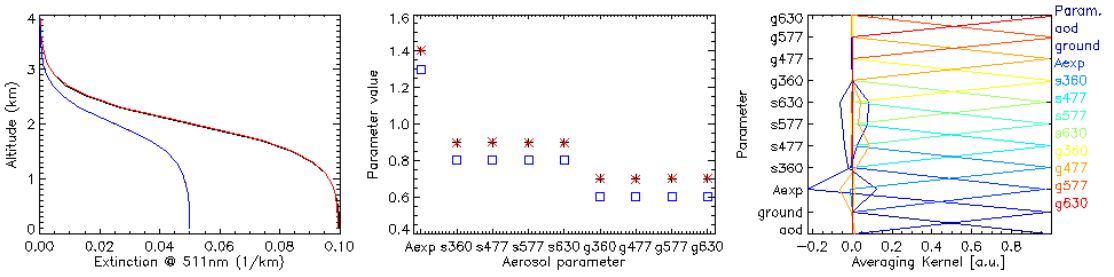

(a) **(b)** **(c)**

Figure 6.20: *Simultaneous retrieval of the two aerosol extinction profile parameters, Ångström exponent, single scattering albedo and asymmetry parameter using the O_4 ΔODs and relative intensities at 360, 477, 577 and 630 nm. (a) The a priori (blue), retrieved (red) and true (black) profile. (b) The a priori (blue, square), true (black, plus) and retrieved (red, cross) optical parameters. (c) The corresponding averaging kernels color coded according the parameters (state vector elements).*

In addition, the simultaneous retrieval of the two aerosol extinction profile parameters, Ångström exponent, single scattering albedo and asymmetry parameter using the O_4 ΔODs and relative intensities at 360, 477, 577 and 630 nm for viewing geometries including different azimuth angles as introduced in Section 6.1.2 is possible and an example is shown in Figure 6.20. In this case, the true profile shape is similar to the assumed profile shape of the two parameter description. Thus, the parameterized retrieval is capable to retrieve all optical parameters, which is indicated by the very good agreement of the retrieved and true parameters. The averaging kernels peak at their nominal position, which is determined by the position of the parameter in the state vector (y-axis in Figure 6.20). This results in the degrees of freedom for signal of 10.9.

6.1.3.2 Aerosol Profile Description by Three Parameters

A more flexible description of the aerosol profile is achieved by using three parameters. A possible description by three parameters that is also capable to account for elevated aerosol layers can be a Gaussian distribution:

$$\epsilon_M(z) = \frac{1}{\sigma \cdot \sqrt{2\,\pi}} \cdot \exp\left(-0.5 \cdot \left(\frac{z - z_{peak}}{\sigma}\right)^2\right) \cdot \tau_M \,, \tag{6.4}$$

where σ and z_{peak} denote the FWHM and height of the peak, respectively.
The resulting profiles for retrievals using τ_M, σ and z_{peak} for the profile description and the O_4 ΔODs and relative intensities at 477 nm as measurement vector are depicted in Figure 6.21. The three different true profiles are the same as in the two parameter retrieval case. The box-shaped and linear decreasing profiles are fairly well reproduced within the capabilities of the three parameter description. In contrast to the two parameter description, the elevated layer is well reproduced by the retrieval with respect to the center height and AOD. Therefore, a combination of a two and three parameter description of the profile should be used and adapted

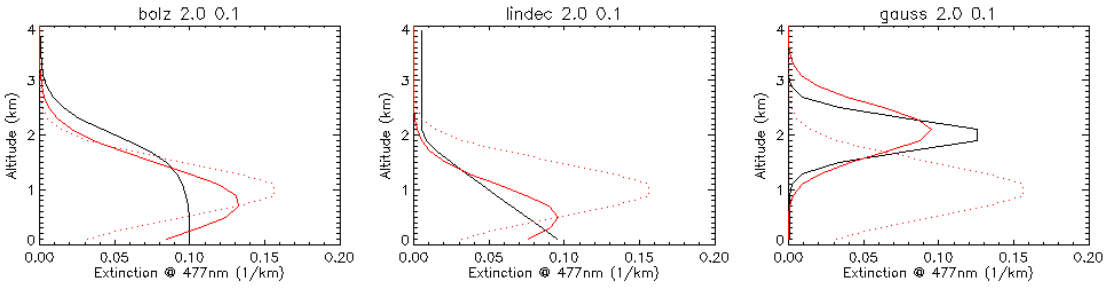

(a) **(b)** **(c)**

Figure 6.21: *Results of the three parameter retrievals of a (a) smoothed box-shaped profile, (b) linear decreasing profile and (c) elevated aerosol layer. The a priori (red, dotted), retrieved (red) and true (black) profiles are shown in each panel.*

according the respective atmospheric conditions. However, the main disadvantage of the parameterized profile retrieval compared to the retrieval of the complete profile is that the parametrization does not cover the whole state space accessible by the measurements.

6.1.4 Retrieval of the Trace Gas Profile

The application of the optimal estimation method for the retrieval of trace gas profiles from MAX-DOAS slant column density measurements of the according trace gas is illustrated using synthetic NO_2 measurements at 470 nm. The measurement vector consists of simulated differential NO_2 slant column densities (ΔSCD) for elevation angles of 1°, 2°, 4°, 8°, 14°, 30° and 90°, a solar zenith angle of 60° and a relative azimuth angle of 30° calculated according to equation (5.34) (Section 5.8). To identify the effects attributable to the retrieval performance, the NO_2 ΔSCD er-

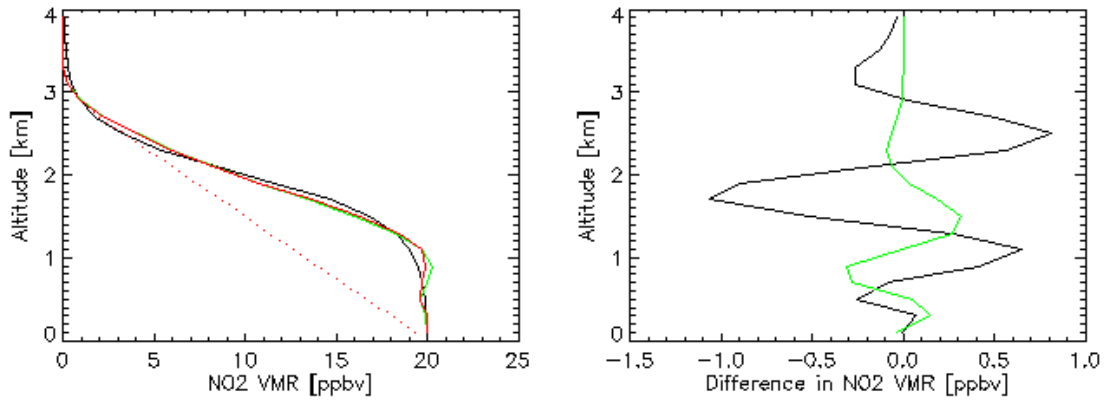

(a) **(b)**

Figure 6.22: *Retrieval of the NO_2 profile: the (a) a priori (red, dotted), retrieved (red), true (black) and convolved true (green) profile; (b) deviation of the retrieved NO_2 from the true (black) and convolved true (green) profile.*

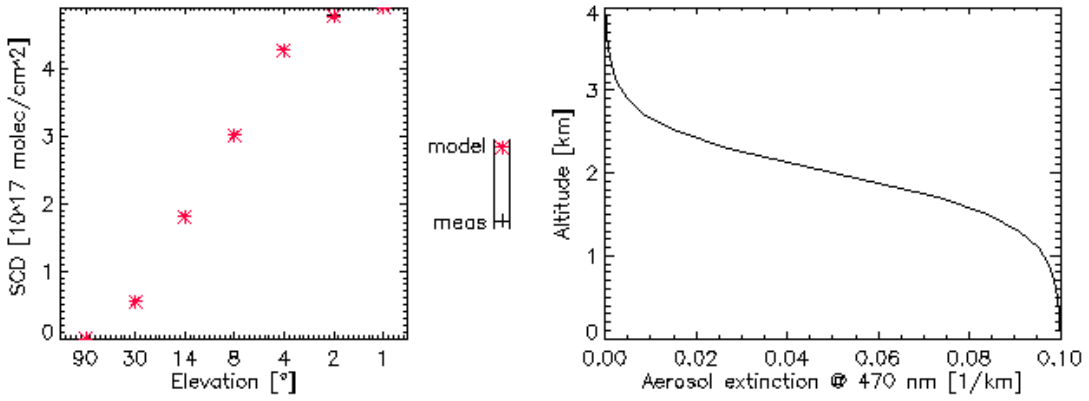

(a) **(b)**

Figure 6.23: *(a) The true (black cross) and retrieved (red asterisk) differential NO_2 slant column densities as a function of the elevation angle and (b) the aerosol extinction profile.*

rors were set to $1 \cdot 10^{15}$ $\frac{\text{molec}}{\text{cm}^2}$ in the measurement covariance matrix, without adding random noise to the synthetic measurements. The profile was described on a height grid with a resolution of 200 m from the surface up to the altitude of 4 km.
Figure 6.22a shows the results of the NO_2 mixing ratio profile retrieval. The true profile is reproduced with a high accuracy by the retrieval with respect to the absolute mixing ratio values as well as the vertical extent of the NO_2 layer. The deviation of the retrieved from the true and convolved true profile are depicted in Figure 6.22b. The true and retrieved NO_2 ΔSCDs are shown in Figure 6.23a and lie on top of each other. The assumed aerosol extinction profile is shown in Figure 6.23b and has a similar shape as the NO_2 profile, according to a well mixed atmospheric boundary

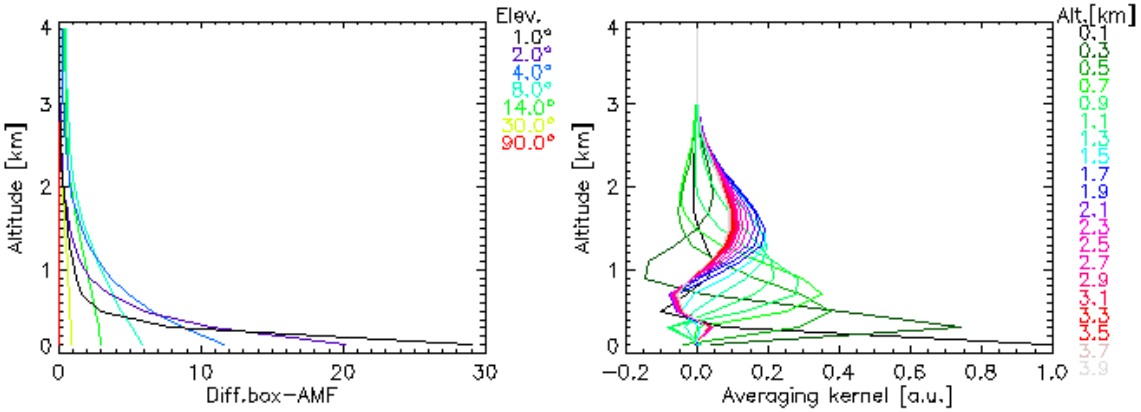

(a) **(b)**

Figure 6.24: *(a) The Weighting functions of the NO_2 profile retrieval color coded according the corresponding elevation angles of the measurements. (b) The averaging kernels of the profile retrieval color coded according the corresponding altitudes.*

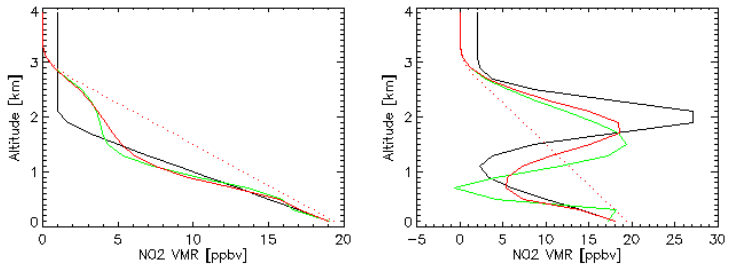

(a) (b)

Figure 6.25: *Retrieval of (a) a linear decreasing NO_2 profile and (b) a combined NO_2 profile featuring a linear decrease and an elevated layer centered around 2 km altitude.*

layer.
The weighting functions of the NO_2 profile retrieval are determined by the box airmass factors (Section 5.8) and quantify the sensitivity of the measurement to perturbations of the NO_2 partial vertical column density at different altitudes. The box airmass factors normalized according to equation (5.36) are shown in Figure 6.24a. In the case of weakly absorbing trace gases, the corresponding box airmass factors depend on the aerosol, temperature and pressure profile as well as other strong absorbers. The box airmass factors are characterized by a peak at the surface and a rapid decrease with altitude indicating high sensitivities in the lowermost altitude ranges. Furthermore, the sensitivities near the surface are highest at small elevation angles due to the increased light paths through the lowermost atmospheric layers. The averaging kernels for the NO_2 profile retrieval are depicted in Figure 6.24b, and quantify the sensitivity of the retrieved to the true profile. The averaging kernels show distinct peaks for altitude layers below ≈ 2 km, while the averaging kernels for the lowermost ≈ 1.8 km peak at around their nominal altitudes. Similar to the retrieval sensitivity, the vertical resolution decreases with altitude and ranges from ≈ 150 m at the surface to ≈ 900 m at 1.5 km altitude, which is better than the vertical resolution achieved by the aerosol profile retrieval using the O_4 ΔODs and relative intensities at 477 nm. The degrees of freedom for signal of 3.8 is larger than the value achieved in the standard example of the aerosol profile retrieval.

6.1.4.1 Influence of the True Trace Gas Profile

The capability of the retrieval to reproduce NO_2 profiles with different shapes was tested for scenarios with a linearly decreasing NO_2 distribution and a combined distribution featuring a linear decrease in the lower altitudes and an elevated layer around 2 km altitude. The retrievals were performed assuming the aerosol profile shown in Figure 6.23. The linearly decreasing profile is well reproduced by the retrieval at lower altitudes, while the retrieved profile tends to the a priori at altitudes above ≈ 1.7 km due to the low sensitivity at these altitudes (Figure 6.25a). In the case of the combined NO_2 profile shape, the retrieved profile is a smoothed version

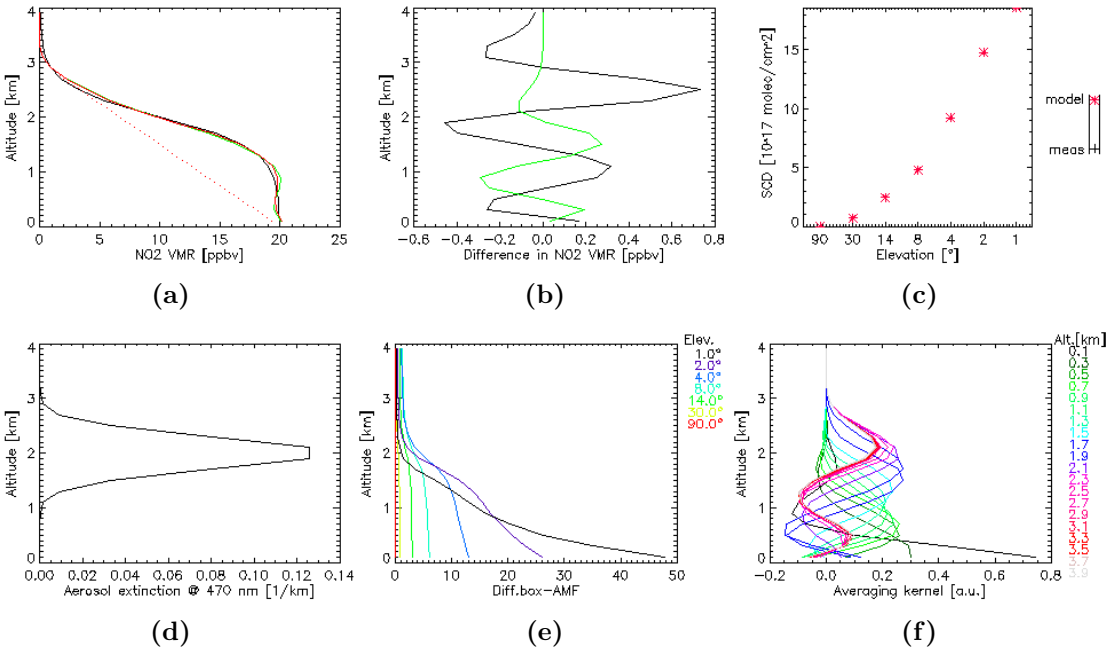

Figure 6.26: *Overview of the NO_2 profile retrieval quantities for the presence of an elevated aerosol layer: (a) NO_2 profiles; (b) differences in the NO_2 profiles; (c) NO_2 $\Delta SCDs$; (d) assumed aerosol profile; (e) retrieval weighting functions; (f) retrieval averaging kernels. (Compare with Figures 6.22, 6.23 and 6.24)*

of the true profile. This demonstrates the capability of the retrieval to distinguish two separated NO_2 layers in the atmospheric boundary layer (Figure 6.25b).

6.1.4.2 Influence of the Aerosol Profile

To determine the influence of the aerosol profile on the retrieval, the NO_2 profile retrieval was performed assuming an elevated aerosol layer centered around 2 km. The retrieval settings and conditions were the same as in the previous example for the retrieval of a smoothed box-shaped NO_2 profile. Figure 6.26a and Figure 6.26b show the retrieved profile and its difference to the true and convolved true profile, respectively. The comparison to Figure 6.22 illustrates the improvement of the retrieval capabilities with respect to a better agreement between the retrieved, true and convolved true profile. The aerosol profile is depicted in Figure 6.26d and causes significant changes in the NO_2 box airmass factors, which are shown in Figure 6.26e. The comparison to Figure 6.24a illustrates the remarkable increase of the light paths at altitudes between ≈ 1 km and ≈ 2 km, since the light reaching the instruments is now scattered at higher altitudes. The resulting increase in the retrieval sensitivity at these altitudes is quantified by the averaging kernels in Figure 6.26f. In this case, the averaging kernels show distinct peaks for altitude layers up to ≈ 2.5 km, and the averaging kernels for the lowermost ≈ 2.2 km peak at around their nominal altitudes. However, the vertical resolution of the retrieval of ≈ 300 m at the surface is degraded compared to the averaging kernels of Figure 6.24b and

the degrees of freedom for signal are slightly decreased to 3.5.

6.2 Application of the Regularization Method

The constraint used in the optimal estimation method is based on a priori knowledge on the atmospheric profile to be inverted. It is implemented in the retrieval in form of the inverse a priori covariance matrix. The resulting estimated errors, degrees of freedom for signal and vertical resolution depend on the type and strength of the constraint. However, situations may occur, in which the according data is not available and inappropriate a priori covariance matrices are used resulting in contributions from the effective null-space or the loss of information. In contrast to the optimal estimation method, the way the least squares conditions are balanced in the regularization method is controlled by the regularization matrix (Section 5.6.2). Therefore, the retrieval is rather constrained with respect to the profile shape than the absolute values. The strength of the constraint is determined by the regularization parameter, which has to be chosen appropriately.

6.2.1 Retrieval of the Aerosol Extinction Profile and Optical Depth

The application of the regularization method for the retrieval of aerosol extinction profiles and optical depths from MAX-DOAS O_4 and intensity measurements was performed using the synthetic measurements from the standard example in Section 6.1.1. Figure 6.27 shows the retrieved profiles using the discrete first-derivative operator for different regularization parameters. The true smoothed box-shaped profile is depicted in black, while the a priori and retrieved profiles are shown in dotted red and solid red, respectively. The green lines are the true profiles after the application of the retrieval averaging kernels. The regularization parameters are indicated on top of each panel. It can be clearly identified how the increasing regularization parameter constrains the smoothness of the retrieved profile. Thus, the shape of the true profile cannot be reproduced by the retrieval for regularization parameters larger than $\approx 1 \cdot 10^5$. The according averaging kernels of the retrievals are summarized in Figure 6.28. For regularization parameters smaller than $\approx 1 \cdot 10^{-4}$, the averaging kernels are mainly characterized by oscillatory features, which diminish for increasing values of the regularization parameter. These structures arise from inadequate filtering of contributions from the effective null space, which occur for the corresponding regularization parameters. Thus, the determination of the appropriate regularization parameter is crucial to avoid these contributions and simultaneously constrain the retrieval without loosing information.
The dependence of the degrees of freedom for signal on the regularization parameter was determined by retrievals using different regularization operators, namely the identity matrix, discrete first- and second-derivative operators. The resulting degrees of freedom for signal as a function of the regularization parameter are shown in Figure 6.29. With an increasing regularization parameter, the contributions from the effective null space are more and more filtered out. The remaining degrees of

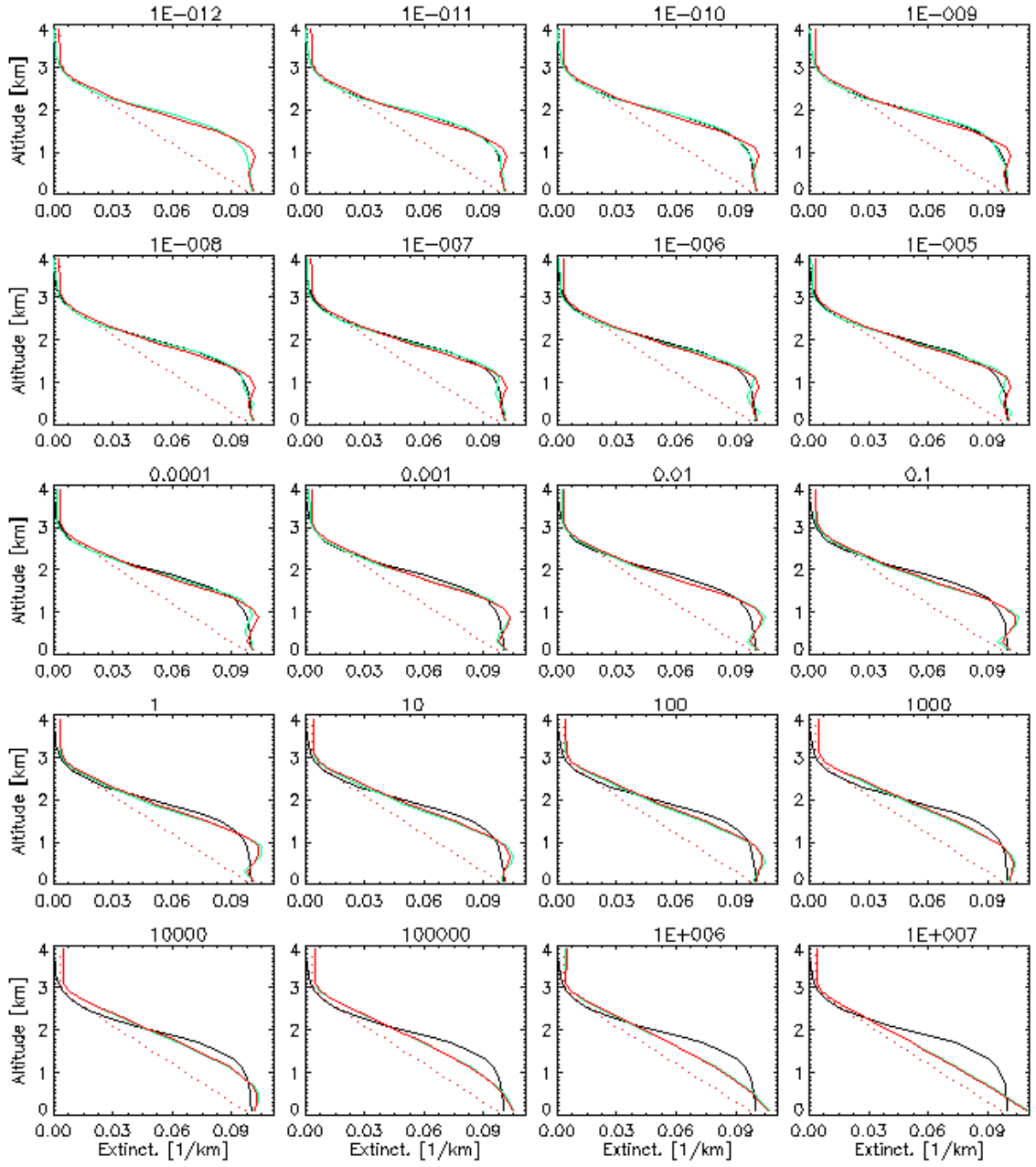

Figure 6.27: *Retrievals of the aerosol extinction profiles using the discrete first-derivative operator and different regularization parameters indicated on top of each panel. The a priori (red, dotted), retrieved (red, solid), true (black), and convolved true (green) profile is shown in each panel.*

freedom for signal at large regularization parameter values depends on the used regularization operator. In the case of the identity matrix, the retrieved profile becomes identical to the a priori profile, since no degrees of freedom for signal is left in the retrieval. The remaining degrees of freedom for signal of 1 and 2 for the discrete first and second-derivative operator, respectively, are due to the nature of the operators, since the first and second derivative of the profile difference are weighted in the cost function (equation 5.27). Thus, any constant or linear profile has no contribution

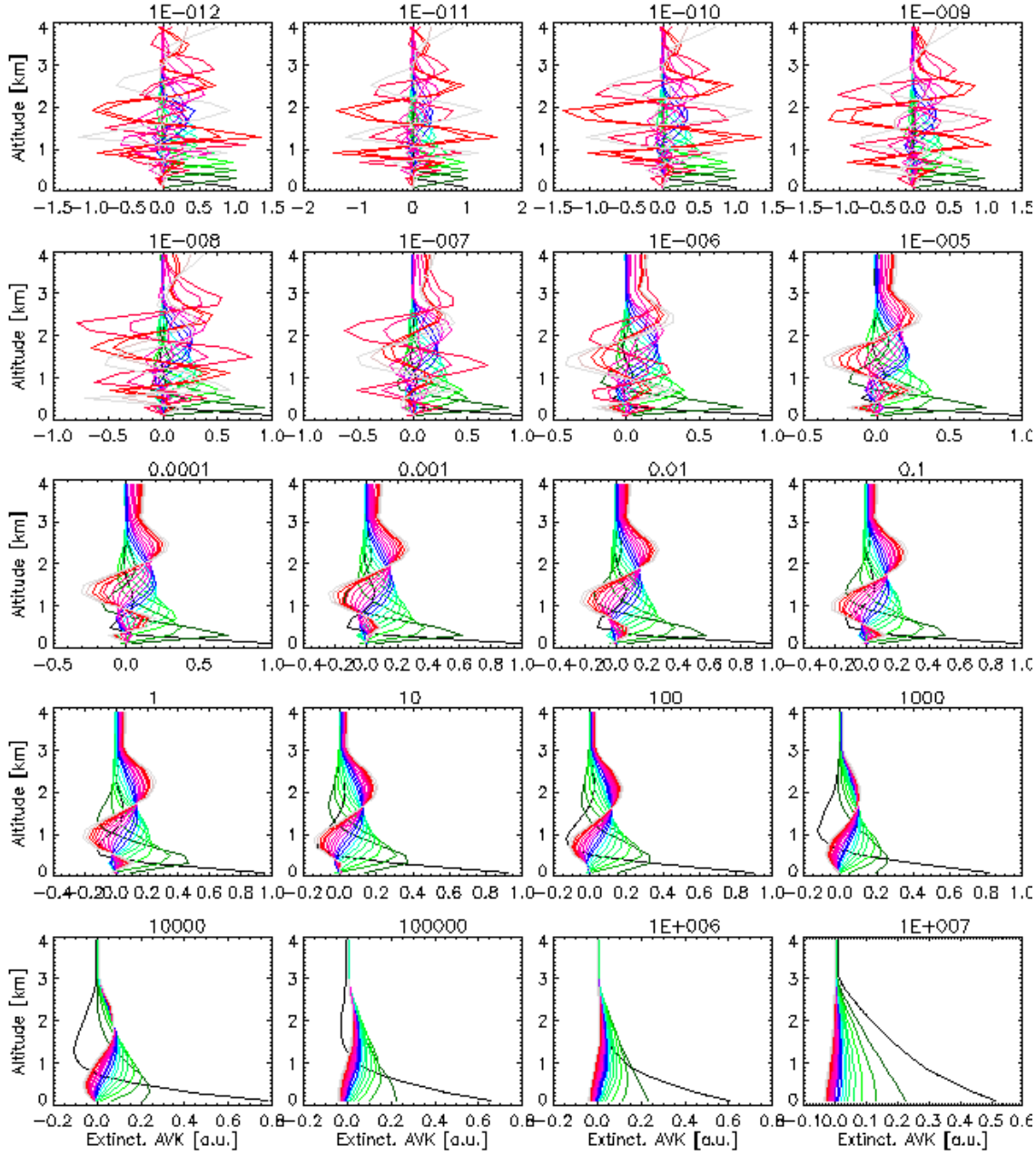

Figure 6.28: *The averaging kernels of the aerosol profile retrievals shown in Figure 6.27. The regularization parameters are indicated on top of each panel, while the corresponding altitudes are indicated by different colors (see legend in Figure 6.5).*

to the cost function in the case of the discrete first- or second-derivative operator, respectively.

The retrieval errors also depend on the used regularization matrix. The errors resulting from retrievals using the discrete first-derivative operator are shown in Figure 6.30. The mean relative total, noise and smoothing errors are depicted as a function of the regularization parameter. For small regularization parameters, the total error is dominated by the retrieval noise. Large regularization parameters result

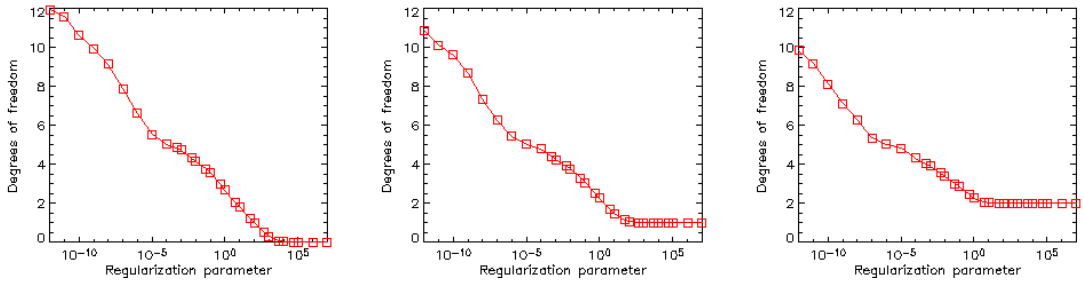

Figure 6.29: *The degrees of freedom for signal as a function of the regularization parameter for the (a) identity matrix, (b) discrete first- and (c) second-derivative operator.*

in total errors which are mainly caused by the smoothing effect, while the noise error converges to values determined by the remaining degrees of freedom for signal. The determination of the appropriate regularization parameter depends on the retrieval properties to be optimized. When the retrieval error should be minimal, the according regularization parameter can be determined from Figure 6.30. A commonly used approach is the L-curve method, which is illustrated in Figure 6.31 for retrievals using the discrete first-derivative operator. It shows the norm, defined as the root of the sum over the squared elements, of the first derivative of the retrieved profile $||\mathbf{L}\hat{\mathbf{x}}||$ as a function of the residual norm $||\mathbf{f}(\hat{\mathbf{x}}) - \mathbf{y}||$, which is the norm of the difference between model and measurement. The different colors indicate the corresponding regularization parameters. The curve has a vertical and a horizontal part. The regularization parameters, which lie on the horizontal part, are too large. A decrease in the regularization parameter results in smaller residuals, while the profile norm is not affected. Regularization parameters corresponding to the horizontal part of the L-curve lead to retrieval results, which do not contain all information available in the measurement. In contrast, when the vertical part is reached, a further decrease of the regularization parameter does not result in an improvement of the residual but increases the profile norm. Thus, the retrieved profile contains noise dominated contributions from the effective null space. Therefore, the

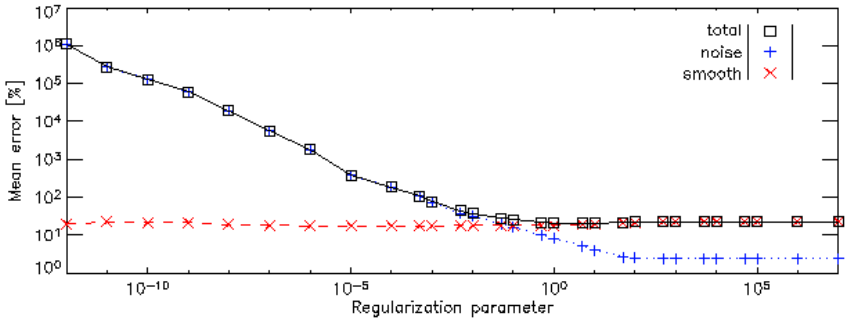

Figure 6.30: *The mean relative total (black, square), noise (blue, plus) and smoothing (red, cross) errors of retrievals using the discrete first-derivative operator as a function of the regularization parameter.*

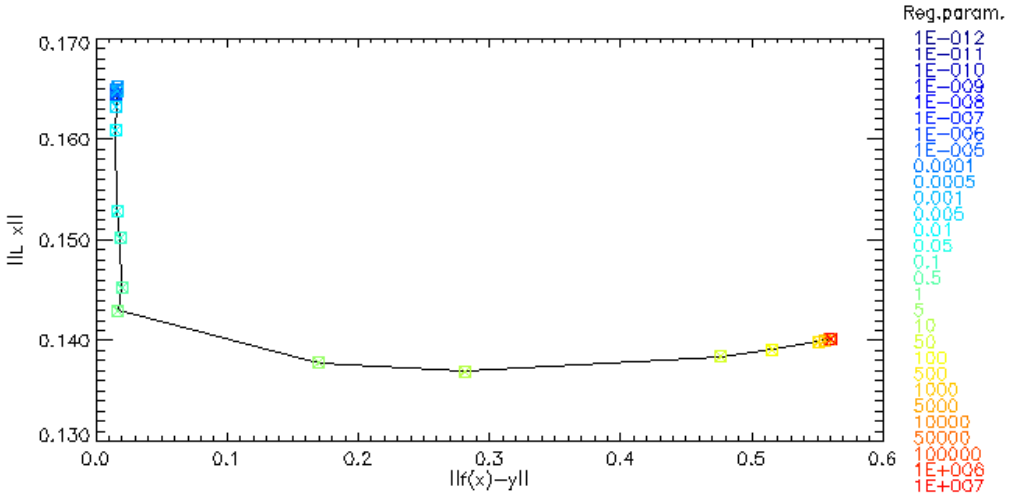

Figure 6.31: *The L-curve of retrievals using the discrete first-derivative operator. The regularization parameters are indicated by different colors.*

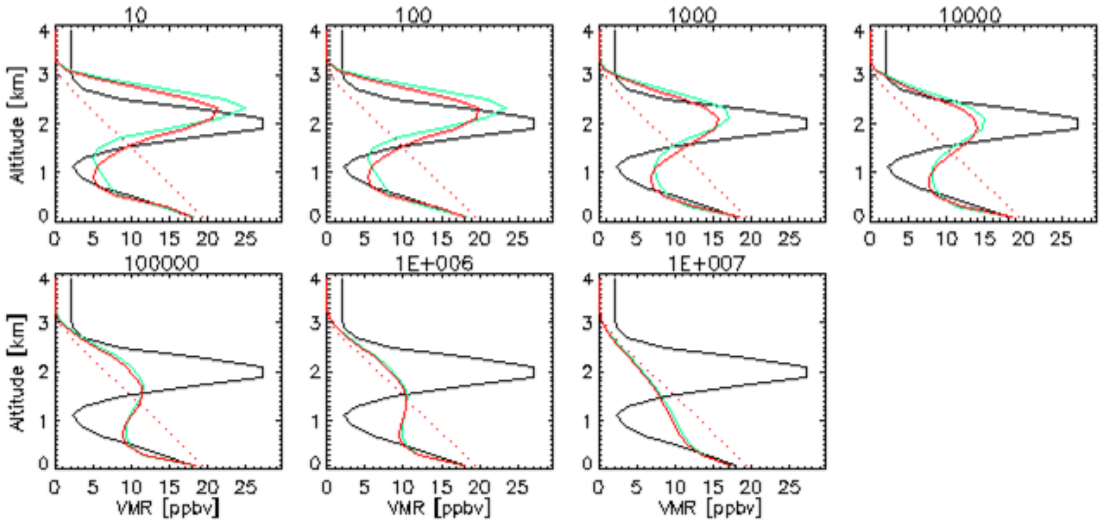

Figure 6.32: *Retrievals of the NO_2 profiles using the discrete first-derivative operator and different regularization parameters indicated on top of each panel. The a priori (red, dotted), retrieved (red), true (black), and convolved true (green) profile is shown in each panel.*

optimal value for the regularization parameter is quantified by the corner of the L-curve. This optimal value depends on the aerosol profile and has to be individually determined for different atmospheric conditions.

6.2.2 Retrieval of the Trace Gas Profile

The application of the regularization method using the discrete first-derivative operator for the retrieval of NO_2 profiles from MAX-DOAS measurements is shown in Figure 6.32 for selected regularization parameters. The synthetic measurements

for geometries and conditions from the examples in Section 6.1.4 were used for the retrieval. Large regularization parameters filter the information on the elevated NO_2 layer. Since the optimal regularization parameter depends on the specific inversion problem, its determination requires an additional iteration process within the retrieval. The determination can be performed using e.g. the L-curve method. However, these additional calculations increase the computational effort, since they have to be carried out for each retrieval sequence.

Chapter 7

Instrumentation

In the scope of this work, a new type of MAX-DOAS instrument was developed. The aim of this new development was to design and build an instrument, which enables MAX-DOAS measurements covering a wide spectral range. Furthermore, the telescope of the instrument should be able to point to any direction in the sky. After its construction, the MAX-DOAS instrument was deployed at several European sites in the framework of a joint research activity of the European project EUSAAR (European Supersites for Atmospheric Aerosol Research) (Philippin et al., 2009; Philippin and Laj, 2009; Laj and Philippin, 2009). The aim of the project activity was the development and application of the MAX-DOAS technique for the retrieval of atmospheric aerosol profiles. Several intercomparison campaigns were performed with the new MAX-DOAS instrument at measurement sites equipped with established aerosol in-situ and remote sensing measurement techniques. In this chapter, the MAX-DOAS instrument is presented in Section 7.1. The measurement techniques and instruments, which are used for the comparisons with the results obtained from MAX-DOAS, are introduced and described in Section 7.2. The latter Section deals only briefly with the properties of the complementary measurement techniques, since the main focus of this work is the MAX-DOAS technique. The interested reader is therefore referred to supplemental literature referenced at the corresponding place.

7.1 MAX-DOAS Instrument

The basic components of a MAX-DOAS instrument are the telescope and spectrometer. The telescope collects the scattered Sun light, which is then coupled into an optical fiber using appropriate optical elements. The optical fiber is connected to the spectrometer, which records the spectrum to be analyzed using DOAS. This simple principle of a MAX-DOAS instrument is one of its main advantages. It allows for the realization of robust and cost-effective instruments capable for autonomous measurements and therefore highly suitable for the integration in world wide measurement networks even at remote stations.

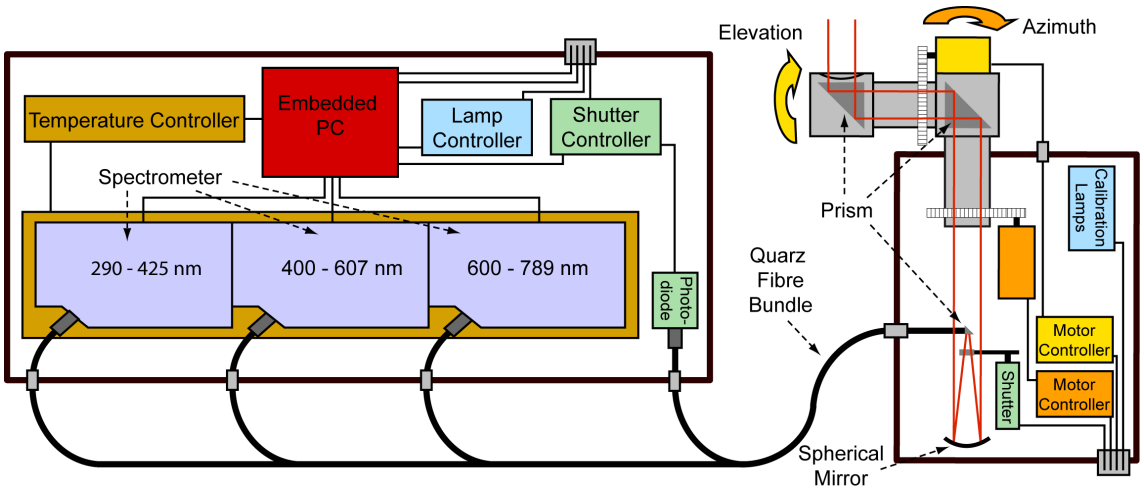

Figure 7.1: *Schematic drawing of the MAX-DOAS instrument: the spectrometer (left) and telescope unit (right)*

7.1.1 Instrumental Concept

MAX-DOAS instruments with the telescope and spectrometer integrated in one housing are well suited for measurements in the field, since the compact design allows for easy transportation. Additionally, the hardware requirements can be fulfilled with low power consumption devices, which enables measurements using rechargeable batteries without the need for a local power supply. However, reliable MAX-DOAS measurements require a high degree of stability for the spectrometer and detector temperature. Any changes in the optical properties of the spectrometer caused by a temperature drift have a negative influence on the DOAS retrieval quality when not accounted for thoroughly. Thus, situations can occur, when e.g. the ambient temperature is relatively high and the instrument is not appropriately shielded against direct illumination by the Sun, in which the temperature of the spectrometer can not be regulated accurately although the temperature control is efficient. An additional limitation of the single housing design is the available space for the integration of instrument components such as an additional spectrometer for the extension of the observable wavelength range.

The MAX-DOAS instrument developed in this work consists of a separate spectrometer and telescope unit to overcome the above mentioned limitations. A schematic drawing of the instrument is shown in Figure 7.1. The spectrometer unit contains three miniature spectrometers, since the instrument is aimed to cover a wide wavelength range with an high spectral resolution. The telescope unit is designed to allow for varying the elevation angle as well as the azimuth angle of the viewing direction without moving the housing as a whole. Figure 7.2 contains photographs of the instrument showing the inner workings of the units. Both units are connected via an optical quartz fiber bundle. During the field operation, the telescope unit is mounted outdoors, while the spectrometer unit is positioned indoors under stable conditions, guarantying measurements unaffected by large ambient temperature

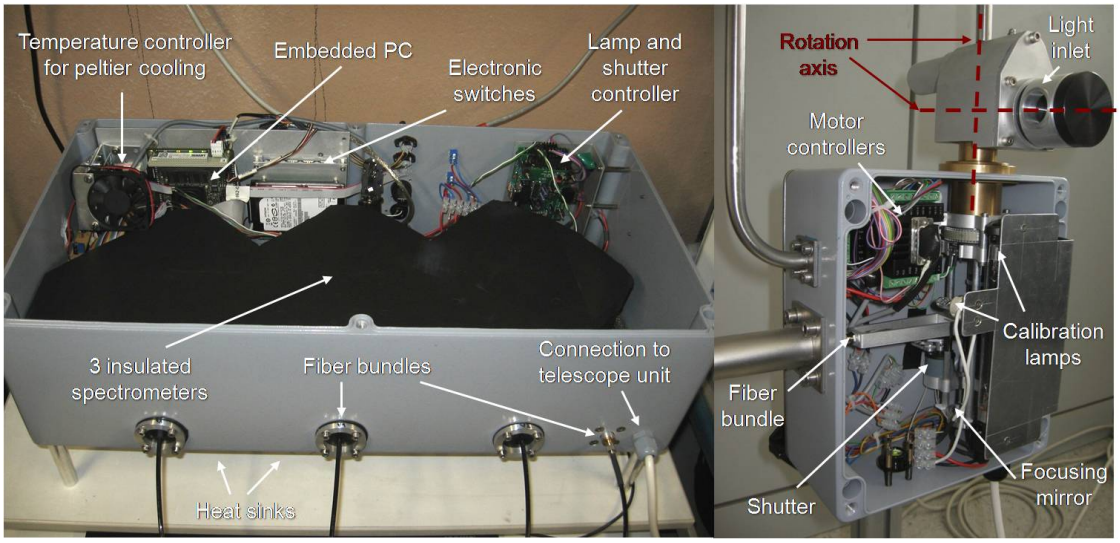

Figure 7.2: *Photograph of the MAX-DOAS instrument: the spectrometer (left) and telescope unit (right)*

variations possibly occurring outdoors. A typical field measurement setup of the instrument is depicted in Figure 7.3.

Telescope Unit

The design of the optical bench integrated in the telescope unit is based on the concept developed by Kern (2009). It is used in compact MAX-DOAS instruments designed and applied for the monitoring of gaseous volcanic emission within the European NOVAC project (Network for Observation of Volcanic and Atmospheric Change) (Galle et al., 2010).
In contrast to the NOVAC mark II instrument, which controls the azimuth angle of the viewing direction by moving the whole instrument, an additional top part was developed within this work, that carries out the movements necessary for the double axis viewing direction variation. The resulting rotation directions and axis for the azimuth and elevation angles are depicted in Figure 7.1 and 7.2, respectively. The top part configuration enables an easy dismantling for applications, where the azimuth angle is kept fixed and only the elevation angle is varied during the measurements. The entrance aperture has a diameter of 21 mm. The moving parts of the telescope optical bench contain two quartz prisms used for the 90° deflection of the incoming light. The 25 x 25 mm prisms were utilized instead of mirrors to avoid variable sensitivity to different directions of polarization. The red lines in Figure 7.1 indicate the light path and how the light is focused by the spherical concave mirror, which has a diameter of 25.4 mm and a focal length of 76.2 mm. The focused light is deflected by 90° using a miniature 3.5 x 2 mm quartz prism and coupled into a single quartz fiber of 1250 μm diameter. An FSMA coupling connects this fiber with the quartz fiber bundle, which transmits and distributes the light to the spectrometer unit.
The positioning of both rotation axes are maintained using Faulhaber© brushless

Figure 7.3: *Typical setup of the MAX-DOAS instrument: the telescope (left, outdoors) and spectrometer unit (right, indoors). The pictures were taken during the field campaign in Cabauw, the Netherlands in 2008*

DC servomotors with position encoders, which are controlled by Faulhaber© MCBL motor drivers. The rotation of the motors are transmitted to the azimuth and elevation axis by a gear wheel and drive belt combination with a transmission of 3:1 and 22:10, respectively. Additionally, the motors are equipped with a gear reduction of 592:1. Between the mirror and the miniature prism, a diffuser plate can be moved into the light path driven by a rotating solenoid for direct Sun light measurements. For spectrometer calibration and characterization, a mercury vapor and a halogen lamp are integrated in the telescope unit. The 20 x 30 x 11 cm aluminum pressure casting housing ensures IP67 conformity.

Spectrometer Unit

The spectrometer unit contains the three Ocean Optics© HR2000 spectrometer with a focal length of 101.6 mm at f/4 and an 100 μm entrance slit. The symmetrical crossed Czerny-Turner design of the optical bench is depicted in Figure 7.4. The first spectrometer for the ultra-violet covers the wavelength range of 290 - 425 nm using a 1800 groove/mm grating. The second and third spectrometer for the visible cover the wavelength ranges of 400 - 607 nm and 600 - 789 nm, both using a 1200 groove/mm grating. All spectrometers utilize the same type of linear CCD array, namely the Sony© ILX511 detector with 2048 pixel each sizing 14 x 200 μm. A cylinder lens attached on the detector maps the 1000 μm entrance slit height onto the 200 μm detector pixel height. The standard BK7 detector window of the ultra-

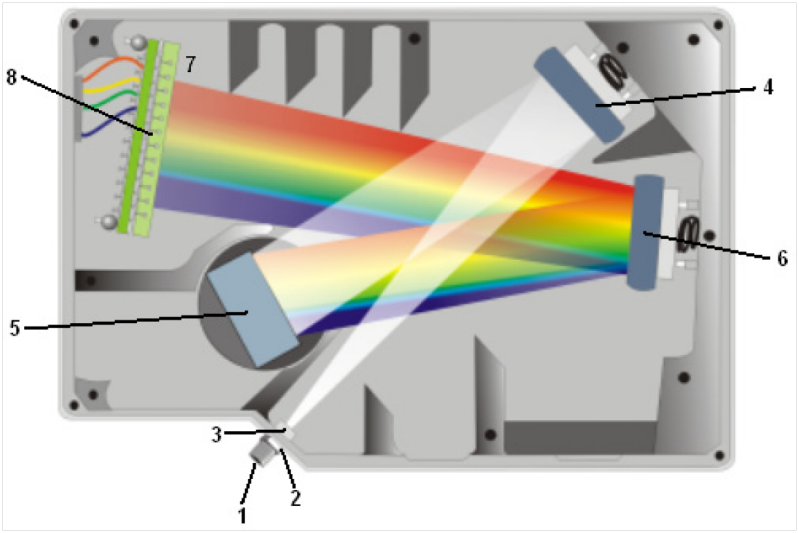

Figure 7.4: *Sketch of the Ocean Optics HR2000 spectrometer: (1) FSMA fiber connector; (2) entrance slit; (3) filter; (4) collimating mirror; (5) grating; (6) focusing mirror; (7) cylinder lens; (8) CCD detector*

violet spectrometer is replaced by a quartz window to enhance the sensitivity, which is relatively low compared to the visible wavelength range. The HR2000 spectrometers are equipped with a 12 bit A/D converter, an USB 1.1 and serial interface.
The spectrometers are each mounted on 40 x 40 x 3.8 mm thermoelectric Peltier modules. The other side of the modules are attached to heat sinks to dissipate excess heat. The SuperCool© PR-59 temperature controller regulates the temperature of the spectrometers by operating the thermoelectric modules using constant voltage pulse-width modulation. The spectrometers are insulated using Armaflax© foam.
The spectrometer unit is equipped with a Lippert© Cool Lite Runner 2 single board computer, which has the configuration of the PC/104 standard. It features an AMD© Geode GX 466 processor at 333 MHz. It has 256 MB working memory and utilizes an 80 GB 2.5" hard disk drive. The interfaces are four USB 2.0 and three serial ports, enabling the connection and control of all relevant devices of the instrument. The two 100 MBit Ethernet connections allow for the remote control of the instrument and the synchronization of system time.
The shutter and the lamps are controlled by a Mattronik© USB relay card. Additionally, the photo diode is connected to a HMT© transimpedance amplifier which controls the shutter to avoid spectrometer damages due to high intensities, e.g. in unintended direct Sun viewing geometry.

Fiber Bundle

The quartz fiber bundle for the optical connection of the telescope and spectrometer unit consist of seven individual 400 μm quartz glass fibers. The configuration, which enables the distribution of the light collected by the telescope to the individual spectrometer and photo diode, is sketched in Figure 7.5. The individual fibers of the bundle are arranged in a circular dense packing configuration at the end, which

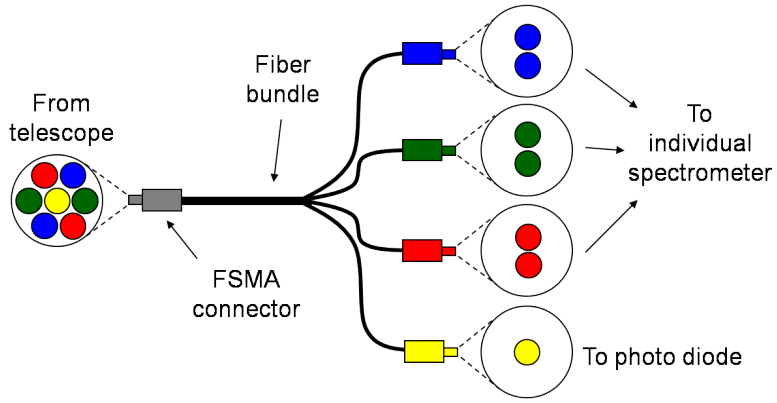

Figure 7.5: *Illustration of the fiber bundle configuration*

is connected via FSMA to the telescope unit. At this end, the optically relevant diameter of the fiber bundle is 1280 μm due to the 20 μm thick clading of the individual fibers. The bundle is divided into three bundles containing two individual fibers and one single fiber at the other end. The three bundles each consist of two fibers, which are located oppositely at the dense packing end, and are connected with the spectrometers, while the single fiber originating from the center position is connected to the photo diode. This configuration minimizes the differences in the field of view seen by the individual spectrometers. Each fiber of the bundle has a numerical aperture of 0.104 matching the f/# of the telescope as well as the spectrometers.

Measurement Program

The MAX-DOAS instrument is controlled by the single board PC embedded in the spectrometer unit. It operates using Windows© XP, which enables full functionality

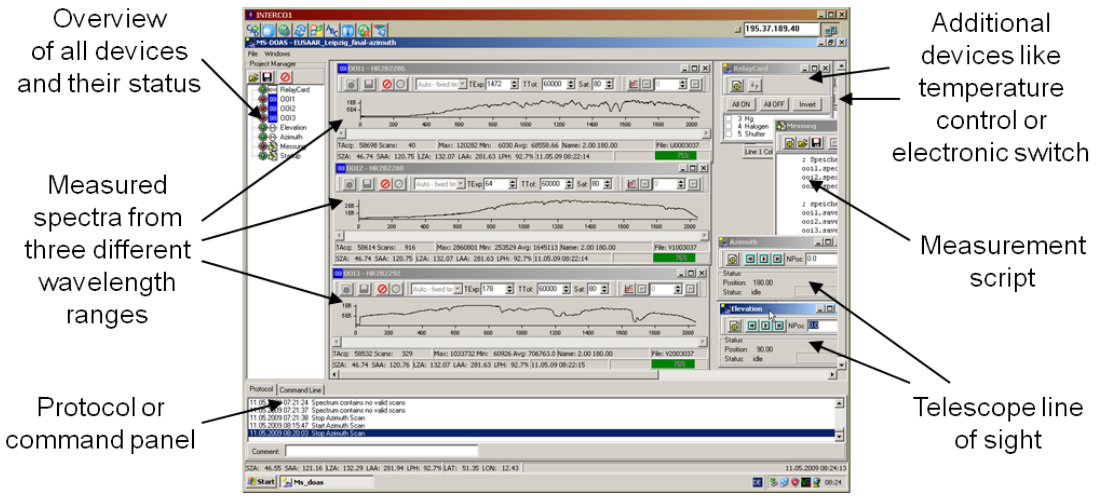

Figure 7.6: *Screenshot of the measurement program MS-DOAS*

known from desktop computers. The measurement program MS-DOAS was developed by Udo Frieß and is illustrated with a screenshot in Figure 7.6. The modular structured program allows for the simultaneous operation and synchronization of the three HR2000 spectrometers due to multitasking capability. The individual devices of the instrument are controlled using a script-based command module within the program. Thus, the measurement program and routine can be adapted and optimized according the properties of the instrument to be controlled. In combination with the embedded PC, the MS-DOAS program allows for fully automated MAX-DOAS measurements. The measurement program demonstrated its stable performance during long term measurements within this work.

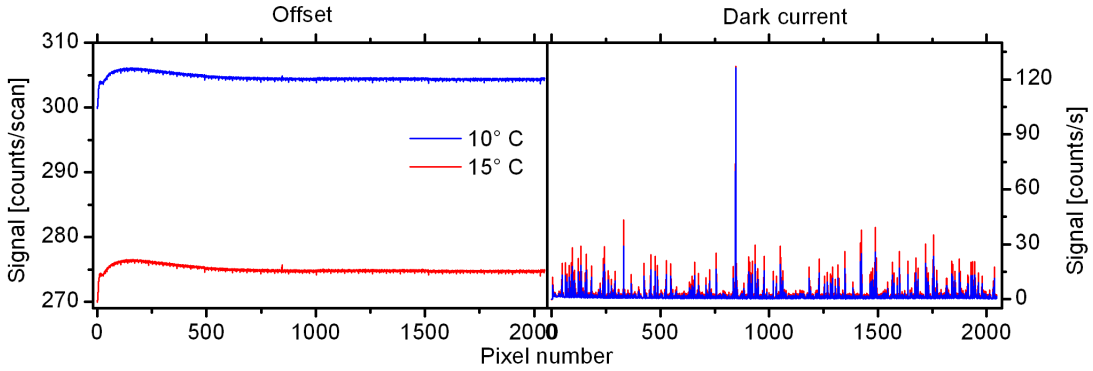

Figure 7.7: *Electronic offset (left) and dark current (right) signal of the HR2000 spectrometer at two different temperatures*

7.1.2 Instrument Characteristics

The MAX-DOAS instrument developed within this work is rather suited for the installation at measurement stations than for the employment during field measurement campaigns. The concept of the instrument of utilizing three spectrometers required the usage of a aluminum pressure casting housing for the spectrometer unit, due to its stability against deformation. Furthermore, the excess heat of the built-in electronics, mainly from the embedded PC and the temperature control unit, can effectively dissipate, since the housing serves as a large heat sink. To avoid additional heat sources within the spectrometer unit, an external 12 V power supply is utilized. The temperature regulation determines the main fraction of the total power consumption, which is low enough to integrate the instrument even at remote sites with limited power supply resources. The embedded PC consumes 8.5 W and the three HR2000 spectrometers consume in total 1.4 W. The movement of the telescope along the azimuth and elevation axis require a power consumption of 1.3 W each, including the motor controller electronics. The remaining electronic devices consume in total less than 1 W. The temperature regulation requires approximately 6.1 W per °C temperature difference to the ambient. Thus, the typical total power consumption of the instrument is approximately 75 W for a temperature difference of 10°C between spectrometer and ambient.

Electronic Offset and Dark Current

The A/D converter of the HR2000 spectrometer adds an artificial electronic offset signal to the measured spectrum in each scan. It serves for avoiding negative analog signals, which can occur due to detector noise but cannot be interpreted by the A/D converter. The left panel of Figure 7.7 shows the electronic offset signal at 10° and 15°C spectrometer temperature. The measured spectra have to be corrected for the electronic offset according to:

$$I_{corr}(n) = I(n) - \frac{N_{meas}}{N_{OS}} \cdot I_{OS}(n) \,, \tag{7.1}$$

where $I(n)$ and $I_{corr}(n)$ indicate the signal of pixel n before and after the correction, respectively. $I_{OS}(n)$ is the offset signal. N_{meas} and N_{OS} are the number of scans performed for recording the measured spectrum and offset signal, respectively. The electronic offset signal depends on the spectrometer and thus the electronics temperature as depicted in Figure 7.7. Therefore, the measured spectra have to be corrected for the offset of the according temperature. The measurement routine is programed to record the offset signal during night by measuring 10000 scans at minimal integration time, which is 3 ms.
The dark current signal is caused by thermal excitation in each individual pixel of the CCD detector. It is proportional to the Boltzmann factor: $I_{DC} \propto \exp(-\frac{\Delta E}{kT})$. Thus, the dark current increases with the temperature, which is shown in the right panel of Figure 7.7 for 10° and 15°C spectrometer temperature. The shown dark current signals are corrected for the offset signal and comprise a hot pixel, whose signal is in saturation due to endowment defects in the silicon semiconductor material of the detector. The measured spectra have to be corrected for the dark current according to:

$$I_{corr}(n) = I(n) - \frac{t_{meas}}{t_{DC}} \cdot I_{DC,corr}(n) \,, \tag{7.2}$$

where $I_{DC,corr}(n)$ is the dark current signal of pixel n and is corrected for the offset signal. Here, the weighting is applied with respect to the total integration times t_{meas} and t_{DC} of the measured spectrum and the dark current, respectively. The dark current is recorded also during night, but for one scan and 30000 ms integration time. The temperature of the detector should be as low as the temperature regulation allows for, to reduce the dark current signal. However, the utilized HR2000 spectrometers do not allow for the separate cooling of the CCD detector. Therefore, the spectrometers are temperature stabilized as a whole, which has also an effect on the instrument function (see below), since the optical components of these spectrometers are calibrated during room temperature conditions in the manufacturer's laboratories.

Wavelength Calibration and Instrument Function

The three spectrometers of the MAX-DOAS instrument cover the wavelength ranges of 290 - 425 nm, 400 - 607 nm and 600 - 789 nm, referred to as UV, Vis1 and Vis2, respectively. The spectral resolution of the individual spectrometers can be determined by recording emission lines of mercury and neon vapor lamps. The neon lamp

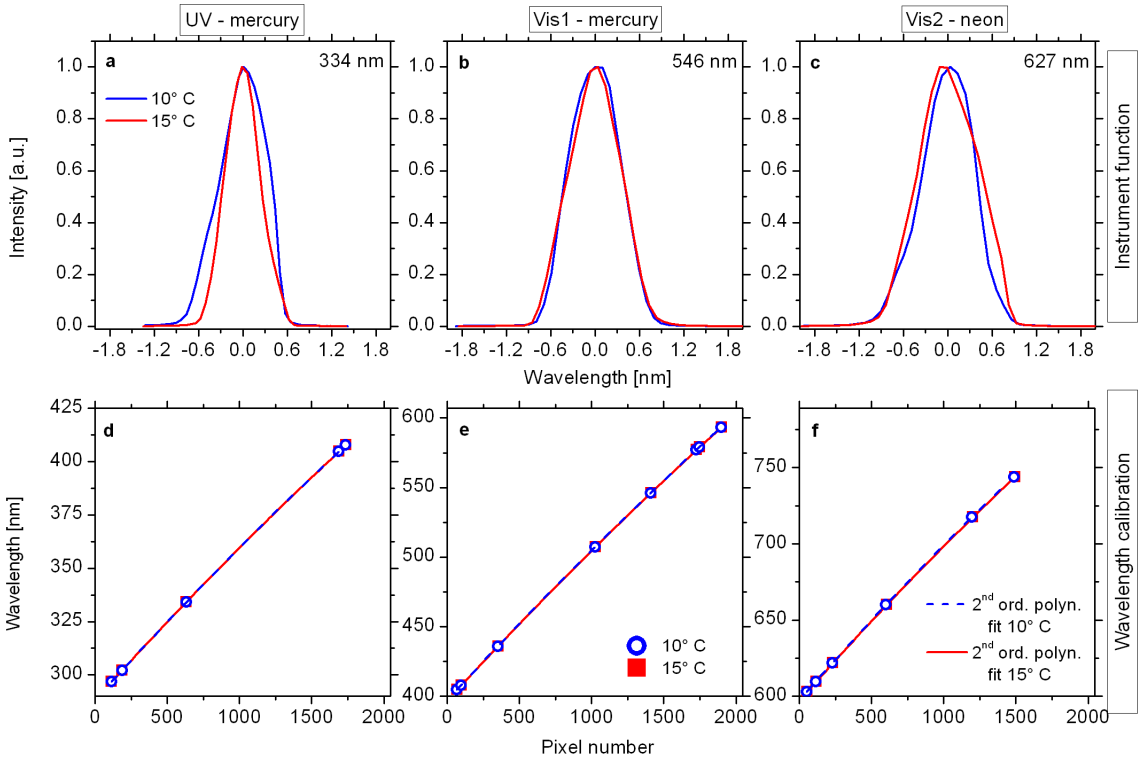

Figure 7.8: *Instrument functions at different wavelengths (a-c) and wavelength to pixal mapping (d-f) of the individual HR2000 spectrometers (UV, Vis1 and Vis2) recorded at two different temperatures. The symbols in the lower panels indicate the position of the mercury (d,e) and neon (f) emission lines, while the solid and dashed lines indicate the second order polynomial fit results.*

is necessary, since mercury only provides appropriate emission lines below approximately 580 nm. The individual lines allow for the determination of the wavelength dependent instrument functions as well as the calibration of the wavelength to pixel mapping of the according spectrometer. Figure 7.8a and 7.8b show the mapping of mercury emission lines at selected wavelengths onto the detector for two different temperatures recorded with the UV and Vis1 spectrometer, respectively. Figure 7.8c contains a selected neon emission line recorded with the Vis2 spectrometer. These instrument functions H depend on the wavelength as well as on the temperature and are used for the convolution of the high resolution trace gas absorption spectra from literature (see Section 3.2). The spectral resolution determined by the full width at half maximum (FWHM) of the instrument functions depicted in Figure 7.8 are listed in Table 7.1 for the according wavelengths and temperatures.
The wavelength to pixel mapping of the different spectrometers were determined by attributing several known mercury and neon emission line positions to the according pixel numbers. The wavelength calibration was retrieved by a second order polynomial fit on these points, since their relationship is non-linear for the HR2000 spectrometers. The wavelength to pixel mapping is temperature dependent and is shown in Figure 7.8a - 7.8c for the different spectrometers and two temperatures.
Since the offset, dark current, instrument function and wavelength calibration de-

Table 7.1: *FWHM of the instrument functions from Figure 7.8*

Spectro-meter	Position (nm)	Temperature (°C)	FWHM	
			(nm)	(pixel)
UV	334	10	0.74	11
		15	0.57	9
Vis1	546	10	0.81	8
		15	0.84	8
Vis2	627	10	0.82	9
		15	0.99	11

pend on the temperature, a reliable temperature regulation enabling an high degree of temperature stability is of crucial importance for MAX-DOAS instruments, since varying spectrometer properties would result in significant error in the spectral fit.

Signal to Noise Ratio

An example for the signal to noise ratio (SNR) of the utilized HR2000 spectrometers is shown in Figure 7.9. The determined SNR at the according total integration time was normalized with respect to the considered wavelength range. It was calculated from repeatedly recorded spectra of a diffuser plate illuminated by an halogen lamp. Two subsequent spectra of equal integration time were divided by each other and a high pass filter was applied to the ratio spectra. After taking the logarithm, the standard deviation in the according wavelength range was determined and divided by $\sqrt{2}$. Finally, the inverse was calculated and normalized with respect to the wavelength interval. The shown example refers to the analysis wavelength window of the 577 nm O_4 absorption band for a signal saturation of 80 % and two different spectrometer temperatures. Since photon noise is the dominating noise fraction and

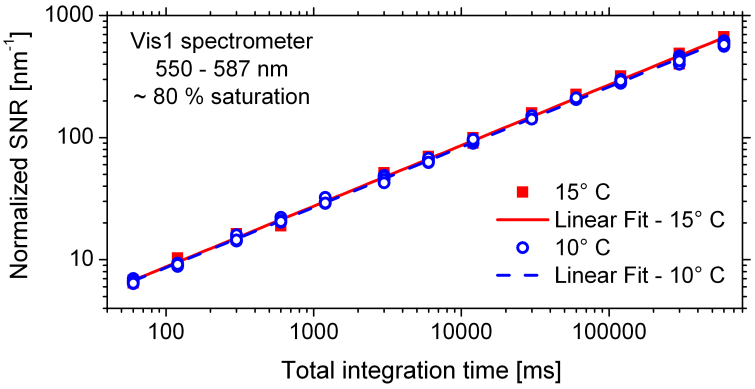

Figure 7.9: *Example for the signal to noise ratio of the HR2000 spectrometer, normalized according the considered wavelength range, as a function of the total integration time for two different temperatures. The solid and dashed line indicate the linear fit with a slope of 0.5.*

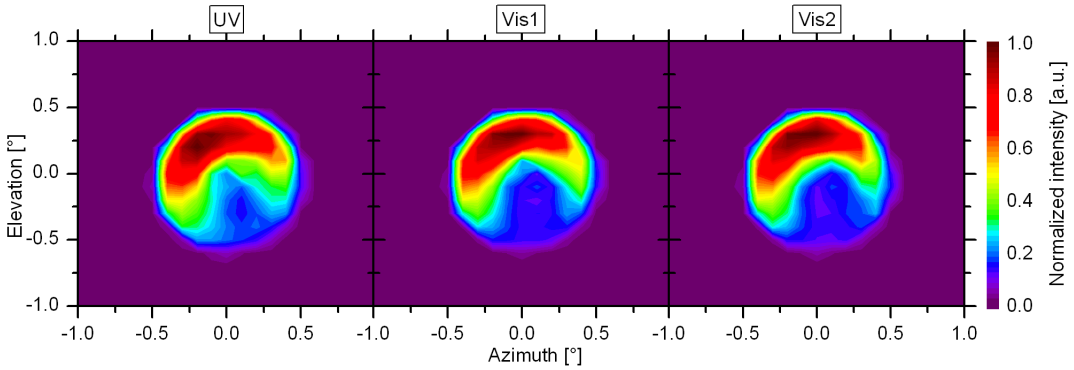

Figure 7.10: *Field of view for the individual spectrometers (UV, Vis1 and Vis2). The normalized intensity is plotted as a function of the azimuth and elevation angle of the viewing direction.*

the difference in the considered temperatures is relative small, the relationship between SNR and total integration time shows no remarkable differences between both temepratures.

Field of View

An halogen lamp setup in the laboratory at a distance of 5 m from the telescope aperture was utilized for the determination of the field of view (FOV). The lamp was scanned by recording spectra at short integration times. The azimuth angle of the telescope viewing direction was increased by steps of 0.1° while keeping the elevation angle constant. Afterwards, the elevation angle was reduced by 0.1° and the azimuth angle was scanned again. Subsequent repetitions of this procedure allowed for the mapping of the measured average intensities as a function of the viewing direction, which is used to quantify the field of view and depicted in Figure 7.10. The theoretical field of view α_{FOV} is defined by:

$$\alpha_{FOV} = 2 \cdot \arctan\left(\frac{D}{f}\right) , \tag{7.3}$$

where D is the entrance diameter of the single quartz fiber in the telescope unit and f is the focal length of the spherical mirror. The resulting theoretical α_{FOV} for the telescope is 0.9° which is in good agreement with the measured value of approximately 1.0°, apparent in Figure 7.10 for the different spectrometers. The areas of lower intensity appearing at equal viewing direction for all spectrometers is caused by the shadowing effect of the miniature prism and the single fiber guidance tube, which both are located in the light path. However, the similar intensity distributions in Figure 7.10 indicate, that the differences in the FOV of all spectrometers are small, which is achieved by utilizing the single fiber.

7.2 Complementary Dataset

The retrieval of atmospheric aerosol profiles is a relative new application of the MAX-DOAS technique (see Chapter 5). The validations of the retrieved profiles require independent observations by established aerosol measurement techniques. However, these established techniques comprise characteristic limitations depending on the utilized measurement principle, which has to be accounted for when comparing to MAX-DOAS observations. The retrieval of atmospheric trace gas profiles from MAX-DOAS requires the knowledge on the aerosol profile. With the newly explored capability of MAX-DOAS to derive the necessary information on aerosols from the measurements performed with the same instrument without further effort, the retrieval of trace gas profiles is possible without the need for independent aerosol measurements. However, the retrieved trace gas profiles from MAX-DOAS have to be validated with independent trace gas measurements.
The measurement techniques and instruments used for the comparison of the MAX-DOAS results in this work are described in the following.

7.2.1 Remote Sensing of Aerosols from the Ground

In the field of remote sensing of aerosols by ground based measurements, two different established measurement principles are widely applied, which can be divided into passive and active techniques. The passive ground based technique utilizes Sun photometers for the determination of aerosol optical properties of the total observed atmospheric column above the instrument. However, the information on the aerosol vertical distribution cannot be gained from Sun photometer measurements. For this purpose, an active technique is used, which is the lidar (light detection and ranging) technique and allows the determination of aerosol profiles.

Sun Photometer

The Sun photometer utilizes a radiometer measuring the spectral radiance from either the direct Sun or sky at discrete wavelengths using appropriate filters. Its detector measures voltages which are proportional to the radiance. By using high mountain Sun photometer measurements at the Mauna Loa Observatory in Hawaii for the estimated spectral radiance in terms of voltage at the top of the atmosphere, the total optical depth of the observed air mass is retrieved by applying the Lambert-Beer law. The aerosol optical depth (AOD) is then determined by subtracting the Rayleigh and trace gas optical depth from the total optical depth (Holben et al., 1998). The AOD measured at different wavelengths of the solar spectrum allow the retrieval of the Ångström exponent (Eck et al., 1999). Furthermore, the aerosol size distribution and absorption is determined from the Sun photometer measurements by applying inversion algorithms (Dubovik et al., 2000; Dubovik and King, 2000). However, the Sun photometer observations rely on absolute measurements, which requires regular calibration and maintenance of the instruments.
The AOD retrieved from MAX-DOAS measurements are compared to values measured by Cimel© Sun photometers of AERONET (Aerosol Robotic Network, http://aeronet.gsfc.nasa.gov/), which is a world wide network with standards for instru-

ments, calibration techniques, processing and data-distribution (Holben et al., 1998). Depending on the station, these instruments are equipped with filters for 380, 440, 500, 670, 870 and 1020 nm. The AERONET instruments perform measurements in intervals no longer than 15 min, except for cases when the direct view of the Sun is blocked by clouds. Thus, the absence of Sun photometer measurements at the according times can be used as a proxy for the presence of clouds (Kaufman and Koren, 2006).

Lidar

The lidar technique utilizes lasers, which send short collimated radiation pulses into the atmosphere. The time-resolved detection of intensity scattered back to the instrument allows the determination of the vertical structure along the direction of the emitted and received radiation, e.g., in the troposphere. Lidar instruments consist of an emitter, namely the laser, and a receiver. The optical axis of the receiver is generally tilted by a small angle off the vertical to allow for a geometrical overlap of the receiver field of view and the laser beam. The emitted laser pulses undergo extinction and scattering by air molecules and particles. The temporal distance between the time when the laser pulse was emitted and the time when the backscattered signal was detected allows the determination of the layer height at which the scattering occurred. The strength of the signal contains the information on the amount of back scattering air molecules and particles. For the determination of quantitative aerosol backscatter and extinction profiles from lidar measurements, the so called lidar equation has to be solved (see e.g., Ansmann and Müller, 2005). Several different types of lidar instruments have been developed up to now. The following two lidar instrument principles are used for the comparisons within this work.

The **ceilometer** and **elastic backscatter lidar** instruments emit laser radiation at only one wavelength. The detection of the backscattered signal is also limited to the single wavelength. Ceilometer instruments are mainly used to determine cloud base heights, but are limited in their capability to measure quantitative aerosol backscatter and extinction profiles (Heese et al., 2010). These instruments are commercially available and mainly deployed in meteorological measurement networks. In contrast, backscatter lidar instruments with a better signal to noise ratio allow the retrieval of aerosol backscatter and extinction profiles by applying several assumptions when solving the lidar equation. This is necessary since the lidar equation contains two unknown quantities, namely the particle backscatter and extinction, while only one signal is measured by the backscatter lidar. The assumption of an altitude independent particle extinction to backscatter ratio, the so-called lidar ratio, can be used for the retrieval of extinction profiles (Klett, 1981; Fernald, 1984). However, this assumption is generally not valid since the lidar ratio varies with altitude, which results in remarkable errors in the retrieved extinction profile (Sasano et al., 1985).

The **Raman lidar** instruments contain an additional receiver channel to detect the signal caused by inelastic Raman scattering by air molecules. This signal depends only on the aerosol extinction, in contrast to the elastic signal depending on both, the aerosol backscattering and extinction. Thus, the retrieval of the aerosol extinction profile without the assumption of the lidar ratio is possible (Ansmann et al.,

1990, 1992).
The aerosol extinction profiles retrieved from MAX-DOAS measurements are compared to profiles measured by two different ceilometers. A collocated Vaisala© LD40 ceilometer was used for the comparisons of the profiles measured during the field campaigns in Cabauw in 2009 and 2010. This ceilometer measures at the wavelength of 855 nm using an InGaAs laser diode (see Emeis et al. (2009) for details) and was operated by the Royal Netherlands Meteorological Institute (KNMI) in DeBilt, the Netherlands. The other ceilometer is a Jenoptik© CHM15K, which uses an diode-pumped neodymium-doped yttrium aluminum garnet (Nd:YAG) solid-state laser emitting at the wavelength of 1064 nm (see Flentje et al. (2010) for details) and was installed in Rheinstetten, Germany, and operated by the German Weather Service (DWD) in Hohenpeissenberg, Germany. The profiles measured by this ceilometer were regarded for the MAX-DOAS measurements in Heidelberg in 2010.
For the field campaign in Cabauw in 2008, the measurements of the HTRL backscatter lidar developed and operated by the Dutch National Institute for Public Health and the Environment (RIVM) in Bilthoven, the Netherlands, was used for the aerosol profile comparisons. This backscatter lidar is based on an Nd:YAG laser emitting at 1064 nm. During the field campaign in Ispra in 2009, collocated backscatter lidar measurements were performed by the European Commission Joint Research Center (EC-JRC) in Ispra, Italy. The Clouds and Aerosol Micropulse Lidar (CAML) instrument manufactured by Cimel© utilizes an Nd:YAG laser operating at 532 nm (see Barnaba et al. (2010) for details).
During the campaign in Cabauw in 2008, also collocated measurements with the Raman lidar CEALI (CESAR Water Vapour, Aerosol and Cloud Lidar) were performed. This instrument was developed and operated by RIVM. The utilized Nd:YAG laser emits at 355, 532 and 1064 nm and the additional receiver channels detect the Raman signals at 387 and 607 nm (see Apituley et al. (2009) for details). The German Leibniz Institute for Tropospheric Research (IFT) in Leipzig, Germany, developed and operated the Raman lidar POLLY (Portable Lidar System) during the field campaigns in Melpitz in 2008 and Leipzig in 2009. It emits at 355, 532 and 1064 nm using an Nd:YAG laser and receives also the additional Raman signals at 387 and 607 nm (see Baars et al. (2008); Althausen et al. (2009) for details).
The basic quantity measured by ceilometers and elastic backscatter lidars is the range corrected signal (RCS), which is the detected signal multiplied with the square of the signal altitude. The RCS is also corrected for the overlap function, which determines the height dependent overlap of the laser beam and receiver field of view. However, this correction requires the knowledge of the true overlap function, which is not always given. When the true overlap function cannot be determined for any reason, the correction is then applied using approximated overlap functions inducing uncertainties for obvious reasons. Only the further analysis of the RCS using the Fernald-Klett method allows the retrieval of aerosol backscatter and extinction profiles, which also contain uncertainties due to above mentioned necessary assumptions.
Since the Raman signal is very weak, daytime Raman lidar measurements can only be performed using high power laser systems to allow the unambiguous detection in

the presence of the sky light background. Such lasers are strongly limited in their applicability in mobile platforms, if not even unsuitable. Thus, the POLLY instrument, designed for mobile applications was operated as a backscatter lidar during the inter-comparison campaigns.
The aerosol extinction profiles from the POLLY and CAML instruments presented in this work were retrieved using the Fernald-Klett method. In contrast, the RCS of the LD40 ceilometer and the HTRL backscatter lidar were scaled using the AOD from Sun photometer measurements to convert in aerosol extinction profiles, which is a simple approximation of the Fernald-Klett method. The CEALI instrument was in an early stage of its development and performance assessment during the inter-comparison campaign. Therefore, the instrument potential was not fully available and the extinction profiles were determined using the same method as for the LD40 ceilometer and HTRL lidar.
The general limitation of lidar instruments is the missing overlap of laser beam and receiver field of view for the lowermost altitude range due to the measurement principle. This area, where lidars are blind, can reach altitudes up to several km, depending on the instrument design.
The solution of the lidar equation requires the knowledge of the actual temperature and pressure profile to account for the backscattering and extinction by air molecules appropriately. In cases where radiosonde measurements are not available, the estimations from in-situ measurements can induce uncertainties.

7.2.2 Ground Based In Situ Measurements

The results obtained from the MAX-DOAS measurements are also compared to in situ measurements of the aerosol extinction coefficient and trace gas concentration. The elements of the profiles retrieved from MAX-DOAS are representative for atmospheric layers of a certain extent, which is determined by the used altitude grid resolution. For the comparison to in situ measurements, the MAX-DOAS results for the lowermost altitude ranges are used. While the concentration of NO_2 can be measured in situ by one instrument, the aerosol extinction is determined by the combination of three independent measurement principles and thus instruments.

7.2.2.1 In Situ Measurements of the Aerosol Extinction

The aerosol extinction coefficient from in situ measurements is calculated as the sum of the aerosol scattering coefficient measured by a nephelometer and the aerosol absorption coefficient measured by an aethalometer and a multi angle absorption photometer (MAAP) (see, e.g. Barnaba et al., 2010; Zieger et al., 2011).

Commercial Nephelometer

One of the widely used nephelometer instrument is the TSI© 3563. It measures the aerosol scattering coefficient at 450, 550 and 700 nm. The measurement principle is based on the detection of light scattered in the sampled air containing the particles. The scattered light of the Lambertian light source is integrated by the detector over the sensing volume. The use of a shutter system allows also the measurement

of the backscattering coefficient. Nephelometers have to be calibrated using air or other gases with known Rayleigh scattering coefficients. The measured aerosol scattering coefficients are derived after the correction for the Rayleigh scattering occurring in the probed air. Furthermore, several instrument specific corrections have to be applied, one of which being the truncation correction. It is necessary, since the nephelometer misses certain scattering angles due to the optical integration (Anderson and Ogren, 1998).

Humidified Nephelometer

Following the recommendation of the Global Atmospheric Watch (GAW) programme of the World Meteorological Organisation (WMO) the nephelometer measurements are applied to dried air to allow the comparability of the aerosol scattering measurements performed at different stations (WMO/GAW, 2003). However, the drying of the sampled air results in changes in the scattering properties of the particles due to the loss of the aggregated water. To account for this effect and to quantify the scattering enhancement due to the hygroscopic growth of the aerosol particles, humidified nephelometers were developed (see, e.g Zieger et al., 2010; Fierz-Schmidhauser et al., 2010). These instruments utilize special humidification systems consisting of an humidifying and drying unit, which is integrated in the air sample line before the nephelometer. This setup allows to control the relative humidity in the sampled air and to measure the scattering coefficient at these defined conditions. By varying the relative humidity over a wide range, the relationship between relative humidity and scattering enhancement can be determined and the measured scattering coefficient can be corrected for the according ambient relative humidity.

Aethalometer

The aerosol absorption coefficient is measured with an Aethalometer. A commonly used instrument is the Magee© AE-31, which measures at 370, 470, 520, 590, 660, 880 and 950 nm. The working principle of this instrument is to draw a known amount of particle laden air through a filter and measure the decrease of light transmission in time. One well-known effect of this method is, that filter-based measurement reads changes in the transmission that are not caused by absorbing particles but by e.g. multiple scattering of the light beam at the filter fibers, light scattering effects of the particles and reduced sensitivity when the particle load becomes substantial. The latter effect is referred to as the loading effect. To account for all these unwanted responses of the Aethalometer, correction methods were developed (e.g., Weingartner et al., 2003; Virkkula et al., 2007; Collaud Coen et al., 2010). However, these corrections seem not to be sufficient (Müller et al., 2011).

Multi Angle Absorption Photometer

The multi angle absorption photometer (MAAP) like e.g. the Thermo Scientific© model 5012 also measures the aerosol absorption coefficient. The basic principle of the MAAP is similar to the aethalometer, but in addition to the transmission, reflection is measured and a radiation transfer code is used to obtain the absorption

coefficient. Studies using generated aerosol particles showed, that MAAP absorption measurements agreed closely with reference absorption measurements (Sheridan et al., 2005).

The in situ measured aerosol extinction coefficients used for the comparisons for the field campaign in Cabauw in 2008 were retrieved by the Netherlands Organization for Applied Scientific Research (TNO) from a combination of aethalometer, MAAP and nephelometer measurements in Cabauw. The absorption coefficients were derived by converting MAAP measurements to the according wavelength using the Ångström exponent of absorption determined with the aethalometer. The aethalometer measurements were corrected according to Virkkula et al. (2007) for the loading effect, which minimizes the uncertainties in the Ångström exponent of absorption. The nephelometer scattering coefficient measurements were truncation corrected according to Anderson and Ogren (1998). Furthermore, scattering enhancement factors determined with an humidified nephelometer aboard an airplane (Morgan et al., 2010) were used to account for the ambient relative humidity in the measured scattering coefficients.
The in situ measurements in Ispra in 2009 were performed by EC-JRC and calculated in a similar manner. However, the absorption coefficients were determined using only aethalometer measurements, which were corrected for loading and multiple scattering according to Schmid et al. (2006). The scattering coefficients were measured with a nephelometer and corrected for truncation (Anderson and Ogren, 1998), while the ambient relative humidity was not taken into account.
During the CINDI campaign and the following field campaign in Cabauw in 2009 and 2010, collocated humidified nephelometer measurements were performed by the Swiss Paul Scheerer Institue (PSI), Villingen. The aerosol extinction coefficients were calculated using additionally the absorption coefficient derived from MAAP and aethalometer measurements performed by TNO and RIVM, respectively. The detailed description of the humidified nephelometer and the data analysis is given in Zieger et al. (2011).

The direct comparison of the MAX-DOAS results to in situ measurements is accompanied by discrepancies due to the differences in the probed airmass. While in situ measurements are point-like, the airmass probed by MAX-DOAS can extend over several kilometers. Furthermore, the values retrieved from MAX-DOAS are representative for the altitude range from the surface up to several hundred meters and are assumed to be constant in this range. Thus, gradients in the vertical distribution can result in additional discrepancies.

7.2.2.2 In Situ NO_2 Measurements

The Dutch National Institute for Public Health and Environment in Bilthoven operates a national network equipped with instruments for the in situ measurement of NO_2. The deployed instruments are chemiluminescence monitors equipped with photolytic converters (Kley and McFarland, 1980). The NO_2 measurements from a station in close vicinity of the Cabauw site are used for the comparison with the results from the MAX-DOAS retrievals.

7.2.3 Satellite Trace Gas Observations

The tropospheric vertical column densities of NO_2 calculated by integrating the profiles retrieved from MAX-DOAS are compared to tropospheric NO_2 VCD values retrieved from passive DOAS observations aboard different satellite instruments. These comparisons are made for the field campaigns in Cabauw. The satellite data was provided by KNMI (http://www.temis.nl/airpollution/no2.html).

The Scanning Imaging Absorption Spectrometer for Atmospheric Chartography (**SCIAMACHY**)is part of the atmospheric chemistry payload aboard the European Space Agency's (ESA) Environmental Satellite (ENVISAT), which was launched in March 2002. Its spectrometer covers the ultra-violet to near-infrared wavelength range. The spatial resolution in nadir is approximately 30 by 240 km. The details of the tropospheric NO_2 VCD retrieval algorithm for the nadir viewing observations are described in Boersma et al. (2004).

The Ozone Monitoring Instrument (**OMI**) is the Dutch-Finnish ultra-violet and visible spectrometer on the EOS-Aura satellite of the American National Aeronautics and Space Administration (NASA). Aura was launched in July 2004. The tropospheric NO_2 vertical column densities are retrieved using nadir observations. The dimensions of the ground pixels are 13 - 26 km along track and 24 - 128 km across track depending on the satellite viewing angle. The details of the retrieval algorithm are described in Boersma et al. (2007, 2011). From 25 June 2007 onwards, OMI has been affected by a number of so-called row anomalies that appear as signal suppressions in the radiance spectra for particular satellite viewing angles over the complete illuminated orbit. The origin of these anomalies is currently unknown. Thus, data from rows affected by the anomalies are excluded for the comparisons in this work.

The Global Ozone Monitoring Experiment 2 (**GOME-2**) aboard the MetOp-A satellite of ESA is the first of a series of three identical instruments. MetOp-A was launched in October 2006. The tropospheric NO_2 vertical column densities are retrieved using nadir observations of the ultra-violet and visible spectrometer. With a pixel size of 80 by 40 km, GOME-2 observes about 4 times smaller ground pixels than its predecessor GOME on ERS-2. The retrieval algorithm is described in detail in Boersma et al. (2004).

For the studies in the context of the detection of the volcanic plume of the Eyjafjallajokull volcano over Heidelberg by MAX-DOAS, the retrievals of SO_2 from measurements of the GOME-2 instrument are considered, which were provided by Christoph Hörmann (Max Planck Institute for Chemistry, Mainz, Germany). For the SO_2 retrieval, the wavelength range of 312.1–324 nm was used. Besides a cross section for SO_2 (Bogumil et al., 2003), a O_3 cross section (Gür et al., 2005), the individual Sun Mean Reference Spectrum (SMR) from GOME-2 for each regarded day (containing no atmospheric absorptions), the Ring spectrum (calculated from the SMR) and the inverse SMR spectrum were included into the fitting process (the inverse SMR spectrum should compensate the effects of possible spectrograph stray-light). Since the atmospheric light paths within the selected fitting window

change systematically with wavelength (e.g., Van Roozendael et al., 2006), not only the original ozone absorption cross section but also a second one (the original cross section scaled with a fourth order polynomial in wavelength) was included. A fifth order polynomial was applied to remove the broad-band structures and a shift was allowed for the measured spectra. Additionally, for the O_3 references a first order stretch was applied.
In order to correct the resulting column densities for a possible offset (mainly caused by the spectral interference with ozone and/or imperfect fitting of the ring effect), the data has been normalized by using the results from a 2-dimensional linear fit of third degree to all pixels where the SO_2 geometrical vertical column density does not exceed 2σ (and therefore are supposed to be not part of a possible volcanic plume). This correction process was only applied to a pre-selected region of interest (38°W–15°E; 35°–72°N), covering Iceland and most parts of Europe.

7.2.4 Total Sky Imager

For the estimation of the cloud cover conditions during the measurements in Cabauw, the observations of the YES© Total Sky Imager Model 440 installed at the site is used. It captures images from the sky using a solid state CCD imaging camera that looks downward on a heated hemispherical mirror. The mirror images the hemisphere over the instrument into the camera lens. A shadow band attached on the rotating mirror blocks the intensive direct solar radiation. The raw color image is analyzed for fractional cloud cover, using a sophisticated image-analysis algorithm, which determines the fraction of opaque and thin clouds within the image.

7.2.5 Transport Model FLEXPART

During the MAX-DOAS measurements in Heidelberg in 2010, the volcanic plume of the Eyjafjallajokull eruption in Iceland was detected by the observation of elevated SO_2 slant column densities. For the comparison with the MAX-DOAS SO_2 measurements, model predictions are used for the estimation of the vertical and horizontal distribution evolution of the Eyjafjallajokull volcanic plume. The Lagrangian particle dispersion model FLEXPART developed at the Norwegian Institute for Air Research (NILU, Stohl et al., 2005) was used to simulate the horizontal distribution of the volcanic plume after the eruption. Furthermore, the vertical distribution as well as the column of the particles of volcanic origin were simulated for the location of Heidelberg. Since the model considers the particle transport, the simulations for the comparison with MAX-DOAS SO_2 measurements were performed regarding only small particles, which serve as a proxy for SO_2 emitted by the volcano (Stohl et al., 2011).

Chapter 8

Field Campaigns

Several intercomparison campaigns were performed within a joint research activity on the development of aerosol retrieval algorithms from MAX-DOAS measurements of the European EUSAAR project. The aim of these campaigns was the development and validation of the newly developed MAX-DOAS instrument (Section 7.1) and the methods for the retrieval of aerosol and trace gas profiles from MAX-DOAS measurements (Chapter 6). The main focus of the EUSAAR project was the integration of atmospheric aerosol measurements performed at 20 European ground-based stations. The integration was aimed to contribute to a sustainable aerosol data base, which provides reliable support for atmospheric research issues. The intercomparison campaigns were performed at several sites in Europe involved in the EUSAAR project. Most of the sites are equipped with a number of instruments measuring atmospheric aerosol properties and are located in urban, rural and background areas. The results of the intercomparison campaigns are presented in this Chapter. The extinction profiles of atmospheric aerosols retrieved from MAX-DOAS O_4 and intensity measurements are compared to results obtained from established aerosol measuring instruments, i.e. in situ and remote sensing techniques. In addition, NO_2 profiles retrieved from MAX-DOAS measurements are compared to in situ measurements as well as satellite observation. Furthermore, the observation of a highly diluted volcanic plume by MAX-DOAS measurements is presented.
The different measurement sites and their specific instrumental equipment are summarized in Section 8.1. Section 8.2 addresses the first field campaign in Cabauw in 2008. In this section, the comparisons between MAX-DOAS and the other techniques are carried out for different inversion methods, settings and parameters of the MAX-DOAS profile retrieval to identify their influence on the results. The MAX-DAOS measurements of the subsequent field campaigns were analyzed using standardized settings of the profile retrievals. The Sections 8.3 and 8.4 contain the results of the field campaigns in Melpitz and Ispra, respectively. The field campaigns in Leipzig and Cabauw in 2009 were performed in the framework of the EARLINET 2009 and CINDI campaigns, and are content of Section 8.5 and 8.6, respectively.
Finally, the long term measurements in Cabauw in 2009 and 2010 are presented in Section 8.7. In addition to these intercomparison campaigns, which were carried out within the EUSAAR project, MAX-DOAS measurements subsequently performed in Heidelberg in 2010 allowed for the successful detection of the highly diluted plume

Figure 8.1: *Overview of the measurement sites (source: Google Maps).*

of the Eyjafjallajokull volcano, which is discussed in Section 8.8.

8.1 Measurement Sites and Instrumentation

The intercomparison campaigns were carried out at sites located in Central Europe. These are Cabauw in The Netherlands, Melpitz and Leipzig in Germany and Ispra in Italy. The map in Figure 8.1 shows an overview of the measurement site locations. Table 8.1 summarizes the geographic positions of the sites and includes the periods of the different intercomparison campaigns.
The Cabauw Experimental Site for Atmospheric Research (CESAR) is operated by seven Dutch Research Institutes and Universities. The CESAR observatory is lo-

Table 8.1: *The measurement sites and the periods of the intercomparison campaigns.*

Site	Lat. N [°]	Lon. E [°]	Period
Cabauw	52.0	4.9	03.05. – 30.06.2008
Melpitz	51.5	12.9	21.05. – 09.07.2008
Ispra	45.8	8.6	11.12.2008 – 25.03.2009
Leipzig	51.4	12.4	08.05. – 29.05.2009
Cabauw	52.0	4.9	09.06.2009 – 12.04.2010

cated in the western part of the Netherlands in a polder at 0.7 m below average sea level. The nearby region is agricultural, and surface elevation changes are at most a few meters over 20 km. The closest city is Utrecht at about 19 km, while Amsterdam, The Hague and Rotterdam are farther away. Major highways pass the site at about 5 km to the East and 10 km to the North. The shortest distance to the North Sea is 44 km to the WNW.
During the first campaign in Cabauw in 2008, colocated remote sensing aerosol measurements with the CEALI Raman lidar, HTRL backscatter lidar and AERONET Sun photometer were performed. In situ measurements of the aerosol optical properties at the ground were made by a nephelometer, MAAP and aethalometer. During the campaigns in Cabauw in 2009 and 2010, the colocated lidar measurements were performed by the LD40 ceilometer, and the in situ aerosol measurements used humidified nephelometer, MAAP and aethalometer. Ground based in situ NO_2 measurements are routinely performed at the site in Cabauw using instruments equipped with photolytic converters. Furthermore, overpass data of the tropospheric NO_2 vertical column densities are available from different satellites, namely SCIAMACHY, OMI and GOME-2 for the Cabauw site (see Section 7.2).
For continuous measurements of atmospheric aerosols in the continental rural background, the Leibniz Institute for Tropospheric Research (IFT) in Leipzig operates a ground based research station, which is situated near the village Melpitz in the river Elbe valley at 87 m above sea level. A federal main road crosses the region in a minimum distance of 1.5 km in northern direction. The distance to Leipzig in the SW is 41 km. Leipzig is a large city with remarkable industrial settlement located at 112 m above sea level.
During the campaigns in Melpitz and Leipzig, colocated Raman lidar measurements were performed with the portable POLLY instrument, while AERONET Sun photometer measurements are only available for the Leipzig site (see Section 7.2).
The atmospheric research station of the Joint Research Center (JRC) in Ispra is located at 225 m above sea level, and is situated in a semi-rural area, at the edge of one of the most polluted regions in Europe, namely the Po valley. Large pollution sources are located at distances larger than 20 km, while the distance between Ispra and the Alpine chain is ≈ 100 km.
The CAML backscatter lidar and AERONET Sun photometer were installed in Ispra during the intercomparison campaigns. In addition, in situ measurements of aerosol optical properties were performed using a nephelometer and aethalometer (see Section 7.2).

8.2 Cabauw 2008

Figure 8.2 shows the areal view for the measurement site in Cabauw. The large cities of Amsterdam, The Hague, Rotterdam and Utrecht are located at distances of about 45, 45, 31 and 19 km to Cabauw, respectively. The MAX-DOAS measurements within the scope of the first intercomparison campaign in Cabauw were performed from 3 May to 30 June 2008. During the first half of this period the EU-CAARI Intensive Observation Period campaign tool place in Cabauw. The newly developed MAX-DOAS instrument provides a two dimensional scanning capability

Figure 8.2: *Areal view for the measurement site in Cabauw (source: Google Maps).*

of the viewing geometry, and the measurements were performed for a constant relative azimuth angle. The telescope was set to follow the solar azimuthal position with a difference of 30° in the course of the day. Since the surrounding of the measurement site is characterized by a agricultural and rural topography, the field of view of the instrument was not disturbed remarkably by obstacles. The telescope unit of the MAX-DOAS instrument was installed on the roof of a remote cabin, while the spectrometer unit was setup indoors. However, additional instrumentation installed on the cabin roof obstructed the field of view for smaller elevation angles during to two time periods, namely between 5:00 and 6:45 UT as well as 9:15 and 10:15 UT. The measurements during these period were therefore neglected in the profile retrievals. The elevation angles were set to values of 2°, 5°, 10°, 20° and 90° for one measurement sequence, which was repeated consecutively for solar zenith angles below 90°. In addition to these elevation scans, azimuthal scans were performed once per hour, in which the relative azimuth angle was set to values of ±5°, ±6°, ±8°, ±10°, ±15°, ±20°, ±30°, ±45°, ±60°, ±75°, ±90°, ±100°, ±120°, ±150° and 180°. During these azimuth scans, the elevation angle of the viewing direction was chosen to point to 5° below the solar elevation angle. The azimuth scans were carried out to explore the capability of MAX-DOAS O_4 and intensity measurements to provide information on the aerosol phase function and single scattering albedo (Section 6.1.2). To avoid damaging the instrument by direct sunlight, measurements in the solar almucantar and at smaller relative azimuth angle, which would have a larger information content with respect to the aerosol phase function owing to the dominating forward scattering of aerosols (Dubovik and King, 2000), were not performed. The total integration times per measurement during the elevation scans were set to 60 s for solar zenith angles (SZA) less then 80° and 120 s for

SZAs greater 80°. The total integration times during the azimuth scans were set to 5 s.

8.2.1 Comparison of the O_4 and Intensity Measurements to Simulations Using Independent Aerosol Data

During the period from 6 May to 11 May 2008, persistent meteorological conditions with a high-pressure system over the northern part of Europe caused cloud free conditions over Cabauw. The measurements during these days are very well suited to validate the used radiative transfer model and to explore the capabilities of the profile inversion method in combination with real measurements.
To test the capabilities of the radiative transfer model, the MAX-DOAS O_4 and intensity measurements were simulated with the radiative transfer model SCIATRAN 2 for the period from 7 May to 10 May 2008 using independent aerosol measurements. Aerosol backscatter profiles measured by the CEALI Raman lidar were combined with Sun photometer measurements of the aerosol optical depth (AOD) τ_M, Ångström exponent α_M, single scattering albedo ω_0 and the asymmetry parameter for the Henyey-Greenstein parametrization of the aerosol phase function g. The basic quantity measured by the lidar instrument is referred to as the range corrected signal (RCS) and was provided by Arnoud Apituley (Dutch National Institute for Public Health and the Environment (RIVM), personal communication). The RCS was converted to aerosol extinction profiles $\epsilon_M(z)$ using a scaling factor determined by the Sun photometer AOD measurements. Thereby, the integrated $\epsilon_M(z)$ along the height was constrained to match the AOD at the according wavelength of the simulation. Since the lidar instrument is blind for the lowermost altitude ranges, the RCS at altitudes around 400 m were adapted for the altitudes below. Thus, possible gradients within this range are not considered. Furthermore, the profiles of ω_0 and g were assumed to be constant with altitude in the radiative transfer calculations.
The absolute values of the O_4 absorption cross section obtained from laboratory measurements by Greenblatt et al. (1990) and Hermans (2002) were reported to differ from observations by MAX-DOAS measurements in the literature (e.g., Wagner et al., 2009; Clémer et al., 2010). The laboratory measurements were found to be smaller than the values retrieved from the atmospheric measurements. Thus, a scaling factor was proposed to account for the difference of $\approx 25\,\%$. To identify the influence of this uncertainty in the O_4 absorption cross section, the simulations of the measurements were performed using different scaling factors. Thereby, the values of 1.0, 1.125 and 1.25 were applied for the scaling of the O_4 absorption cross section. An additional simulation using a surface albedo of 0.3 instead of 0.05 was performed to determine the influence on the simulated measurement.
Figure 8.3 shows correlation plots of the measured and simulated differential O_4 optical densities (ΔOD) and relative intensities at 360, 477, 577 and 630 nm. In these comparisons, only the data of the elevation scans, but not of the azimuth scans, are considered. Panels (a)–(f) in Figure 8.3 show comparisons for different scaling factors, while the surface albedo of 0.05 is equal for these three cases. Measured and simulated relative intensities are in very good agreement and show no remarkable differences for different scaling factors, while the correlation of the O_4 ΔODs is best

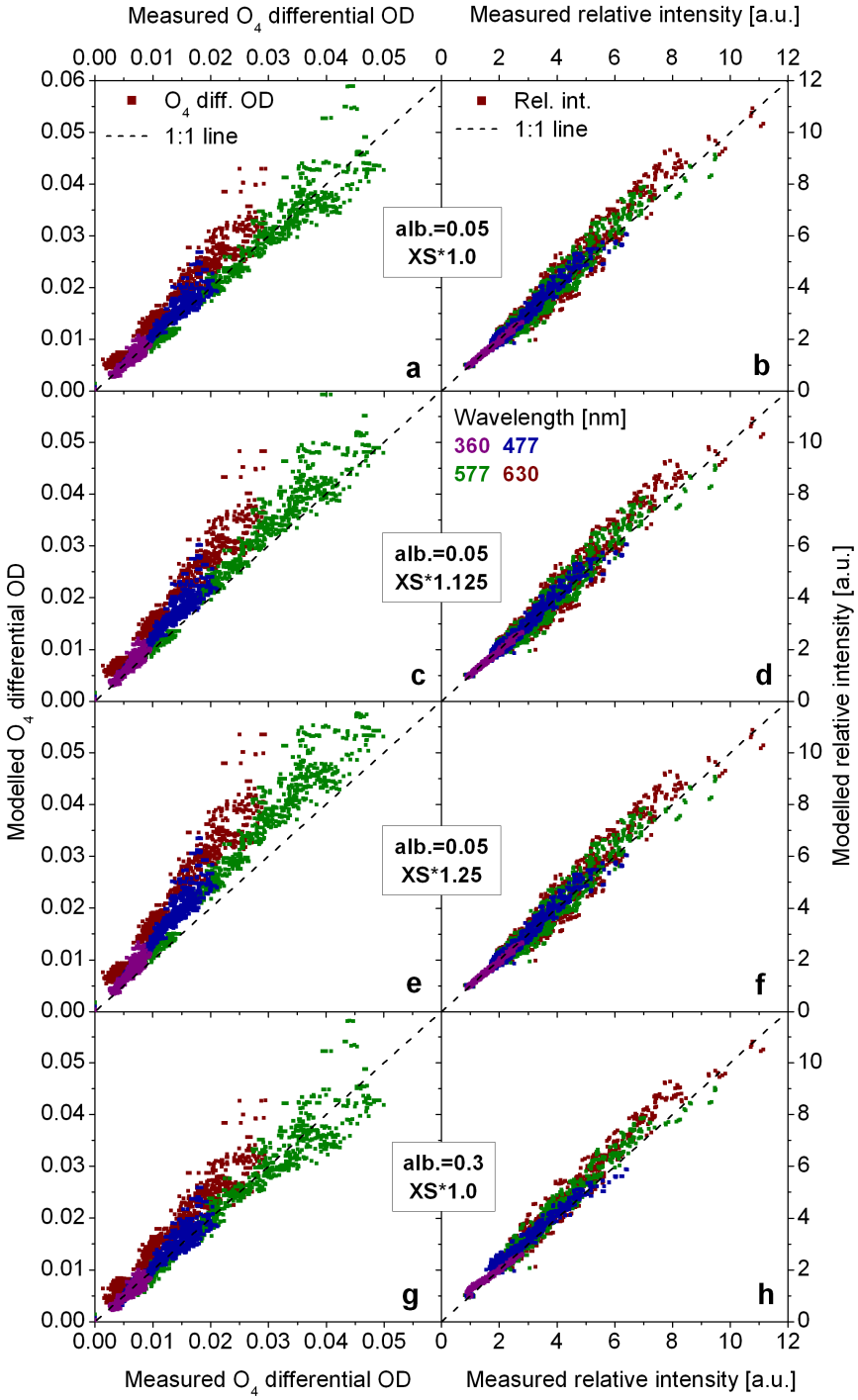

Figure 8.3: *Correlation of measured and simulated O_4 ΔODs (left panels) and relative intensities (right panels) at four wavelengths indicated by different colors. Only the data of the elevation scans from 7 May to 10 May 2008 are considered for different model settings: (a,b) surface albedo of 0.05 and scaling factor for the O_4 absorption cross-section (XS) of 1.0, (c,d) 0.05 and 1.125, (e,f) 0.05 and 1.25 and (g,h) 0.3 and 1.0, respectively.*

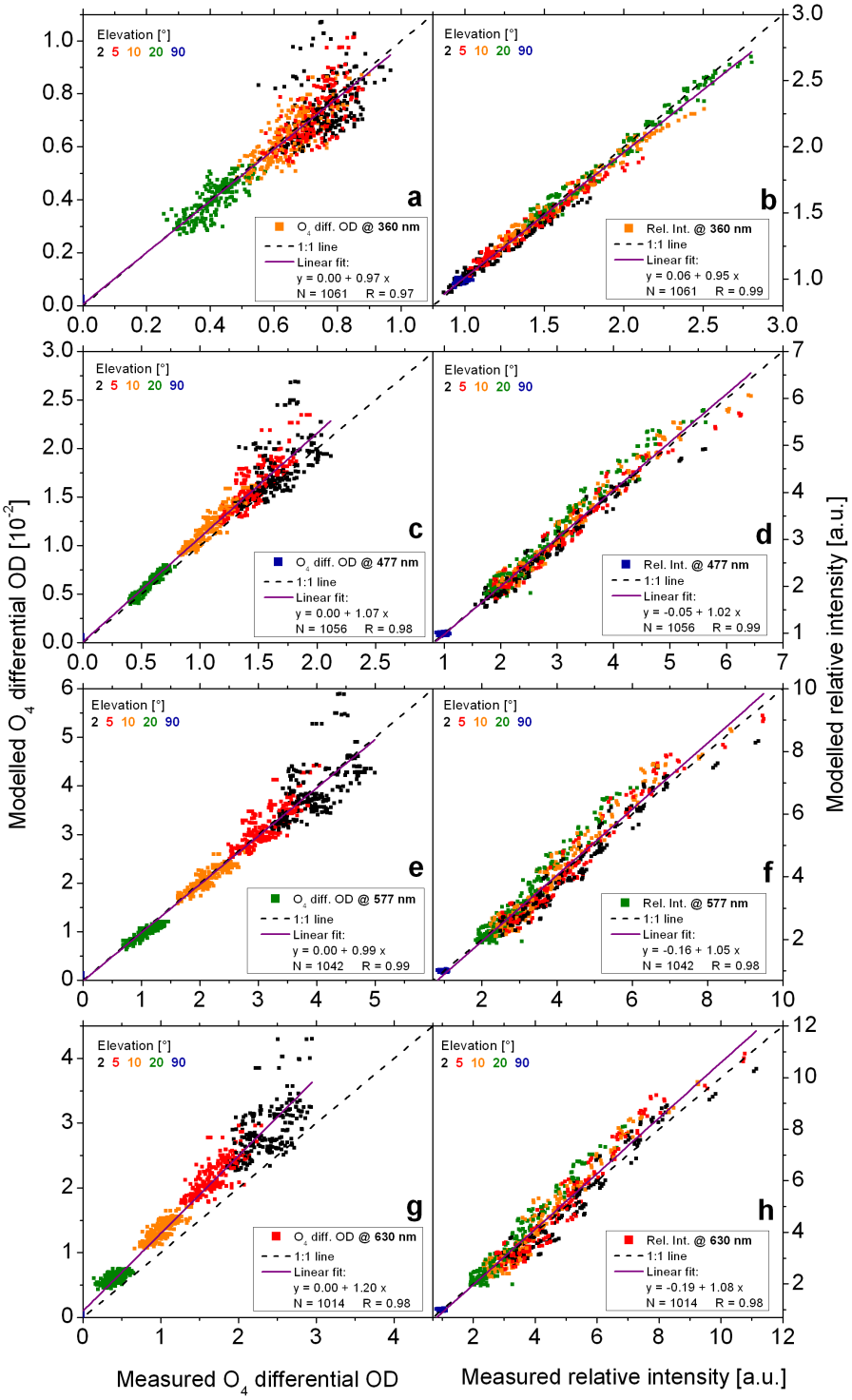

Figure 8.4: *Correlation of measured and simulated O_4 ΔODs (left panels) and relative intensities (right panels) color-coded according the elevation angle, for (a,b) 360, (c,d) 477, (e,f) 577 and (g,h) 630 nm (data from panel (a) and (b) of Figure 8.3). The purple lines indicate the results of the linear regression.*

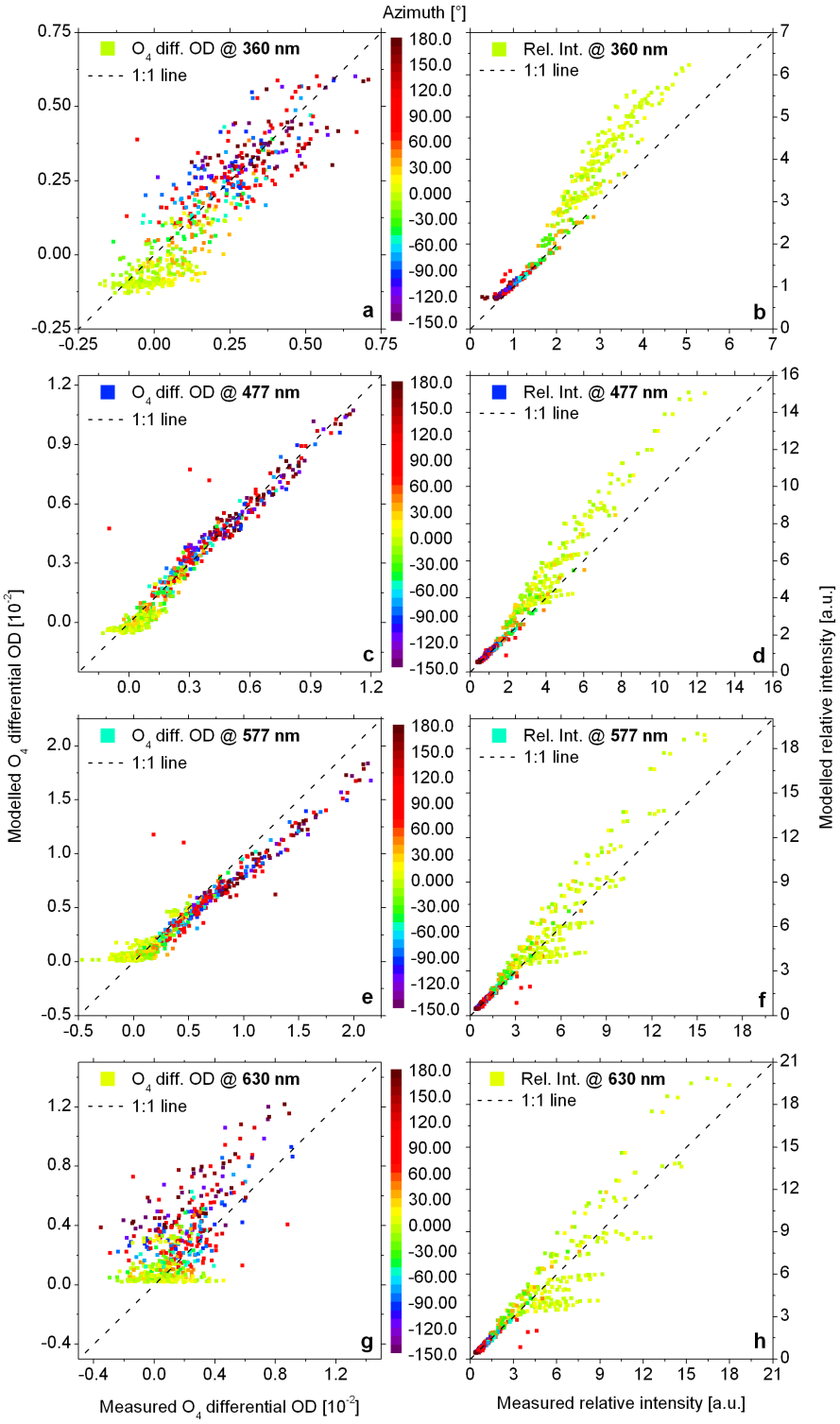

Figure 8.5: *Correlation of measured and simulated O_4 ΔODs (left panels) and relative intensities (right panels) color-coded according to the azimuth angle for (a,b) 360, (c,d) 477, (e,f) 577 and (g,h) 630 nm. Only the data of the azimuth scans from 7 May to 10 May 2008 are considered.*

for a scaling factor of 1.0 and degrades for increasing scaling factors by means of an increasing overestimation of the modeled values. The temperature dependence of the O_4 absorption cross section could be the reason, why the better agreement in this case is observed when the scaling factor is avoided, which is in contrast to the reported findings of the above mentioned studies. Panels (g) and (h) show the comparisons for a scaling factor of 1.0 and a surface albedo of 0.3. In this case, the modeled and measured O_4 ΔODs correlate well, while the modeled intensities are systematically smaller/larger than the measurements.
The same data as in Figures 8.3a and 8.3b are plotted in Figure 8.4, but this time each panel shows data from individual wavelengths, and color coded with the elevation angle. The comparisons of both O_4 ΔOD and relative intensity are generally in very good agreements. While the correlation of the relative intensity at 360 nm shows the lowest level of scatter compared to the intensities at the other wavelengths, the opposite is valid for the 360 nm O_4 ΔODs, which is due to the limited instrumental performance in the ultra-violet. The correlations of the O_4 ΔODs at all wavelengths feature an increased scatter for smaller elevation angles, which is most probably due to the missing knowledge on the true aerosol profiles at the lowermost altitudes. The linear regression of the 630 nm O_4 ΔODs has the largest deviation in the slope from the optimal value of 1.0. The most probable reason is the difficulty in the spectral retrieval to adequately remove the absorption features of H_2O and O_2 in this wavelength range, leading to an underestimation of the 630 nm O_4 ΔODs compared to the modeled values.
The comparisons of the O_4 ΔODs and relative intensities retrieved from the azimuth scans are depicted in Figure 8.5. The different panels contain the correlation plots separated according the wavelengths and color coded with the relative azimuth angle. The scatter in the correlation of the 360 nm O_4 ΔODs is higher compared to the correlations of the 477 and 577 nm ΔODs, which can also be attributed to the instrumental limitations in the ultra-violet, even more for the relative short integration times of the azimuth scans. While the 477 nm ΔODs show the best correlations compared to the ΔODs at the other wavelengths, the measured 577 nm ΔODs tend to be higher than the modeled values for larger relative azimuth angles. The 630 nm ΔODs show a rather less correlated relationship between the measured and modeled values. Similar to the correlation of the elevation scans, the measured ΔODs are smaller than modeled. Significant deviations from a linear relationship in the correlation plots of the relative intensities can be identified for all wavelengths. While the modeled and measured relative intensities agree well for large azimuth angles, their comparison for relative azimuth angles between -20° and 20° show remarkable structured differences. Possible reasons could be a height dependent g, which was assumed to be constant in the calculations, and increasing uncertainties for these geometries in the radiative transfer model, which applies several numerical approximations. These discrepancies between measured and modeled relative intensities for small relative azimuth angles hamper the application of the inversion method to retrieve ω_0 and g from the MAX-DOAS azimuth scanning measurements.

The simulation studies show that the radiative transfer model is capable to reproduce the measurement with a very good agreement. The best agreement was found when

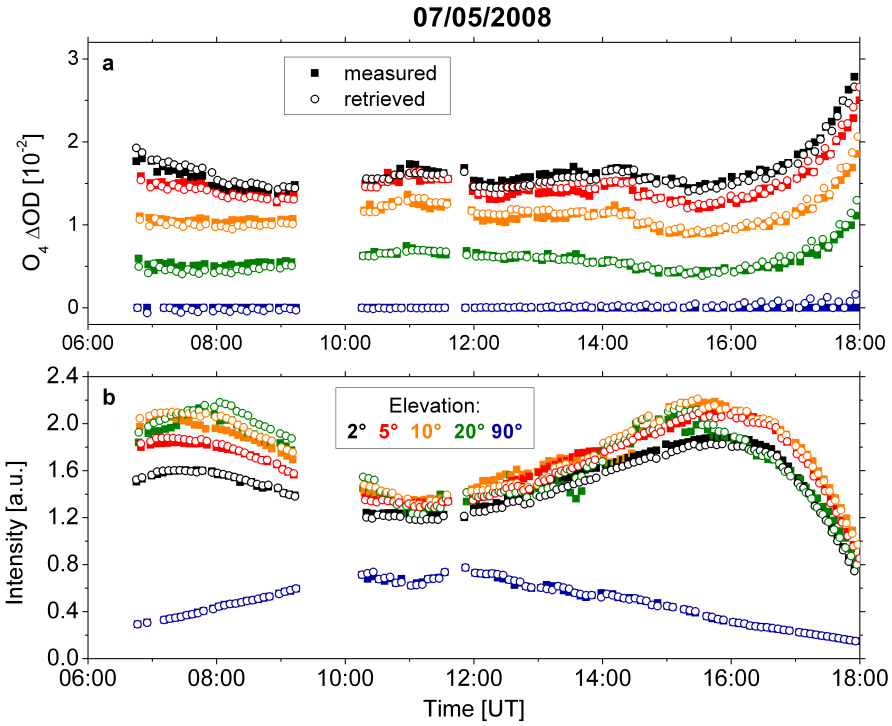

Figure 8.6: *Retrieved and measured (a) O_4 ΔODs and (b) intensities at 477 nm for the aerosol profile retrievals from MAX-DOAS measurements on 7 May 2008.*

using the O_4 absorption cross section as published without applying a correction factor and using a realistic surface albedo. The simulation of the O_4 measurements at 630 nm indicate uncertainties induced by inaccurate spectral retrievals in the according wavelength range (see Section 3.6.2). The observed discrepancies between simulated and measured relative intensities of the azimuth scans prevent the retrieval of ω_0 and g from the MAX-DOAS measurements (see Section 6.1.2).

8.2.2 Retrieval of Aerosol Extinction Profiles and Optical Depths

The results of the aerosol extinction profile and optical depth retrievals from the MAX-DOAS measurements are presented in this section. First, the results retrieved from MAX-DOAS using the optimal estimation method are compared to the observations of the established techniques. The cloudless conditions during the period from 6 to 11 May 2008 allowed to investigate the performance of the retrieval without the disturbing influence of clouds. After this first overview on the capabilities of the results retrieved from MAX-DOAS O_4 and intensity measurements, the influence of selected retrieval settings and parameters on the comparisons are explored. Subsequently, the comparison of the results retrieved using the optimal estimation method is extended over the whole field campaign period. Finally, the parameterized profile retrieval using optimal estimation as well as the full profile retrieval using the regularization method are applied for the cloudless period and the performance

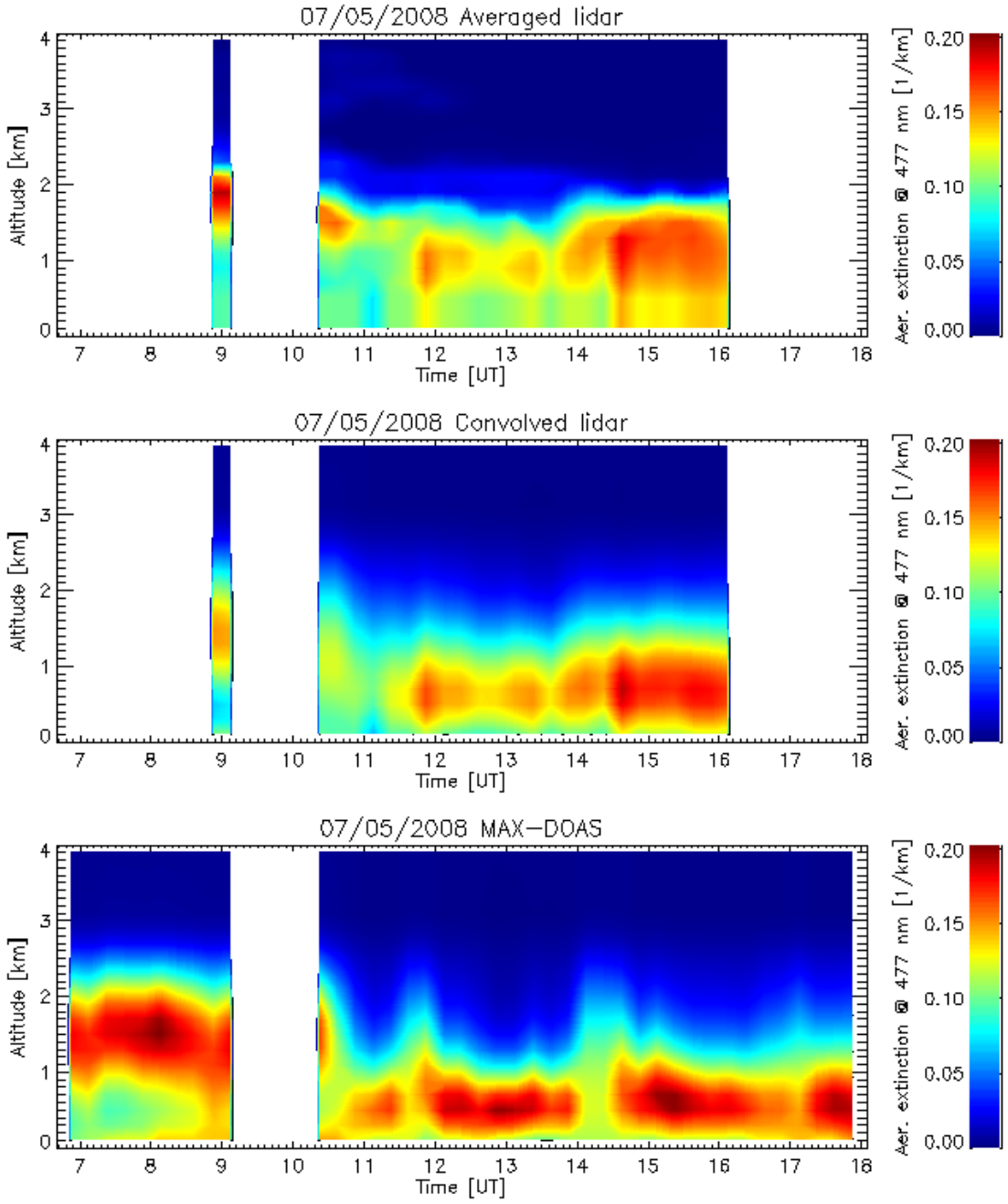

Figure 8.7: *Comparison of $\epsilon_M(z)$ at 477 nm retrieved from lidar and MAX-DOAS for 7 May 2008: (top) averaged profiles from lidar, (center) profiles from lidar convolved with the AVK of the MAX-DOAS retrieval and (bottom) profiles from MAX-DOAS.*

of the different retrieval approaches is compared.
Figure 8.6 shows an example for the retrieved and measured O_4 ΔODs and intensities at 477 nm resulting from the aerosol profile retrieval for 7 May 2008. The retrieved and measured quantities are in very good agreement. Figures 8.7 – 8.10 show the comparison of $\epsilon_M(z)$ retrieved from MAX-DOAS and the CEALI instrument for

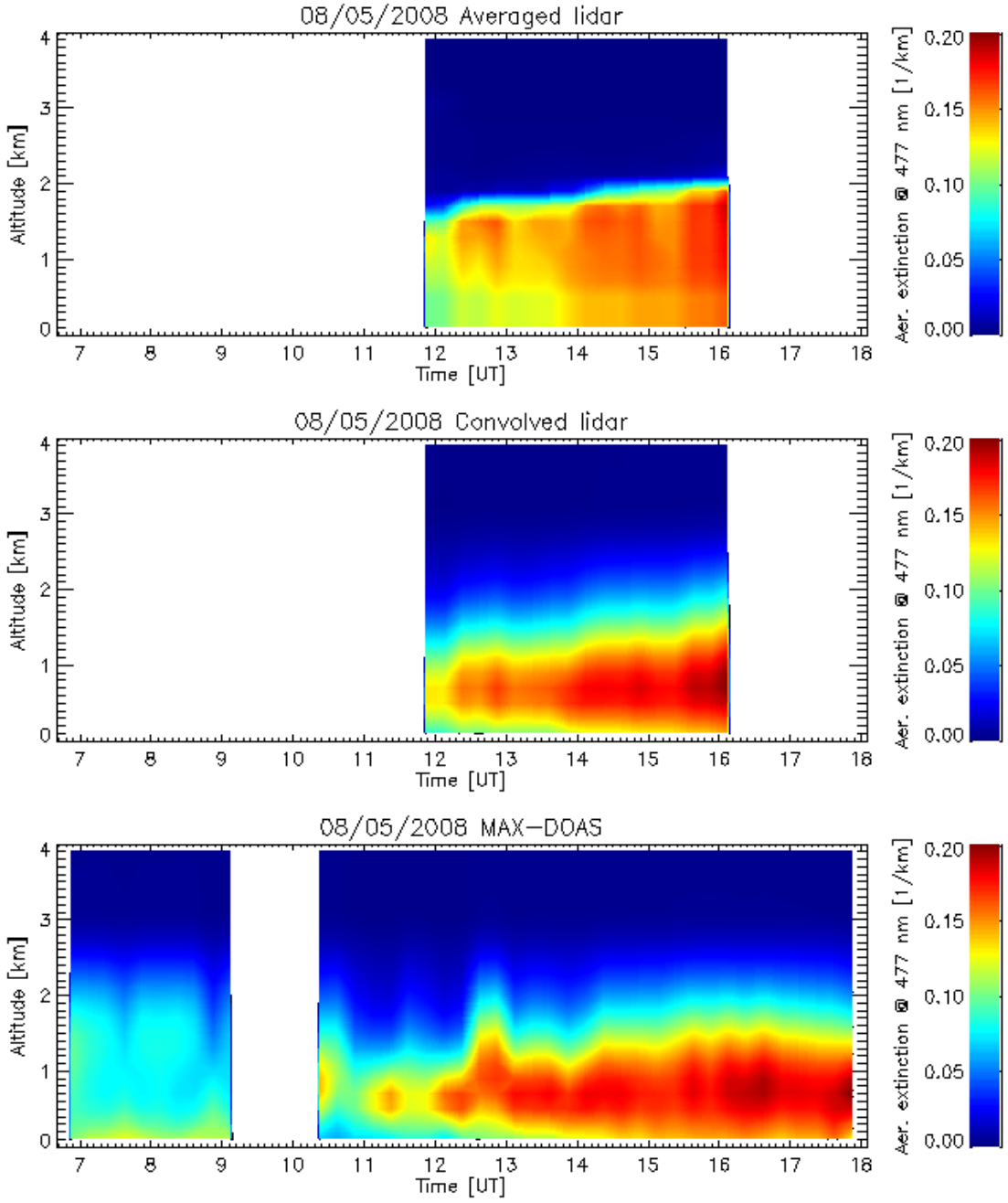

Figure 8.8: *Same as Figure 8.7 but for 8 May 2008.*

the period of 7 to 10 May 2008. The upper panels show the diurnal development of $\epsilon_M(z)$ measured by the lidar. These profiles were determined from the RCS as described in Section 8.2.1. Since the lidar provides a high resolution with respect to time and height (11 s and 7.5 m, respectively), the profiles were averaged according the height grid as well as the temporal resolution of the MAX-DOAS retrieval. The center panels contain the plots of the lidar profiles, which were convolved according to equation (6.2) with the averaging kernel (AVK) of the MAX-DOAS retrieval. The bottom panels show the profiles retrieved from the MAX-DOAS O_4 ΔOD and

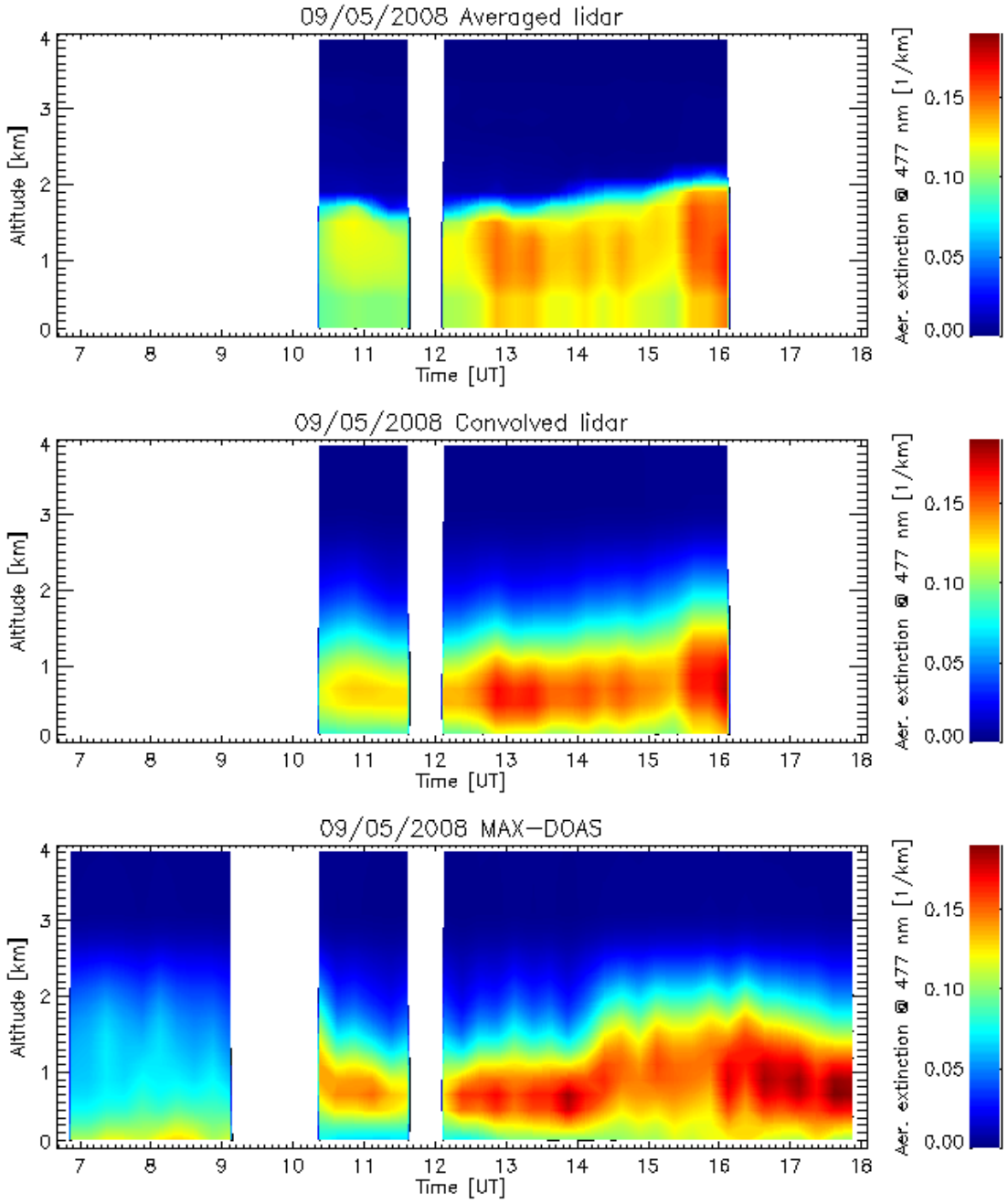

Figure 8.9: *Same as Figure 8.7 but for 9 May 2008.*

relative intensity measurements of the elevation scans at 477 nm. The inversion was performed using the optimal estimation method (see Section 5.6.1). The retrievals were performed using settings, which will be referred to as standard settings in the following. These standard settings were applied for all aerosol profile retrievals presented in this work for the different campaigns. An exception is Section 8.2.2.1, where the sensitivities of the aerosol profile retrievals to changes in the settings and parameters of the standard settings are tested. Any differences in the applied retrieval settings to the standard settings are pointed out where relevant.

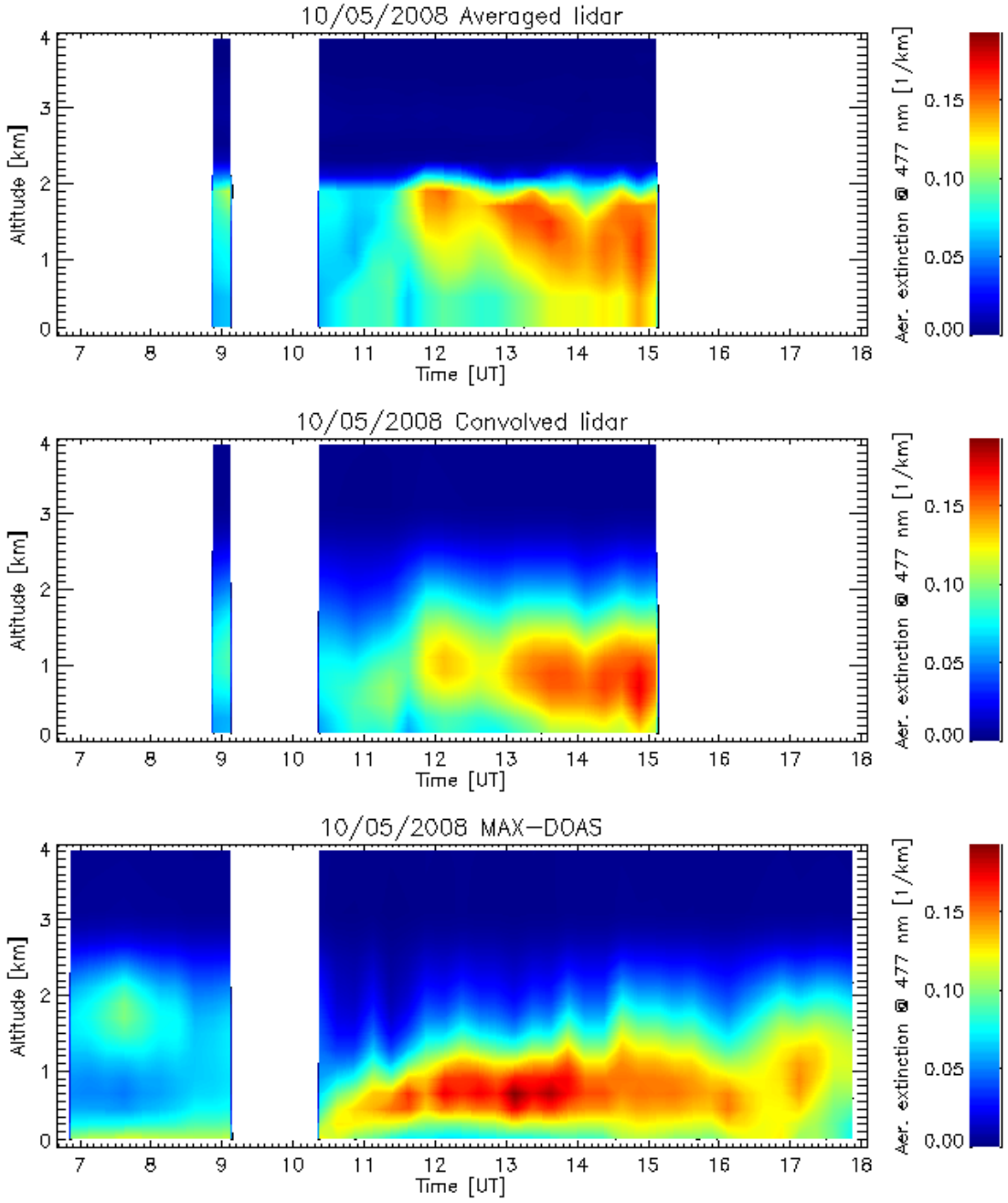

Figure 8.10: *Same as Figure 8.7 but for 10 May 2008.*

The **standard settings** of the aerosol profile retrievals are:

- A height grid with a resolution of 200 m was used.
- Due to the findings in Section 8.2.1, the O_4 absorption cross section was not corrected with a scaling factor.
- The surface albedo of 0.05 was assumed due to the findings in Section 8.2.1.
- The profiles of pressure, temperature and trace gases were adapted from the climatological data base (see Section 4.4.2).

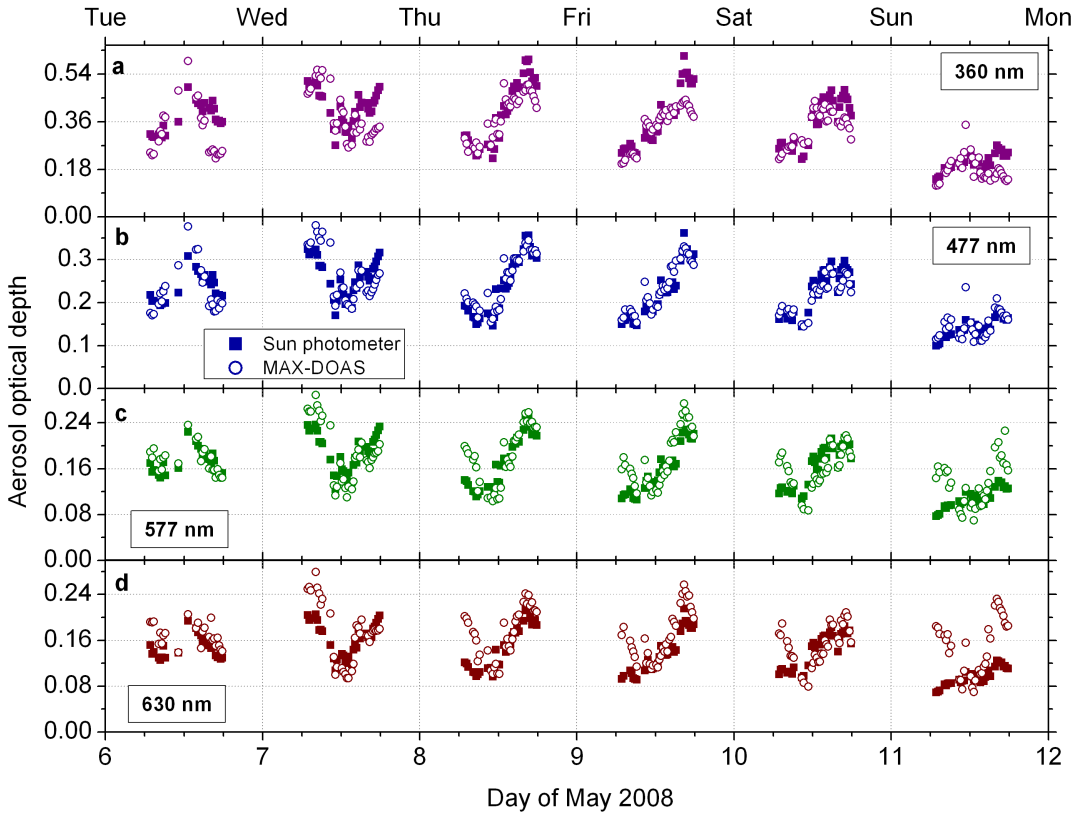

Figure 8.11: *Time series of the AOD retrieved from MAX-DOAS (open circles) and Sun photometer (solid squares) at (a) 360, (b) 477, (c) 577 and (d) 630 nm for the period of 6 to 11 May 2008 .*

- The aerosol optical parameters ω_0 and g were adapted from AERONET Sun photometer measurements (see Section 7.2.1). Thereby, coincident measurements of these values were used as far as available and daily or monthly averages otherwise.

- The weighting functions of the retrievals were calculated for the a priori profile for each retrieval sequence and used throughout the iteration sequence.

- A linearly decreasing a priori profile was used with a surface aerosol extinction of 0.1 km^{-1} and a height of 3 km (see Figure 6.2). The error of the a priori profile was set 100 %

- The O_4 ΔODs and relative intensities at 477 nm were used as measurement vector unless stated otherwise.

For better comparability, the color code in the different contour plot panels in Figures 8.7 – 8.10 for the individual days cover the same range of $\epsilon_M(z)$ values. The profiles measured by lidar and retrieved from MAX-DOAS show generally a very good agreement for the considered period. The temporal changes in $\epsilon_M(z)$ reflect the diurnal development of the boundary layer. In the morning hours of 7 May, an increased aerosol load localized at altitudes around 1.8 km is present in the residual

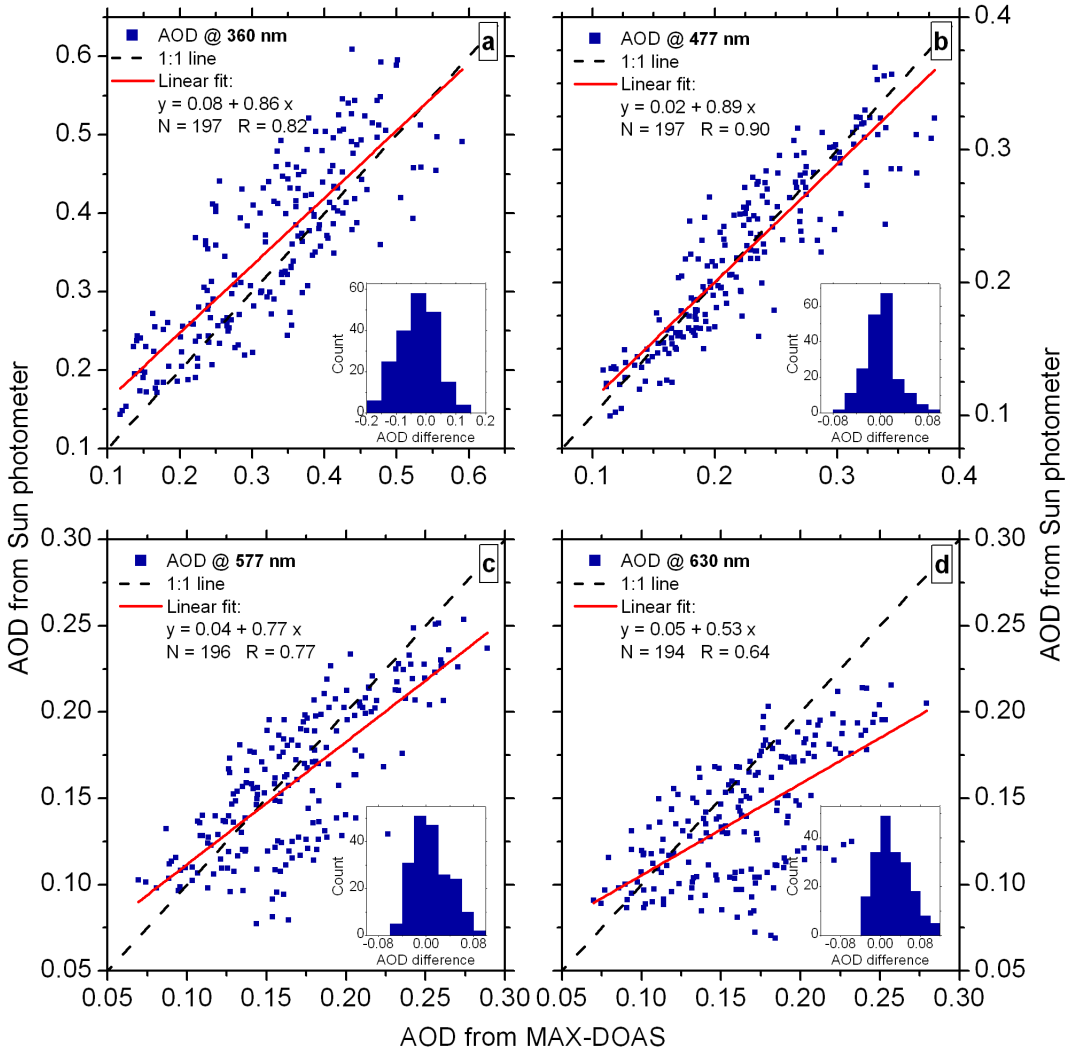

Figure 8.12: *Correlation of the AOD retrieved from MAX-DOAS and Sun photometer at (a) 360, (b) 477, (c) 577 and (d) 630 nm for the period of 6 to 11 May 2008. The one to one line is indicated in dashed black and the linear regression in red. The implemented histograms show the frequency of the differences in the AOD.*

layer as observed by lidar (upper panel of Figure 8.7). The comparison with the convolved lidar profiles shows, that this elevated aerosol layer is well reproduced by the MAX-DOAS retrieval with respect to its height and vertical extent. Between 10:00 and 11:00 UT, increased heating of the lowermost air masses by the surface results in an increase in the mixing layer height, which is well reproduced by the MAX-DOAS retrieval. Furthermore, the higher aerosol load in the afternoon and the height of the boundary layer apparent in the profiles retrieved from MAX-DOAS are in very good agreement with the convolved lidar profiles. The comparison of the profiles for 8 and 9 May in Figure 8.8 and 8.9, respectively, indicate the very good agreement between the lidar and MAX-DAOS measurements with respect to the development of boundary layer height as well as the absolute values of $\epsilon_M(z)$ in the

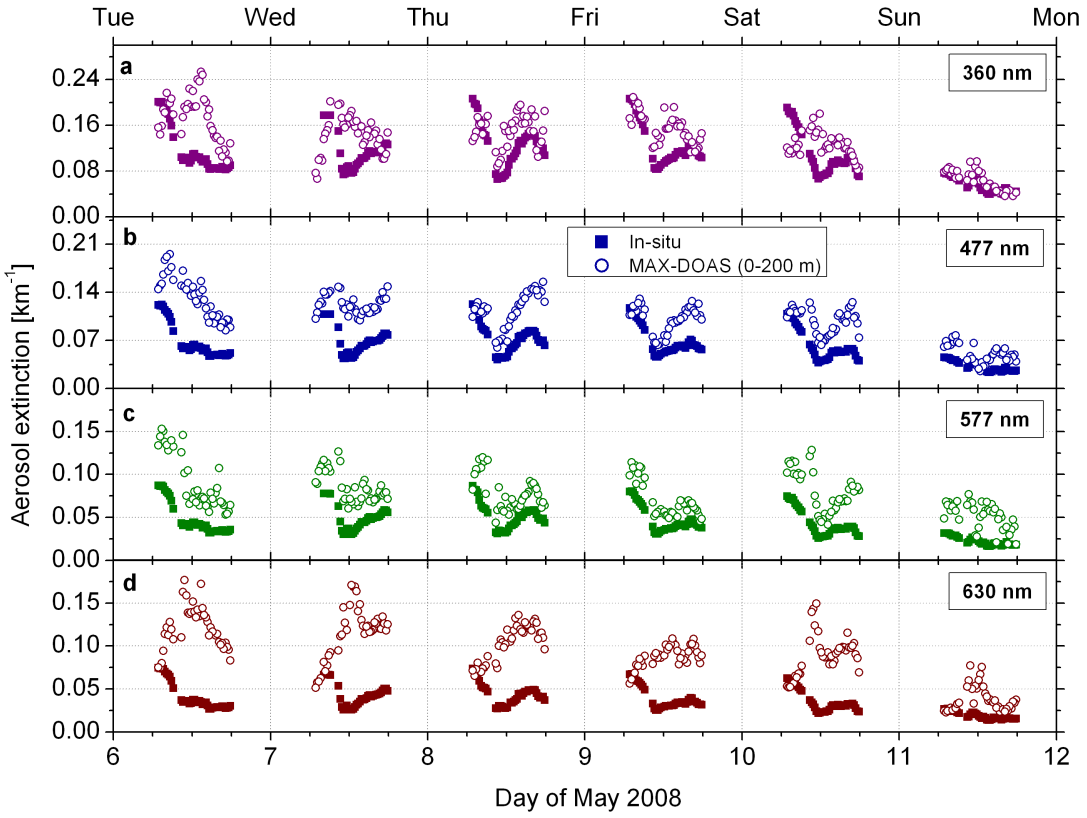

Figure 8.13: *Time series of ϵ_M retrieved from MAX-DOAS for 0–200 m (open circles) and in situ measurements (solid squares) at (a) 360, (b) 477, (c) 577 and (d) 630 nm for the period of 6 to 11 May 2008.*

course of the day. The increase in the convective mixing layer height between 10:00 and 12:00 UT of 10 May apparent in the lidar profiles, is very well resembled by the MAX-DOAS profiles demonstrating the capability of the MAX-DOAS retrieval to capture these processes in the boundary layer.

The integrated extinction profiles from Max-DOAS are compared to AOD measurements from the AERONET Sun photometer in Figure 8.11 for the wavelengths of 360, 477, 577 and 630 nm. Here, the AODs from MAX-DOAS were retrieved using the O_4 ΔODs and relative intensities at the individual wavelengths. The panels (a) – (d) contain the time series of the AODs for the period from 6 to 11 May, separated according to wavelength. The AODs from the Sun photometer were calculated using the measurements at 440 and 675 nm and α_M of the according wavelength range. Overall, a good agreement between the AODs from MAX-DOAS and Sun photometer is achieved for all wavelengths with respect to the daily trend. The best correlation is achieved for 477 nm for the considered period with the lowest AOD values occurring on 11 May. In contrast to the AODs retrieved from MAX-DOAS for 477 nm, increased differences to the values from the Sun photometer occur during individual time periods on several days for the other wavelengths.

The correlation of the AODs from MAX-DOAS and Sun photometer are shown in individual scatter plots in Figure 8.12. The panels also include frequency histograms of the AOD differences. As expected from the comparisons of the time series, the

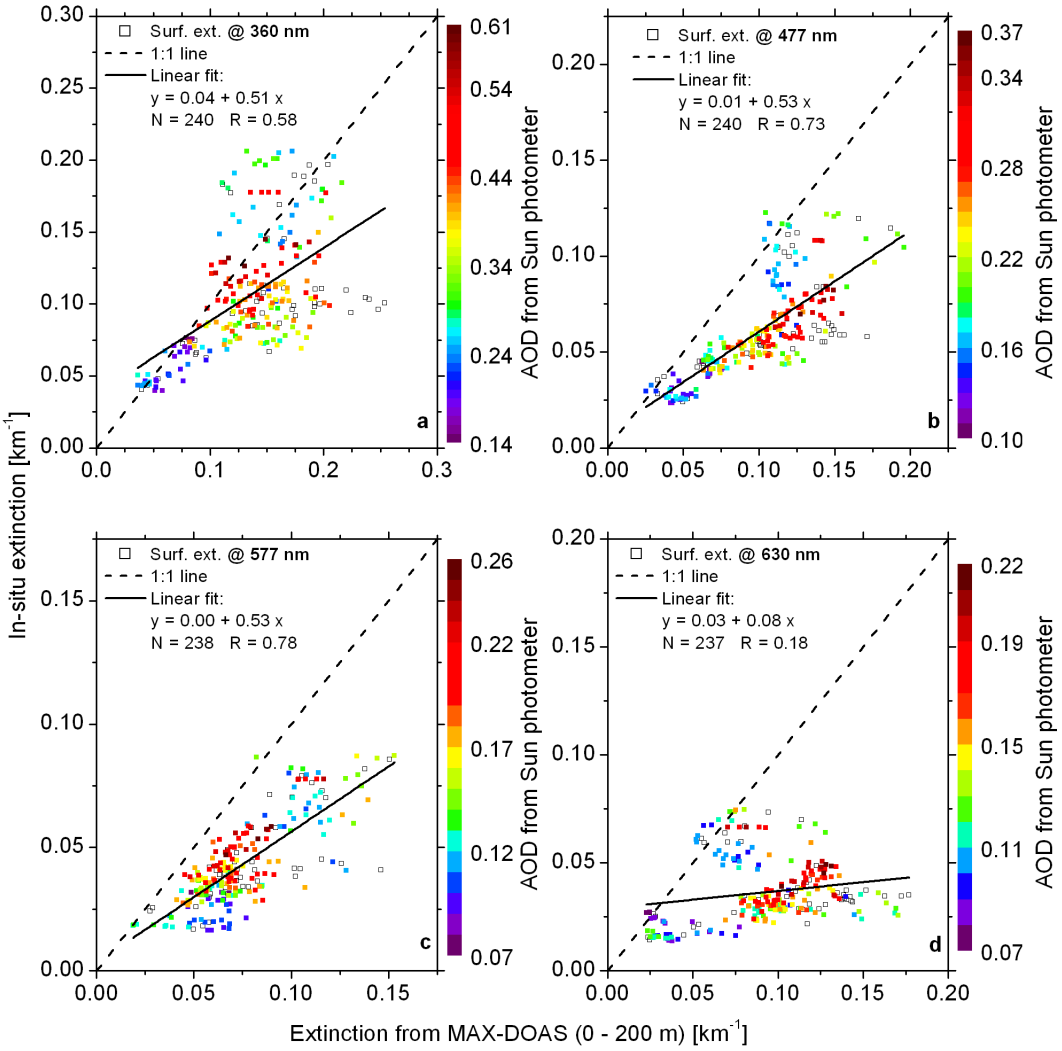

Figure 8.14: *Correlation of ϵ_M retrieved from MAX-DOAS for 0–200 m and in situ measurements at (a) 360, (b) 477, (c) 577 and (d) 630 nm for the period of 6 to 11 May 2008, color coded with the AOD from Sun photometer. The one to one line is indicated in dashed black and the linear regression in solid black.*

correlation of the AODs at 477 nm show the best agreement with respect to the offset, slope and correlation coefficient R of the linear regression. Furthermore, the scatter in the correlation is lowest for 477 nm compared to the other wavelengths indicated and quantified by the histograms. Possible larger differences in the AODs from MAX-DOAS and Sun photometer at 360, 577 and 630 nm were already discussed in Section 8.2.1 in the context of the comparison of measured and simulated O_4 ΔODs and relative intensities. The poorer instrumental performance in the ultra-violet results in larger errors and scatter in the measured O_4 ΔODs at 360 nm, which influence the retrieval performance, are the likely reason for the observed differences. In the case of the AODs at 577 and 630 nm, the larger differences are

most probably due to an inaccurate spectral retrieval of the O_4 ΔODs caused by an improper removal of H_2O and O_2.
Figure 8.13 shows the comparison of ϵ_M retrieved from MAX-DOAS for the altitude range of 0–200 m and derived from in situ measurements at the ground. The values of ϵ_M measured in situ are calculated from a combination of nephelometer, MAAP and aethalometer measurements (Section 7.2.2.1) and were provided by Bas Henzing (The Netherlands Organization for Applied Scientific Research (TNO), personal communication). Although the surface extinction from MAX-DOAS exhibits a similar diurnal pattern as the in situ measurements, significant differences in the absolute extinction values are present. The aerosol extinction values retrieved from MAX-DOAS are significantly larger than those from in situ measurements. The largest discrepancies occur at 630 nm with respect to both the diurnal developments as well as absolute values. This is most likely due to the difficulties in the MAX-DOAS spectral retrieval. On the other hand, the in situ values were calculated from the 477 and 577 nm measurements according to equation (4.13), under the assumption of a similar relationship with respect to the wavelength for the necessary corrections applied on the in situ measurements, which is not the case. Therefore, the in situ values at 630 nm are rather an approximation than real measurements in this case. The correlation of ϵ_M at the surface is shown in Figure 8.14 as scatter plots, which are color coded according the AOD from Sun photometer. The best correlation coefficients of the linear regressions are obtained for the 477 and 577 nm data sets with a slope of 0.53 in both cases. Thus, ϵ_M retrieved from MAX-DOAS for the lowermost 200 m is generally larger by a factor of roughly 2 compared to the in situ measurements. While the correlation of ϵ_M at 577 nm shows no obvious dependency on the AOD, the data set for 477 nm tends to larger differences between the MAX-DOAS and in situ values for higher AOD values. The possible reasons for these discrepancies are diverse since the comparisons of quantities measured by remote sensing and in situ techniques are difficult and challenging. The values of ϵ_M retrieved from MAX-DOAS are representative for the lowermost 200 m of the boundary layer assuming homogeneous aerosol properties within this layer, while the in situ values originate from point measurements. Thus, possible gradients of $\epsilon_M(z)$, which are not resolved by the MAX-DOAS retrieval due to the coarse height resolution can result in differences in ϵ_M compared to the in situ values. On the other hand, in situ aerosol measurements can be affected by losses in the inlet system as well as inside the instrument itself. Furthermore, ϵ_M is calculated from measurements of three different in situ measuring instruments, where each of which requires instrument specific corrections of the measured quantity. These correction may induce uncertainties (see Section 7.2.2.1). An additional source for uncertainties in in situ measurements is the fact that the sampled air is dried prior to the measurement. The aerosol scattering coefficient measured by a nephelometer is corrected according the ambient humidity to account for the scattering enhancement due to the hygroscopic growth of the aerosol particles. This correction can also induce uncertainties. However, given the very good agreement of the aerosol extinction profiles from MAX-DOAS and lidar as well as the highly correlated AODs from MAX-DOAS and Sun photometer especially at 477 nm, the major fraction of the differences between the ϵ_M values for the surface from MAX-DOAS and in situ measurements is most

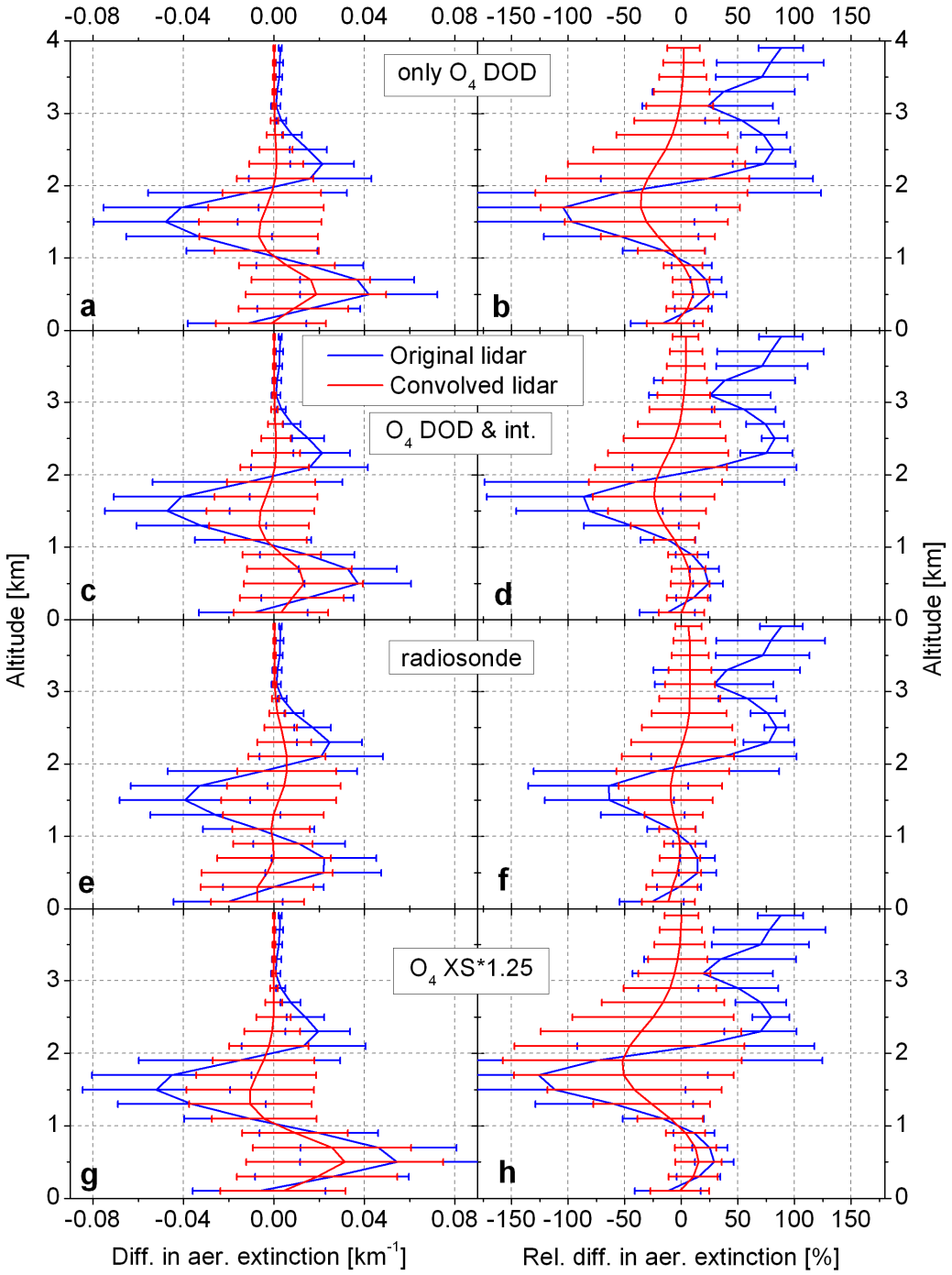

Figure 8.15: *The mean (left panel) absolute and (right panel) relative differences and corresponding standard deviations of $\epsilon_M(z)$ at 477 nm retrieved from MAX-DOAS and lidar for the period of 7 to 10 May 2008. The differences to the (blue) original and (red) convolved lidar profiles for different retrieval setting: (a,b) only O_4 ΔODs are used; (c,d) O_4 ΔODs and relative intensities are used; (e,f) radiosonde data is used; (g,h) scaling factor of 1.25 is applied on the O_4 absorption cross section (see text for details).*

probably caused by uncertainties in the in situ measurements. Similar discrepancies between in situ and MAX-DOAS were observed by Zieger et al. (2011).

8.2.2.1 Sensitivity Studies on the Aerosol Profile Retrieval

The aerosol profile retrievals from the MAX-DOAS measurements were performed using different retrieval settings and parameters to identify the influence of these changes on the retrieval results.
These changes in the retrieval settings and parameters relate to modifications of the standard settings listed on page 144. The applied cases for the tests are:

- The retrievals were performed using only the O_4 ΔODs at 477 nm to determine the resulting changes in the retrieved profiles, which are attributable to the composition of the measurement vector. In all other retrievals performed in the scope of these sensitivity studies, except the ones using several wavelengths, the O_4 ΔODs and relative intensities at 477 nm were used as measurement vector (Case A).

- The influence of different retrieval iteration strategies was explored by several tests, in which the following changes were made compared to the standard settings. The maximum number of the iteration steps, which was normally set to 5, was changed to a value of 10. The iteration sequence was repeated using the retrieved profile as the starting point of the second iteration sequence with a recalculated weighting function. The weighting function was recalculated for each iteration step (Cases B).

- The retrieval was performed using the monthly mean values of σ_0 and g instead of the coincident measurements from the Sun photometer. The surface albedo was set to 0.3 instead of 0.05. Scaling factors of 1.125 and 1.25 were applied on the O_4 absorption cross sections. The profiles of pressure and temperature were adapted from radiosonde measurements of the according days instead of the usage of climatology data (Cases C).

- The radiative transfer model assumes homogeneous conditions within the individual atmospheric layers, while horizontal inhomogeneities in the atmospheric aerosol distribution may occur in reality. To account for this limitation of the radiative transfer model, the errors of the measurement vector components were increased using a factor of 5. Different cases were tested, in which the O_4 ΔOD and relative intensity errors were increased separately as well as simultaneously (Cases D).

- The influence of the measurement vector components was explored by retrievals simultaneously using O_4 ΔODs and relative intensities at several wavelengths. Different combinations of the measurement vector containing 2, 3 and 4 wavelengths were used for the retrieval (Cases E).

The average differences between $\epsilon_M(z)$ retrieved from MAX-DOAS and lidar as well as the corresponding standard deviations were calculated with respect to absolute

and relative differences. The differences were calculated for the original and convolved lidar profiles. The mean differences allow for the quantitative comparison of the profiles from MAX-DOAS and lidar as well as the comparison of the retrieval performance for the different settings. Figure 8.15 shows the average profile differences for selected retrieval settings. Panels (a) and (b) show the mean absolute and relative profile differences, respectively, for retrievals using only the O_4 ΔODs as measurement vector. The considered time period is the 7 to 10 May 2008. The differences resulting from retrievals with standard settings as shown in the Figures 8.7 – 8.10 are depicted in panels (c) and (d) of Figure 8.15. The panels (e,f) and (g,h) contain the results for the retrievals using radiosonde measurements of pressure and temperature profiles and a scaling factor of 1.25 for the O_4 absorption cross section, respectively. The considered profile differences for the different retrieval settings have several features in common. The average profile differences are characterized by a sigmoidal shape which is attributable to the height dependent sensitivity and resolution of the retrieval. Since the convolution of the lidar profile accounts for the height dependent sensitivity and resolution of the retrieval, the differences are smaller for the convolved lidar profiles. The higher retrieval sensitivity for altitudes below ≈ 1.5 km results in smaller relative difference at these altitudes. The compar-

Table 8.2: *The influence of different retrieval settings. Linear regression fit and statistical parameters for the correlation of the AOD retrieved from MAX-DOAS and Sun photometer for the period of 6 to 11 May 2008 (see text for details).*

Case	Retrieval setting	Wave-length	N	Slope	Offset	R	Bias	Std. dev.
Std.	360 nm	360	197	0.86	0.08	0.82	-0.03	0.06
	477 nm	477	197	0.89	0.02	0.90	0.00	0.03
	577 nm	577	196	0.71	0.04	0.77	0.01	0.03
	630 nm	630	197	0.53	0.05	0.64	0.02	0.03
A	Only O_4 ΔOD	477	197	0.71	0.07	0.76	-0.01	0.04
B	$n_{max} = 10$	477	197	0.88	0.03	0.89	0.00	0.03
	2 iteration runs	477	197	0.83	0.036	0.89	0.00	0.03
	Vary. weight. func.	477	197	0.82	0.04	0.90	0.00	0.03
C	Mean ω_0 and g	477	197	0.89	0.02	0.89	0.01	0.03
	Surf. albedo = 0.3	477	197	0.59	0.07	0.70	0.04	0.05
	O_4 scale = 1.125	477	197	0.91	0.01	0.92	0.01	0.03
	O_4 scale = 1.25	477	197	0.91	0.00	0.93	0.02	0.02
	Radiosonde	477	197	0.89	0.03	0.95	0.00	0.03
D	O_4 error $\times 5$	477	197	0.85	0.03	0.88	0.00	0.03
	Int. error $\times 5$	477	197	0.81	0.05	0.86	0.00	0.03
	O_4 & int. error $\times 5$	477	197	1.04	0.01	0.91	-0.02	0.03
E	360 and 477 nm	418	197	0.91	0.03	0.90	-0.01	0.04
	477 and 577 nm	527	196	0.84	0.03	0.85	0.01	0.03
	360,477,577 nm	471	196	0.91	0.02	0.89	0.00	0.03
	360,477,577,630 nm	511	193	0.84	0.02	0.84	0.01	0.03

ison of the differences depicted in panels (a,b) and (c,d) shows that the additional usage of the relative intensities results in a better agreement of the profiles retrieved from MAX-DOAS and lidar. The differences decrease for altitudes above ≈ 1 km due to the additional information from the intensities. The agreement between MAX-DOAS and lidar profiles further improves, when radiosonde measurements of the pressure and temperature profiles is used instead of profiles from the climatological data base. This improvement can be attributed to the O_4 profile, which depends on pressure (see Section 2.3). The assumed O_4 profile for the radiative transfer calculations agrees better with the actual O_4 profile, when the radiosonde data is used for its calculation. In contrast, the usage of a scaling factor of 1.25 for the O_4 absorption cross section results in an increase in the profile differences (Figure 8.15g,h) compared to the retrievals omitting a scaling factor (Figure 8.15c,d).

The details of the correlation between the AOD retrieved from Sun Photometer and from MAX-DOAS using the different retrieval settings are summarized in Table 8.2, where the linear regression fit and statistical parameters are listed. The average difference between the AOD values is referred to as bias with the corresponding standard deviation. N indicates the number of points. The reference wavelengths,

Table 8.3: *The influence of different retrieval settings. Linear regression fit and statistical parameters for the correlation of ϵ_M (in km^{-1}) retrieved from MAX-DOAS for 0–200 m and in situ measurements for the period of 6 to 11 May 2008 (see text for details).*

Case	Retrieval setting	Wave-length	N	Slope	Offset	R	Bias	Std. dev.
Std.	360 nm	360	240	0.51	0.04	0.56	0.03	0.04
	477 nm	477	240	0.53	0.01	0.73	0.04	0.02
	577 nm	577	238	0.53	0.00	0.78	0.03	0.02
	630 nm	630	237	0.08	0.03	0.18	0.06	0.04
A	Only O_4 ΔOD	477	240	0.56	0.01	0.76	0.04	0.02
B	$n_{max} = 10$	477	240	0.51	0.01	0.76	0.04	0.02
	2 iteration runs	477	240	0.54	0.01	0.79	0.04	0.02
	Vary. weight. func.	477	240	0.54	0.01	0.75	0.04	0.02
C	Mean ω_0 and g	477	240	0.54	0.01	0.72	0.04	0.02
	Surf. albedo = 0.3	477	240	0.58	0.01	0.71	0.03	0.02
	O_4 scale = 1.125	477	240	0.41	0.01	0.69	0.06	0.03
	O_4 scale = 1.25	477	240	0.32	0.02	0.64	0.07	0.04
	Radiosonde	477	240	0.56	0.01	0.74	0.03	0.02
D	O_4 error $\times$ 5	477	240	0.22	0.04	0.35	0.05	0.04
	Int. error $\times$ 5	477	240	0.56	0.01	0.76	0.04	0.02
	O_4 & int. error $\times$ 5	477	240	0.30	0.03	0.46	0.05	0.03
E	360 and 477 nm	418	240	0.59	0.01	0.75	0.04	0.03
	477 and 577 nm	527	238	0.56	0.00	0.80	0.04	0.02
	360,477,577 nm	471	238	0.61	0.00	0.82	0.05	0.02
	360,477,577,630 nm	511	235	0.56	0.00	0.81	0.04	0.02

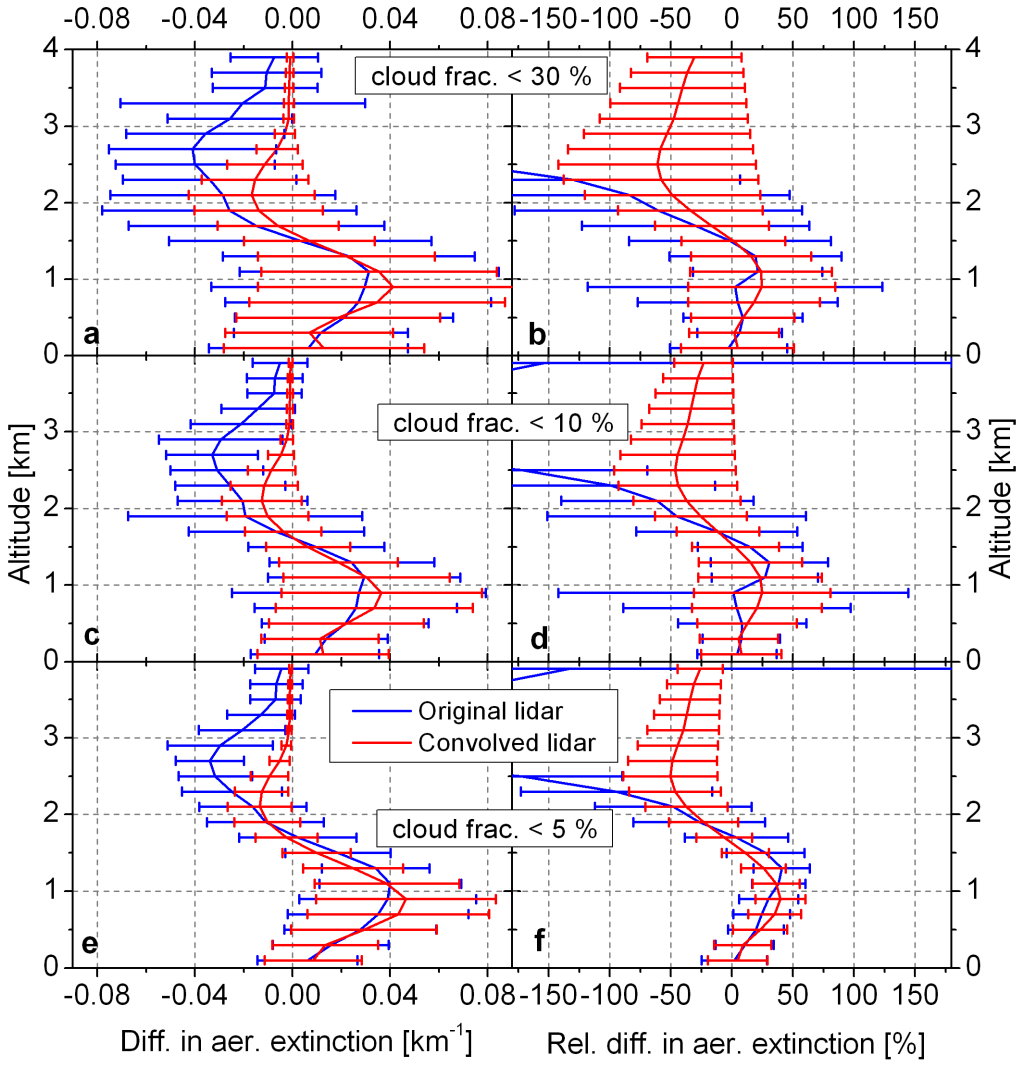

Figure 8.16: *The mean (left panel) absolute and (right panel) relative differences and corresponding standard deviations of $\epsilon_M(z)$ at 477 nm retrieved from MAX-DOAS and lidar for the period of 3 May to 30 June 2008. The differences to the (blue) original and (red) convolved lidar profiles for opaque cloud fraction less than (a,b) 30 %, (c,d) 10 % and (e,f) 5 % (see text for details).*

for which the AODs are calculated, are also listed. In addition to the results of this sensitivity study, the details of the linear regression fits of the correlations for the standard settings shown in Figure 8.12 are listed at the beginning of Table 8.2. The most significant change in the agreement between the AODs from MAX-DOAS and Sun photometer compared to the retrievals using standard settings at 477 nm with respect to the correlation coefficient R and slope of the linear regression occur for the retrieval using ground albedo of 0.3. Table 8.3 summarizes the details of the correlation between ϵ_M retrieved from MAX-DOAS and measured in situ. The results for the different retrieval settings show that the increase of the O_4 ΔOD error sig-

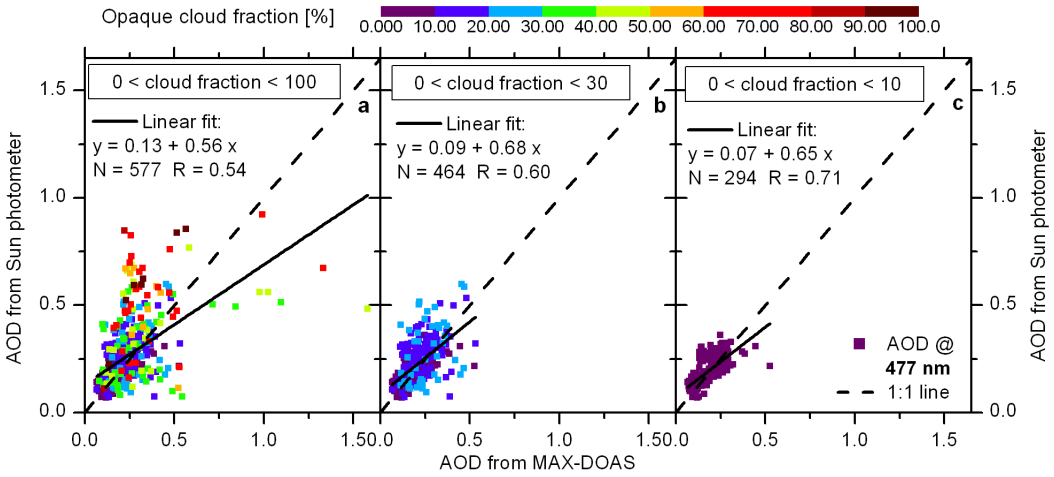

Figure 8.17: *Correlation of the AOD at 477 nm retrieved from MAX-DOAS and Sun photometer for the period of 3 May to 30 June 2008 and conditions with an opaque cloud fraction of (a) < 100 %, (b) < 30 % and (c) < 10 %. The one to one line is indicated in dashed black and the linear regression in solid black.*

nificantly worsens the agreement between the values from the different techniques. The average differences of the retrieved profiles for all the different retrieval settings are summarized in the Appendix A in plots similar to Figure 8.15

8.2.2.2 Aerosol Profile Retrieval for the Entire Campaign

For the entire campaign from 3 May to 30 June 2008, aerosol extinction profiles were retrieved using only the O_4 ΔODs at 477 nm. Due to the high sensitivity of the intensity for the presence of clouds, the inclusion of the relative intensity in the measurement vector was omitted for this long period. Since lidar profiles from the CEALI instrument are of high quality but merely available for selected days, the comparisons of $\epsilon_M(z)$ were related to measurements of the HTRL backscatter lidar. The RCS of the HTRL instrument was provided by Arnoud Apituley (RIVM, personal communication) The aerosol extinction profiles were calculated from the RCS in the same way as for the CEALI instrument. The RCS of the HTRL instrument has a poorer signal to noise ratio at altitudes above ≈ 2 km compared to the CEALI instrument, which induces overestimations in $\epsilon_M(z)$ at these altitudes for the applied conversion from the RCS. While Sun photometer measurement were available for the whole campaign duration, in situ measurements of ϵ_M cover only the period of 3 to 31 May 2008.

Figure 8.16 shows the average differences in the retrieved profiles for conditions with different opaque cloud fractions. The profiles were selected according to the cloud fraction measured by the total sky imager (see Section 7.2.4). The agreement of the profiles from MAX-DOAS and lidar improves when conditions with smaller cloud fractions are considered, since the possibility for influences of clouds on both the MAX-DOAS and lidar measurements decreases.

Figure 8.17 shows the correlation of the AODs from MAX-DOAS and Sun photome-

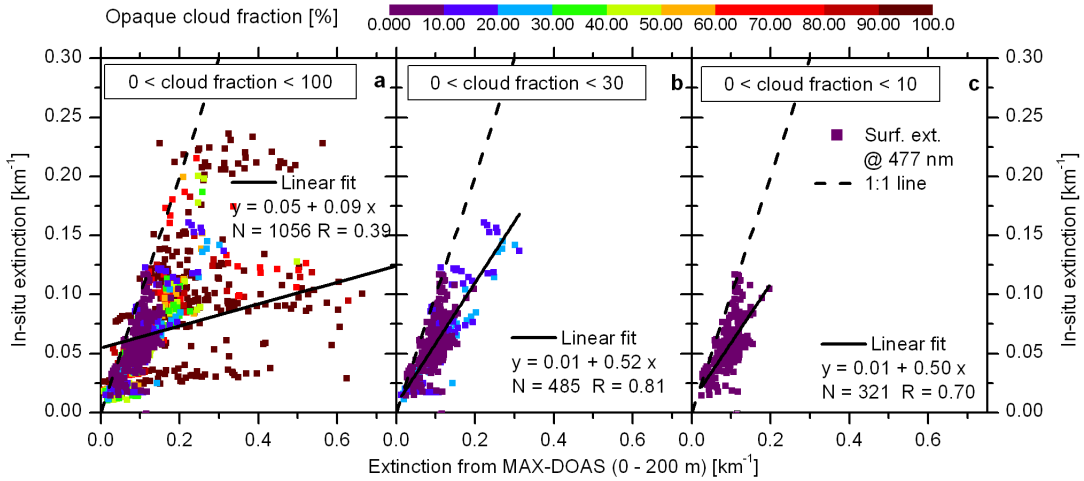

Figure 8.18: *Correlation of ϵ_M at 477 nm retrieved from MAX-DOAS for 0–200 m and in situ measurements for the period of 3 to 31 May 2008 and conditions with an opaque cloud fraction of (a) < 100 %, (b) < 30 % and (c) < 10 %. The one to one line is indicated in dashed black and the linear regression in solid black.*

ter. The correlation of ϵ_M from MAX-DOAS and in situ measurements are shown in Figure 8.18. The scatter plots are color coded according to the opaque cloud fraction. In both cases, for conditions with cloud fractions less than 30 %, agreements in AOD and ϵ_M values are achieved, which are comparable to the cloudless cases discussed in Section 8.2.2.1.

8.2.2.3 Parameterized Retrieval of Aerosol Profiles

The parameterized version of the retrieval of $\epsilon_M(z)$ using the optimal estimation method was applied using the two and three parameters descriptions of the aerosol profile (see Section 6.1.3). An overview on the results and their comparison to lidar, Sun photometer and in situ measurements is given in this Section for the cloudless period from 6 to 11 May 2008. The general retrieval settings were equal to the standard settings for the retrievals of the complete profiles (see page 144). For the retrievals using two parameters, an a priori AOD of 0.2 and surface extinction of $0.1\,\mathrm{km}^{-1}$ were applied. For the three parameter description of the profile, the a priori parameters were set to 0.2, 1.0 km and 0.5 km for the AOD, aerosol layer center height and layer FWHM, respectively. The a priori errors of the parameters were set to 100 %. The O_4 ΔODs and relative intensities were used as measurement vector.

The comparison of $\epsilon_M(z)$ is shown in Figures 8.19 and 8.20 for 7 and 9 May 2008, respectively. Since the profile shape is constrained by the parameterized description, the elevated aerosol layer in the morning hours of 7 May is not well reproduced by the retrieval using two parameters. However, the top of the residual layer is roughly reproduced by the smoothed box-shaped representation. In contrast, the diurnal development in the remaining part of the day is well captured by the two parameter retrieval with respect to boundary layer height and increase in aerosol load. A

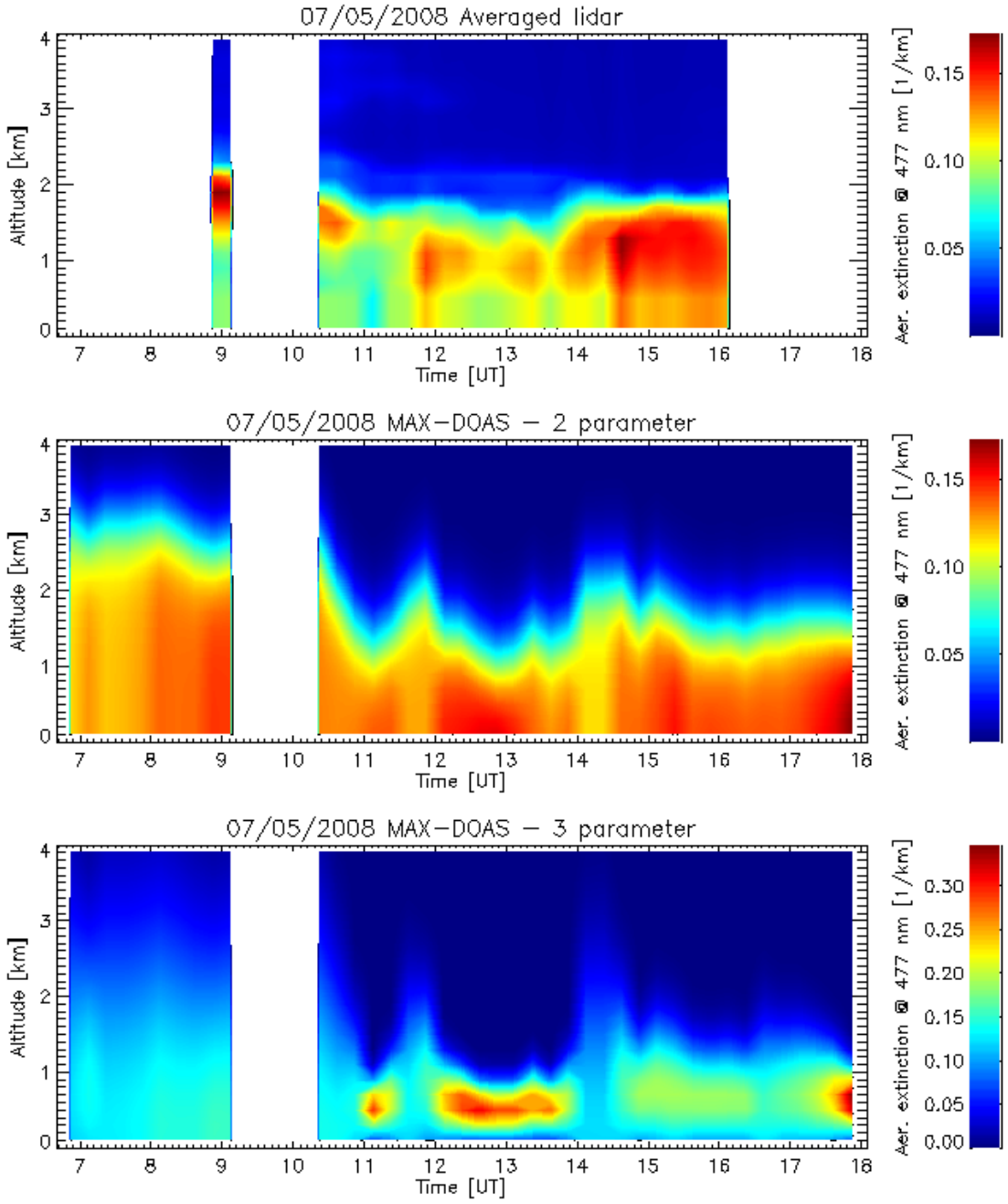

Figure 8.19: *Comparison of $\epsilon_M(z)$ at 477 nm retrieved from lidar and MAX-DOAS for 7 May 2008: (top) averaged profiles from lidar, (center) profiles retrieved from MAX-DOAS using 2 and (bottom) 3 parameters for the profile description.*

similarly good agreement with the lidar profiles is achieved on 9 May. Although the three parameters representation allows for a description of an elevated layer, the retrieved profiles in the morning hours of 7 May remarkably differ from the lidar profiles. The aerosol extinction at altitudes near the surface can hamper the retrieval, since a two-layered profile can not be approximated by the three parameter description. Furthermore, the retrieved boundary layer heights are generally lower

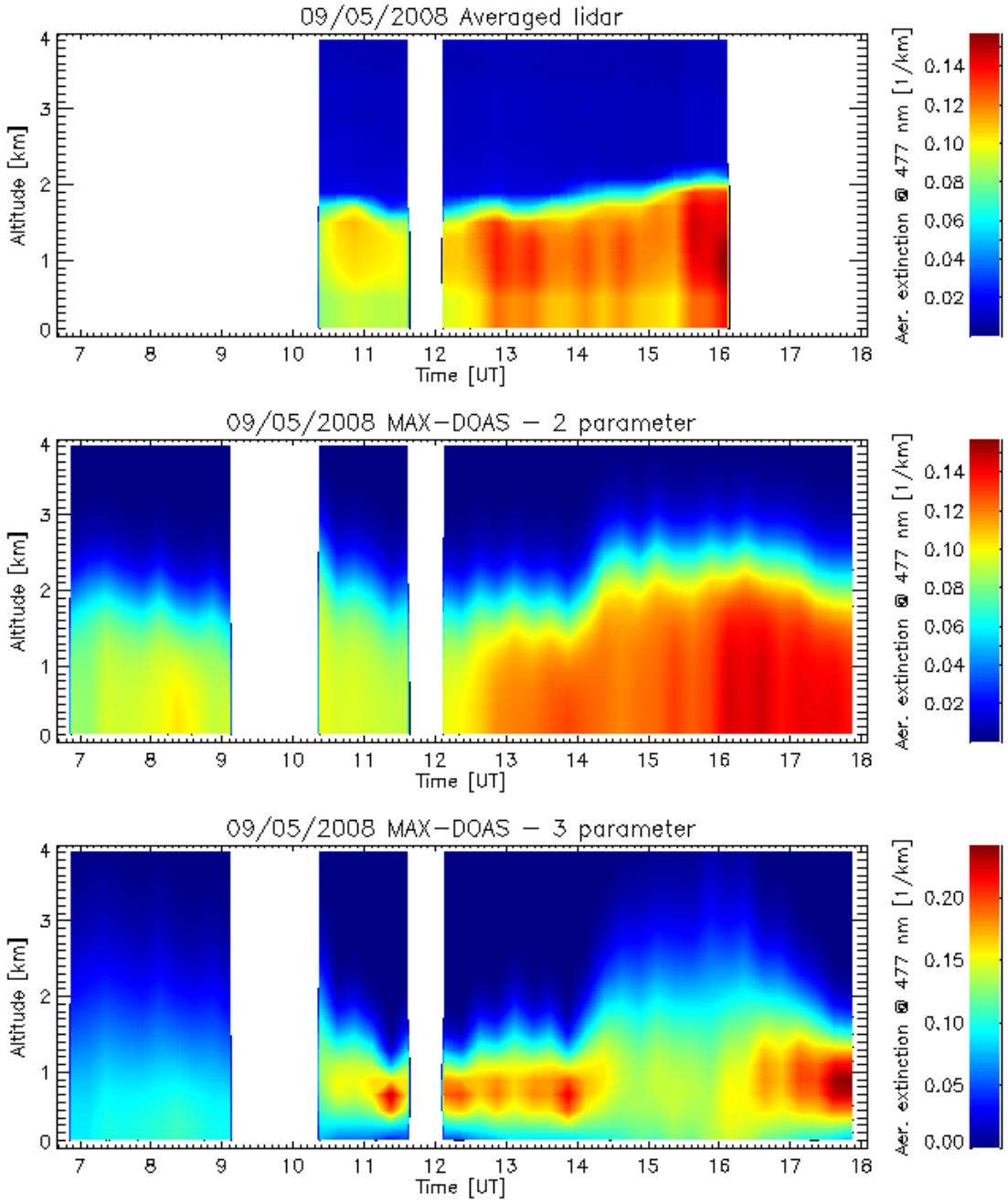

Figure 8.20: *Same as Figure 8.19 but for 9 May 2008.*

than observed by the lidar and retrieved with the two parameter description.
The correlations of the AODs retrieved from Sun photometer and MAX-DOAS are shown in Figure 8.21 for both versions of the parametrization. Although the shapes of the retrieved profiles using two and three parameters remarkably differ, the correlations with the AODs from Sun photometer show similar properties for both versions and are comparable to the results achieved with the complete profile retrieval in Figure 8.12b.
Figure 8.22 shows the correlations of ϵ_M retrieved from MAX-DOAS and measured

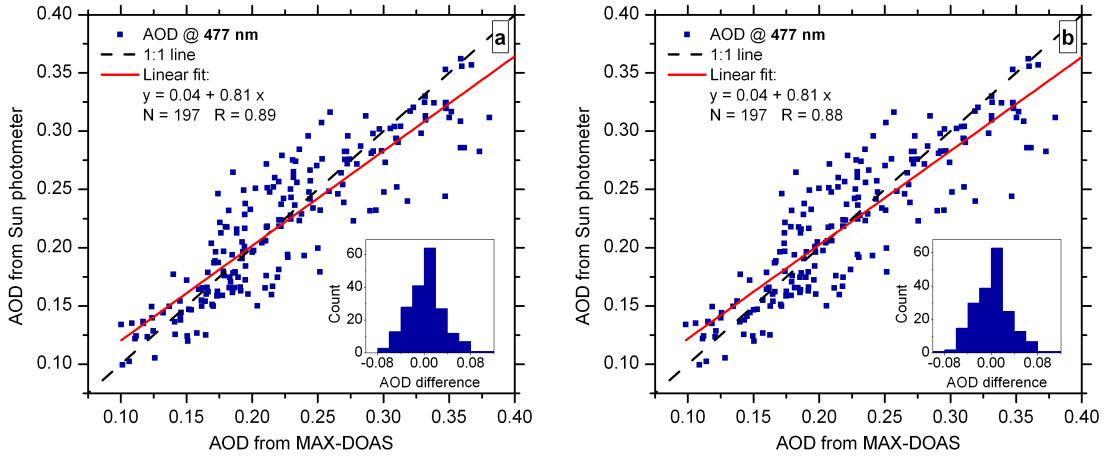

Figure 8.21: *Correlation of the AOD at 477 nm retrieved from MAX-DOAS and Sun photometer for the period of 6 to 11 May 2008 using (a) two and (b) three parameters for the profile description. The one to one line is indicated in dashed black and the linear regression in red. The implemented histograms show the frequency of the differences in the AOD.*

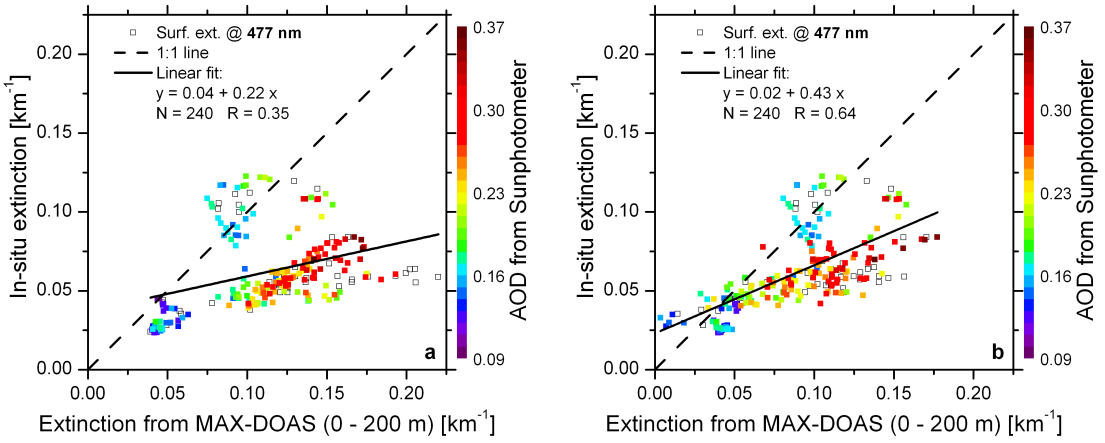

Figure 8.22: *Correlation of ϵ_M at 477 nm retrieved from MAX-DOAS for 0–200 m and in situ measurements for the period of 6 to 11 May 2008 using (a) two and (b) three parameters for the profile description, color coded with the AOD from Sun photometer. The one to one line is indicated in dashed black and the linear regression in solid black.*

in situ. In this case, the agreements are poorer compared to the results from the full profile retrieval in Figure 8.14b due to the limitation of representable profile shapes. Possible gradients in the true profiles are not resolved appropriately.

8.2.2.4 Retrieval of Aerosol Profiles Using the Regularization Method

The regularization method was applied to retrieve $\epsilon_M(z)$ using the O_4 ΔODs and relative intensities as measurement vector. The retrievals were performed using the identity matrix, discrete first- and second-derivative operator as regularization operators. The general retrieval settings were equal to the standard settings for the retrievals of the complete profiles using the optimal estimation method (see page 144). The applied regularization parameters were determined from retrievals using synthetic measurements and the L-curve method (see Section 6.2.1). The parameter values of 10, 1 and 0.01 were used for the the retrievals with the identity matrix, discrete first- and second-derivative operator, respectively. The comparisons of the results to lidar, Sun photometer and in situ measurements for the cloudless period from 6 to 11 May 2008 are content of this Section.
Figure 8.23 shows the correlations of the AODs retrieved from Sun photometer and MAX-DOAS for the different regularization operators. The best agreement is achieved for the retrievals using the identity matrix. The linear regression fit parameters of the correlation are comparable to values determined for the retrievals using the optimal estimation method with the standard settings shown in Figure 8.12b.
In Figure 8.24, the diurnal development of $\epsilon_M(z)$ retrieved by applying different regularization operators are compared for 7 May 2008. While the general features of $\epsilon_M(z)$ agree well between the different operators, the elevated layer in the morning hours is reproduced differently. It should be noted that the used regularization parameters are not optimal, since they were not determined for the actual inversion problem but only for a particular aerosol scenario. The determination of the regu-

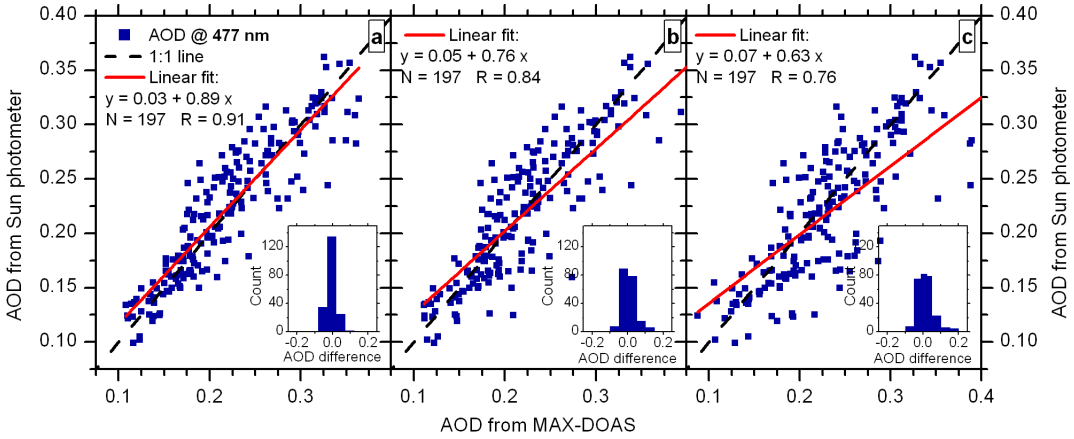

Figure 8.23: *Correlation of the AOD at 477nm retrieved from Sun photometer and MAX-DOAS for the period of 6 to 11 May 2008 using the (a) identity matrix, (b) discrete first- and (c) second-derivative operator with regularization parameters of 10, 1 and 0.01, respectively. The one to one line is indicated in dashed black and the linear regression in red. The implemented histograms show the frequency of the differences in the AOD.*

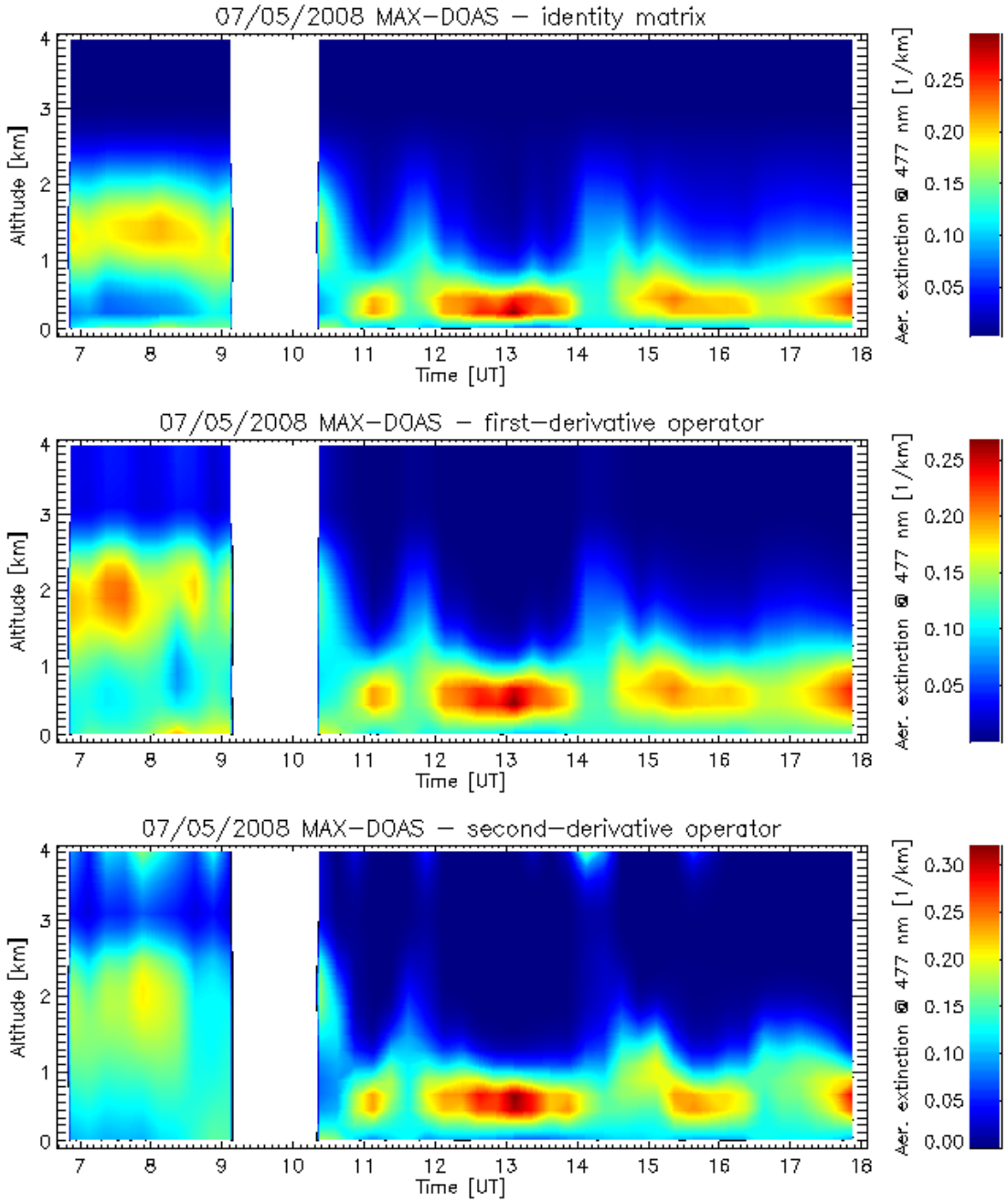

Figure 8.24: *$\epsilon_M(z)$ at 477nm on 7 May 2008 retrieved from MAX-DOAS using different regularization operators: (top) identity matrix, (center) discrete first- and (bottom) second-derivative operator with regularization parameters of 10, 1 and 0.01, respectively.*

larization parameter for each individual retrieval would require several retrieval runs for a number of parameters, which would significantly increase the computational effort.

Figure 8.25 shows the correlations of ϵ_M retrieved from MAX-DOAS and measured in situ. Compared with the results from the optimal estimation method in Figure

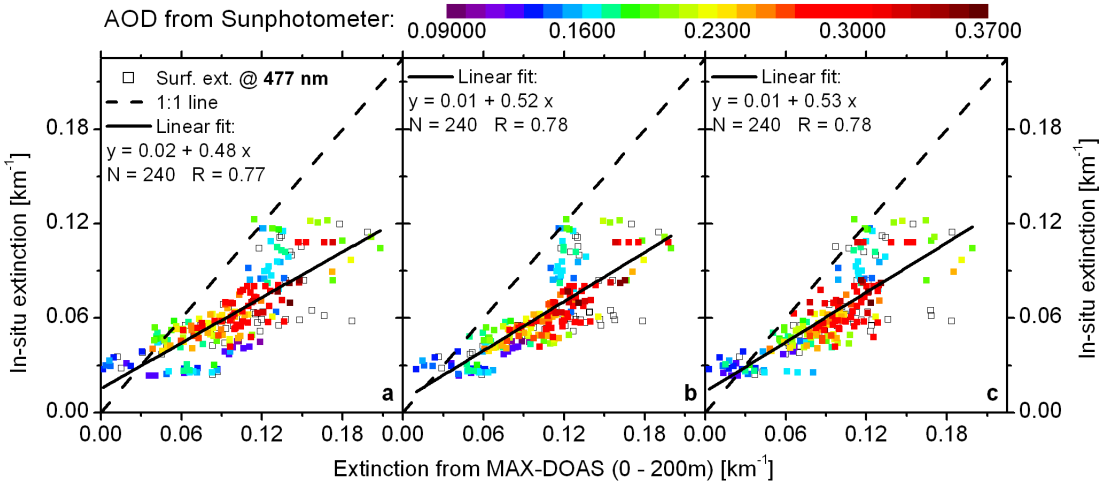

Figure 8.25: *Correlation of ϵ_M at 477 nm retrieved from in situ measurements and MAX-DOAS for 0–200 m for the period of 6 to 11 May 2008 using the (a) identity matrix, (b) discrete first- and (c) second-derivative operator with regularization parameters of 10, 1 and 0.01, respectively. The color code is according the AOD from Sun photometer. The one to one line is indicated in dashed black and the linear regression in solid black.*

8.14b, significant improvements in the agreement of the different data sets are not achieved by using the regularization method.

8.2.3 Retrieval of NO_2 Profiles

The retrieval of NO_2 profiles from the MAX-DOAS ΔSCDs measurements is content of this Section. First, the retrieved NO_2 profiles from MAX-DOAS using the optimal estimation method are compared to co-located observations from satellite instruments and in situ measurements for the cloudless period of 6 to 11 May 2008. After these comparisons, the influence of selected retrieval settings and parameters on the retrieved NO_2 profiles are explored. In the subsequent Section, the com-

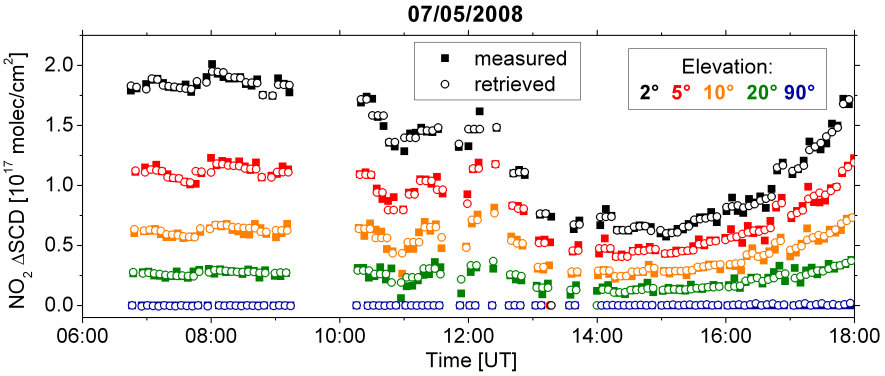

Figure 8.26: *Retrieved and measured NO_2 ΔSCDs for the profile retrievals from MAX-DOAS measurements on 7 May 2008.*

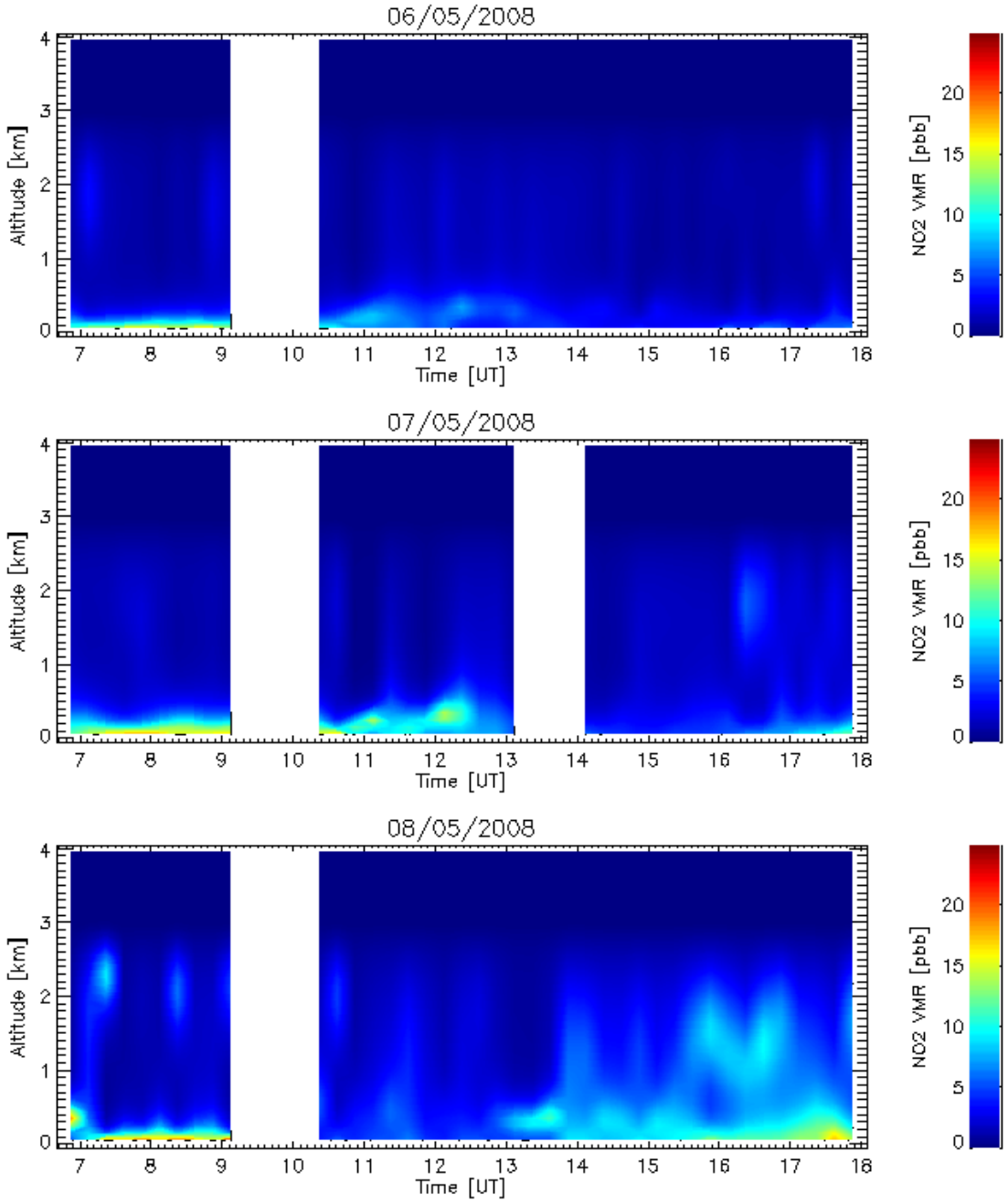

Figure 8.27: *Diurnal development of the NO_2 VMR profile retrieved from MAX-DOAS for the period of 6 to 8 May 2008.*

parison of the MAX-DOAS results retrieved using the optimal estimation method is extended over the whole field campaign period. Finally, the resulting profiles retrieved using the regularization method for the cloudless period are shown in selected examples.

Figure 8.26 shows an example for the simulated and measured NO_2 ΔSCDs resulting from the profile retrieval for 7 May 2008. The simulated and measured ΔSCDs are in very good agreement. Figures 8.27 and 8.28 show the diurnal development

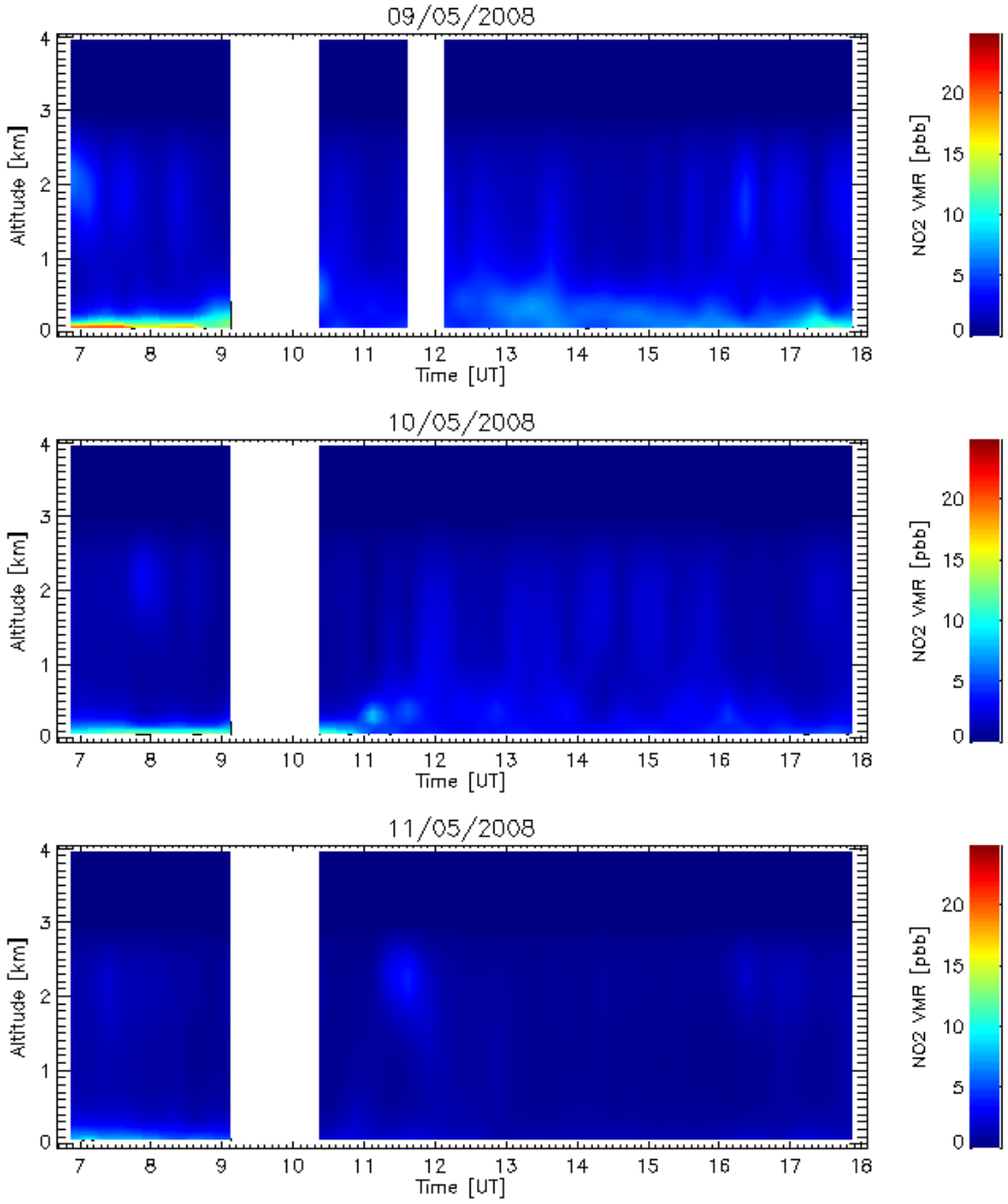

Figure 8.28: *Same as Figure 8.27 but for the period of 9 to 11 May 2008.*

of the NO_2 VMR profiles retrieved from MAX-DOAS using the optimal estimation method (see Section 5.6.1). The NO_2 retrievals were performed using settings, which will be referred to as standard settings for the trace gas retrieval in the following. These standard settings were applied for all trace gas profile retrievals presented in this work for the different campaigns. An exception is Section 8.2.3.1, where the sensitivities of the profile retrievals to changes in the settings and parameters of the standard settings are tested. Any differences in the applied retrieval settings to the standard settings are pointed out where relevant.

The **standard settings** of the trace gas profile retrievals are:

- A height grid with a resolution of 100 m was used. The trace gas profile retrieval from MAX-DOAS has a better height resolution than the aerosol profile retrieval, which is accounted for by the usage of this finer resolution.
- The surface albedo of 0.05 was assumed due to the findings in Section 8.2.1.
- The profiles of pressure, temperature and other trace gases were adapted from the climatological data base (see Section 4.4.2).
- The aerosol optical parameters ω_0 and g were adapted from AERONET Sun photometer measurements (see Section 7.2.1). Thereby, coincident measurements of these values were used as far as available and daily or monthly averages otherwise.
- A linearly decreasing a priori profile was used with a surface VMR of 10 ppb and 0 ppb at 3 km altitude. The error of the a priori profile was set 100 %
- The NO_2 ΔSCDs retrieved from the elevation scan measurements in the visible wavelength range of 425–490 nm were used as measurement vector.
- The aerosol profiles retrieved from the MAX-DOAS O_4 ΔOD and relative intensity measurements using the standard settings were used as input for the NO_2 profile retrievals, unless stated otherwise.

The NO_2 VCDs determined by the integration of the profiles over the altitude range considered in the MAX-DOAS retrievals is shown in Figure 8.29a. The tropospheric NO_2 VCDs retrieved from measurements of the SCIAMACHY, OMI and GOME-2 satellite instruments (see Section 7.2.3) are also plotted in this panel and color coded according to the individual pixel center distances to the Cabauw site. The satellite data was provided by Ankie Piters and Ronald van der A (both KNMI, personal communication). Since the OMI instrument shows pixel anomalies, the affected measurements for the Cabuaw site were neglected for the comparisons.
Figure 8.29b shows the NO_2 surface concentrations from in situ measurements (see Section 7.2.2.2) and retrieved from MAX-DOAS for the altitude range of 0–100 m. The retrieved surface concentrations are generally highest in the morning, when NO_2 is strongly confined to the lowermost 100 m (Figure 8.27 and 8.28). This daily trend can be attributed to processes and conditions occurring during the night. The radiative cooling of the surface often leads to surface air that is colder than the air above it. This leads to an inversion near the ground resulting in a stable layer of some hundred meters extent, in which the ventilation of NO_2 emissions is prevented. Furthermore, the missing NO_2 photolysis during the night enables the generation of the reservoir species N_2O_5. As the sun rises, the onset of photolysis and the increase in mixing layer height results in a decrease in NO_2 surface concentration, with a minimum at noon due to the high photolysis frequency of NO_2. Accordingly, the NO_2 concentration increases in the evening due to its reduced photolysis and the reaction of NO with O_3.

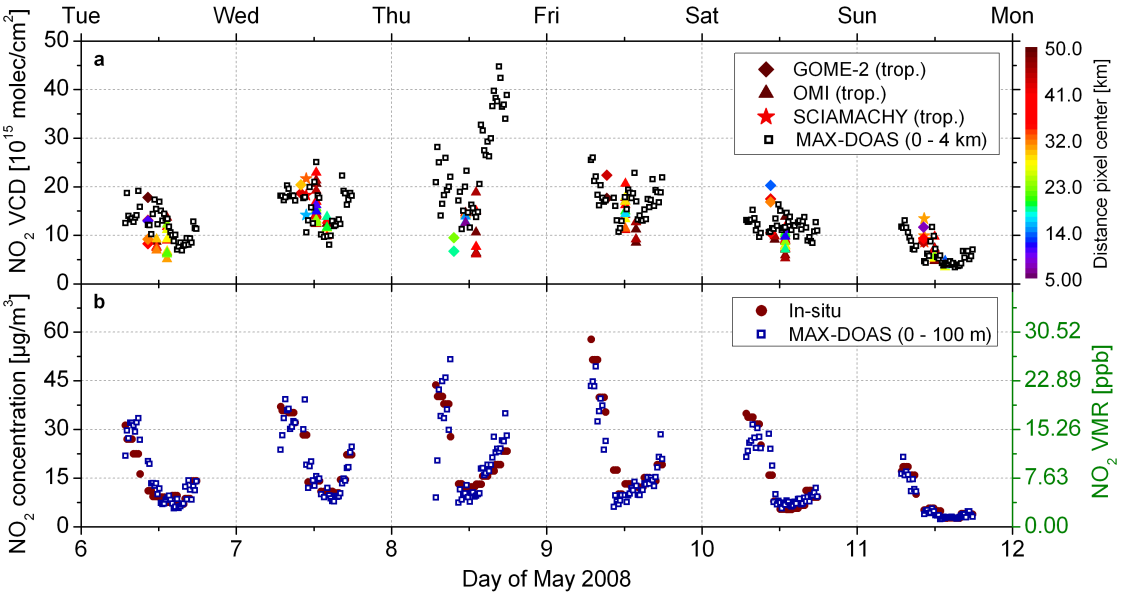

Figure 8.29: *Time series of the NO_2 VCD and surface concentration for the period of 6 to 11 May 2008: (a) NO_2 VCD retrieved from MAX-DOAS for 0–4 km (open black squares) and the tropospheric VCD from SCIAMACHY (stars), OMI (triangles) and GOME-2 (diamonds) color coded according to the distance of the satellite pixel center to the Cabauw site; (b) NO_2 concentration measured in situ (solid red circles) and retrieved from MAX-DOAS for 0–100 km (open blue squares).*

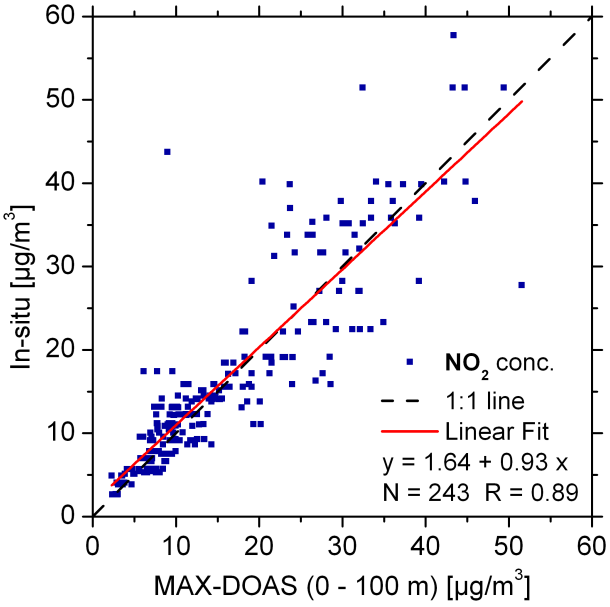

Figure 8.30: *Correlation of the NO_2 surface concentration measured in situ and retrieved from MAX-DOAS for 0–100 m for the period of 6 to 11 May 2008. The one to one line is indicated in dashed black and the linear regression in solid red.*

The NO_2 VCDs from MAX-DOAS are in good agreement with the satellite measurements. Larger discrepancies tend to occur for situations where the satellite pixel center has a larger distance to the Cabauw site. Depending on the actual covered area of the satellite pixels, the large cities in the surrounding of Cabauw can contribute to the observed NO_2 VCDs. The comparison of the surface concentrations shown in Figure 8.30 shows a very good agreement between the MAX-DOAS and in situ measurements.

8.2.3.1 Sensitivity Studies on the NO_2 Profile Retrieval

The NO_2 profile retrievals for the period of 6 to 11 May 2008 were performed using different retrieval settings and parameters to identify the influence of these changes on the retrieval results. Thereby, specific changes compared to the standard settings listed on page 165 were made. The applied cases for the tests are:

- The NO_2 ΔSCDs were also retrieved from the MAX-DOAS measurements in the ultra-violet wavelength range of 338–370 nm. The profile retrievals were also performed for these NO_2 ΔSCDs.
- The retrievals were performed using height grids with resolutions of 50 and 200 m to explore the changes in the resulting profiles compared to the resolution of 100 m in the standard settings (Cases F).
- The errors of the measurement vector components were increased using a factor of 5 (Case G).
- The profiles of the pressure and temperature were adapted from radiosonde measurements of the according days instead of the usage of the climatology data. Different aerosol profiles were used to identify the resulting changes. Instead of aerosol profiles from the MAX-DOAS retrievals using the O_4 ΔODs and relative intensities at 477 nm, the profiles retrieved with measurement vectors containing only the O_4 ΔODs were used. Furthermore, the aerosol profiles retrieved using the two parameters description of the profile were used as well as the aerosol profiles measured by the CEALI instrument (Cases H).

The details of the correlation between the NO_2 surface concentration retrieved from in situ measurements and MAX-DOAS using the different retrieval settings are summarized in Table 8.4, where the linear regression fit and statistical parameters are listed. The average difference between the surface concentrations is referred as bias with the corresponding standard deviation. N indicates the number of points. The wavelengths, at which the radiative transfer calculations were performed, are also indicated.
Best agreement between MAX-DOAS and in situ is achieved for a height grid with 100 m vertical resolution. The shallow NO_2 layers in the morning hours are not appropriately resolved for a 200 m height grid. In contrast, the height grid resolution of 50 m is smaller than the vertical resolution of the retrieval at lower altitudes. Therefore, the agreement in the surface concentrations is not improved significantly. The usage of the aerosol profiles retrieved from MAX-DOAS with the two different approaches result in relative small changes in the correlation properties.

Table 8.4: *The influence of different retrieval settings. Linear regression fit and statistical parameters for the correlation of the NO_2 surface concentration (in $\mu g/m^3$) retrieved from MAX-DOAS for 0–100 m and in situ measurements for the period of 6 to 11 May 2008 (see text for details).*

Case	Retrieval setting	Wave-length	N	Slope	Offset	R	Bias	Std. dev.
Std.	NO_2 SCD Vis.	458	243	0.93	1.64	0.89	-0.60	5.36
	NO_2 SCD UV	354	237	1.19	1.59	0.91	-4.05	5.01
F	Height grid 50 m	458	243	0.86	2.32	0.88	-0.01	5.71
	Height grid 200 m	458	243	1.17	0.24	0.88	-2.52	5.68
G	NO_2 SCD error $\times 5$	458	243	1.12	0.25	0.86	-1.95	6.03
H	Radiosonde	458	243	0.93	1.69	0.89	-0.67	5.37
	Aer. retr. only O_4	458	243	0.90	2.16	0.89	-0.63	5.34
	Aer. retr. 2 param.	458	243	1.01	0.16	0.84	-0.25	6.22
	Aer. prof. CEALI	458	243	0.94	3.00	0.82	-2.12	6.63

8.2.3.2 NO_2 Profile Retrieval for the Whole Campaign Duration

The NO_2 profiles were retrieved for the whole duration of the campaign. In these retrievals, the aerosol profiles retrieved using only the O_4 ΔODs at 477 nm were used. Figure 8.31 shows the correlation of the NO_2 surface concentration from MAX-DOAS and in situ measurements. The scatter plots are color coded according to the opaque cloud fraction. The level of agreement increases with decreasing

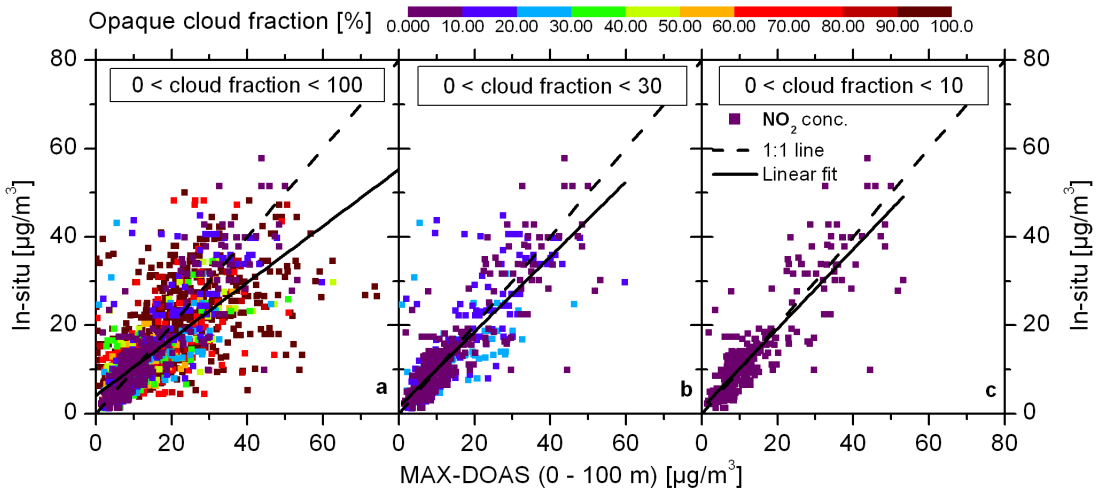

Figure 8.31: *Correlation of the NO_2 surface concentration measured in situ and retrieved from MAX-DOAS for 0–100 m for the period of 3 May to 30 June 2008 and conditions with an opaque cloud fraction of (a) < 100 %, (b) < 30 % and (c) < 10 %. The one to one line is indicated in dashed black and the linear regression in solid black.*

Table 8.5: *The influence of the cloud fraction. Linear regression fit and statistical parameters for the correlations shown in Figure 8.31.*

Cloud fraction	Number of points	Slope	Offset	R	Bias	Standard deviation
$< 100\,\%$	2368	0.64	4.14	0.75	0.88	7.64
$< 30\,\%$	740	0.85	1.51	0.84	0.36	7.64
$< 10\,\%$	378	0.90	1.22	0.88	0.02	5.10

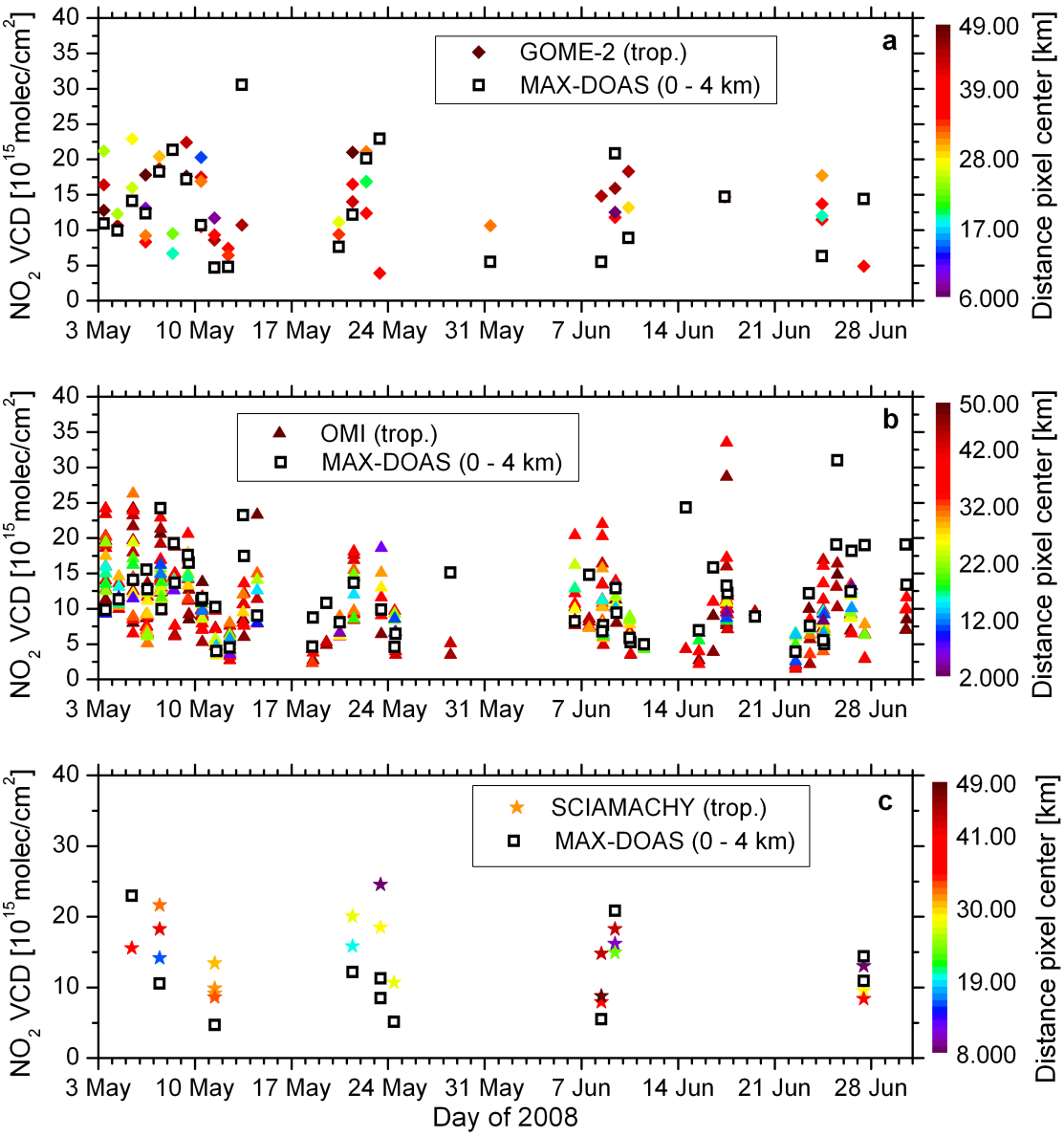

Figure 8.32: *Time series of the NO_2 VCD for the period of 03 May to 30 June 2008 retrieved from MAX-DOAS for 0–4 km and the tropospheric VCD from (a) GOME-2, (b) OMI and (c) SCIAMACHY. The color code is according the distance of the satellite pixel center to the Cabauw site.*

cloud fraction (Table 8.5). Correlation properties, which are comparable to cloudless conditions discussed in Section 8.2.3.1, are achieved for cloud fractions of less than 10 %.
The time series of the NO_2 VCD retrieved from MAX-DOAS and coincident measurements of the different satellite instruments are depicted in Figure 8.32. The relatively large variation of the VCDs measured by OMI reflect the large horizontal variability of the NO_2 distribution, since the OMI instrument has the smallest pixel size compared to the other satellite instruments (see Section 7.2.3). However, the VCDs retrieved from MAX-DOAS agree well with the OMI measurements, with larger differences occurring at large pixel center distances to the Cabauw site. The pixel sizes of the SCIAMACHY and GOME-2 instruments are larger. Therefore, the probed air masses by the SCIAMACHY and GOME-2 instruments and the MAX-DOAS instrument may differ remarkably, which is most probably the reason for the larger differences in the NO_2 VCDs.

8.2.3.3 Retrieval of NO_2 Profiles Using the Regularization Method

Figure 8.33 shows the diurnal variation of the NO_2 profile retrieved by applying different regularization operators. The applied regularization parameters were determined from retrievals using synthetic measurements and the L-curve method (see Section 6.2) The parameter values of 5, 0.1 and 0.05 were used for the the retrievals with the identity matrix, discrete first- and second-derivative operator, respectively. The diurnal development of the NO_2 profiles show comparable features between the different regularization operators. However, the enhanced NO_2 VMRs at altitudes between 500 m and 2 km are attributed to different heights, due to the different strengths of the constraints on the smoothness of the profiles. Table 8.6 summarizes the correlation results for the comparison of the surface concentrations to in situ measurements. The different constraints result in comparably correlated surface concentrations, while the slope of the linear regression differs between the different regularization operators. Best agreement is achieved for the first-derivative operator.

Table 8.6: *The influence of the regularization operator. Linear regression fit and statistical parameters for the correlation of the NO_2 surface concentration (in $\mu g/m^3$) retrieved from in situ measurements and MAX-DOAS for 0–100 m for the period of 6 to 11 May 2008 (see text for details).*

Regularization operator	Regul. param.	Number of points	Slope	Offset	R	Bias	Standard deviation
Unity matrix	5	243	0.73	2.87	0.88	2.03	6.54
first-derivative	0.1	243	1.04	1.29	0.88	-1.90	5.55
second-derivative	0.05	243	1.10	0.62	0.87	-2.08	5.79

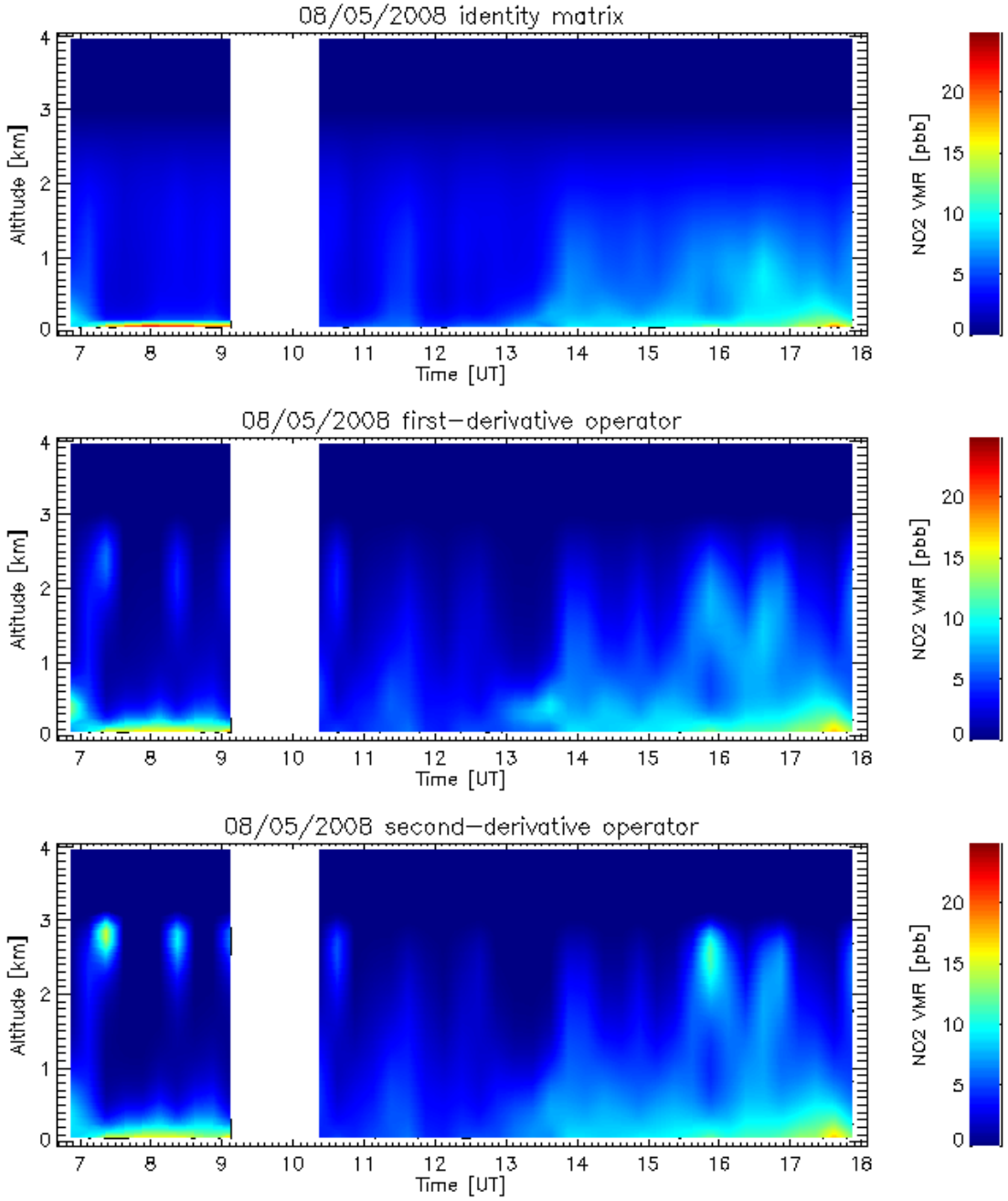

Figure 8.33: *The NO_2 VMR profiles on 8 May 2008 retrieved from MAX-DOAS using different regularization operators: (top) identity matrix, (center) discrete first- and (bottom) second-derivative operator with regularization parameters of 5, 0.1 and 0.05, respectively.*

8.3 Melpitz 2008

The intercomparison campaign in Melpitz took place in the period of 21 May to 9 July 2008. The MAX-DOAS measurements were performed with a constant relative azimuth angle of 90° following the solar azimuthal position in the course of the day. The surroundings of the measurement site are characterized by an agricultural and rural areas with a flat topography, so that only minor obstacles disturbed the field of view of the instrument. The measurements during the time periods between 5:30 and 6:45 UT as well as 9:15 and 10:15 UT were neglected in the analysis. The elevation angles were set to values of 2°, 5°, 10°, 20° and 90° for one measurement sequence. The total integration times per measurement during the elevation scans were set to 60 s for solar zenith angles (SZA) less then 80° and 120 s for SZAs greater 80°.
The meteorological conditions during this campaign were mainly characterized by the presence of a closed cloud cover. Completely cloudless conditions did not occur, while broken cloud cover was occasionally present. Time periods with measurement conditions, which allow the undisturbed retrieval of aerosol profiles from MAX-DOAS O_4 and intensity measurements were strongly limited. In addition, the POLLY lidar instrument failed for two weeks due to a defect of the laser.
The Melpitz site was not equipped with a Sun photometer. Therefore, data from the AEORNET station in Leipzig (located in SW direction at a distance of 41 km to the measurement site) were used for the comparison with the results from MAX-DOAS (Figure 8.1). Figure 8.34 shows the comparison of $\epsilon_M(z)$ at 477 nm retrieved from lidar and MAX-DOAS for the periods of 10:30 to 11:00 UT and 12:30 to 13:00 UT on 10 June 2008. The profiles from MAX-DOAS were retrieved using the standard settings (see page 144) and the O_4 ΔODs and relative intensities. The temperature and pressure profiles were adapted from the climatological data base and ω_0 and g were adapted from Sun photometer measurements. The lidar profiles were deter-

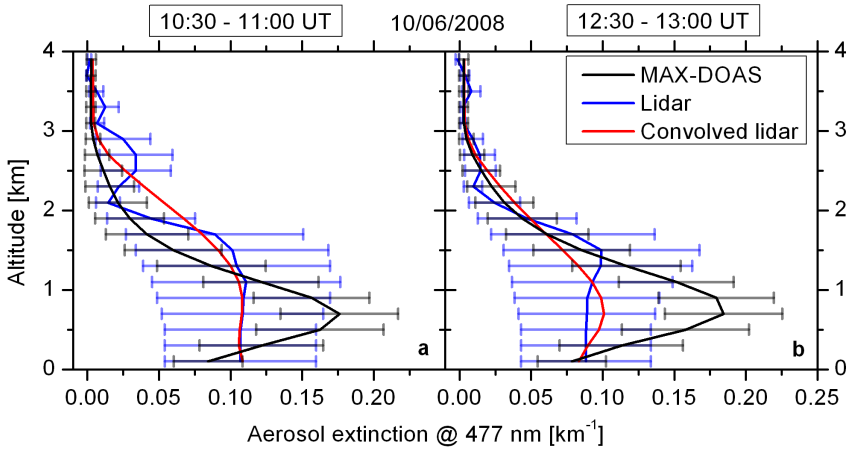

Figure 8.34: *Comparison of $\epsilon_M(z)$ at 477 nm retrieved from lidar and MAX-DOAS for two periods on 10 June 2008. The original (blue) and convolved lidar (red) profiles and the profiles from MAX-DOAS (black).*

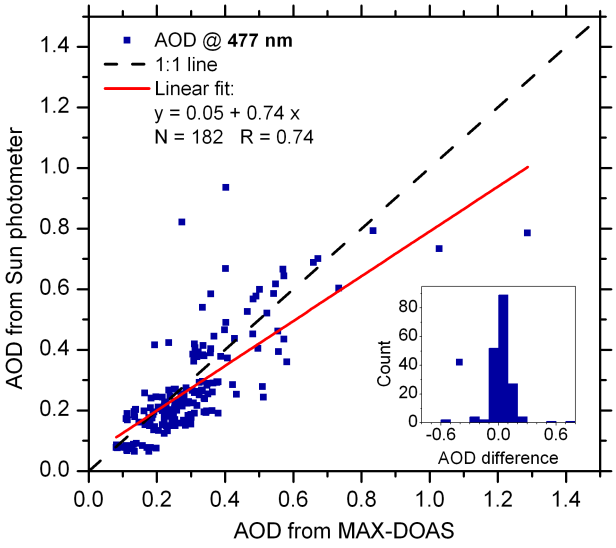

Figure 8.35: *Correlation of the AOD at 477 nm retrieved from Sun photometer in Leipzig and from MAX-DOAS in Melpitz for cloudless conditions during 21 May to 9 July 2008. The one to one line is indicated in dashed black and the linear regression in red. The implemented histograms show the frequency of the differences in the AOD.*

mined using the Fernald-Klett method and the backscatter signal (see Section 7.2.1) and provided by Holger Baars (Institute for Tropospheric Research (IFT), personal communication). The conversion from the lidar wavelength of 532 nm to 477 nm was calculated with α_M from the Sun photometer. The error bars of the lidar profiles in Figure 8.34 indicate the uncertainty due to a change of ± 10 sr in the applied lidar ratio of 50 sr, which is assumed to be constant in height in this case. This uncertainty range illustrates that the appropriate choice of the lidar ratio is crucial and indicates the possible changes in the profile shape due to a height dependent lidar ratio. The error bars of the profiles from MAX-DOAS represent the total (noise + smoothing) retrieval error. The profiles from MAX-DOAS and lidar show good agreement within the uncertainty ranges. The weak $\epsilon_M(z)$ feature between 2 and 3 km in the lidar profile of Figure 8.34a is not resolved by the MAX-DOAS retrieval, due to the limited sensitivity and height resolution at these altitudes indicated by the convolved lidar profile.

The comparison of the AOD for cloudless conditions during the whole duration of the campaign is depicted in Figure 8.35. Although the distance between both sites is roughly 41 km, the retrieved AODs show a high degree of correlation.

8.4 Ispra 2009

The intercomparison campaign in Ispra was carried out, during the period from 11 December 2008 to 25 March 2009. During the winter period, the MAX-DOAS measurements were restricted to shorter daily time periods accompanied by small solar zenith angles. Initially, the MAX-DOAS measurements were performed with a constant relative azimuth angle of 30°. Since the field of view of the instrument was obstructed by trees in the surrounding of the measurement site, the observation geometry was changed to a fixed azimuth angle of 212° roughly corresponding to SSW on 18 February 2009. Due to the obstacles in the field of view, the measurements before 18 February are limited to the second half of the day. The elevation angles were set to values of 2°, 5°, 10°, 20° and 90° for one measurement sequence. The solar zenith angle dependent total integration time of each measurement was set to the same values as in the previous campaigns.
The measurement site in Ispra is equipped with an AERONET Sun photometer and the CAML lidar instrument (see Section 7.2.1). The CAML instrument has an emitter optics, which simultaneously serves as receiver. This concept of the optical bench has the advantage of an overlap region starting at lower altitudes compared

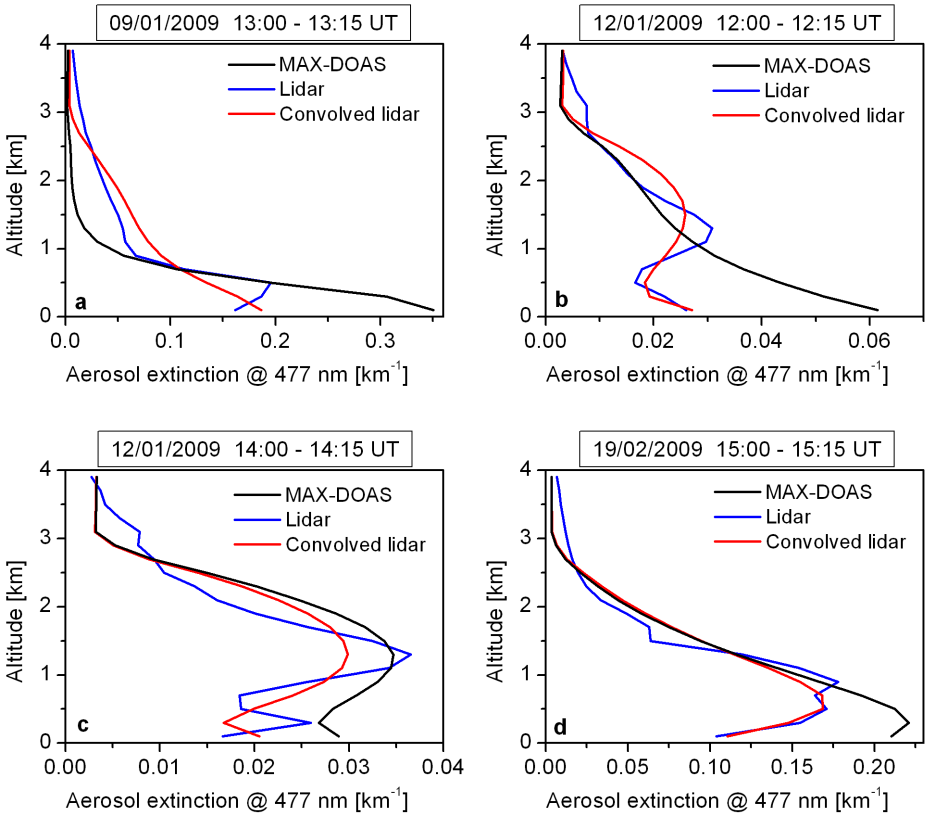

Figure 8.36: *Comparison of $\epsilon_M(z)$ at 477 nm retrieved from MAX-DOAS and lidar for selected time periods: the original (blue) and convolved lidar profiles (red) and the profiles from MAX-DOAS (black).*

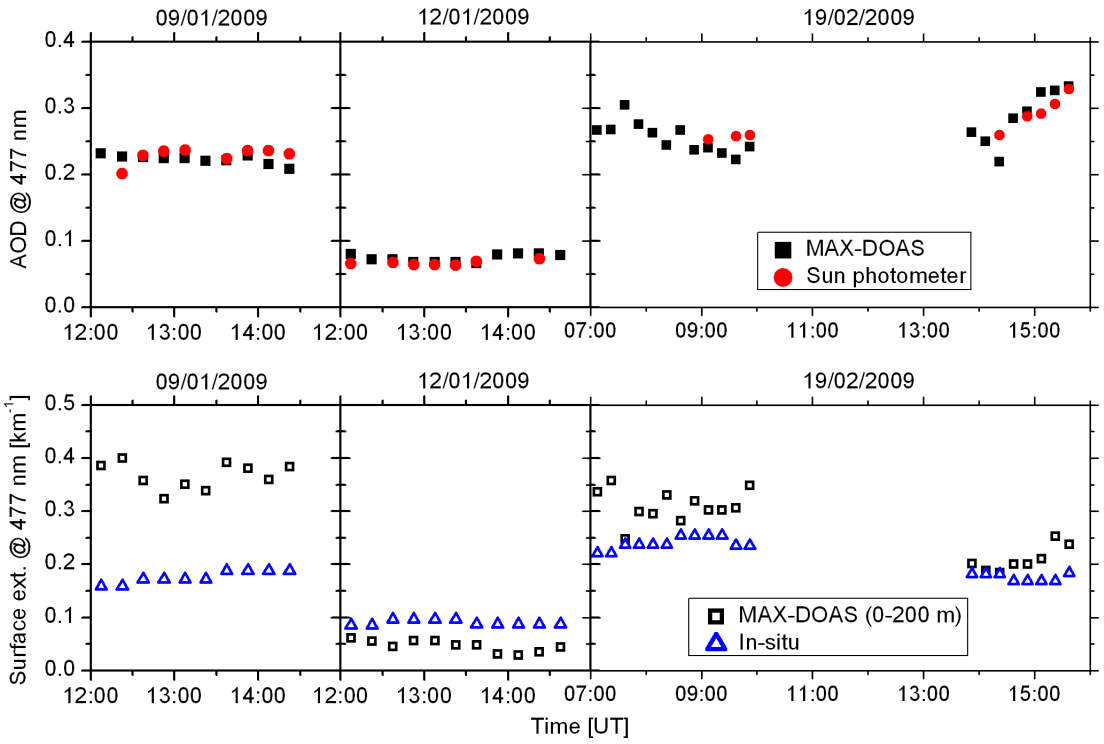

Figure 8.37: *Time series of the (top) AOD at 477 nm retrieved from MAX-DOAS and Sun photometer and (bottom) ϵ_M from MAX-DOAS for 0–200 m and measured in situ for selected time periods.*

to instruments with a separate emitter and receiver. On the other hand, in case of the CAML instrument, it was found that the performance of this single optical bench setup shows remarkable temperature dependencies with respect to the signal quality and overlap region. These effects result in a general overestimation of $\epsilon_M(z)$ at altitudes above 1 to 1.5 km.

Figure 8.36 shows the comparison of $\epsilon_M(z)$ at 477 nm retrieved from lidar and MAX-DOAS for selected periods with cloudless conditions. The profiles from MAX-DOAS were retrieved using the standard settings (see page 144) and the O_4 ΔODs and relative intensities. Temperature and pressure profiles were adapted from the climatological data base. The optical aerosol parameters ω_0 and g were adapted from Sun photometer measurements. The lidar profiles were determined using the Ferald-Klett method and the backscatter signal (see Section 7.2.1) and provided by Maria Adam (European Commission Joint Research Center (EC-JRC), personal communication). The lidar profiles were converted from 532 nm to 477 nm using α_M from the Sun photometer. The comparison of the AODs retrieved from MAX-DOAS and Sun photometer for cloud free conditions is depicted the upper panel of Figure 8.35. The lower panel shows the comparisons of ϵ_M retrieved from MAX-DOAS for 0–200 m and in situ measurements. The latter were determined from a combination of nephelometer and aethalometer measurements (see Section 7.2.2.1) and were provided by Carsten Grüning (EC-JRC, personal communication).

The aerosol profiles retrieved from MAX-DOAS compare very well with the profiles

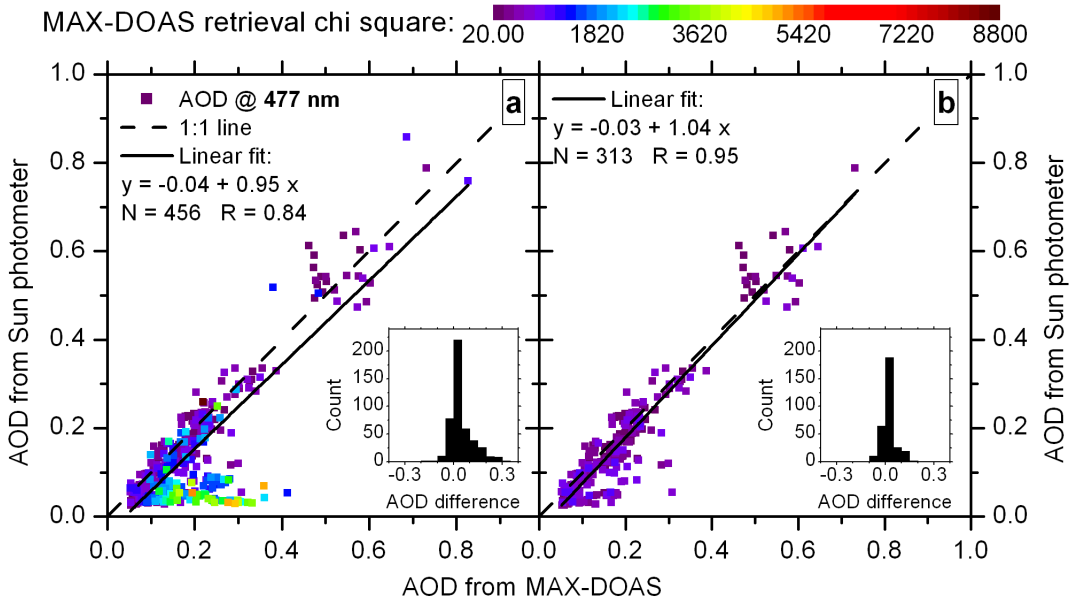

Figure 8.38: *Correlation of the AOD at 477 nm retrieved from Sun photometer and MAX-DOAS for the period of 11 December 2008 to 25 March 2009, color coded according χ^2 of the MAX-DOAS retrieval: (a) all data points and (b) cases with $\chi^2 < 1000$. The one to one line is indicated in dashed black and the linear regression in solid black. The implemented histograms show the frequency of the differences in the AOD.*

from lidar. The height of the shallow boundary layer on 9 January 2009 is reproduced very well by the MAX-DOAS retrieval (Figure 8.36a). The linearly decreasing shape of the lidar profile above ≈ 1 km is rather due to the above mentioned problem of the optics than a true feature. Since the lidar profiles are constrained with the AOD from Sun photometer, the overestimations in the profile at higher altitudes result in the opposite for the lowermost altitudes. Therefore, the extinction values from MAX-DOAS retrieved for the lower altitudes are generally higher than the lidar profiles. The elevated aerosol layer present in the afternoon of 12 January 2009 is reproduced by MAX-DOAS as well as the boundary layer height on 19 February 2009 (Figures 8.36c and 8.36d, respectively). While the AODs from MAX-DOAS and Sun photometer show an excellent agreement for the considered periods, the aerosol extinctions at the surface measured in situ remarkably differ from the MAX-DOAS values (Figure 8.37).

Figure 8.38 shows the correlation of the AODs for the period of 11 December 2008 to 25 March 2009, color coded according χ^2 of the MAX-DOAS profile retrieval, which is determined by equation (5.2). The correlation of the data set improves significantly when the AODs from MAX-DOAS retrievals with $\chi^2 > 1000$ are neglected. Although the availability of level 2 AERONET data indicates cloudless conditions during direct Sun observations (see Section 7.2.1), the MAX-DOAS measurements can be influenced by scattered clouds at the same time. The dependency of the correlation on χ^2 illustrated in Figure 8.38 can be used to determine a threshold

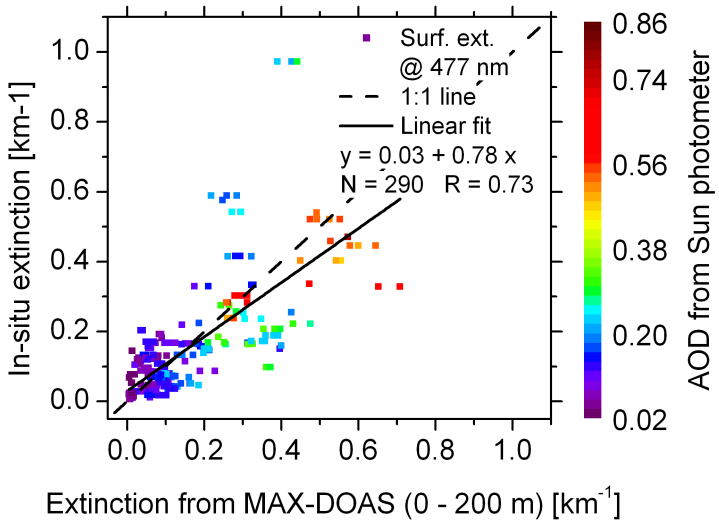

Figure 8.39: *Correlation of ϵ_M at 477 nm retrieved from MAX-DOAS for 0–200 m and measured in situ for the period of 11 December 2008 to 25 March 2009, color coded according the AOD from Sun photometer. The one to one line is indicated in dashed black and the linear regression in solid black.*

value of χ^2, which enables to filter the MAX-DOAS results to ensure high quality AOD measurements.
The correlation of the aerosol extinction at the surface from MAX-DOAS and in situ measurements is shown Figure 8.39. While the values from the different instruments differ during the short periods of Figure 8.37, the retrieved surface aerosol extinctions for the period of 11 December 2008 to 25 March 2009 during cloudless conditions are well correlated. In contrast to the correlation observed during the field campaign in Cabauw in 2008 (Figure 8.14), the measurements of ϵ_M at 477 nm in Ispra do not show larger differences at higher AODs and the slope of the linear regression is closer to one.

8.5 Leipzig 2009

The intercomparison campaign in Leipzig was performed in the period from 8 to 29 May 2009. The instrument was set up on the roof of the Institute for Tropospheric Research (IFT). Due to the surrounding buildings, the azimuth angle of the MAX-DOAS viewing geometry was set to a fixed value of 180°, i.e. pointing to the South. The elevation angles were set to values of 2°, 5°, 10°, 20° and 90°. The total integration time for each spectrum recorded for the according viewing geometry was set to the same values as in the previous campaigns.

As an AERONET site, the IFT is equipped with a Sun photometer. The lidar measurements were performed with the POLLY instrument, which was also deployed during the field campaign in Melpitz (Section 8.3). The aerosol profiles from lidar were determined in the same way using the Fernald-Klett method (see Section 7.2.1) and provided by Holger Baars (IFT, personal communication).

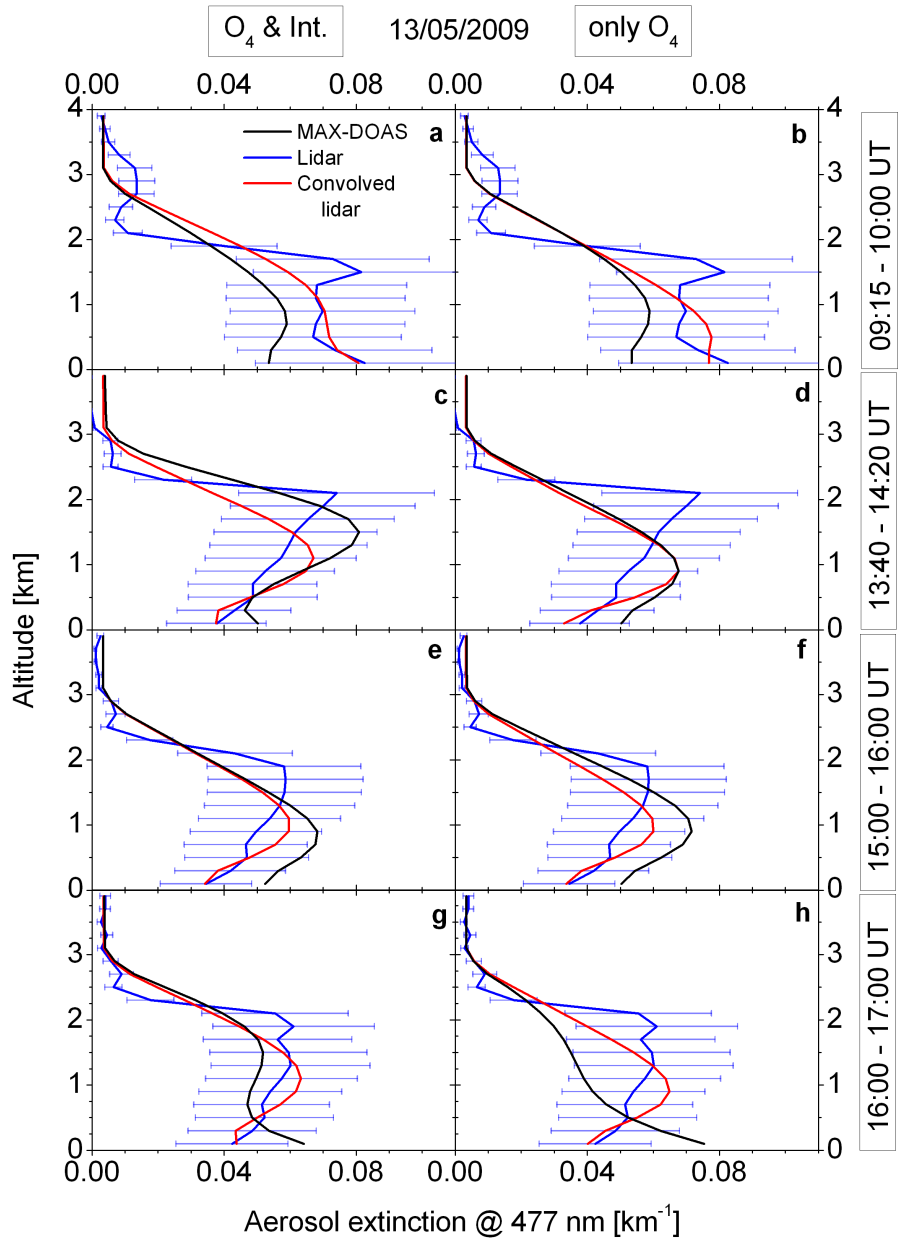

Figure 8.40: *Comparison of $\epsilon_M(z)$ at 477 nm retrieved from lidar and MAX-DOAS using (left panels) the O_4 ΔODs and relative intensities and (right panels) only the O_4 ΔODs for selected periods of 13 May 2009: the original (blue) and convolved lidar profiles (red) and the profiles from MAX-DOAS (black).*

The MAX-DOAS retrieval settings and parameters used for the previous campaigns in Melpitz and Ispra were adapted for the retrievals presented for this campaign. The comparison of the profiles is depicted in Figure 8.40 for cloudless periods on 13 May 2009. In addition to the profiles retrieved from MAX-DOAS using the O_4 ΔODs and relative intensities at 477 nm, the results of retrievals with measurement

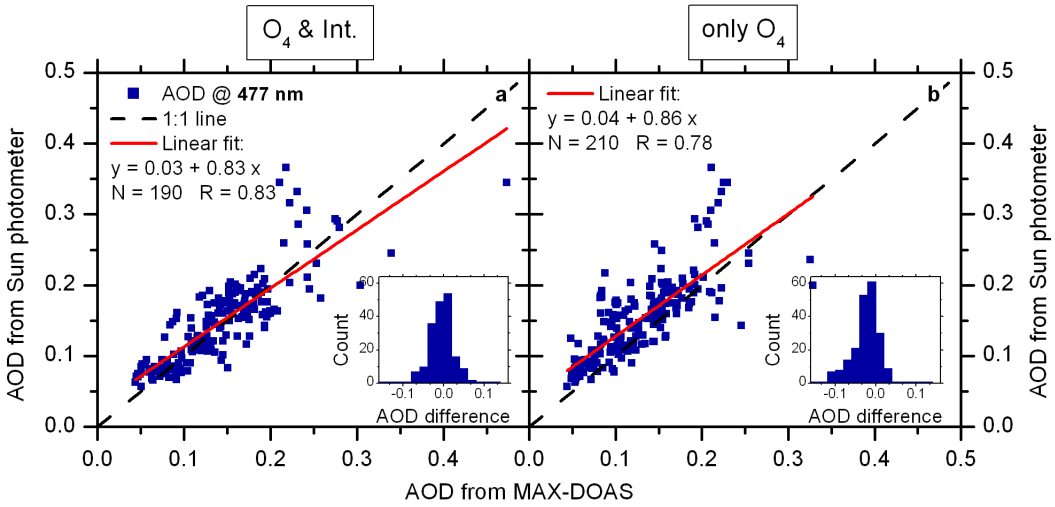

Figure 8.41: *Correlation of the AOD at 477 nm retrieved from Sun photometer and MAX-DOAS using (a) the O_4 ΔODs and relative intensities and (b) only the O_4 ΔODs for the period of 8 to 29 May 2009. The one to one line is indicated in dashed black and the linear regression in red. The implemented histograms show the frequency of the differences in the AOD.*

vectors consisting only of O_4 ΔODs are shown for comparison in the panels on the right hand side. In the morning hours, the profiles from MAX-DOAS using different measurement vectors show no significant differences and compare well with the profiles from lidar within their uncertainty range (Figure 8.40a and 8.40b). This range illustrates the changes in the lidar profile when the lidar ratio varies by $\pm$10 sr around the used value of 50 sr. The small peak in aerosol extinction between 2–4 km measured by lidar between 09:15 and 10:00 UT is not reproduced by MAX-DOAS due to the lower sensitivity for these altitudes. The increased boundary layer top height between 13:40 and 14:20 UT and the sharp edge in the aerosol distribution with decreasing extinction towards the ground, indicated by the lidar profile, is reproduced differently by two MAX-DOAS retrievals (Figure 8.40c and 8.40d). The consideration of the relative intensities in the measurement vectors slightly increases the sensitivity at higher altitudes, which results in a shift of the retrieved maximum extinction toward higher altitudes. This increased sensitivity also results in the better agreement of the profiles from lidar and MAX-DOAS when the intensities are considered for the period of 16:00 to 17:00 UT. For the whole campaign duration, the AODs retrieved for cloudless conditions from MAX-DOAS and Sun photometer compare well and the correlation improves when the relative intensities are considered in the MAX-DOAS retrievals (Figure 8.41). Thus, the retrievals using only the O_4 ΔODs in the measurement vector deliver sufficient results, but atmospheric conditions can occur in which the consideration of the relative intensities improves the accuracy of the results.

8.6 CINDI 2009

The MAX-DOAS instrument was installed at the Cabauw site on 9 June 2009 to perform a long term intercomparison campaign, which was scheduled in the scope of the EUSAAR project. This schedule allowed for the participation in the CINDI (Cabauw Intercomparison of Nitrogen Dioxide measuring Instruments) campaign, in the period of 9 June to 8 July 2009. After this period, the instrument remained in Cabauw and made continuous measurements until 12 April 2010. The results of this long term measurements are addressed in the Section 8.7, while this section contains the results from the CINDI campaign.
Around 22 MAX-DOAS instruments operated by different working groups from all over the world made simultaneous measurements of atmospheric trace gases during the CINDI campaign. The main focus of the campaign was on the measurement of NO_2, HCHO and O_4, as well as the retrieval of trace gas and aerosol profiles from MAX-DOAS measurements. An overview of this campaign is given in Piters et al. (2011) including selected highlights of the campaign outcomes. A detailed comparison of the NO_2 and O_4 dSCDs retrieved from the measurements of the different MAX-DOAS instruments is presented in Roscoe et al. (2010), showing that they are mostly consistent within 5 to 10 %, when retrieved with standardized settings.
In addition to the standardized settings of the DOAS retrieval, the participating instruments made measurements for standardized viewing geometries. The elevation angles were set to 2°, 4°, 8°, 15°, 30° and 90°, and differ from the values for the previous campaigns. The azimuth angle of the viewing direction was set to 287°

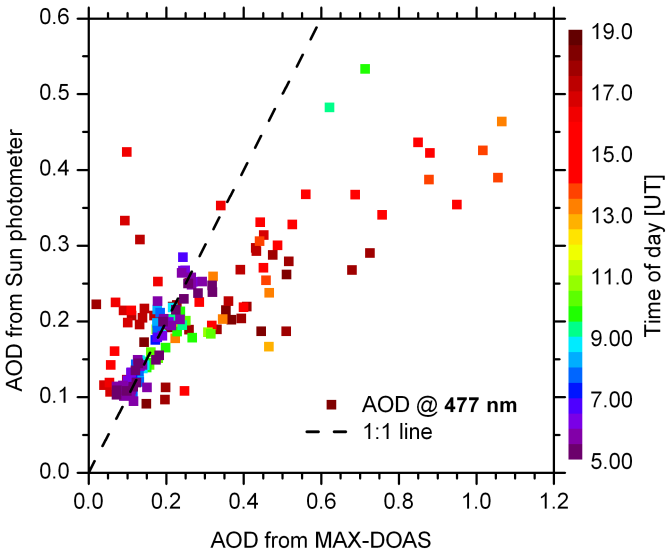

Figure 8.42: *Correlation of the AOD at 477 nm retrieved from Sun photometer and MAX-DOAS using the O_4 ΔODs and relative intensities for conditions with opaque cloud fractions $< 10\,\%$ in the period of 9 June to 8 July 2009, color coded according to the time of day. The one to one line is indicated in dashed black. The larger differences in the AODs occur in the afternoon.*

(WNW). The total integration times per measurement were set to 60 s for SZAs less than 80° and 120 s for SZAs greater than 80°.

8.6.1 Retrieval of Aerosol Extinction Profiles and Optical Depths

The value for the constant azimuth angle of the viewing direction, on which the participating groups agreed, has an implication on the results of the MAX-DOAS aerosol profile retrieval. In the afternoon, when the Sun is proceeding to set, the relative azimuth angles become smaller than ≈ 25°. The viewing directions close to the Sun increased the difficulties for the correct modeling of the aerosol phase function in the radiative transfer calculations, which affected the retrieval and is illustrated in Figure 8.42. It shows the comparison of the AOD retrieved from Sun photometer and MAX-DOAS using the optimal estimation method with the O_4 ΔODs and relative intensities as measurement vector. The retrieval settings and parameters were selected according the standard settings (see page 144). The comparison dataset in Figure 8.42 for the period of 9 June to 8 July 2009 considers conditions with an opaque cloud fraction less than 10 % to minimize the interference of the retrieval with clouds. The larger differences in the AODs from MAX-DOAS and Sun photometer occur in the afternoon, for small relative azimuth angles. These deviations can be attributed to larger discrepancies between the measured and modeled relative intensities, which were determined in Section 8.2.1 by the comparison of the measured relative intensities of the azimuthal scans to radiative transfer calculations using independent aerosol data (Figure 8.5). Therefore, the retrievals of the aerosol profiles were performed using only the O_4 ΔODs in the measurement vector. The retrieved AODs are compared to Sun photometer measurements in Figure 8.43 for the whole campaign duration. Increased AODs are retrieved from MAX-DOAS for conditions with opaque cloud fraction larger than ≈ 30 % and the highest values generally occur for cloud fractions larger than ≈ 50 %. The AODs from MAX-DOAS for these high cloud fractions are shown to illustrate the influence of clouds on the retrieval results. These values should rather be regarded as effective aerosol optical depths than the true optical depths caused by the presence of clouds, since an appropriate consideration of clouds in the radiative transfer model is challanging and not applied in these retrievals. The AODs from MAX-DOAS for conditions with a cloud fraction smaller than ≈ 30 % compare well with the Sun photometer measurements. Their correlation improves when regarding measurements for cloud fractions smaller than 10 % (Figure 8.44).

During the CINDI campaign, in situ measurements of aerosol scattering coefficients were performed with the humidified nephelometer developed and operated by PSI (see Seciton 7.2.2.1). These measurements were combined with aethalometer and MAAP measurements of the aerosol absorption coefficient to calculate ϵ_M. The comparison of ϵ_M retrieved from MAX-DOAS for 0–200 m and measured in situ during the CINDI campaign and the subsequent period until October 2009 is discussed in detail in Zieger et al. (2011) for a previous version of the MAX-DOAS profile retrieval, in which the radiative transfer model SCIATRAN 1 (Rozanov et al., 2002)

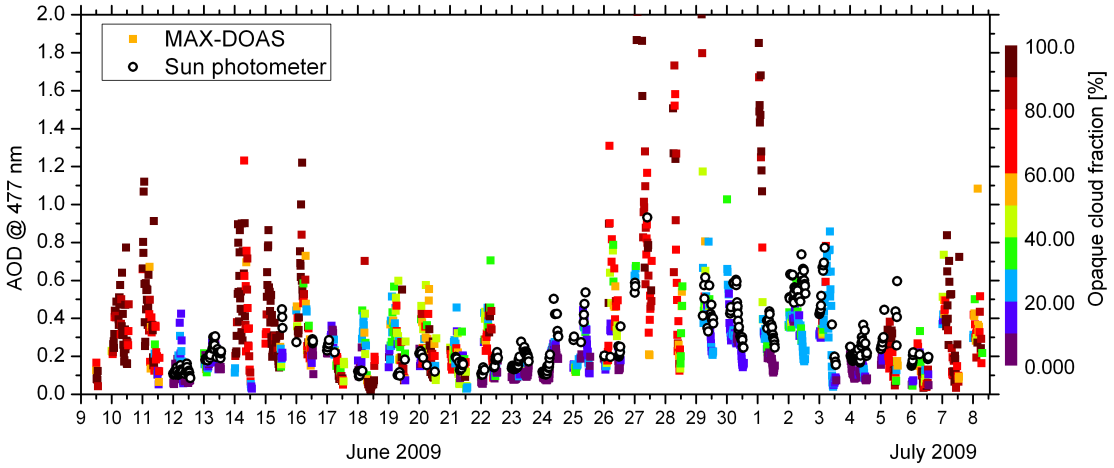

Figure 8.43: *Time series of the AOD at 477 nm retrieved from Sun photometer (open black circles) and MAX-DOAS (solid squares) using only the O_4 ΔODs for the period from 9 June to 8 July 2009, color coded according to the opaque cloud fraction.*

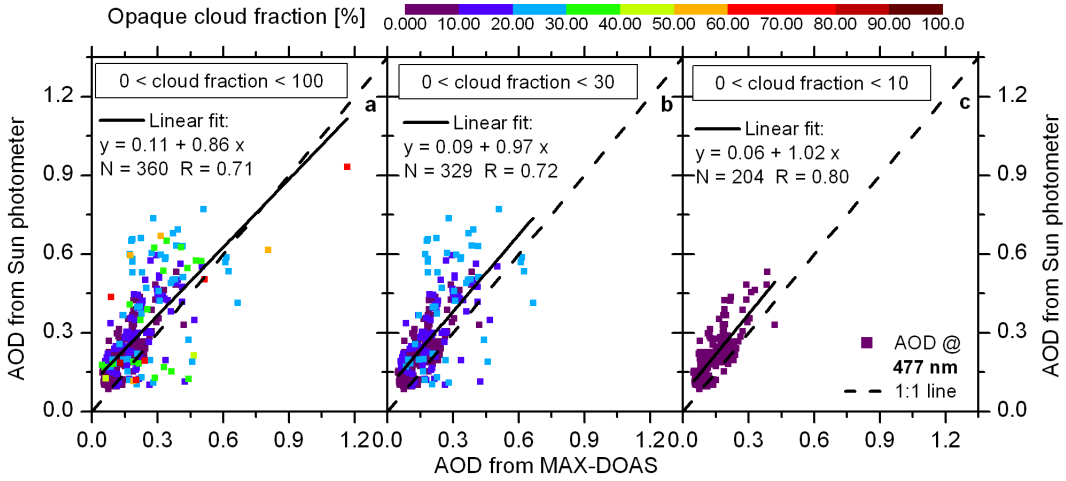

Figure 8.44: *Correlation of the AODs from Sun photometer and MAX-DOAS shown in Figure 8.43 for conditions with an opaque cloud fraction of (a) < 100 %, (b) < 30 % and (c) < 10 %. The one to one line is indicated in dashed black and the linear regression in solid black. The correlation improves for decreasing cloud fractions.*

was used.

Figure 8.45 shows the times series of ϵ_M measured in situ and retrieved from MAX-DOAS for 0–200 m for the period of the CINDI campaign. The MAX-DOAS retrievals were performed using only the O_4 ΔODs and the radiative transfer model SCIATRAN 2. The comparison features a similar relationship between ϵ_M and the prevailing cloud fraction as in Figure 8.43. As observed during the first intercom-

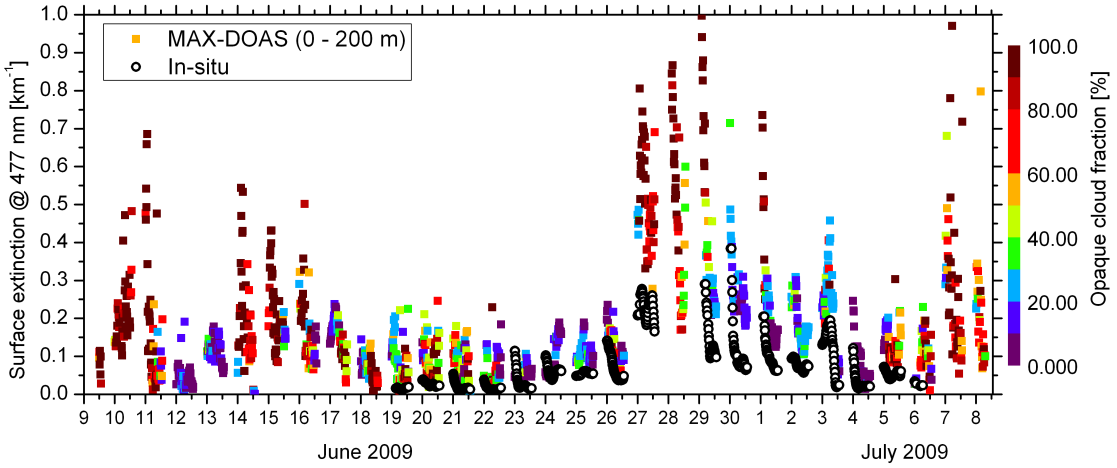

Figure 8.45: *Time series of ϵ_M at 477 nm measured in situ (open black circles) and retrieved from MAX-DOAS (solid squares) for 0–200 m using only the O_4 ΔODs for the period of 9 June to 8 July 2009, color coded according the opaque cloud fraction.*

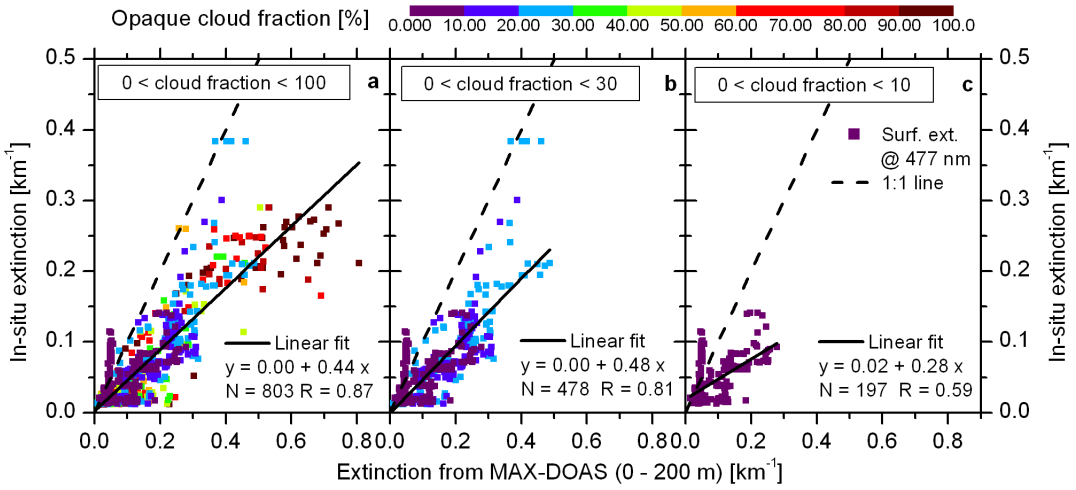

Figure 8.46: *Correlation of ϵ_M at 477 nm from MAX-DOAS and in situ measurements shown in Figure 8.45 for conditions with an opaque cloud fraction of (a) < 100 %, (b) < 30 % and (c) < 10 %. The one to one line is indicated in dashed black and the linear regression in solid black. An improvement of the correlation with decreasing cloud fraction is not observed.*

parison campaign in Cabauw 2008, the retrieved surface aerosol extinction from MAX-DAOS is generally larger than the in situ measurements. In contrast to the AODs, the correlations of ϵ_M for cases considering all data points and conditions with opaque cloud fractions of less than 30 % are comparable, while a further limitation of the considered data to conditions with opaque cloud fractions of less than 10 % degrades the correlation. This indicates that the surface extinction retrieval from MAX-DOAS is not much affected by clouds. During the field campaign in

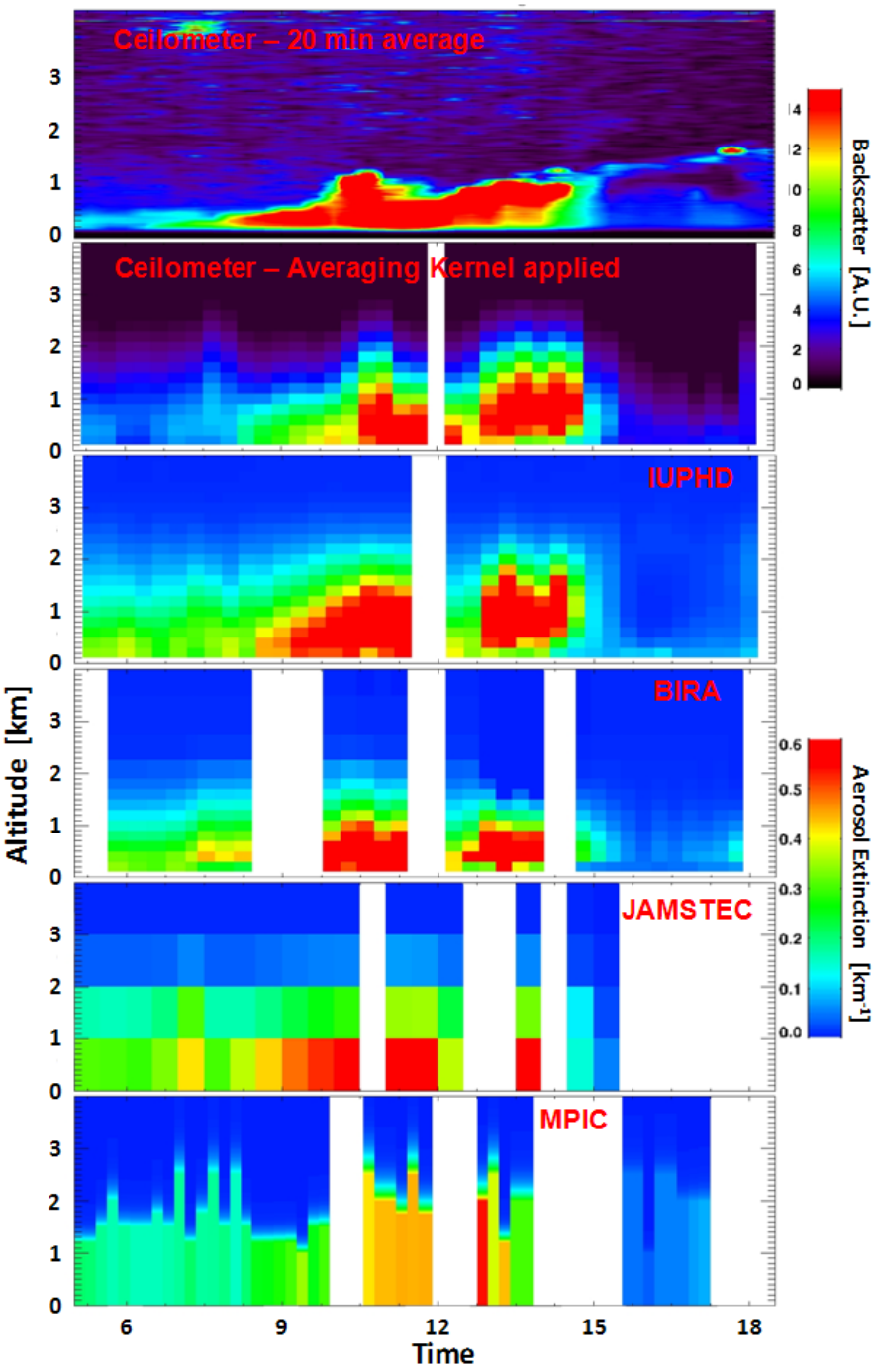

Figure 8.47: *Comparison of the aerosol profiles retrieved from MAX-DOAS O_4 measurements of different groups for 3 July 2009. The top plot shows the backscatter profile from ceilometer and the second plot shows the convolved profiles from ceilometer. The plots below that show $\epsilon_M(z)$ retrieved from MAX-DOAS instruments from BIRA, IUPHD, JAMSTEC and MPIC (top-down), respectively (Udo Frieß, IUPHD, personal communication).*

Cabauw in 2008, a better agreement in ϵ_M was achieved for the in situ and MAX-DOAS measurements for a similar limitation of the considered data set (see Figure 8.18c). Thus, in addition to the difficulties of a comparison of ϵ_M from MAX-DOAS and in situ measurements, which was discussed in Section 8.2.2, uncertainties which are specific for the used humidified nephelometer instrument could be the reason for the worse correlation in Figure 8.46. The additional drying and humidifying of the drawn particles could result in underestimations of certain aerosol types due to their loss during these processes.

A further objective of the CINDI campaign was the comparison of aerosol profiles retrieved from MAX-DOAS O_4 ΔOD measurements of the different groups. An example for this ongoing study is shown Figure 8.47. The different DOAS groups apply different approaches for the aerosol profile retrievals. BIRA (Belgian Institute for Space Aeronomy, Brussels, Belgium) applies the optimal estimation method for the retrieval of the complete aerosol profile (see Clémer et al., 2010, for details). JAMSTEC (Japan Agency for Marine-Earth Science and Technology, Yokohama, Japan) also applies the optimal estimation method, but retrieves the profile on a coarse height grid of 1 km vertical resolution (see Irie et al., 2011, for details). MPIC (Max Planck Institute for Chemistry, Mainz, Germany) applies a least squares approach in which the aerosol profile is described by two parameters (see Wagner et al., 2011, for details). The profiles in the panel indicated by IUPHD (Institute of Environmental Physics, Heidelberg, Germany) were retrieved in the scope of this work using the optimal estimation method and a previous version of the retrieval, which used the radiative transfer model SCIATRAN 1. The two panels at the top of Figure 8.47 shows the averaged and convolved profiles from the LD40 ceilometer (see Section 7.2.1). The RCS from ceilometer was provided by Henk Klein Baltink (The Royal Netherlands Meteorological Institute (KNMI), personal communication).
The retrieved aerosol extinction profiles from IUPHD and BIRA show good agreement with respect to the absolute extinction values and the diurnal development of the boundary layer. Also their qualitative comparison to the profiles from ceilometer exhibit an overall good agreement. The profiles from JAMSTEC and MPIC differ from the profiles retrieved by IUPHD and BIRA due to the difference in the applied retrieval approaches.

8.6.2 Retrieval of NO_2 Profiles

The aerosol profiles retrieved using the O_4 ΔODs served as input for the NO_2 profile retrievals, which were performed using the standard settings for the trace gas profile retrieval (see page 165).
The time series of the retrieved NO_2 VCDs is compared to satellite measurements of the SCIAMACHY, OMI and GOME-2 instruments in Figure 8.48a. The comparison considers only simultaneous MAX-DOAS and satellite measurements. Furthermore, satellite measurements with cloud radiance fractions larger than 50 % were neglected. Figure 8.48b shows the time series of the NO_2 surface concentration measured in situ and retrieved from MAX-DOAS for 0–100 m for conditions with an opaque cloud fraction of less than 30 % determined by the total sky imager. The NO_2 VCDs

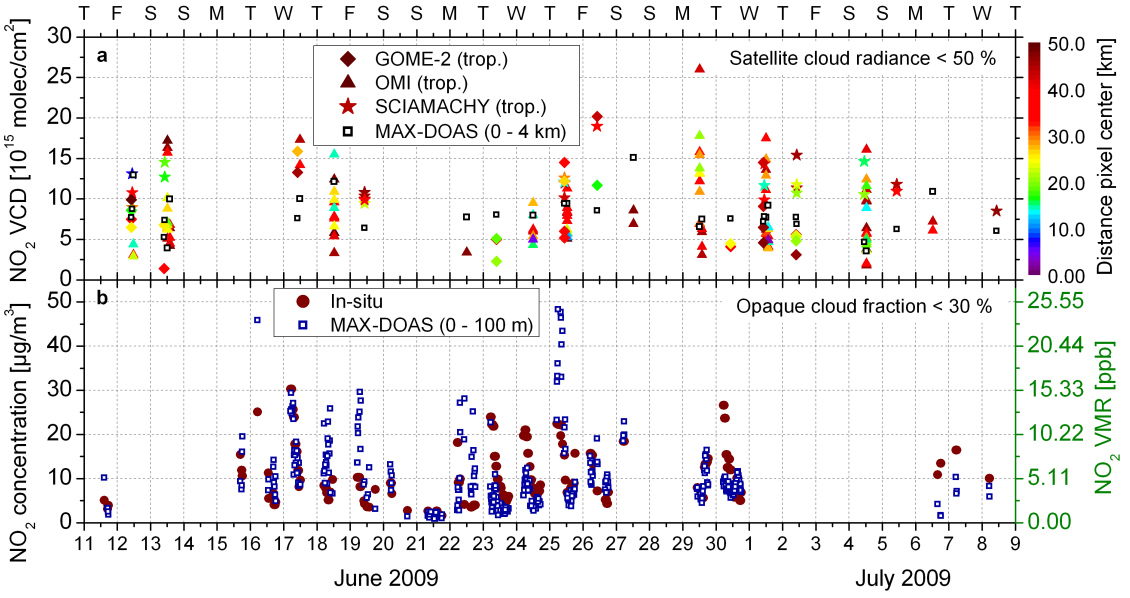

Figure 8.48: *Time series of the NO_2 VCD and surface concentration for the period of 11 June to 8 July 2009: (a) NO_2 VCD retrieved from MAX-DOAS for 0–4 km (open black squares) and the tropospheric VCD from SCIAMACHY (stars), OMI (triangles) and GOME-2 (diamonds) color-coded according the distance of the satellite pixel center to the Cabauw site; (b) NO_2 concentration measured in situ (solid red circles) and retrieved from MAX-DOAS for 0–100 km (open blue squares).*

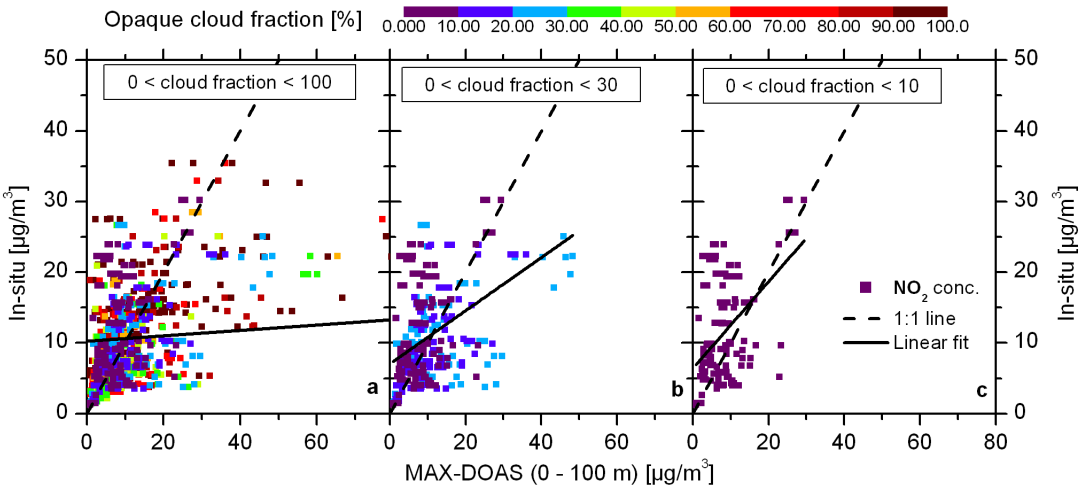

Figure 8.49: *Correlation of the NO_2 surface concentration measured in situ and retrieved from MAX-DOAS for 0–100 m for the period of 9 June to 8 July 2009 and conditions with an opaque cloud fraction of (a) < 100 %, (b) < 30 % and (c) < 10 %. The one to one line is indicated in dashed black and the linear regression in solid black.*

Table 8.7: *The influence of the cloud fraction. Linear regression fit and statistical parameters for the correlations shown in Figure 8.49.*

Cloud fraction	Number of points	Slope	Offset	R	Bias	Standard deviation
$< 100\,\%$	938	0.04	10.26	0.23	2.61	39.92
$< 30\,\%$	364	0.38	7.05	0.46	-0.76	7.65
$< 10\,\%$	150	0.61	6.37	0.50	-3.15	6.68

retrieved from MAX-DOAS favorably compare with the satellite observations. In cases with a large variation of the NO_2 VCD measured by the satellite instruments for a certain time period, the values retrieved from MAX-DOAS are within the variation range. In cases with individual satellite measurements, the differences to the VCD from MAX-DOAS tend to be larger for longer distances of the satellite pixel center to the Cabauw site. The agreement of the NO_2 surface concentrations retrieved from MAX-DOAS and in situ measurements is poorer compared to the observations during the field campaign in Cabauw in 2008 (see Figure 8.31). However, the correlation improves when only conditions with an opaque cloud fraction of less than 10 % are considered (Figure 8.49 and Table 8.7).

8.7 Cabauw 2009 and 2010

After the CINDI campaign, the MAX-DOAS instruments remained installed at the Cabauw site to perform a long-term intercomparison until 12 April 2010. For these measurements, the viewing geometry of the instrument was changed to follow the azimuthal position of the Sun with a constant relative azimuth angle of 30°. The elevation angles of 2°, 4°, 8°, 15°, 30° and 90° were adapted from the settings used during the CINDI campaign. The total integration times for the measured spectra were equal to the values used in the previous campaigns.

8.7.1 Retrieval of Aerosol Extinction Profiles and Optical Depths

The aerosol profile retrievals were performed using the standard settings (see page 144). Figure 8.50a shows the correlation of the AOD retrieved from MAX-DOAS and Sun photometer for the period of 9 July 2009 to 11 April 2010, while Figure 8.50b depicts the correlation of ϵ_M measured in situ and retrieved from MAX-DOAS for the surface layer. For these comparisons, only the measurements for conditions with an opaque cloud fraction of less than 10 % are considered. Since the humidified nephelometer was installed at the Cabauw site only until the end of October 2009, the comparison data set for ϵ_M includes less measurements than the AOD comparison. The comparison of ϵ_M shows that the values retrieved from MAX-DOAS are generaly larger than the in situ measured ones, which was also observed during the CINDI camapaign and is most probably attributable to the effects described in Section 8.6.1. However, the good agreement of the AODs and the well correlated suface

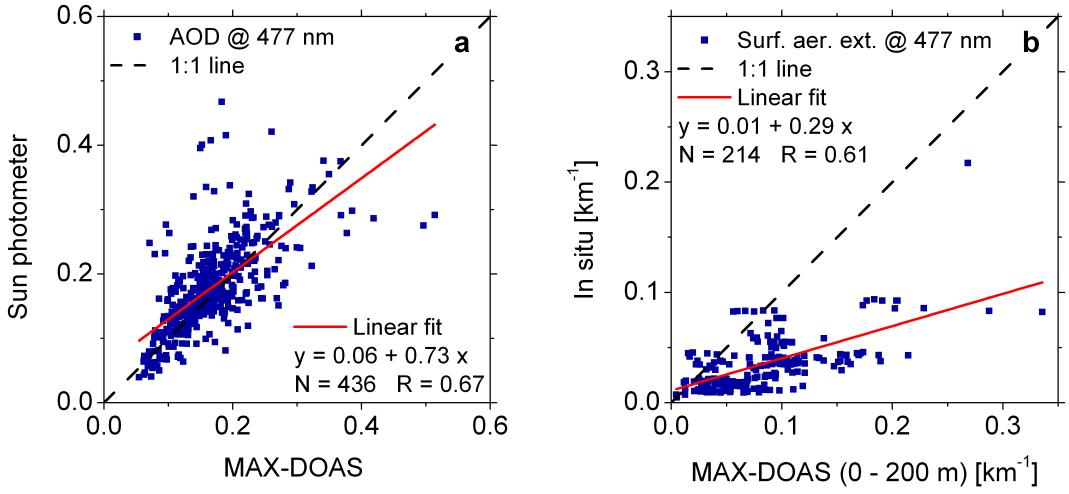

Figure 8.50: *Correlation of the (a) AOD and (b) ϵ_M at 477nm retrieved from MAX-DOAS, Sun photometer and in situ measurements for cloudless conditions during 9 July 2009 to 11 April 2010. The one to one line is indicated in dashed black and the linear regression in red.*

extinctions for the long time period demonstrate the capability of the MAX-DOAS aerosol retrieval to provide reliable information on atmospheric aerosols over long a time period.

8.7.2 Retrieval of NO_2 Profiles

The results of the NO_2 profile retrievals for the long-term measurements are shown in Figure 8.51. The aerosol extinction profiles retrieved from MAX-DOAS served as input for the NO_2 profile retrievals. The compared VCDs retrieved from MAX-DOAS and the different satellite instruments consider only simultaneous measurements with cloud radiance fractions less than 50 % with respect to the satellite observations. The NO_2 surface concentrations are shown for conditions with an opaque cloud fraction of less than 30 %. The time series in Figure 8.51 illustrates that MAX-DOAS is a powerful tool. It provides reliable information on the vertical distribution of atmospheric NO_2 and enables measurements containing information whose determination usually requires several different measurement techniques.

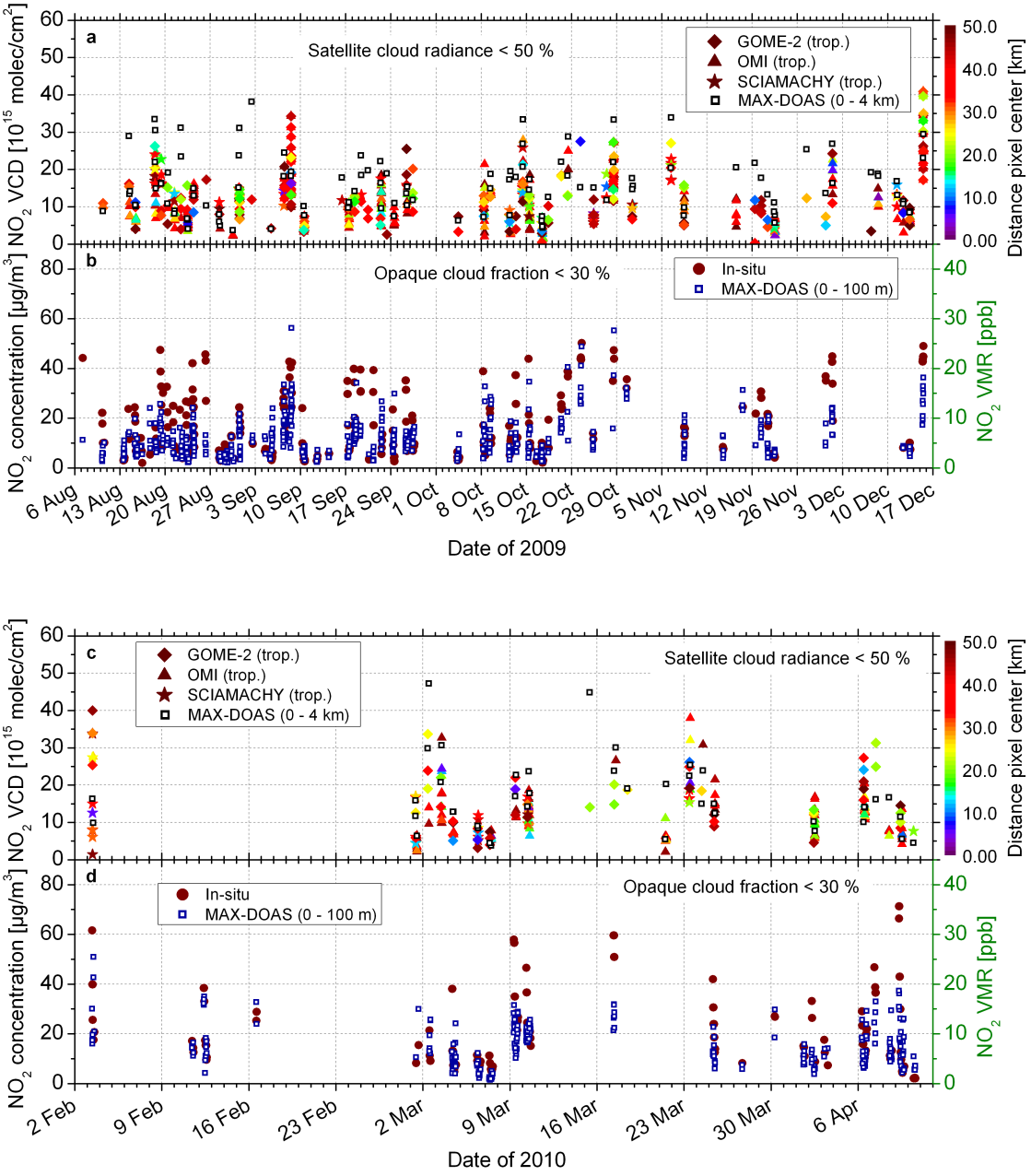

Figure 8.51: *Time series of the NO_2 VCD and surface concentration for the period of (a,b) 9 July to 17 December 2009 and (c,d) 2 February to 11 April 2010: (a,c) NO_2 VCD retrieved from MAX-DOAS for 0–4 km (open black squares) and the tropospheric VCD from SCIAMACHY (stars), OMI (triangles) and GOME-2 (diamonds) color-coded according the distance of the satellite pixel center to the Cabauw site; (b,d) NO_2 concentration measured in situ (solid red circles) and retrieved from MAX-DOAS for 0–100 km (open blue squares).*

8.8 Observation of the Volcanic Plume of Eyjafjallajokull over Heidelberg in 2010

In March 2010 the Eyjafjallajokull volcano, situated at the southern part of Iceland (Figure 8.52), started to erupt after being in a state of unrest for more than 15 years (e.g., Pedersen and Sigmundsson, 2004) with a more intense seismic unrest beginning in 2009 (Sigmundsson et al., 2010). The eruption was a small to intermediate size eruption, but due to its large amount of ash emission combined with the intermittent prevailing wind direction from northwest it caused high levels of dust in the mid-troposphere, which led to the closure of the European airspace between the 14 and 20 April 2010 and in some places even until the 18 May 2010. The 2010 Eyjafjallajokull eruption lasted until 19 May 2010.
Ash emission during volcanic eruptions is a common phenomenon, nothing unexpected or new, nevertheless not much attention was paid to the potential problems Icelandic volcanic eruptions can cause on the European and American air traffic. Notwithstanding volcanic eruptions take place on Iceland on average about every 4 years (Gudmundsson et al., 2010). Volcanoes generally emit large amount of aerosols and gases, the latter being mainly H_2O, CO_2, SO_2 and lower levels of hydrogen halides in the state of quiescent degassing as well as during eruptions. Ash emission is usually observed in phases of higher volcanic activity and often accompanied by increased gas emissions. Due to the high atmospheric background, volcanic H_2O and CO_2 are usually difficult to measure with remote sensing methods available today. In contrast, SO_2 is the easiest measurable gas tracer of volcanic plumes. In aged volcanic clouds, a separation of SO_2 and ash can appear due to fall out of larger particles resulting in a movement of both clouds in different directions due to wind shear. For young volcanic clouds, SO_2 and ash concentrations remain highly correlated up to three days after the emission (Schumann et al., 2011).
Shortly after the long-term measurements in Cabauw, the MAX-DOAS instrument

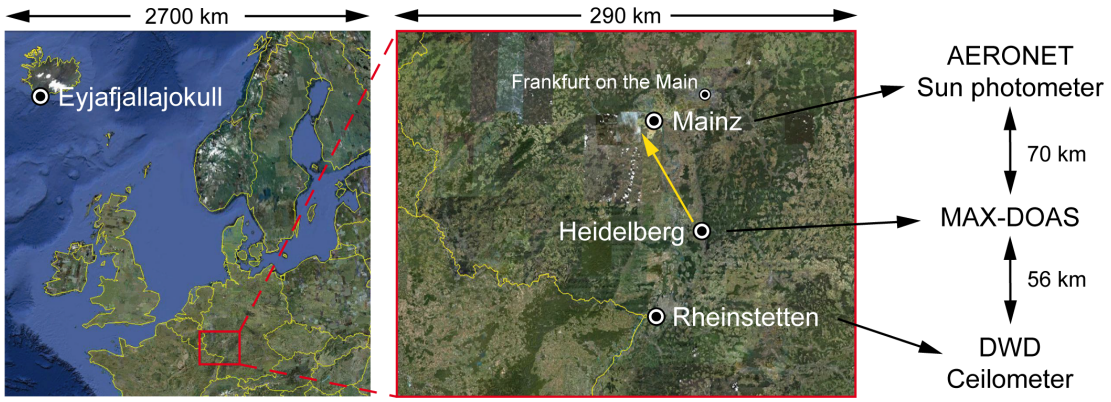

Figure 8.52: *The location of the Eyjafjallajokull volcano and the overview of the measurement sites and considered instrumentation (source: Google Maps). The yellow array indicates the viewing direction of the MAX-DOAS instrument.*

was installed on the roof of the Institute of Environmental Physics in Heidelberg (49.4°N, 8.7°E, 114 m above sea level (asl)). Figure 8.52 shows the location of the Eyjafjallajokull volcano and the measurement sites of the considered instruments, which are used for the comparison of the MAX-DOAS observations. The viewing direction of the MAX-DOAS instrument is indicated by the yellow array in the map and corresponds to an azimuth of 330° (NNW). The AERONET Sun photometer closest (70 km) to Heidelberg is located at the Max Planck Institute for Chemistry in Mainz (50.0°N, 8.3°E, 150 m asl). The ceilometer in Rheinstetten (49.0°N, 8.3°E, 117 m asl) is operated by the German Weather Service (DWD) and is located at a distance of 56 km) to Heidelberg. The eruption style of the Eyjafjallajokull volcano changed from an effusive to a more violent explosive eruption on 14 April 2010, and continuous MAX-DOAS measurements were performed beginning on 17 April 2010.

8.8.1 Detection of the Volcanic Plume of Eyjafjallajokull by SO_2 Measurements

To increase the retrieval quality of the spectral retrieval of SO_2 dSCDs from the MAX-DOAS measurements, three subsequent spectra of equal viewing directions were added prior the analysis (see Section 3.6.2). The wavelength range of 310.8–330 nm was used for the spectral retrieval and the zenith measurement at noontime of the according day was used as referenc spectrum (see Section 3.5).
Figure 8.53 shows the overview of the simulated volcanic ash vertical columns and measured SO_2 dSCDs over Heidelberg for the period of 17 April to 23 May 2010. The simulations of the volcanic ash vertical columns over Heidelberg were performed with the Lagrangian particle dispersion model FLEXPART (see Section 7.2.5) and provided by Nina Iren Kristiansen (Norwegian Institute for Air Research (NILU), personal communication). The simulations of the atmospheric transport and evolution of the volcanic plume of the Eyjafjallajokull volcano were performed considering ash particles with a diameter of 0.25–3 μm. This limitation of the considered size range to fine particles was made to approximate the transport of volcanic SO_2, which means that the simulated volcanic ash particle vertical columns over Heidelberg serve as proxy for volcanic SO_2. However, the different removal processes of fine particles and SO_2 (see Section 2.4 and 2.2.2, respectively) as well as wind shear can cause the separation of both components in aged volcanic plumes. Figure 8.53b shows only SO_2 dSCDs from MAX-DOAS, which are above the detection limit of 6 σ for clarity. Three periods with a significant number of increased SO_2 dSCDs can be identified. These periods are shown in more detail in Figures 8.53c - 8.53h. On 19 April, a day with cloudless conditions, increased SO_2 dSCDs occur during the entire period of the MAX-DOAS measurements for all off-axis viewing directions, and the simulations predict the occurrence of volcanic fine particles over Heidelberg. In contrast, on 29 April, SO_2 dSCDs above the detection limit are measured by MAX-DOAS only during the morning, while the simulation does not predict the occurrence of volcanic fine particles. Therefore, the measured SO_2 dSCDs are most probably due to local emissions of pollution sources. On 18 May, the FLEXPART simulation predicts increased vertical columns of volcanic fine particles, which is correlated to the MAX-DOAS SO_2 dSCD observations with increased values for all

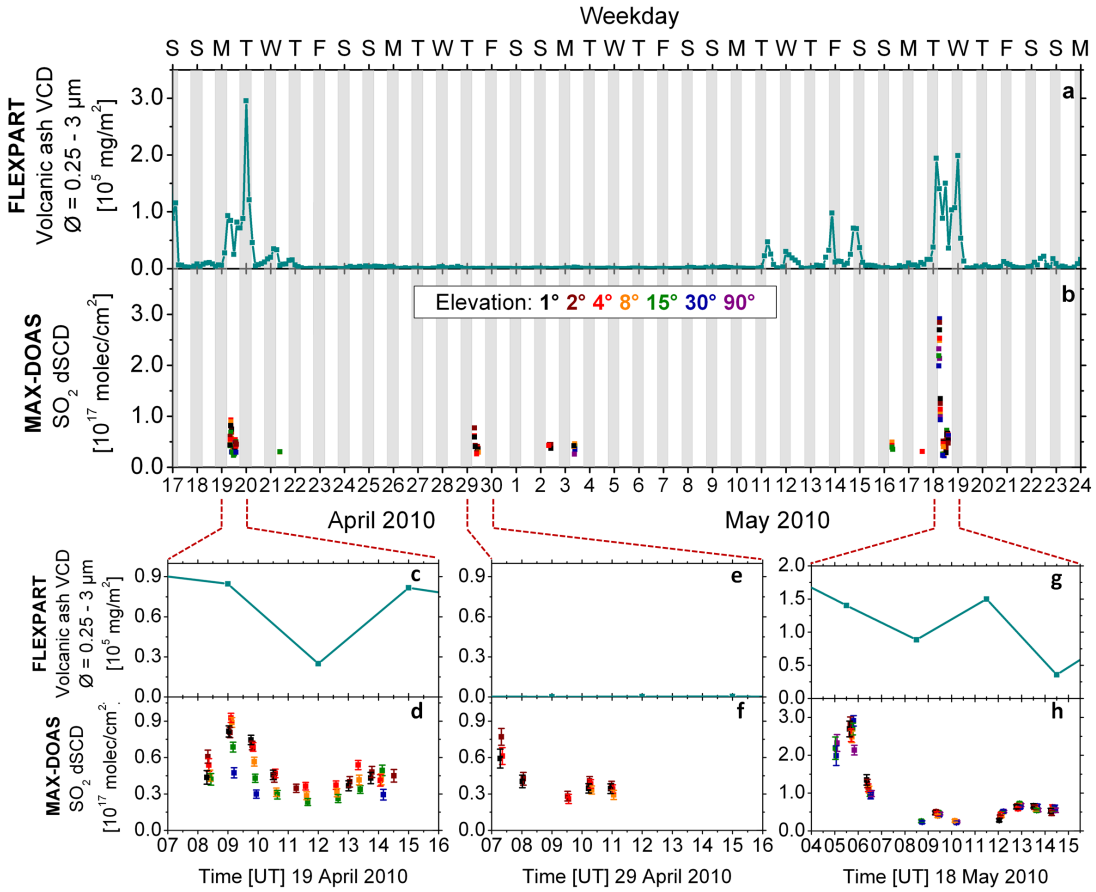

Figure 8.53: *The (a) simulated volcanic ash vertical columns and (b) measured SO_2 dSCDs over Heidelberg for the period of 17 April to 23 May 2010. Volcanic ash particles with a diameter of 0.25–3 µm were considered in the FLEXPART simulations and serve as proxy for volcanic SO_2. For clarity, the SO_2 dSCDs from MAX-DOAS are only shown for values above the detection limit of 6σ. The light grey areas indicate nighttimes. Periods with a significant number of increased SO_2 dSCDs are enlarged in the bottom panels (c-h).*

viewing directions. In the period of 11 to 15 May, several smaller peaks in the simulated vertical columns of fine particles appear (Figure 8.53). For this period, the MAX-DOAS measurements do not detect SO_2 dSCDs which are above the detection limit. Figure 8.54 shows the comparison of the SO_2 VCDs observed by the GOME-2 satellite instrument (see Section 7.2.3) and the simulation of the volcanic ash vertical column for 19 April and 18 May 2010 over northern Europe. The GOME-2 data was provided by Christoph Hörmann (Max Planck Institute for Chemistry, personal communication). The FLEXPART simulations for the horizontal distribution of the volcanic ash vertical column were performed considering particles with a diameter of 0.25–250 µm.

The increased SO_2 dSCDs measured by MAX-DOAS on 19 April indicate the detection of the volcanic plume over Heidelberg, since these observations are in agreement

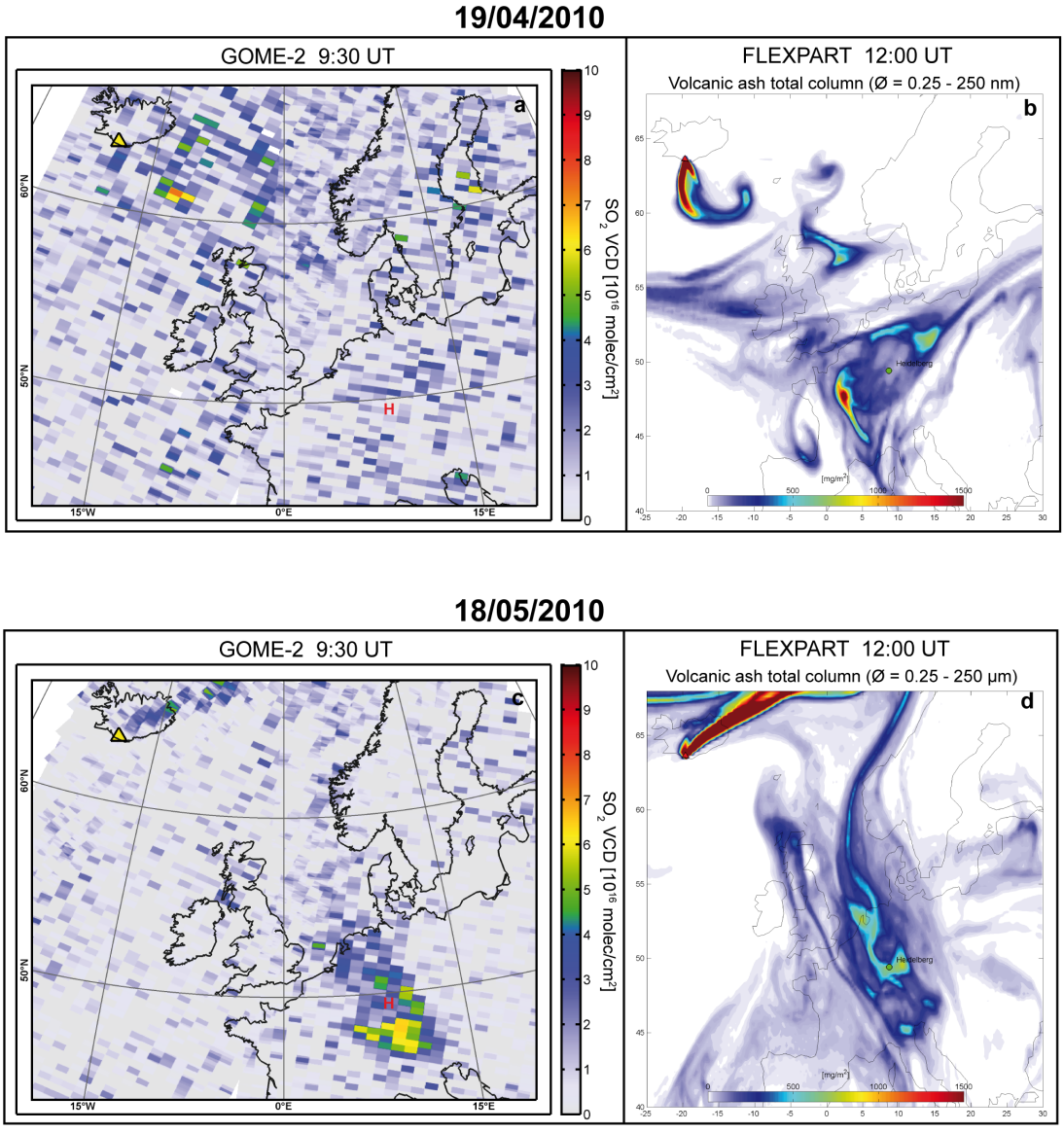

Figure 8.54: *(a,c) GOME-2 measurements of the SO_2 VCD and (b,d) FLEXPART simulations of the volcanic ash vertical column for (top) 19 April and (bottom) 18 May 2010 over northern Europe. Volcanic ash particles with a diameter of 0.25–250 µm were considered in the FLEXPART simulations. The location of the Eyjafjallajokull volcano and Heidelberg is indicated in the maps.*

with the predicted vertical columns of volcanic ash particles. However, the GOME-2 measurements show no significant SO_2 VCDs over Heidelberg. The observations during this cloudless day require a detailed analysis to determine whether the observed SO_2 dSCDs by MAX-DOAS are attributable to local pollution sources or arise due to an actual detection of the volcanic plume. The appropriate considerations and discussions are presented below in Section 8.8.3.

In contrast, the situation for 18 May is unambiguous. The simulations, MAX-DOAS

and GOME-2 measurements are in agreement with respect to the presence of the volcanic plume over Heidelberg. During this day, a persistent complete cloud cover was present. The SO_2 dSCDs measured by MAX-DOAS show no separation according the elevation angle. This relationship confirms that the location of the observed SO_2 layer in or above the water clouds. In such a case, the light paths through the SO_2 layer is approximately equal for all viewing directions. Furthermore, the spectral retrieval of the MAX-DOAS spectra using the zenith measurement from the current elevation sequence as reference spectrum showed that no increased SO_2 ΔSCDs can be observed. Therefore, the detected SO_2 dSCDs on 18 May arise from volcanic emissions of Eyjafjallajokull. The location of the volcanic SO_2 layer in or above the water clouds is favorable for the satellite measurements, since the sensitivity increases for these conditions. The light paths in the water clouds are increased due to multiple scattering, and the amount of scattered light reaching the satellite instrument from directly above the cloud is increased due to the high albedo of water clouds.

The period from 17 to 20 April 2010 was characterized by persistent cloudless conditions. For this period, aerosol extinction profiles were retrieved to explore the capabilities of MAX-DOAS measurements to detect volcanic ash related enhancements in the atmospheric aerosol load. The results of the aerosol profile retrieval are discussed in the following section. The retrieved aerosol profiles were used as input parameter for the trace gas profile retrievals presented in Section 8.8.3.

8.8.2 Retrieval of Aerosol Extinction Profiles and Optical Depths

The aerosol profile retrievals were performed using the standard settings and parameter described in Section 8.2.2 using the O_4 ΔODs and relative intensities. An overview of the AOD retrieved from MAX-DOAS and Sun photometer, $\epsilon_M(z)$ retrieved from MAX-DOAS, RCS from ceilometer and FLEXPART simulations of the volcanic ash vertical distribution is shown in Figure 8.55. The AODs from Sun Photometer were measured at the AERONET site in Mainz (Figure 8.2.2a,b,i,j). The aerosol profiles from the DWD ceilometer in Rheinstetten were provided by Harald Flentje (Meteorological Observatory Hohenpeissenberg of the German Weather Service, personal communication) and are expressed as RCS (Figure 8.2.2e,f,m,n). The FLEXPART simulations show the vertical distribution of the volcanic ash plume over Heidelberg (Figure 8.2.2g,h,o,p). These simulations were performed considering volcanic ash particles with a diameter of 0.25–20 μm.
The AODs retrieved from MAX-DOAS agree well with the Sun photometer measurements with respect to the trend observed for the period of 17 to 20 April. The differences in the AODs from both instruments partly arise due to the distance of the measurement sites of roughly 70 km. A remarkable increase in atmospheric aerosol load is observed for Mainz and Heidelberg for 19 April with AODs of up to ≈ 1.2 (Figure 8.2.2i).
Despite the distance of the measurement sites of roughly 56 km, several similar features in the RCS from ceilometer and $\epsilon_M(z)$ from MAX-DOAS can be identified. In

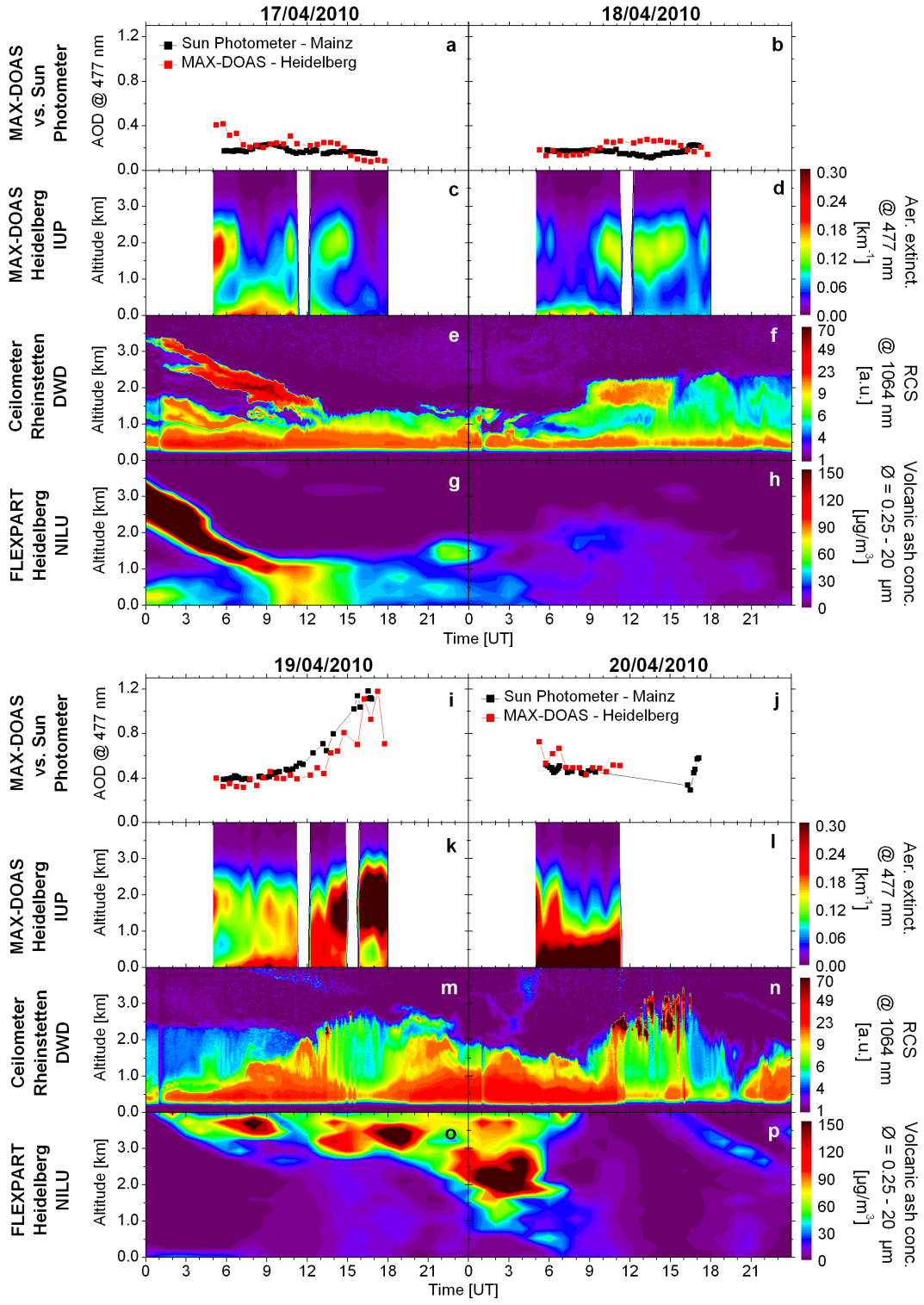

Figure 8.55: *Diurnal developments of the (a,b,i,j) AOD retrieved from MAX-DOAS and Sun photometer, (c,d,k,l) $\epsilon_M(z)$ retrieved from MAX-DOAS, (e,f,m,n) RCS from ceilometer and (g,h,o,p) FLEXPART simulations of the volcanic ash vertical distribution (see text for details). Note that the instruments are located at different sites. The simulations consider the profiles above Heidelberg.*

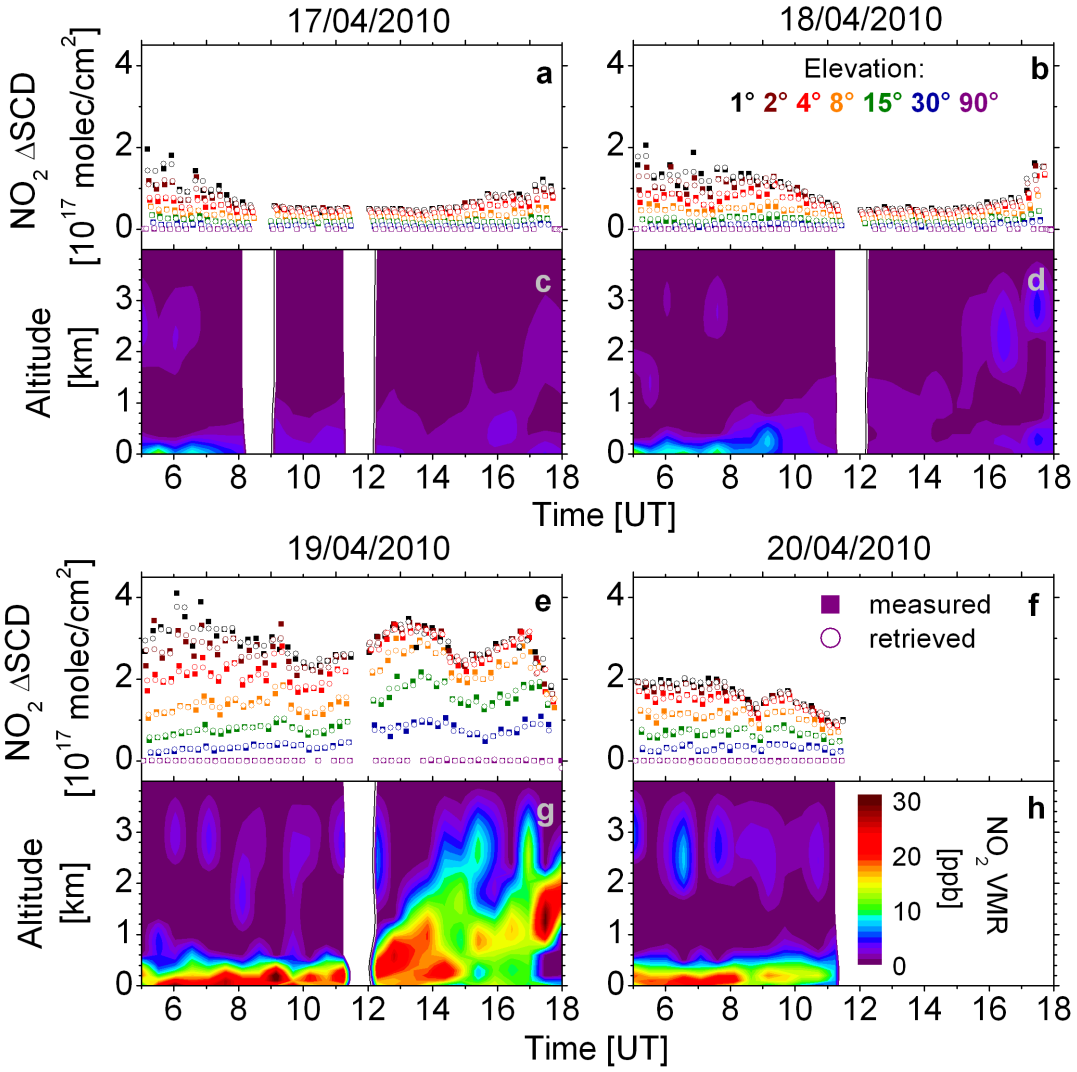

Figure 8.56: *Diurnal developments of the (a,b,e,f) NO_2 ΔSCDs and (c,d,g,h) NO_2 VMR profiles retrieved from MAX-DOAS in Heidelberg for the period of 17 to 20 April 2010. Increased NO_2 VMR were observed on 19 April.*

the morning hours of 17 April, a descending volcanic ash layer at altitudes around 1.5–3.5 km is observed by the ceilometer (Figure 8.55e). Such a development in the vertical distribution of the volcanic ash plume over Heidelberg is predicted by the simulations (Figure 8.55g). Increased aerosol extinction values are retrieved from MAX-DOAS for altitudes between 1.0 and 2.5 km (Figure 8.55c), which is in agreement with the ceilometer observations and FLEXPART simulations. The observed increase in the profiles from MAX-DOAS can therefore be attributed to volcanic ash particles. Around noon and the early afternoon of 18 April, the aerosol profiles from MAX-DOAS reproduce an elevated layer at altitudes between 1.0 and 2.5 km, which is in good agreement with the ceilometer measurements with respect to the layer height and temporal occurrence (Figure 8.55d,f). On 19 April, which is the

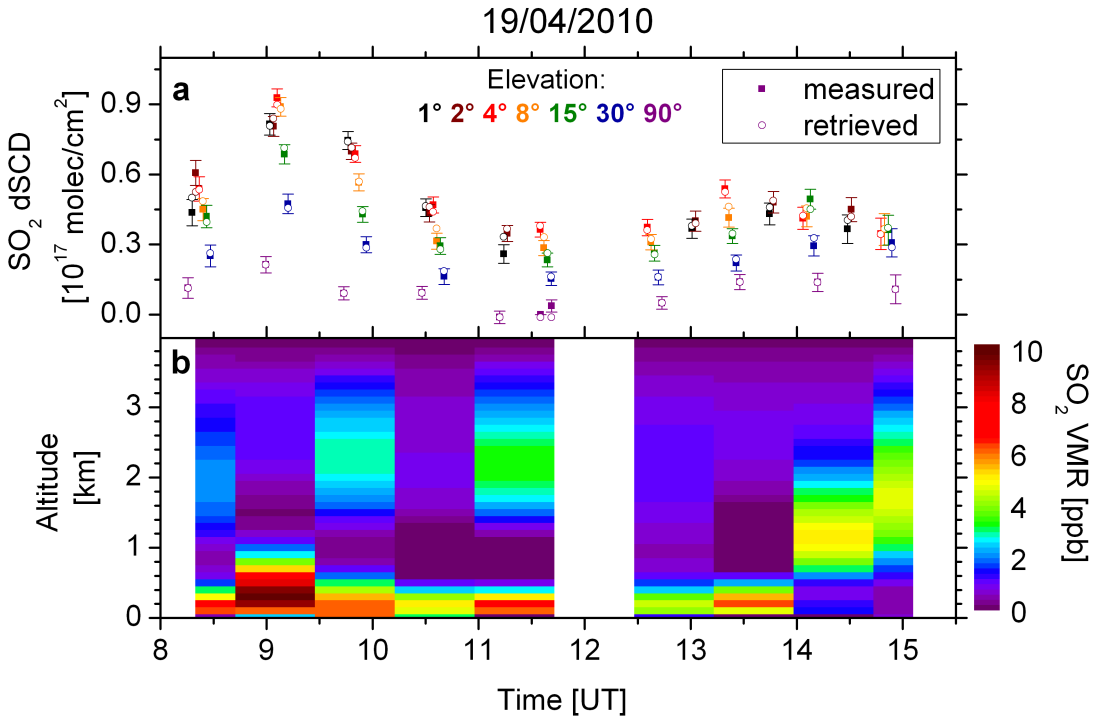

Figure 8.57: *Diurnal developments of the (a) SO_2 dSCDs and (b) SO_2 VMR profiles retrieved from MAX-DOAS in Heidelberg for 19 April 2010. An elevated SO_2 layer is observed in the morning hours.*

day with the increased SO_2 dSCDs and AODs, a good agreement in the diurnal development of the increasing mixing layer height between 5:00 and 14:00 UT can be identified in the profiles from MAX-DOAS and ceilometer (Figure 8.2.2k,m). While the simulations predict increased amounts of volcanic ash at altitudes above ≈ 2.5 km (Figure 8.2.2o), the RCS measured by the ceilometer shows no significantly increased aerosol signals at these altitudes with the according extent. Weak signals at altitudes above ≈ 3 km are detected and indicated by bluish colors, which are possibly due to volcanic ash particles. An increase in $\epsilon_M(z)$ at these altitudes is not observed by MAX-DOAS due to the lower sensitivity and height resolution of the retrieval at the according altitudes. On 20 April, the profiles from MAX-DOAS and ceilometer agree well with respect to the boundary layer height and the increased aerosol load at altitudes below ≈ 1 km.

8.8.3 Retrieval of SO_2 and NO_2 Profiles

The aerosol extinction profiles retrieved from the MAX-DOAS measurements were used as input parameters for the trace gas retrievals. The retrieval parameters and settings were adapted from the standard settings described in Section 8.2.3 for the NO_2 and SO_2 profile retrievals. Figure 8.8.3 shows the measured and retrieved NO_2 ΔSCDs and the retrieved NO_2 VMR profiles. A very good agreement is achieved for the measured and simulated ΔSCDs. The retrieved NO_2 profiles show increased

VMRs at altitudes below $\approx 500\,\mathrm{m}$ in the morning hours of 19 and 20 April. On 19 April the NO_2 layer height increases beginning at noon time, which is attributable to the increasing mixing layer height as reproduced by the MAX-DOAS aerosol profile retrieval (Figure 8.55k).
The measured and retrieved SO_2 dSCDs as well as the retrieved SO_2 VMR profiles are depicted in Figure 8.57. The measured and retrieved dSCDs show a very good agreement. The retrieved SO_2 profiles show increased VMRs in the lowermost altitude range in the morning hours. In the afternoon, the increased SO_2 VMRs are retrieved for higher altitudes. This diurnal development correlates with the retrieved NO_2 profile trend indicating that these SO_2 fractions can be attributed to local emissions form pollution sources. However, the SO_2 profile retrieval also reproduces an elevated layer occurring at altitudes between 1–3 km in the morning hours, which is likely caused by SO_2 originating from emissions of the Eyjafjallajokull volcano. During cloudless conditions, which was the case on 19 April, the satellite measurements have a relatively low sensitivity for trace gases (and in particular for SO_2) at lower altitudes. This explains why the GOME-2 measurements do not show increased SO_2 VCDs over Heidelberg (Figure 8.54).

These findings show that MAX-DOAS is a powerful technique, which is suitable for the detection of elevated volcanic SO_2 plumes. It has the advantage of the SO_2 detection also during conditions with dense cloud cover, when other techniques for the measurement of volcanic ash particles, like lidar and Sun photometer, are impeded in their effectiveness. Furthermore, SO_2 located at lower altitudes can be separated according to its residence altitude, which allows the identification of its origin.

Chapter 9

Conclusions and Outlook

In the scope of this work, the MAX-DOAS technique was combined with sophisticated inversion methods to retrieve the vertical distribution of atmospheric trace gases and aerosols. A new kind of MAX-DOAS instrument was developed, which meets the requirements of automated long term measurements. Following the concept of a separated telescope and spectrometer unit, the instrument was especially designed to provide multi-functional capabilities. The integration of three miniature spectrometers enables MAX-DOAS measurements over a wide wavelength range with a high spectral resolution. This provides the capability to measure a variety of trace gases absorbing at different wavelengths ranging from ultra-violet to visible. The inlet aperture of the telescope unit can rotate around two axes, which allows for collecting scattered Sun light from any direction in the sky. This allows for the adaptation of the viewing geometry of the MAX-DOAS measurements to the surrounding of the measurement site. Furthermore, measurements at several different azimuth angles can be performed. These kind of measurements contain further information on the optical properties of atmospheric aerosols. A further potential application of this telescope design is the measurement of direct sun- and moonlight.

An existing retrieval algorithm, which applies the optimal estimation method for the inversion of aerosol extinction profiles from MAX-DOAS O_4 and intensity measurements, was further developed and improved. A newer version of the radiative transfer model was implemented in the retrieval. With the new algorithm, the aerosol optical properties, i.e. the single scattering albedo, phase function, and Ångström exponent, can be directly chosen in the retrieval without a conversion using a parametrization and aerosol data base. In addition to the optimal estimation method, further inversion approaches where implemented in the retrieval algorithm. A description of the aerosol extinction profile using two and three parameters was introduced for a parameterized retrieval. Also the regularization method was applied for the retrieval of the complete aerosol extinction profile. These developments of the aerosol retrieval algorithm were adapted and adjusted for the retrieval of trace gases from MAX-DOAS measurements, and appropriate algorithms were developed.

Major parts of the work performed within this thesis, including the instrument and retrieval algorithm development, were carried out in the scope of a joint research

activity of the European EUSAAR project. Several field campaigns were performed at different sites in Europe within this project. The aim of these campaigns was the comparison of this relatively new MAX-DOAS application to aerosol measurements with established in situ and remote sensing techniques. The intercomparison campaigns were carried out in Cabauw (The Netherlands), Melpitz (Germany), Ispra (Italy), and Leipzig (Germany).

The improved aerosol and trace gas retrieval algorithms were tested by intensive sensitivity studies using synthetic measurements. The capability of MAX-DOAS O_4 and intensity measurements from azimuth scans to provide information on further aerosol optical properties by the retrieval of the single scattering albedo, phase function parameter, and Ångström exponent was demonstrated, confirming previous studies on the information content of such measurements. The retrievals using a parameterized description of the aerosol profile were found to be limited in their capabilities to reproduce aerosol profiles with structured shapes, which is frequently observed in the atmospheric boundary layer, due to the restrictions of representable shapes by the according parametrization. In contrast, the complete profile retrieval using optimal estimation showed its capability to reproduce a variety of profile shapes, including two-layered structures. An important finding is that this capability is still available at relative low aerosol loads. The regularization method was applied for the retrieval of aerosol and trace gas profiles using different regularization operators, whereat each of which allows for constraining the profile independently from a priori knowledge.

The comparisons of the MAX-DOAS results to the measurements of the other instruments during the numerous field campaigns were used to identify several aspects with respect to the MAX-DOAS aerosol and trace gas profile retrieval using optimal estimation. For cloudless conditions, the comparisons of the aerosol extinction profiles retrieved from MAX-DOAS to measurements from lidar instruments showed very good agreement. Elevated aerosol layers were reproduced by MAX-DOAS and the diurnal development of the aerosol load in the boundary layer was also captured. In addition, the AOD retrieved from MAX-DOAS agreed very well with Sun photometer measurements. The comparison of the aerosol extinction retrieved from MAX-DOAS for the lowermost altitude layer to in situ measurements showed, that both exhibit a similar diurnal pattern, but significant differences in the absolute extinction values were present. The aerosol extinction values retrieved from MAX-DOAS were significantly larger by a factor of 2–3 than those from in situ measurements. While several possible explanations for this difference exist, the actual reason is not known yet and requires further investigation.
NO_2 surface concentrations from the MAX-DOAS profile retrievals show very good agreement with in situ measurements. The retrieved NO_2 VCDs were found to agree well with satellite measurements within the variation expected for satellite measurements as a result of the pixel center distance to the ground based measurement site and the large area of a satellite pixel.

Sensitivity studies considering different MAX-DOAS aerosol retrieval settings and

parameters were performed. These allowed for the identification of several issues from the comparison to the other measurement techniques. The usage of measured intensity in addition to the O_4 measurements increases the information content of the retrieval and improves the comparison of the AODs from MAX-DOAS and Sun photometer as well as the extinction profiles from MAX-DOAS and lidar. While the MAX-DOAS retrieval using the O_4 ΔODs and relative intensities at 477 nm shows the best agreements with the other techniques, the retrieval at 360, 577 and 630 nm resulted in poorer agreements due to difficulties in the spectral DOAS analysis. The usage of co-located measurements of pressure and temperature profiles from radiosondes as retrieval parameters instead of standard profiles improves the quality of the retrieval.
Two different parameterizations for the aerosol retrieval were tested. In the two-parameter approach, the layer height and AOD of a box-profile was assumed. The three-parameter approach describes the aerosol profile as a Gaussian function with AOD, layer height and layer width as parameters. The parameterized version of the retrieval was found to perform better with respect to the aerosol profile results and their comparison to lidar measurements, when two parameters were used for the profile description. However, the comparison of the retrieved AODs to Sun photometer measurements shows similar agreements for the two and three parameter case. The regularization method increases the computational effort due to additional iteration sequences, which are necessary to determine the optimal regularization parameter. This limits its applicability for near real-time retrievals.
When comparing the different approaches for the MAX-DOAS retrieval, the best results were achieved using the optimal estimation method for the retrieval of the complete aerosol profile.

Sensitivity studies for the NO_2 profile retrieval showed that the usage of a height grid, which is too coarse, results in larger differences in the comparisons to in situ measurements. A height resolution of 100 m for the altitude grid was found to be sufficient. Better correlations to in situ measurements were achieved, when the aerosol profiles retrieved from MAX-DOAS were used as input for the NO_2 profile retrievals instead of the co-located lidar profiles.

Overall, the MAX-DOAS aerosol and trace gas profile retrievals performed within this thesis show very good agreements with independent measurements, especially for cloudless conditions but also during the field campaigns over longer periods at sites with different typical levels of aerosol and NO_2 abundances. This demonstrates that the MAX-DOAS technique is a powerful tool for monitoring the vertical distribution of atmospheric constituents. The capability of MAX-DOAS instruments to perform automated measurements allows their operation even at remote stations. Furthermore, the comparably low cost of MAX-DOAS instruments makes the deployment in measurement networks feasible.

The MAX-DOAS instrument was set up in Heidelberg (Germany) after the intercomparison campaigns within the EUSAAR project. The highly diluted plume of the Eyjafjallajokull volcano in Iceland was detected by MAX-DOAS SO_2 measurements

over Heidelberg in 2010. These measurements allowed the unambiguous detection during conditions with complete cloud cover, and were in agreement with satellite observations and model predictions. Since the established techniques for the ground based remote sensing of volcanic ash particles, like lidar and Sun photometer, are impeded in their effectiveness during cloud cover conditions, the MAX-DOAS technique is highly suited to perform complementary measurements of volcanic SO_2. Therefore, the integration of MAX-DOAS instruments in worldwide networks for the real-time observation of volcanic plumes is recommended, since these additional measurements can be used to improve the particle transport models as well as contribute to aviation safety management. To decrease the influence of SO_2 originating from local pollution sources and thus possibly masking the MAX-DOAS measurements of the volcanic plume, the network sites should be located in areas with low pollution levels.

Although the O_4 absorption cross section was reported in previous studies to show uncertainties with respect to the absolute values, the radiative transfer simulations as well as the aerosol profile retrievals in this work showed best results if the original values of the O_4 cross section reported in the literature was used. A possible temperature dependence leading to such differences could be an explanation for the fact that it is necessary to scale the absolute value of the O_4 cross section for measurements at particular sites. Therefore, intensive studies and laboratory measurements of the O_4 absorption cross section and its temperature dependence are necessary to determine the actual reason for the observed discrepancies and to provide more reliable spectroscopic data on the oxygen collision complex.
Since the aerosol profile retrievals using measured intensities are influenced by clouds, retrievals using only the O_4 ΔODs, which enable a more robust retrieval performance, should be used in near real-time applications for long term measurements.
The aerosol profile retrievals using synthetic measurements showed that the simultaneous usage of the O_4 ΔODs and relative intensities at 360, 577 and 630 nm improves the retrieval sensitivity and height resolution. The improvement of the spectral DOAS analysis of the 577 and 630 nm O_4 absorption bands, as well as the application of spectrometers with higher sensitivities in the ultra-violet, e.g., using back-thinned area detectors, could result in aerosol profile retrievals of higher quality and accuracy. The observed difficulties of the radiative transfer model to simulate the appropriate aerosol phase function at small relative azimuth angles requires further investigation. Once these discrepancies are resolved, the retrieval of the aerosol single scattering albedo, phase function, and Ångström exponent from MAX-DOAS azimuth scans would be possible. In a further step, the combination of these retrieved optical parameters with Mie theory could be used to retrieve the aerosol size distribution and complex refractive index.
Additionally, the consideration of the Ring effect can improve the information content of MAX-DOAS measurements on aerosols (Wagner et al., 2009). Also the consideration of polarization would yield additional information on atmospheric aerosols (Seidler, 2008). However, both effects require radiative transfer models, which are capable of modeling Raman scattering and polarization.

The ongoing comparison of the aerosol profile retrievals applied by the different MAX-DAOS groups in the scope of the CINDI project, allows the development of standardization approaches for the profile retrievals. Especially in this early stage of this new technique, such efforts can help to improve the retrieval performance as well as the comparability of the resulting data products from the different instruments. The level of agreement between the profiles retrieved from groups using similar algorithms is already encouraging.

Appendix A

Sensitivity Studies

Figures A.1 – A.5 show the results of the sensitivity studies for the intercomparison campaign in Cabauw 2008 (Section 8.2.2.1). The average differences between the aerosol extinction profile $\epsilon_M(z)$ retrieved from MAX-DOAS and lidar as well as the corresponding standard deviations were calculated with respect to absolute and relative differences. The shown cases are related to the different retrieval settings described on page 151.

Figures A.6 and A.7 show the comparison of $\epsilon_M(z)$ retrieval from lidar and MAX-DOAS using the parameterized retrieval with two and three parameters (Section 8.2.2.3).

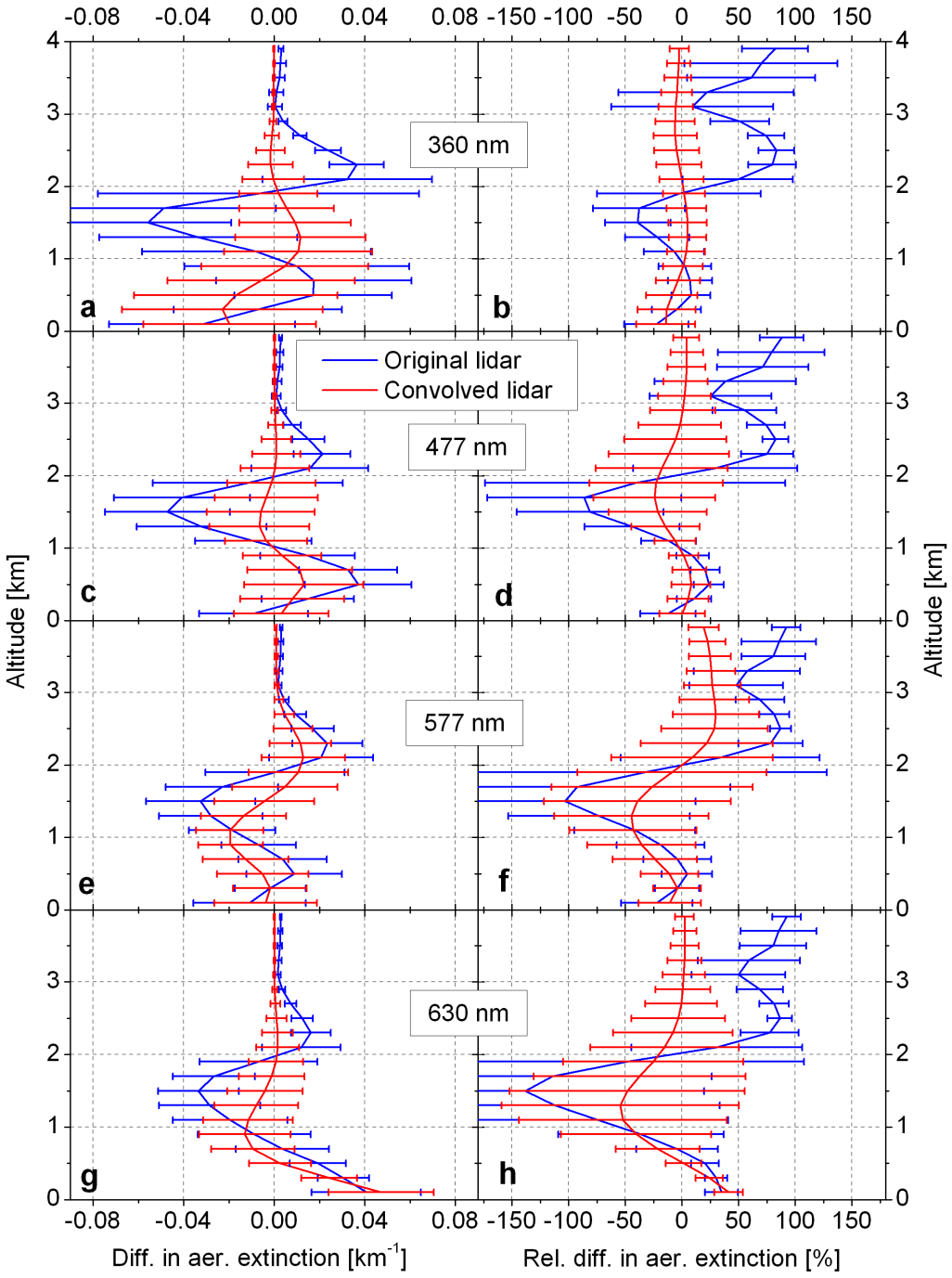

Figure A.1: *The mean (left panel) absolute and (right panel) relative differences and corresponding standard deviations of $\epsilon_M(z)$ retrieved from MAX-DOAS and lidar for the period of 7 to 10 May 2008 in Cabauw. The differences to the (blue) original and (red) convolved lidar profiles for retrievals using O_4 ΔODs and relative intensities at (a,b) 360, (c,d) 477, (e,f) 577 and (g,h) 630 nm (Cases Std. from Section 8.2.2.1).*

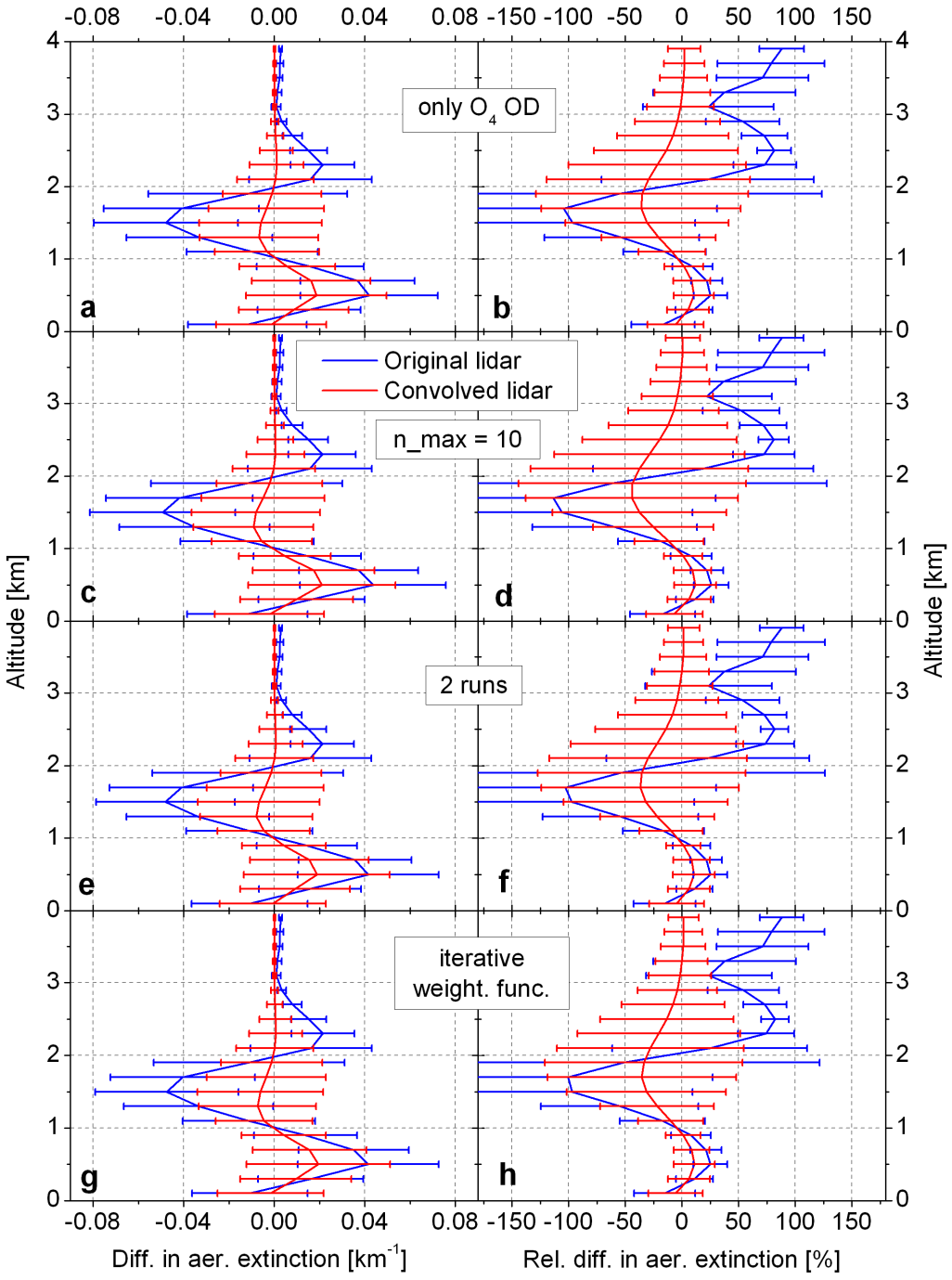

Figure A.2: *The mean (left panel) absolute and (right panel) relative differences and corresponding standard deviations of $\epsilon_M(z)$ at 477 nm retrieved from MAX-DOAS and lidar for the period of 7 to 10 May 2008 in Cabauw. The differences to the (blue) original and (red) convolved lidar profiles for different retrieval setting: (a,b) only O_4 ΔODs are used; (c,d) maximum of 10 iteration steps instead of 5; (e,f) performing two subsequent iteration sequences; (g,h) calculating the weighting function for each iteration step (Cases A and B from Section 8.2.2.1).*

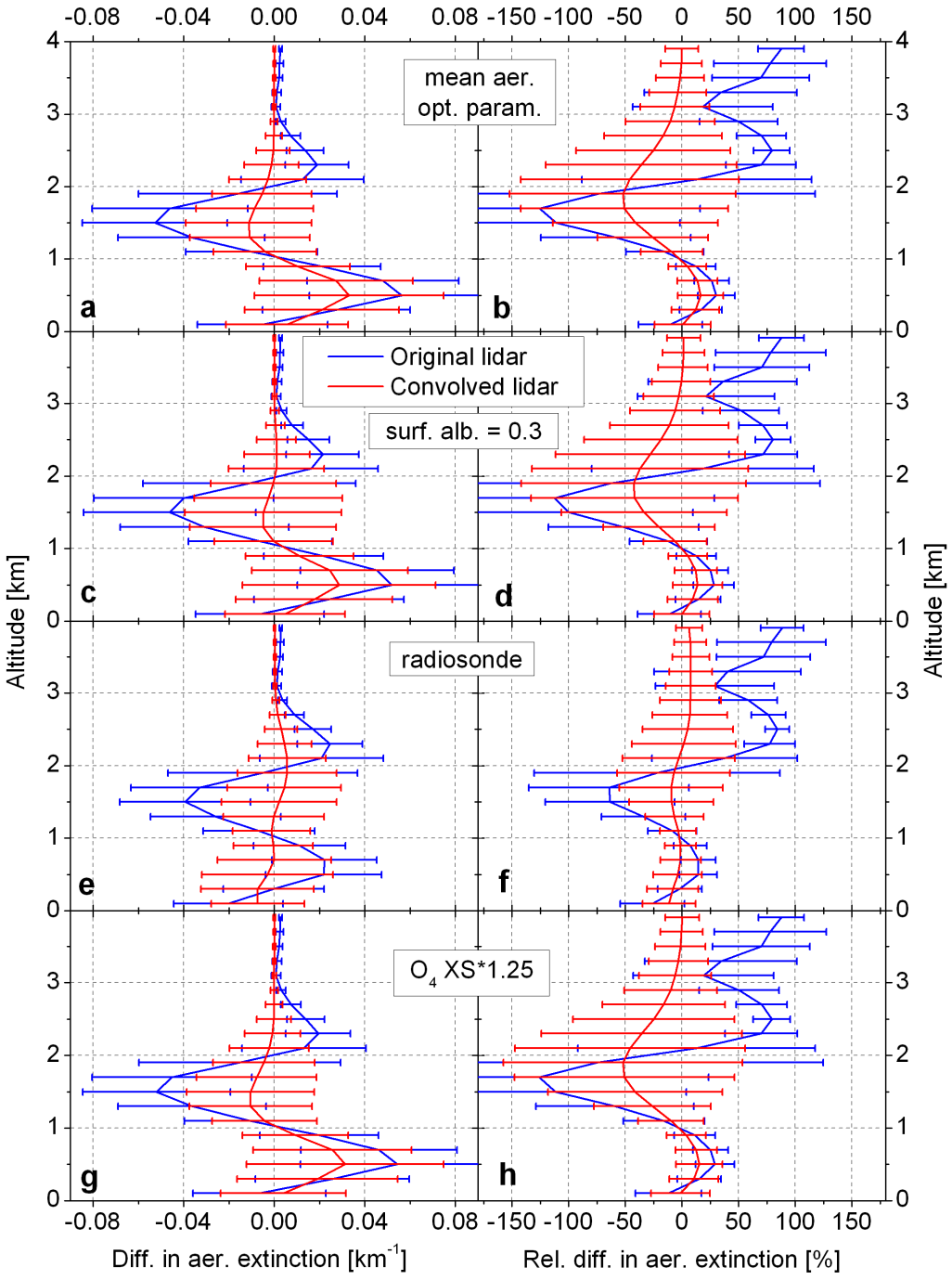

Figure A.3: *The mean (left panel) absolute and (right panel) relative differences and corresponding standard deviations of $\epsilon_M(z)$ at 477 nm retrieved from MAX-DOAS and lidar for the period of 7 to 10 May 2008 in Cabauw. The differences to the (blue) original and (red) convolved lidar profiles for different retrieval setting: (a,b) using the monthly mean aerosol optical properties; (c,d) surface albedo of 0.3 instead of 0.05; (e,f) using radiosonde data; (g,h) using a scaling factor of 1.25 for the O_4 absorption cross-section (Cases C from Section 8.2.2.1).*

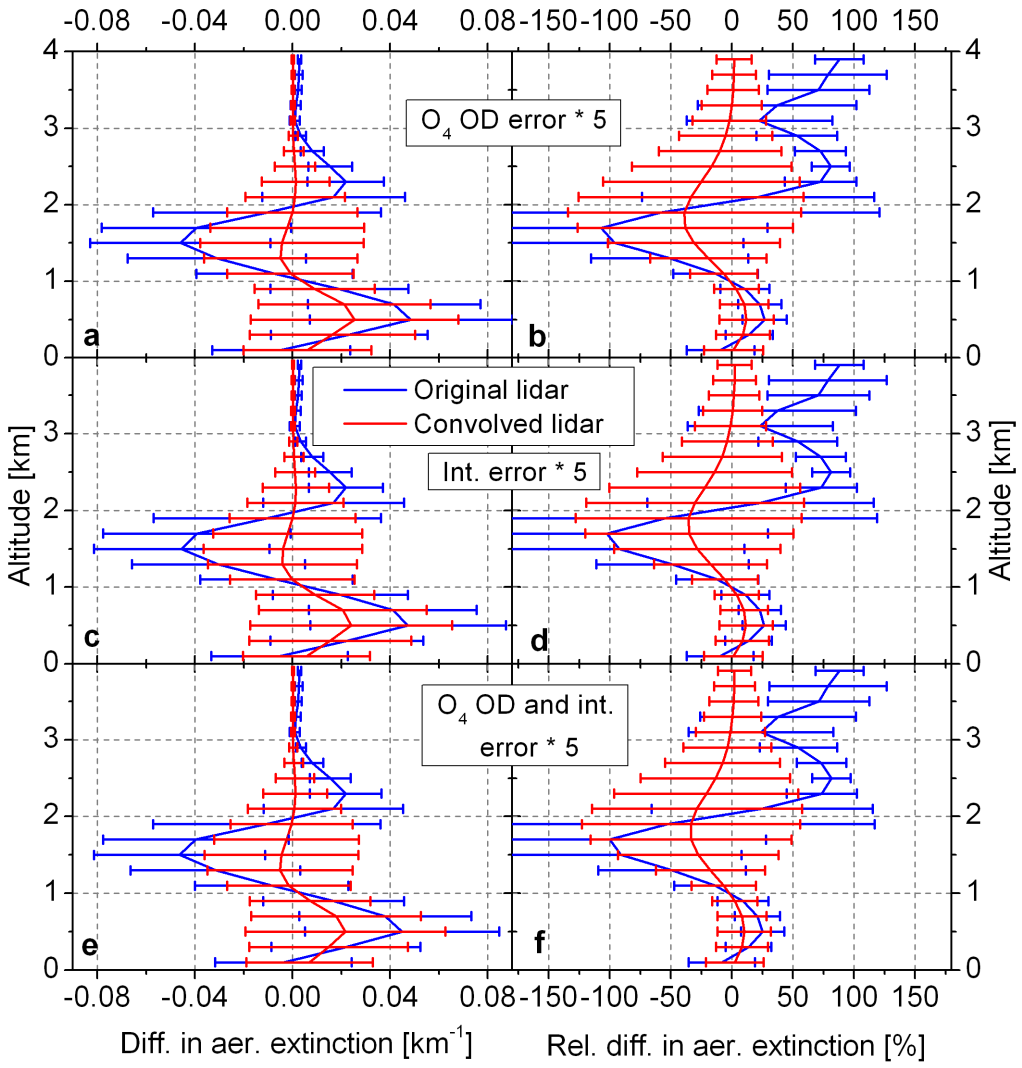

Figure A.4: *The mean (left panel) absolute and (right panel) relative differences and corresponding standard deviations of $\epsilon_M(z)$ at 477 nm retrieved from MAX-DOAS and lidar for the period of 7 to 10 May 2008 in Cabauw. The differences to the (blue) original and (red) convolved lidar profiles for retrievals using a scaling factor of 5 for (a,b) the O_4 ΔOD errors, (c,d) the intensity errors and (e,f) the O_4 ΔOD and intensity errors (Cases D from Section 8.2.2.1).*

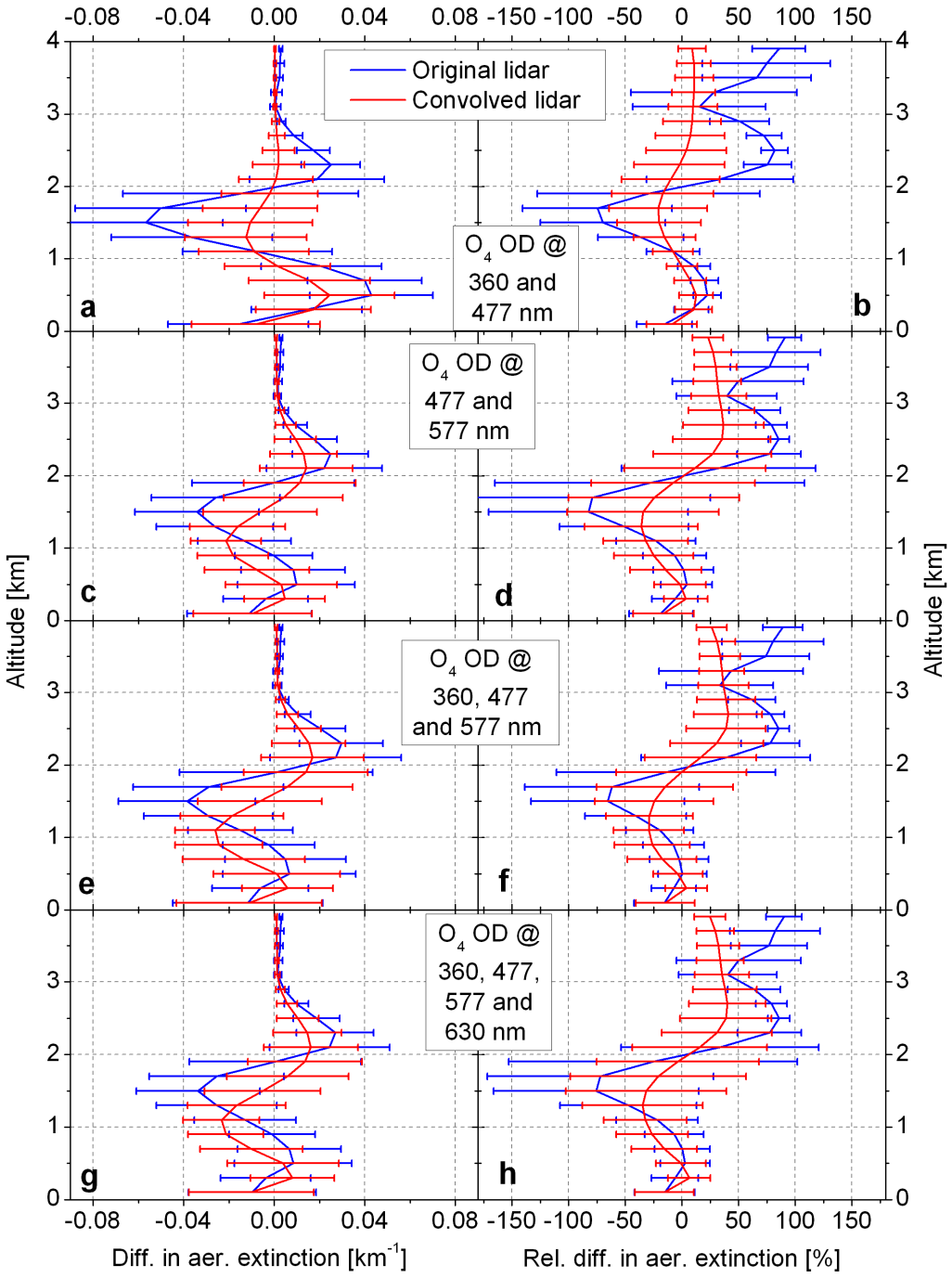

Figure A.5: *The mean (left panel) absolute and (right panel) relative differences and corresponding standard deviations of $\epsilon_M(z)$ retrieved from MAX-DOAS and lidar for the period of 7 to 10 May 2008 in Cabauw. The differences to the (blue) original and (red) convolved lidar profiles for retrievals using simultaneously the O_4 ΔODs and intensities at 360 and 477 nm, (c,d) 477 and 577 nm, (e,f) 360, 477 and 577 nm and (g,h) 360, 477, 577 and 630 nm (Cases E from Section 8.2.2.1).*

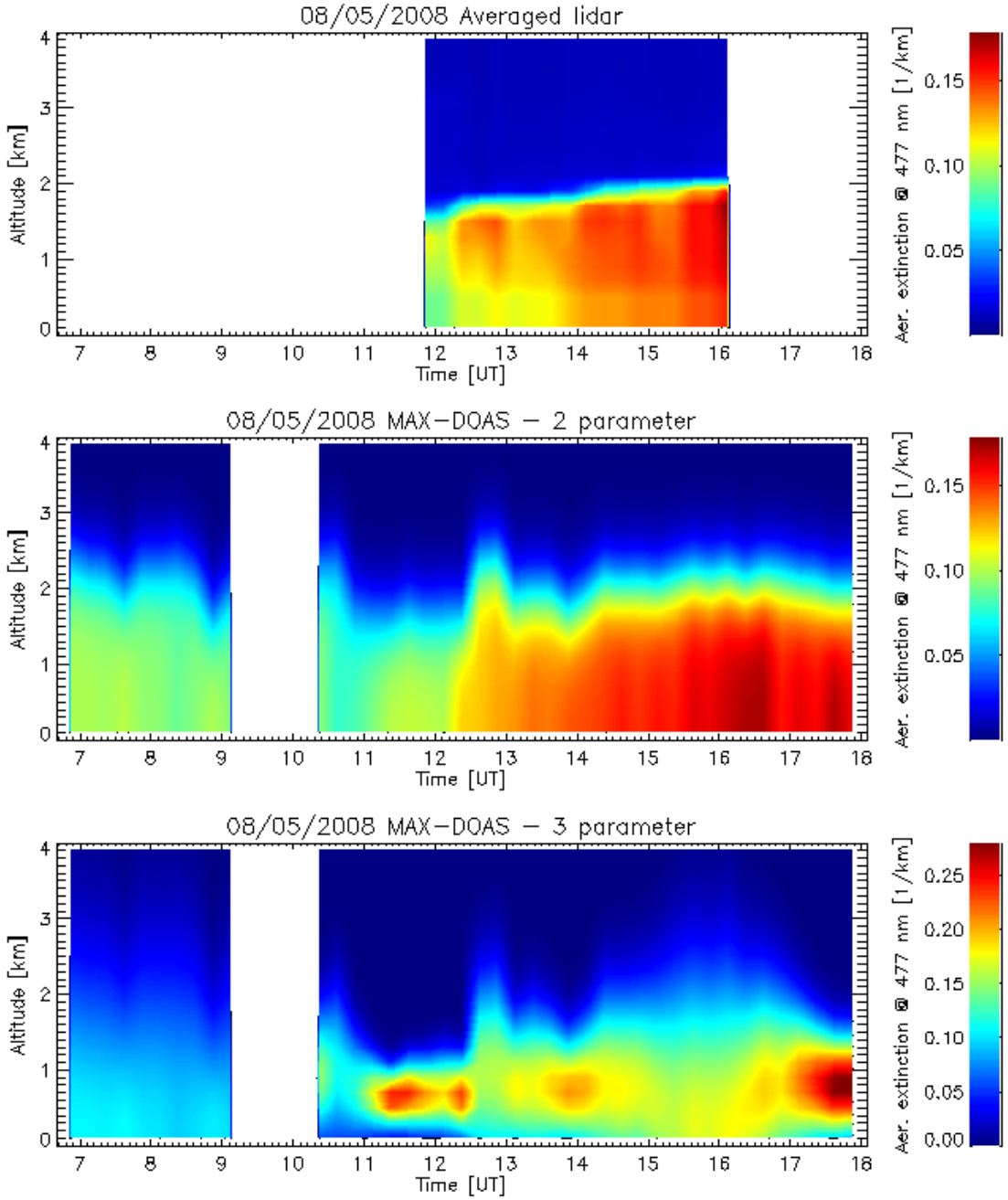

Figure A.6: *Comparison of $\epsilon_M(z)$ at 477 nm retrieved from lidar and MAX-DOAS for 8 May 2008 in Cabauw: (top) averaged profiles from lidar, (center) profiles retrieved from MAX-DOAS using 2 and (bottom) 3 parameters for the profile description (see Section 8.2.2.3).*

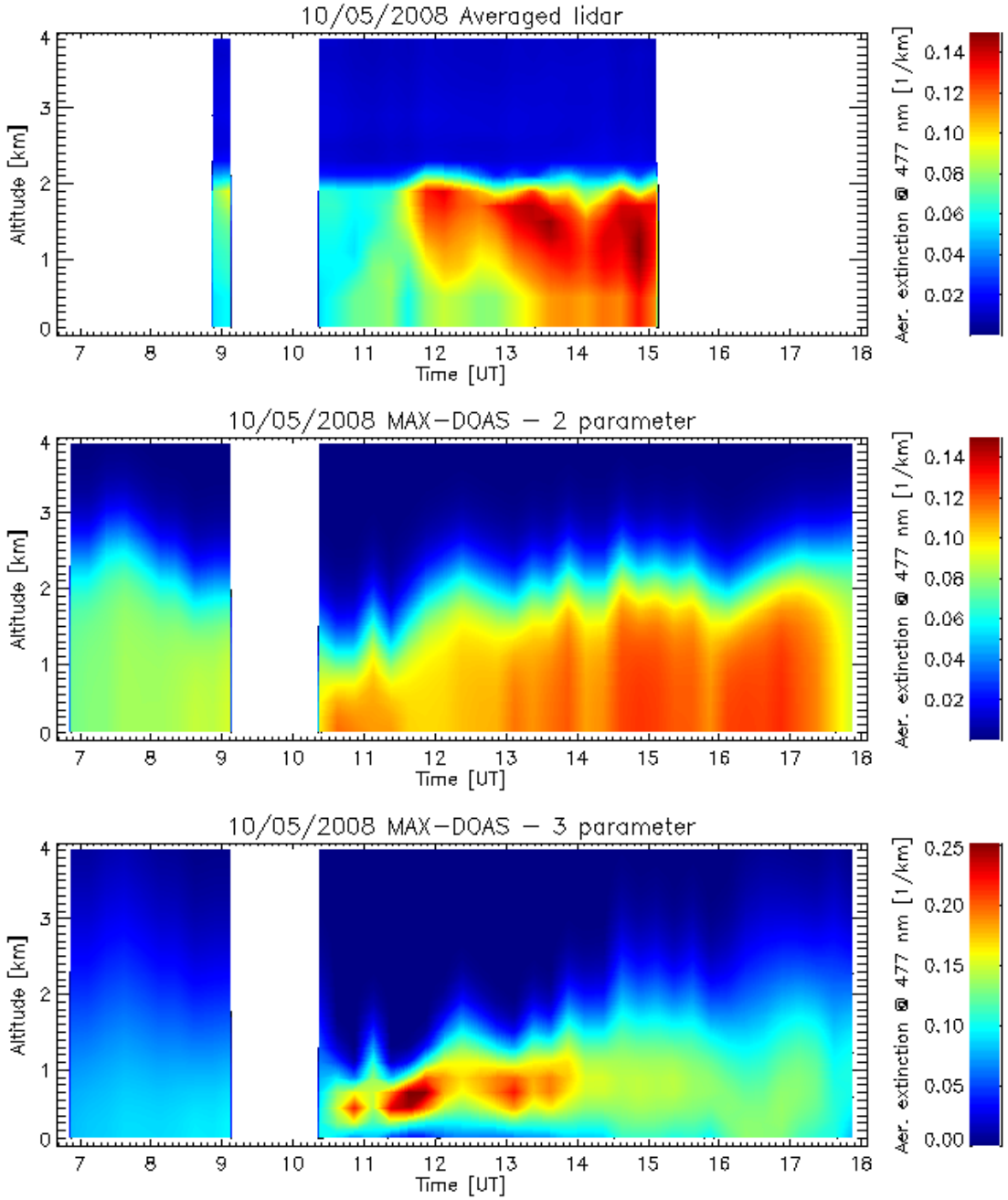

Figure A.7: *Comparison of $\epsilon_M(z)$ at 477 nm retrieved from lidar and MAX-DOAS for 10 May 2008 in Cabauw: (top) averaged profiles from lidar, (center) profiles retrieved from MAX-DOAS using 2 and (bottom) 3 parameters for the profile description (see Section 8.2.2.3).*

Appendix B

Construction Plans

The following figures show the telescope and spectrometer unit construction plans of the MAX-DOAS instrument.

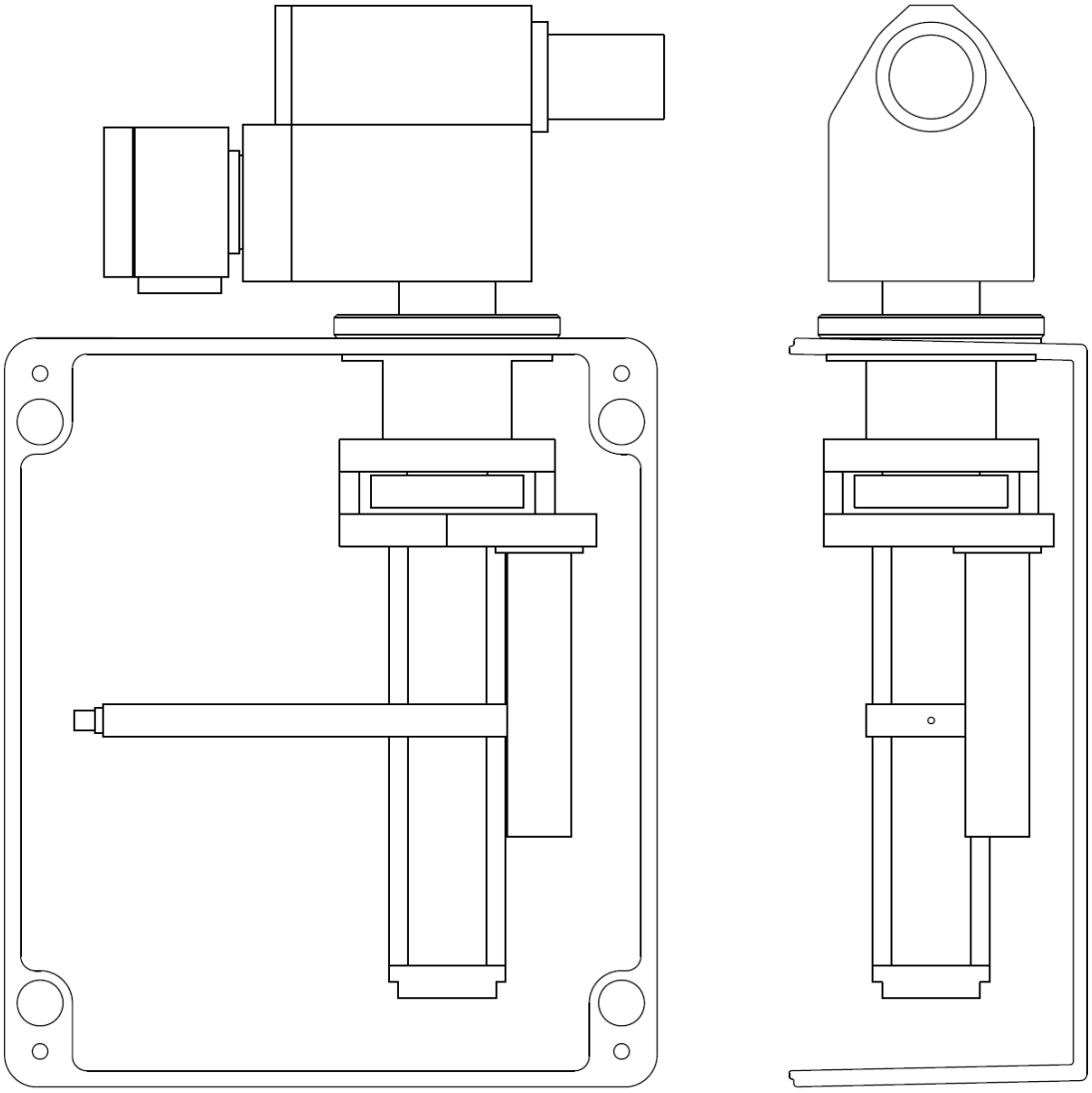

Figure B.1: *Engineering drawing of the telescope unit*

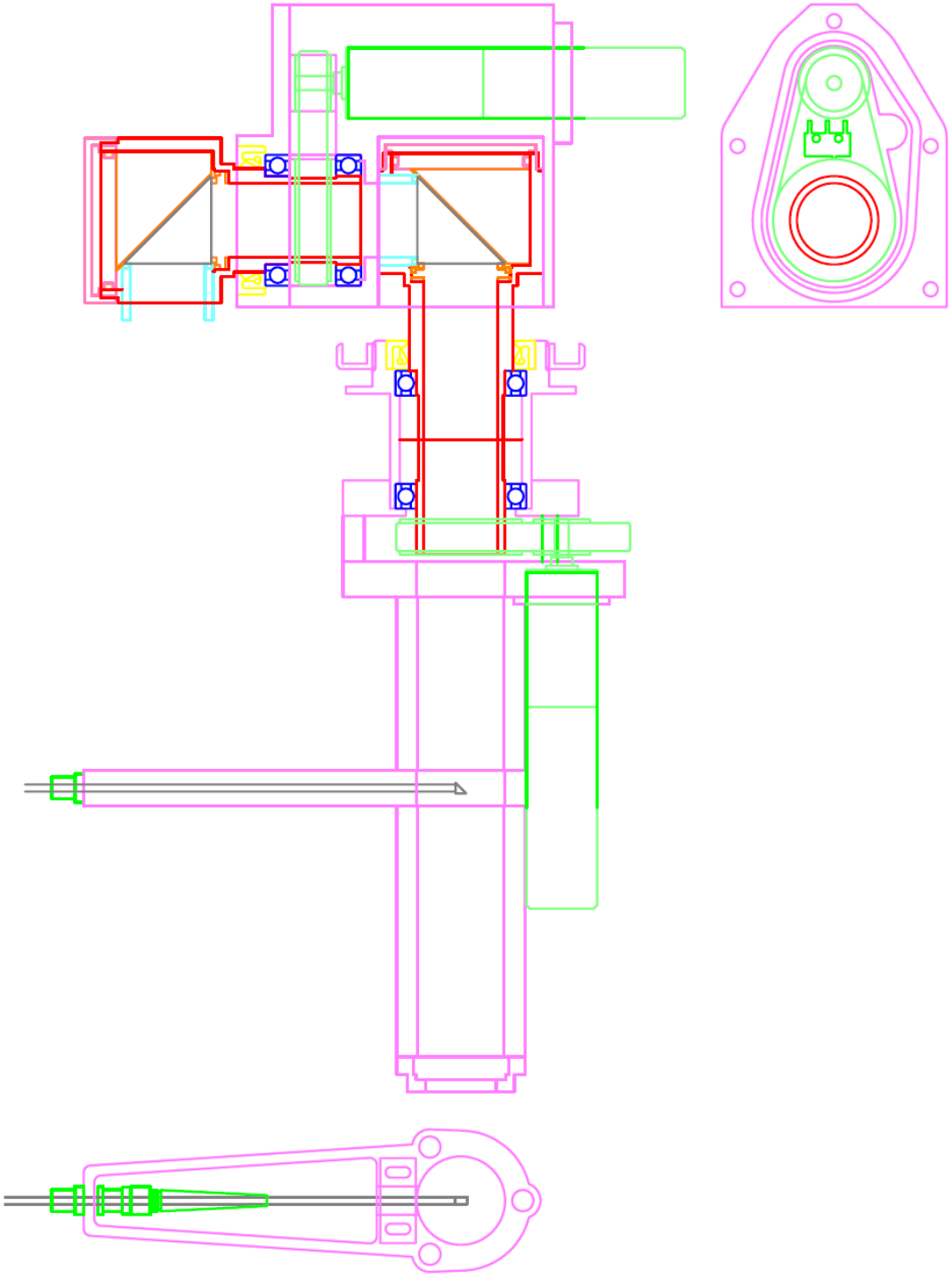

Figure B.2: *Engineering drawing of the telescope optical bench*

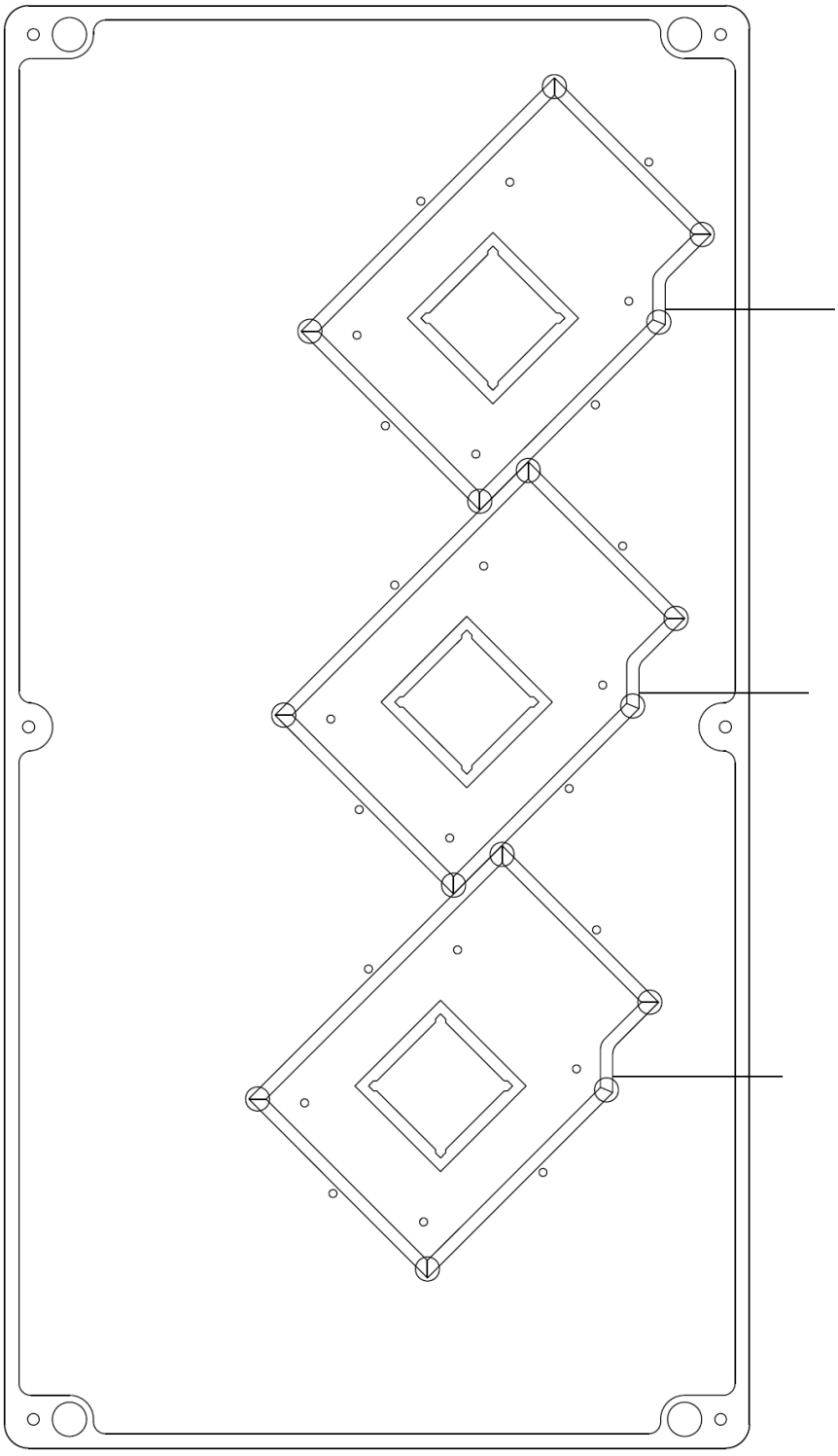

Figure B.3: *Engineering drawing of the spectrometer unit*

List of Figures

2.1 Left panel: thermal structure of the Earth's atmosphere. Adapted from Brasseur and Solomon (1986). Right panel: vertical distribution of solar short wave heating rates by O_3, O_2, NO_2, H_2O, CO_2, and of terrestrial long wave cooling rates by CO_2, O_3, and H_2O. Adapted from London (1980). 5

2.2 The typical diurnal development of the atmospheric boundary layer. Adapted from Stull (1988). 6

2.3 Mean global distribution of the tropospheric NO_2 vertical column density in 10^{15} molecules/cm_2 retrieved from SCIAMACHY satellite measurements for cloud free conditions during 2003–2010 (Steffen Beirle, MPI Mainz, personal communication). 10

2.4 Mean global distribution of the atmospheric SO_2 vertical column density retrieved from GOME-2 satellite measurements (Christoph Hörmann, IUP Heidelberg, personal communication). 11

2.5 Idealized schematic of the distribution of particle surface area of an atmospheric aerosol. Principal modes, sources, and particle formation and removal mechanisms are indicated. Adapted from (Seinfeld and Pandis, 2006). 16

2.6 Atmospheric resistance time as a function of particle diameter for the different atmospheric layers. The predominant removal mechanisms are indicated. Adapted from (Jaenicke, 1978). 17

2.7 Typical number and volume distributions of atmospheric particles with the different modes. Adapted from (John et al., 1990; Seinfeld and Pandis, 2006). 18

2.8 Representative vertical distribution of aerosol mass concentration. Adapted from (Jaenicke, 1993). 19

3.1 Basic principle of DOAS: I_0 and σ are separated by an adequate filtering procedure into a narrow (τ' and σ') and broad band part (I_0' and σ_B). Adapted from Platt and Stutz (2008) 23

3.2 Schematic view of a DOAS instrument used to measure trace-gas concentrations. Collimated light undergoes absorption processes on its way through the atmosphere. In (a), an example of this light entering the spectrograph is given when HCHO is assumed to be the only absorber. (b), the same spectrum convolved with the spectrograph's instrumental function reaches the detector. In the detector the wavelength is mapped to discrete pixels. This spectrum, (c), is then stored in the computer and can be analyzed numerically. Adapted from Stutz and Platt (1996) 26
3.3 Simplified schematic view of a MAX-DOAS measurement. The telescope collects scattered sunlight from viewing directions with different elevation angles. The yellow lines indicate the light paths. 31
3.4 The Last Scattering Altitude LSA: for low elevation angles, the mean free path in the viewing direction is shorter due to higher density and/or aerosol load. This can result in the slant path through absorbing layers at higher altitudes being shorter for lower elevation angles than for higher ones. Adapted from Hönninger et al. (2004) . . 33
3.5 Overview of the literature absorption cross sections in the wavelength range from 250–800 nm listed in Table 3.1. 37
3.6 Wavelength range plot for the spectral retrieval of the O_4 absorption at 360 nm. The plot shows the retrieved O_4 dSCD depending on the lower and upper limit of the wavelength range used in the fit. The color code indicates the dSCDs. The left and bottom panels show the considered absorption cross sections. 38
3.7 Same as Figure 3.6 but for the spectral retrieval of the O_4 absorption at 477 nm. 39
3.8 Wavelength range plot for the spectral retrieval of the O_4 absorption at 577 nm. The plot shows the retrieved O_4 dSCD depending on the lower and upper limit of the wavelength range used in the fit. The color code indicates the dSCDs. The left and bottom panels show the considered absorption cross sections. 40
3.9 Same as Figure 3.8 but for the spectral retrieval of the O_4 absorption at 630 nm. 41
3.10 Wavelength range plot for the spectral retrieval of the NO_2 absorption in the visible wavelength range. The plot shows the retrieved NO_2 dSCD depending on the lower and upper limit of the wavelength range used in the fit. The color code indicates the dSCDs. The left and bottom panels show the considered absorption cross sections. 42
3.11 Same as Figure 3.10 but for the spectral retrieval of the NO_2 absorption in the ultra-violet wavelength range. 43
3.12 Wavelength range plot for the spectral retrieval of the SO_2 absorption. The plot shows the retrieved SO_2 dSCD depending on the lower and upper limit of the wavelength range used in the fit. The color code indicates the dSCDs. The left and bottom panels show the considered absorption cross sections. 44

3.13 Example for the spectral retrieval of the 360 nm band of O_4 (left panel) and NO_2 (right panel) in the ultra-violet wavelength range. The spectrum was recorded in Cabauw on 10 May 2008 for a SZA of 56° and an elevation angle of 2°. The zenith measurement from the same elevation sequence was taken as FRS. The retrieved spectral signatures are indicated in red and the fitted cross sections in black. . 47

3.14 Example for the spectral retrieval of the different O_4 absorption bands and NO_2 in the visible wavelength range. The spectra were recorded in Cabauw on 10 May 2008 for a SZA of 55° and an elevation angle of 20°. The zenith measurement from the same elevation sequence was taken as FRS. The retrieved spectral signatures are indicated in red and the fitted cross sections in black. 48

3.15 Example for the spectral retrieval of SO_2. The spectrum was recorded in Heidelberg on 18 May 2010 for a SZA of 61° and an elevation angle of 1°. The zenith measurement from noon of the same day for a SZA of 30° was taken as FRS. The retrieved spectral signatures are indicated in red and the fitted cross sections in black. 49

4.1 Solar irradiance spectrum at the top of the Earth's atmosphere and at the surface. The solar irradiance spectrum is reshaped by the absorption of atmospheric constituents, such as molecular oxygen, water vapor, ozone and carbon dioxide. Adapted from Finlayson-Pitts and Pitts jr. (2000). 53

4.2 Terrestrial radiance spectrum for cloud free conditions including the absorptions by water vapor, carbon dioxide, ozone and methane. Adapted from Brasseur et al. (1999). 53

4.3 The Earth's annual and global mean energy balance. Adapted from Solomon et al. (2007). 54

4.4 The principal components and corresponding uncertainties of the radiative forcing of climate change. The values represent the forcings in 2005 relative to the start of the industrial era (about 1750). Adapted from Solomon et al. (2007). 55

4.5 Sketch of ro-vibrational energy levels of two electronic states of a (diatomic) molecule. The electronic energies are given as a function of the distance between the nuclei of the atoms within the molecule and are minimal at R_e, which usually depends on electronic state. The equidistant, horizontal groups of lines denote the lowest rotational levels of the vibrational states. 57

4.6 Polar diagram of the Rayleigh scattering phase function $\Phi_R(\theta)$ for unpolarized incident light (see text). Adapted from Hönninger (2002). 58

4.7 Mie scattering phase functions at 550 nm for water droplets with aerosol size parameters $x = 1, 3$ and 10. Left column: Phase function on logarithmic scale; Right column: Polar diagrams of the same phase functions on linear scale. It becomes apparent that forward scattering dominates with increasing particle size. Adapted from Sanghavi (2003). 60

6.1 Flowchart of the aerosol and trace gas profile retrieval procedure using MAX-DOAS measurements. 84

6.2 Retrieval of the aerosol extinction profile: the (a) a priori (red, dotted), retrieved (red, solid), true (black) and convolved true (green) profile; (b) deviation of the retrieved extinction from the true (black) and convolved true (green) profile. 86

6.3 The true (black cross) and retrieved (red asterisk) differential (a) O_4 optical densities and (b) relative intensities as a function of the elevation angle. 87

6.4 The weighting functions of the aerosol extinction profile retrieval with respect to (a) the differential O_4 optical density and (b) relative intensity. The elevation angles of the measurements are indicated by the different colors. 87

6.5 Averaging kernels of the aerosol extinction profile retrieval. The corresponding altitudes are indicated by the different colors. 88

6.6 Retrieval of a smoothed box-shaped profile and corresponding averaging kernels with (a,d) a constant weighting function, (b,e) two subsequent iteration sequences with a recalculated weighting function in the second sequence and (c,f) a recalculated weighting function in each iteration step. 89

6.7 Same as Figure 6.6, but for the retrieval of an elevated aerosol layer centered around 2 km. 90

6.8 Resulting profiles and corresponding averaging kernels for retrievals (a,c) using and (b,d) omitting a state vector transformation. 91

6.9 Resulting profiles and corresponding averaging kernels for retrievals using a linear decreasing a priori profile with (a,d) a surface value of $0.1\,\mathrm{km}^{-1}$ and a height of 2.0 km, (b,e) $0.05\,\mathrm{km}^{-1}$ and 3.0 km, and (c,f) $0.2\,\mathrm{km}^{-1}$ and 3.0 km, respectively. 92

6.10 Retrieval of (a) an elevated aerosol layer centered around 1 km with an AOD of 0.1 and (b) a smoothed box-shaped profile with an AOD of 0.1 and a height of 1.0 km. 93

6.11 Resulting profiles and corresponding averaging kernels for retrievals using (a,d) only the O_4 ΔOD at 477 nm, (b,e) the O_4 ΔODs at four wavelengths and (c,f) the O_4 ΔODs and relative intensities at four wavelengths. 93

6.12 Resulting profiles and corresponding averaging kernels for retrievals using (a,c) O_4 ΔODs with errors of $5 \cdot 10^{-3}$ and relative intensities with errors of $5 \cdot 10^{-2}$ and (b,d) $5 \cdot 10^{-5}$ and $5 \cdot 10^{-4}$, respectively. . . 94

6.13 Resulting profiles and corresponding averaging kernels for retrievals using (a,d) a height grid with 100 m, (b,e) 400 m and (c,f) 800 m resolution. 95

6.14 (a) The a priori (blue), retrieved (red), true (black) and convolved true (green) profiles from 100 retrieval repetitions with random measurement noise. (b) The average and the standard deviations of the retrieved profiles are shown in red instead of the individual profiles. (c) The difference of the retrieved average to the true (black) and convolved true (green) profile with the standard deviations. 96

6.15 The a priori (blue), retrieved (red), true (black) and convolved true (green) profile from a retrieval without random measurement noise. The retrieved profile is shown with the (a) total retrieval error, (b) retrieval noise error and (c) smoothing error. 96

6.16 Resulting profiles for retrievals with an error in the elevation angles of (a) - 0.5° and (b) + 0.5°. 97

6.17 Resulting profiles for retrievals with (a) an underestimation of the O_4 absorption cross-section of 25 % and (b) overestimation of 25 %. . . . 97

6.18 Simultaneous retrieval of the aerosol extinction profile, Ångström exponent, single scattering albedo and asymmetry parameter using the O_4 ΔODs and relative intensities at 360, 477, 577 and 630 nm. (a) The a priori (blue), retrieved (red), true (black) and convolved true (green) profile. (b) The a priori (blue, square), true (black, plus) and retrieved (red, cross) optical parameters. 98

6.19 Results of the two parameter retrievals of a (a) smoothed box-shaped profile, (b) linearly decreasing profile and (c) elevated aerosol layer. The a priori (red, dotted), retrieved (red) and true (black) profiles are shown in each panel. 99

6.20 Simultaneous retrieval of the two aerosol extinction profile parameters, Ångström exponent, single scattering albedo and asymmetry parameter using the O_4 ΔODs and relative intensities at 360, 477, 577 and 630 nm. (a) The a priori (blue), retrieved (red) and true (black) profile. (b) The a priori (blue, square), true (black, plus) and retrieved (red, cross) optical parameters. (c) The corresponding averaging kernels color coded according the parameters (state vector elements). 100

6.21 Results of the three parameter retrievals of a (a) smoothed box-shaped profile, (b) linear decreasing profile and (c) elevated aerosol layer. The a priori (red, dotted), retrieved (red) and true (black) profiles are shown in each panel. 101

6.22 Retrieval of the NO_2 profile: the (a) a priori (red, dotted), retrieved (red), true (black) and convolved true (green) profile; (b) deviation of the retrieved NO_2 from the true (black) and convolved true (green) profile. 101

6.23 (a) The true (black cross) and retrieved (red asterisk) differential NO_2 slant column densities as a function of the elevation angle and (b) the aerosol extinction profile. 102

6.24 (a) The Weighting functions of the NO_2 profile retrieval color coded according the corresponding elevation angles of the measurements. (b) The averaging kernels of the profile retrieval color coded according the corresponding altitudes. 102
6.25 Retrieval of (a) a linear decreasing NO_2 profile and (b) a combined NO_2 profile featuring a linear decrease and an elevated layer centered around 2 km altitude. 103
6.26 Overview of the NO_2 profile retrieval quantities for the presence of an elevated aerosol layer: (a) NO_2 profiles; (b) differences in the NO_2 profiles; (c) NO_2 ΔSCDs; (d) assumed aerosol profile; (e) retrieval weighting functions; (f) retrieval averaging kernels. (Compare with Figures 6.22, 6.23 and 6.24) 104
6.27 Retrievals of the aerosol extinction profiles using the discrete first-derivative operator and different regularization parameters indicated on top of each panel. The a priori (red, dotted), retrieved (red, solid), true (black), and convolved true (green) profile is shown in each panel. 106
6.28 The averaging kernels of the aerosol profile retrievals shown in Figure 6.27. The regularization parameters are indicated on top of each panel, while the corresponding altitudes are indicated by different colors (see legend in Figure 6.5). 107
6.29 The degrees of freedom for signal as a function of the regularization parameter for the (a) identity matrix, (b) discrete first- and (c) second-derivative operator. 108
6.30 The mean relative total (black, square), noise (blue, plus) and smoothing (red, cross) errors of retrievals using the discrete first-derivative operator as a function of the regularization parameter. 108
6.31 The L-curve of retrievals using the discrete first-derivative operator. The regularization parameters are indicated by different colors. 109
6.32 Retrievals of the NO_2 profiles using the discrete first-derivative operator and different regularization parameters indicated on top of each panel. The a priori (red, dotted), retrieved (red), true (black), and convolved true (green) profile is shown in each panel. 109

7.1 Schematic drawing of the MAX-DOAS instrument: the spectrometer (left) and telescope unit (right) 112
7.2 Photograph of the MAX-DOAS instrument: the spectrometer (left) and telescope unit (right) 113
7.3 Typical setup of the MAX-DOAS instrument: the telescope (left, outdoors) and spectrometer unit (right, indoors). The pictures were taken during the field campaign in Cabauw, the Netherlands in 2008 . 114
7.4 Sketch of the Ocean Optics HR2000 spectrometer 115
7.5 Illustration of the fiber bundle configuration 116
7.6 Screenshot of the measurement program MS-DOAS 116
7.7 Electronic offset (left) and dark current (right) signal of the HR2000 spectrometer at two different temperatures 117

7.8 Instrument functions at different wavelengths (a-c) and wavelength to pixal mapping (d-f) of the individual HR2000 spectrometers (UV, Vis1 and Vis2) recorded at two different temperatures. The symbols in the lower panels indicate the position of the mercury (d,e) and neon (f) emission lines, while the solid and dashed lines indicate the second order polynomial fit results. 119
7.9 Example for the signal to noise ratio of the HR2000 spectrometer, normalized according the considered wavelength range, as a function of the total integration time for two different temperatures. The solid and dashed line indicate the linear fit with a slope of 0.5. 120
7.10 Field of view for the individual spectrometers (UV, Vis1 and Vis2). The normalized intensity is plotted as a function of the azimuth and elevation angle of the viewing direction. 121

8.1 Overview of the measurement sites (source: Google Maps). 132
8.2 Areal view for the measurement site in Cabauw (source: Google Maps). 134
8.3 Correlation of measured and simulated O_4 ΔODs (left panels) and relative intensities (right panels) at four wavelengths indicated by different colors. Only the data of the elevation scans from 7 May to 10 May 2008 are considered for different model settings: (a,b) surface albedo of 0.05 and scaling factor for the O_4 absorption cross-section (XS) of 1.0, (c,d) 0.05 and 1.125, (e,f) 0.05 and 1.25 and (g,h) 0.3 and 1.0, respectively. 136
8.4 Correlation of measured and simulated O_4 ΔODs (left panels) and relative intensities (right panels) color-coded according the elevation angle, for (a,b) 360, (c,d) 477, (e,f) 577 and (g,h) 630 nm (data from panel (a) and (b) of Figure 8.3). The purple lines indicate the results of the linear regression. 137
8.5 Correlation of measured and simulated O_4 ΔODs (left panels) and relative intensities (right panels) color-coded according to the azimuth angle for (a,b) 360, (c,d) 477, (e,f) 577 and (g,h) 630 nm. Only the data of the azimuth scans from 7 May to 10 May 2008 are considered. 138
8.6 Retrieved and measured (a) O_4 ΔODs and (b) intensities at 477 nm for the aerosol profile retrievals from MAX-DOAS measurements on 7 May 2008. 140
8.7 Comparison of $\epsilon_M(z)$ at 477 nm retrieved from lidar and MAX-DOAS for 7 May 2008: (top) averaged profiles from lidar, (center) profiles from lidar convolved with the AVK of the MAX-DOAS retrieval and (bottom) profiles from MAX-DOAS. 141
8.8 Same as Figure 8.7 but for 8 May 2008. 142
8.9 Same as Figure 8.7 but for 9 May 2008. 143
8.10 Same as Figure 8.7 but for 10 May 2008. 144
8.11 Time series of the AOD retrieved from MAX-DOAS (open circles) and Sun photometer (solid squares) at (a) 360, (b) 477, (c) 577 and (d) 630 nm for the period of 6 to 11 May 2008 145

8.12 Correlation of the AOD retrieved from MAX-DOAS and Sun photometer at (a) 360, (b) 477, (c) 577 and (d) 630 nm for the period of 6 to 11 May 2008. The one to one line is indicated in dashed black and the linear regression in red. The implemented histograms show the frequency of the differences in the AOD. 146

8.13 Time series of ϵ_M retrieved from MAX-DOAS for 0–200 m (open circles) and in situ measurements (solid squares) at (a) 360, (b) 477, (c) 577 and (d) 630 nm for the period of 6 to 11 May 2008. 147

8.14 Correlation of ϵ_M retrieved from MAX-DOAS for 0–200 m and in situ measurements at (a) 360, (b) 477, (c) 577 and (d) 630 nm for the period of 6 to 11 May 2008, color coded with the AOD from Sun photometer. The one to one line is indicated in dashed black and the linear regression in solid black. 148

8.15 The mean (left panel) absolute and (right panel) relative differences and corresponding standard deviations of $\epsilon_M(z)$ at 477 nm retrieved from MAX-DOAS and lidar for the period of 7 to 10 May 2008. The differences to the (blue) original and (red) convolved lidar profiles for different retrieval setting: (a,b) only O_4 ΔODs are used; (c,d) O_4 ΔODs and relative intensities are used; (e,f) radiosonde data is used; (g,h) scaling factor of 1.25 is applied on the O_4 absorption cross section (see text for details). 150

8.16 The mean (left panel) absolute and (right panel) relative differences and corresponding standard deviations of $\epsilon_M(z)$ at 477 nm retrieved from MAX-DOAS and lidar for the period of 3 May to 30 June 2008. The differences to the (blue) original and (red) convolved lidar profiles for opaque cloud fraction less than (a,b) 30 %, (c,d) 10 % and (e,f) 5 % (see text for details). 154

8.17 Correlation of the AOD at 477 nm retrieved from MAX-DOAS and Sun photometer for the period of 3 May to 30 June 2008 and conditions with an opaque cloud fraction of (a) <100 %, (b) <30 % and (c) <10 %. The one to one line is indicated in dashed black and the linear regression in solid black. 155

8.18 Correlation of ϵ_M at 477 nm retrieved from MAX-DOAS for 0–200 m and in situ measurements for the period of 3 to 31 May 2008 and conditions with an opaque cloud fraction of (a) <100 %, (b) <30 % and (c) <10 %. The one to one line is indicated in dashed black and the linear regression in solid black. 156

8.19 Comparison of $\epsilon_M(z)$ at 477 nm retrieved from lidar and MAX-DOAS for 7 May 2008: (top) averaged profiles from lidar, (center) profiles retrieved from MAX-DOAS using 2 and (bottom) 3 parameters for the profile description. 157

8.20 Same as Figure 8.19 but for 9 May 2008. 158

8.21 Correlation of the AOD at 477 nm retrieved from MAX-DOAS and Sun photometer for the period of 6 to 11 May 2008 using (a) two and (b) three parameters for the profile description. The one to one line is indicated in dashed black and the linear regression in red. The implemented histograms show the frequency of the differences in the AOD. 159

8.22 Correlation of ϵ_M at 477 nm retrieved from MAX-DOAS for 0–200 m and in situ measurements for the period of 6 to 11 May 2008 using (a) two and (b) three parameters for the profile description, color coded with the AOD from Sun photometer. The one to one line is indicated in dashed black and the linear regression in solid black. 159

8.23 Correlation of the AOD at 477 nm retrieved from Sun photometer and MAX-DOAS for the period of 6 to 11 May 2008 using the (a) identity matrix, (b) discrete first- and (c) second-derivative operator with regularization parameters of 10, 1 and 0.01, respectively. The one to one line is indicated in dashed black and the linear regression in red. The implemented histograms show the frequency of the differences in the AOD. 160

8.24 $\epsilon_M(z)$ at 477 nm on 7 May 2008 retrieved from MAX-DOAS using different regularization operators: (top) identity matrix, (center) discrete first- and (bottom) second-derivative operator with regularization parameters of 10, 1 and 0.01, respectively. 161

8.25 Correlation of ϵ_M at 477 nm retrieved from in situ measurements and MAX-DOAS for 0–200 m for the period of 6 to 11 May 2008 using the (a) identity matrix, (b) discrete first- and (c) second-derivative operator with regularization parameters of 10, 1 and 0.01, respectively. The color code is according the AOD from Sun photometer. The one to one line is indicated in dashed black and the linear regression in solid black. 162

8.26 Retrieved and measured NO_2 ΔSCDs for the profile retrievals from MAX-DOAS measurements on 7 May 2008. 162

8.27 Diurnal development of the NO_2 VMR profile retrieved from MAX-DOAS for the period of 6 to 8 May 2008. 163

8.28 Same as Figure 8.27 but for the period of 9 to 11 May 2008. 164

8.29 Time series of the NO_2 VCD and surface concentration for the period of 6 to 11 May 2008: (a) NO_2 VCD retrieved from MAX-DOAS for 0–4 km (open black squares) and the tropospheric VCD from SCIAMACHY (stars), OMI (triangles) and GOME-2 (diamonds) color coded according to the distance of the satellite pixel center to the Cabauw site; (b) NO_2 concentration measured in situ (solid red circles) and retrieved from MAX-DOAS for 0–100 km (open blue squares). 166

8.30 Correlation of the NO_2 surface concentration measured in situ and retrieved from MAX-DOAS for 0–100 m for the period of 6 to 11 May 2008. The one to one line is indicated in dashed black and the linear regression in solid red. 166

8.31 Correlation of the NO_2 surface concentration measured in situ and retrieved from MAX-DOAS for 0–100 m for the period of 3 May to 30 June 2008 and conditions with an opaque cloud fraction of (a) $< 100\,\%$, (b) $< 30\,\%$ and (c) $< 10\,\%$. The one to one line is indicated in dashed black and the linear regression in solid black. 168

8.32 Time series of the NO_2 VCD for the period of 03 May to 30 June 2008 retrieved from MAX-DOAS for 0–4 km and the tropospheric VCD from (a) GOME-2, (b) OMI and (c) SCIAMACHY. The color code is according the distance of the satellite pixel center to the Cabauw site. 169

8.33 The NO_2 VMR profiles on 8 May 2008 retrieved from MAX-DOAS using different regularization operators: (top) identity matrix, (center) discrete first- and (bottom) second-derivative operator with regularization parameters of 5, 0.1 and 0.05, respectively. 171

8.34 Comparison of $\epsilon_M(z)$ at 477 nm retrieved from lidar and MAX-DOAS for two periods on 10 June 2008. The original (blue) and convolved lidar (red) profiles and the profiles from MAX-DOAS (black). 172

8.35 Correlation of the AOD at 477 nm retrieved from Sun photometer in Leipzig and from MAX-DOAS in Melpitz for cloudless conditions during 21 May to 9 July 2008. The one to one line is indicated in dashed black and the linear regression in red. The implemented histograms show the frequency of the differences in the AOD. 173

8.36 Comparison of $\epsilon_M(z)$ at 477 nm retrieved from MAX-DOAS and lidar for selected time periods: the original (blue) and convolved lidar profiles (red) and the profiles from MAX-DOAS (black). 174

8.37 Time series of the (top) AOD at 477 nm retrieved from MAX-DOAS and Sun photometer and (bottom) ϵ_M from MAX-DOAS for 0–200 m and measured in situ for selected time periods. 175

8.38 Correlation of the AOD at 477 nm retrieved from Sun photometer and MAX-DOAS for the period of 11 December 2008 to 25 March 2009, color coded according χ^2 of the MAX-DOAS retrieval: (a) all data points and (b) cases with $\chi^2 < 1000$. The one to one line is indicated in dashed black and the linear regression in solid black. The implemented histograms show the frequency of the differences in the AOD. 176

8.39 Correlation of ϵ_M at 477 nm retrieved from MAX-DOAS for 0–200 m and measured in situ for the period of 11 December 2008 to 25 March 2009, color coded according the AOD from Sun photometer. The one to one line is indicated in dashed black and the linear regression in solid black. 177

8.40 Comparison of $\epsilon_M(z)$ at 477 nm retrieved from lidar and MAX-DOAS using (left panels) the O_4 ΔODs and relative intensities and (right panels) only the O_4 ΔODs for selected periods of 13 May 2009: the original (blue) and convolved lidar profiles (red) and the profiles from MAX-DOAS (black). 178

8.41 Correlation of the AOD at 477 nm retrieved from Sun photometer and MAX-DOAS using (a) the O_4 ΔODs and relative intensities and (b) only the O_4 ΔODs for the period of 8 to 29 May 2009. The one to one line is indicated in dashed black and the linear regression in red. The implemented histograms show the frequency of the differences in the AOD. 179

8.42 Correlation of the AOD at 477 nm retrieved from Sun photometer and MAX-DOAS using the O_4 ΔODs and relative intensities for conditions with opaque cloud fractions $< 10\,\%$ in the period of 9 June to 8 July 2009, color coded according to the time of day. The one to one line is indicated in dashed black. The larger differences in the AODs occur in the afternoon. 180

8.43 Time series of the AOD at 477 nm retrieved from Sun photometer (open black circles) and MAX-DOAS (solid squares) using only the O_4 ΔODs for the period from 9 June to 8 July 2009, color coded according to the opaque cloud fraction. 182

8.44 Correlation of the AODs from Sun photometer and MAX-DOAS shown in Figure 8.43 for conditions with an opaque cloud fraction of (a) $< 100\,\%$, (b) $< 30\,\%$ and (c) $< 10\,\%$. The one to one line is indicated in dashed black and the linear regression in solid black. The correlation improves for decreasing cloud fractions. 182

8.45 Time series of ϵ_M at 477 nm measured in situ (open black circles) and retrieved from MAX-DOAS (solid squares) for 0–200 m using only the O_4 ΔODs for the period of 9 June to 8 July 2009, color coded according the opaque cloud fraction. 183

8.46 Correlation of ϵ_M at 477 nm from MAX-DOAS and in situ measurements shown in Figure 8.45 for conditions with an opaque cloud fraction of (a) $< 100\,\%$, (b) $< 30\,\%$ and (c) $< 10\,\%$. The one to one line is indicated in dashed black and the linear regression in solid black. An improvement of the correlation with decreasing cloud fraction is not observed. 183

8.47 Comparison of the aerosol profiles retrieved from MAX-DOAS O_4 measurements of different groups for 3 July 2009. The top plot shows the backscatter profile from ceilometer and the second plot shows the convolved profiles from ceilometer. The plots below that show $\epsilon_M(z)$ retrieved from MAX-DOAS instruments from BIRA, IUPHD, JAMSTEC and MPIC (top-down), respectively (Udo Frieß, IUPHD, personal communication). 184

8.48 Time series of the NO_2 VCD and surface concentration for the period of 11 June to 8 July 2009: (a) NO_2 VCD retrieved from MAX-DOAS for 0–4 km (open black squares) and the tropospheric VCD from SCIAMACHY (stars), OMI (triangles) and GOME-2 (diamonds) color-coded according the distance of the satellite pixel center to the Cabauw site; (b) NO_2 concentration measured in situ (solid red circles) and retrieved from MAX-DOAS for 0–100 km (open blue squares). 186

8.49 Correlation of the NO_2 surface concentration measured in situ and retrieved from MAX-DOAS for 0–100 m for the period of 9 June to 8 July 2009 and conditions with an opaque cloud fraction of (a) $< 100\,\%$, (b) $< 30\,\%$ and (c) $< 10\,\%$. The one to one line is indicated in dashed black and the linear regression in solid black. 186

8.50 Correlation of the (a) AOD and (b) ϵ_M at 477 nm retrieved from MAX-DOAS, Sun photometer and in situ measurements for cloudless conditions during 9 July 2009 to 11 April 2010. The one to one line is indicated in dashed black and the linear regression in red. 188

8.51 Time series of the NO_2 VCD and surface concentration for the period of (a,b) 9 July to 17 December 2009 and (c,d) 2 February to 11 April 2010: (a,c) NO_2 VCD retrieved from MAX-DOAS for 0–4 km (open black squares) and the tropospheric VCD from SCIAMACHY (stars), OMI (triangles) and GOME-2 (diamonds) color-coded according the distance of the satellite pixel center to the Cabauw site; (b,d) NO_2 concentration measured in situ (solid red circles) and retrieved from MAX-DOAS for 0–100 km (open blue squares). 189

8.52 The location of the Eyjafjallajokull volcano and the overview of the measurement sites and considered instrumentation (source: Google Maps). The yellow array indicates the viewing direction of the MAX-DOAS instrument. 190

8.53 The (a) simulated volcanic ash vertical columns and (b) measured SO_2 dSCDs over Heidelberg for the period of 17 April to 23 May 2010. Volcanic ash particles with a diameter of 0.25–3 μm were considered in the FLEXPART simulations and serve as proxy for volcanic SO_2. For clarity, the SO_2 dSCDs from MAX-DOAS are only shown for values above the detection limit of $6\,\sigma$. The light grey areas indicate nighttimes. Periods with a significant number of increased SO_2 dSCDs are enlarged in the bottom panels (c-h). 192

8.54 (a,c) GOME-2 measurements of the SO_2 VCD and (b,d) FLEXPART simulations of the volcanic ash vertical column for (top) 19 April and (bottom) 18 May 2010 over northern Europe. Volcanic ash particles with a diameter of 0.25–250 μm were considered in the FLEXPART simulations. The location of the Eyjafjallajokull volcano and Heidelberg is indicated in the maps. 193

8.55 Diurnal developments of the (a,b,i,j) AOD retrieved from MAX-DOAS and Sun photometer, (c,d,k,l) $\epsilon_M(z)$ retrieved from MAX-DOAS, (e,f,m,n) RCS from ceilometer and (g,h,o,p) FLEXPART simulations of the volcanic ash vertical distribution (see text for details). Note that the instruments are located at different sites. The simulations consider the profiles above Heidelberg. 195

8.56 Diurnal developments of the (a,b,e,f) NO_2 ΔSCDs and (c,d,g,h) NO_2 VMR profiles retrieved from MAX-DOAS in Heidelberg for the period of 17 to 20 April 2010. Increased NO_2 VMR were observed on 19 April. 196

8.57 Diurnal developments of the (a) SO_2 dSCDs and (b) SO_2 VMR profiles retrieved from MAX-DOAS in Heidelberg for 19 April 2010. An elevated SO_2 layer is observed in the morning hours. 197

A.1 The mean (left panel) absolute and (right panel) relative differences and corresponding standard deviations of $\epsilon_M(z)$ retrieved from MAX-DOAS and lidar for the period of 7 to 10 May 2008 in Cabauw. The differences to the (blue) original and (red) convolved lidar profiles for retrievals using O_4 ΔODs and relative intensities at (a,b) 360, (c,d) 477, (e,f) 577 and (g,h) 630 nm (Cases Std. from Section 8.2.2.1). . . 206

A.2 The mean (left panel) absolute and (right panel) relative differences and corresponding standard deviations of $\epsilon_M(z)$ at 477 nm retrieved from MAX-DOAS and lidar for the period of 7 to 10 May 2008 in Cabauw. The differences to the (blue) original and (red) convolved lidar profiles for different retrieval setting: (a,b) only O_4 ΔODs are used; (c,d) maximum of 10 iteration steps instead of 5; (e,f) performing two subsequent iteration sequences; (g,h) calculating the weighting function for each iteration step (Cases A and B from Section 8.2.2.1). 207

A.3 The mean (left panel) absolute and (right panel) relative differences and corresponding standard deviations of $\epsilon_M(z)$ at 477 nm retrieved from MAX-DOAS and lidar for the period of 7 to 10 May 2008 in Cabauw. The differences to the (blue) original and (red) convolved lidar profiles for different retrieval setting: (a,b) using the monthly mean aerosol optical properties; (c,d) surface albedo of 0.3 instead of 0.05; (e,f) using radiosonde data; (g,h) using a scaling factor of 1.25 for the O_4 absorption cross-section (Cases C from Section 8.2.2.1). . . 208

A.4 The mean (left panel) absolute and (right panel) relative differences and corresponding standard deviations of $\epsilon_M(z)$ at 477 nm retrieved from MAX-DOAS and lidar for the period of 7 to 10 May 2008 in Cabauw. The differences to the (blue) original and (red) convolved lidar profiles for retrievals using a scaling factor of 5 for (a,b) the O_4 ΔOD errors, (c,d) the intensity errors and (e,f) the O_4 ΔOD and intensity errors (Cases D from Section 8.2.2.1). 209

A.5 The mean (left panel) absolute and (right panel) relative differences and corresponding standard deviations of $\epsilon_M(z)$ retrieved from MAX-DOAS and lidar for the period of 7 to 10 May 2008 in Cabauw. The differences to the (blue) original and (red) convolved lidar profiles for retrievals using simultaneously the O_4 ΔODs and intensities at 360 and 477 nm, (c,d) 477 and 577 nm, (e,f) 360, 477 and 577 nm and (g,h) 360, 477, 577 and 630 nm (Cases E from Section 8.2.2.1). 210

A.6 Comparison of $\epsilon_M(z)$ at 477 nm retrieved from lidar and MAX-DOAS for 8 May 2008 in Cabauw: (top) averaged profiles from lidar, (center) profiles retrieved from MAX-DOAS using 2 and (bottom) 3 parameters for the profile description (see Section 8.2.2.3). 211

A.7 Comparison of $\epsilon_M(z)$ at 477 nm retrieved from lidar and MAX-DOAS for 10 May 2008 in Cabauw: (top) averaged profiles from lidar, (center) profiles retrieved from MAX-DOAS using 2 and (bottom) 3 parameters for the profile description (see Section 8.2.2.3). 212

B.1 Engineering drawing of the telescope unit 214
B.2 Engineering drawing of the telescope optical bench 215
B.3 Engineering drawing of the spectrometer unit 216

List of Tables

2.1 The main constituents of the unpolluted dry atmosphere 4
2.2 Tropospheric sources of NO_x emissions (Lee et al., 1997). The source strength is given in million tons of fixed nitrogen [Tg N] per year. . . 8
2.3 Global emission estimates for major aerosol classes (Seinfeld and Pandis, 2006, and references therein). 14
2.4 Concentrations of selected elements found in atmospheric aerosols and the corresponding particle size ranges (Schroeder et al., 1987). 15

3.1 Trace gas absorption cross sections utilized in this work. 35
3.2 Fit scenarios and according optical densities used for the wavelength mapping with artificial spectra. 36
3.3 Spectral retrieval settings. 46

7.1 FWHM of the instrument functions from Figure 7.8 120

8.1 The measurement sites and the periods of the intercomparison campaigns. 132
8.2 The influence of different retrieval settings. Linear regression fit and statistical parameters for the correlation of the AOD retrieved from MAX-DOAS and Sun photometer for the period of 6 to 11 May 2008 (see text for details). 152
8.3 The influence of different retrieval settings. Linear regression fit and statistical parameters for the correlation of ϵ_M (in km^{-1}) retrieved from MAX-DOAS for 0–200 m and in situ measurements for the period of 6 to 11 May 2008 (see text for details). 153
8.4 The influence of different retrieval settings. Linear regression fit and statistical parameters for the correlation of the NO_2 surface concentration (in $\mu g/m^3$) retrieved from MAX-DOAS for 0–100 m and in situ measurements for the period of 6 to 11 May 2008 (see text for details). 168
8.5 The influence of the cloud fraction. Linear regression fit and statistical parameters for the correlations shown in Figure 8.31. 169
8.6 The influence of the regularization operator. Linear regression fit and statistical parameters for the correlation of the NO_2 surface concentration (in $\mu g/m^3$) retrieved from in situ measurements and MAX-DOAS for 0–100 m for the period of 6 to 11 May 2008 (see text for details). 170

8.7 The influence of the cloud fraction. Linear regression fit and statistical parameters for the correlations shown in Figure 8.49. 187

Bibliography

Aben, I., Stam, D. M., and Helderman, F.: The ring effect in skylight polarisation, Geophys. Res. Lett., 28, 519–522, URL http://dx.doi.org/10.1029/2000GL011901, 2001.

Adamantides, V.: Equilibrium structure and vibrational frequencies of the O4 molecule, Chemical Physics, 48, 221 – 225, doi:10.1016/0301-0104(80)80052-8, 1980.

Adamantides, V., Neisius, D., and Verhaegen, G.: Ab initio study of the O4 molecule, Chemical Physics, 48, 215 – 220, doi:10.1016/0301-0104(80)80051-6, 1980.

Akima, H. A.: A new method of interpolation and smooth curve fitting based on local procedures, Journal of Assc. for Comp. Mach., 17, 589–602, 1970.

Albritton, D. L., Schmeltekopf, A. L., and Zare, R. N.: Molecular Spectroscopy: Modern Research, chap. An introduction to the least-squares fitting of spectroscopic data, Orlando, Florida, USA: Academic Press, 1976.

Alicke, B., Hebestreit, K., Stutz, J., and Platt, U.: Iodine oxide in the marine boundary layer, Nature, 397, 572–573, URL http://dx.doi.org/10.1038/17508, 1999.

Althausen, D., Engelmann, R., Baars, H., Heese, B., Ansmann, A., MÃ$\frac{1}{4}$ller, D., and Komppula, M.: Portable Raman Lidar PollyXT for Automated Profiling of Aerosol Backscatter, Extinction, and Depolarization, J. Atmos. Oceanic Technol., 26, 2366–2378, URL http://dx.doi.org/10.1175/2009JTECHA1304.1, 2009.

Altshuller, A. P.: Production of aldehydes as primary emissions and from secondary atmospheric reactions of alkenes and alkanes during the night and early morning hours, Atmos. Environ., 27A, 21–32, 1993.

Anderson, T. L. and Ogren, J. A.: Determining Aerosol Radiative Properties Using the TSI 3563 Integrating Nephelometer, Aerosol Science and Technology, 29, 57–69, doi:10.1080/02786829808965551, 1998.

Andreae, M., Ferek, R., Bermond, F., Byrd, K., Chatfield, R., Engstrom, R., Hardin, S., Houmere, P., LeMarrec, F., and Raemdonck, H.: Dimethyl sulfide in the marine atmosphere, J. Geophys. Res., 90, 12 891–12 900, 1985.

Angström, A.: On the atmospheric transmission of sun radiation, II. Geogr. Ann. Stockholm, 12, 130–159, 1930.

Ansmann, A. and Müller, D.: Lidar - range-resolved optical remote sensing of the atmosphere, chap. Lidar and atmospheric aerosol particles, Springer, New York., 2005.

Ansmann, A., Riebesell, M., and Weitkamp, C.: Measurement of atmospheric aerosol extinction profiles with a Raman lidar, Optics Letters, 15, 746–748, 1990.

Ansmann, A., Riebesell, M., Wandinger, U., Weitkamp, C., Voss, E., Lahmann, W., and Michaelis, W.: Combined raman elastic-backscatter LIDAR for vertical profiling of moisture, aerosol extinction, backscatter, and LIDAR ratio, Applied Physics B: Lasers and Optics, 55, 18–28, URL http://dx.doi.org/10.1007/BF00348608, 10.1007/BF00348608, 1992.

Apituley, A., Wilson, K. M., Potma, C., Volten, H., and de Graaf, M.: Performance Assessment 10 and Application of CAELI - A high-performance Raman lidar for diurnal profiling of Water Vapour, Aerosols and Clouds, in: Proceedings of the 8th International Symposium on Tropospheric Profiling, Delft, The Netherlands, 19-23 October 2009, ISBN 978-90-6960-233-2, 2009.

Atkinson, R., Baulch, D. L., Cox, R. A., Crowley, J. N., Hampson, R. F., Hynes, R. G., Jenkin, M. E., Rossi, M. J., and Troe, J.: Evaluated kinetic and photochemical data for atmospheric chemistry: Volume I - gas phase reactions of O_x, HO_x, NO_x and SO_x species, Atmospheric Chemistry and Physics, 4, 1461–1738, doi:10.5194/acp-4-1461-2004, URL http://www.atmos-chem-phys.net/4/1461/2004/, 2004.

Baars, H., Ansmann, A., Engelmann, R., and Althausen, D.: Continuous monitoring of the boundary-layer top with lidar, Atmospheric Chemistry and Physics, 8, 7281–7296, doi:10.5194/acp-8-7281-2008, URL http://www.atmos-chem-phys.net/8/7281/2008/, 2008.

Backus, G. E. and Gilbert, J. F.: Uniqueness in the inversion of inaccurate gross Earth data, Philos. Trans. R. Soc., 266, 123–192., 1970.

Barnaba, F., Putaud, J. P., Gruening, C., dell'Acqua, A., and Dos Santos, S.: Annual cycle in co-located in situ, total-column, and height-resolved aerosol observations in the Po Valley (Italy): Implications for ground-level particulate matter mass concentration estimation from remote sensing, J. Geophys. Res., 115, D19 209–, URL http://dx.doi.org/10.1029/2009JD013002, 2010.

Barret, B., De Mazière, M., and Demoulin, P.: Retrieval and characterization of ozone profiles from solar infrared spectra at the Jungfraujoch, J. Geophys. Res., 107, 4788–, URL http://dx.doi.org/10.1029/2001JD001298, 2002.

Beirle, S., Platt, U., Wenig, M., and Wagner, T.: Weekly cycle of NO_2 by GOME measurements: a signature of anthropogenic sources, Atmospheric Chemistry and Physics, 3, 2225–2232, doi:10.5194/acp-3-2225-2003, URL http://www.atmos-chem-phys.net/3/2225/2003/, 2003.

Beirle, S., Boersma, K. F., Platt, U., Lawrence, M. G., and Wagner, T.: Megacity Emissions and Lifetimes of Nitrogen Oxides Probed from Space, Science, 333, 1737–1739, doi:10.1126/science.1207824, URL `http://www.sciencemag.org/content/333/6050/1737.abstract`, 2011.

Bevington, P. R.: Data Reduction and Error Analysis for the Physical Sciences, McGraw Hill, first edn., 1969.

Boersma, K. F., Eskes, H. J., and Brinksma, E. J.: Error analysis for tropospheric NO2 retrieval from space, J. Geophys. Res., 109, D04 311–, URL `http://dx.doi.org/10.1029/2003JD003962`, 2004.

Boersma, K. F., Eskes, H. J., Veefkind, J. P., Brinksma, E. J., van der A, R. J., Sneep, M., van den Oord, G. H. J., Levelt, P. F., Stammes, P., Gleason, J. F., and Bucsela, E. J.: Near-real time retrieval of tropospheric NO_2 from OMI, Atmospheric Chemistry and Physics, 7, 2103–2118, doi:10.5194/acp-7-2103-2007, URL `http://www.atmos-chem-phys.net/7/2103/2007/`, 2007.

Boersma, K. F., Eskes, H. J., Dirksen, R. J., van der A, R. J., Veefkind, J. P., Stammes, P., Huijnen, V., Kleipool, Q. L., Sneep, M., Claas, J., Leitão, J., Richter, A., Zhou, Y., and Brunner, D.: An improved tropospheric NO_2 column retrieval algorithm for the Ozone Monitoring Instrument, Atmospheric Measurement Techniques, 4, 1905–1928, doi:10.5194/amt-4-1905-2011, URL `http://www.atmos-meas-tech.net/4/1905/2011/`, 2011.

Bogumil, K., Orphal, J., Homann, T., Voigt, S., Spietz, P., Fleischmann, O. C., Vogel, A., Hartmann, M., Kromminga, H., Bovensmann, H., Frerick, J., and Burrows, J. P.: Measurements of molecular absorption spectra with the SCIAMACHY pre-flight model: instrument characterization and reference data for atmospheric remote-sensing in the 230-2380 nm region, Journal of Photochemistry and Photobiology A: Chemistry, 157, 167 – 184, doi:10.1016/S1010-6030(03)00062-5, atmospheric Photochemistry, 2003.

Brasseur, G. and Granier, C.: Mount Pinatubo Aerosols, Chlorofluorocarbons, and Ozone Depletion, Science, 257, 1239–1242, doi:10.1126/science.257.5074.1239, URL `http://www.sciencemag.org/content/257/5074/1239.abstract`, 1992.

Brasseur, G. and Solomon, S.: Aeronomy of the middle atmosphere, Dordrecht, Boston, Lancaster, Tokyo: D. Reidel Publ, 1986.

Brasseur, G. P., Orlando, J. J., and Tyndall, G. S.: Chapter no. 5: Trace gas exchanges and biogeochemical sulfur cycles, Oxford University Press, Inc., 1999.

Brühl, C. and Crutzen, P. J.: MPIC two-dimensional model. In The atmospheric effects of stratospheric aircraft, NASA Ref. Publ., 1292, 103–104, 1993.

Brinkmann, R. T.: Rotational Raman scattering in planetary atmospheres, Astrophys. J., 154, 1087–1093, 1968.

Brinksma, E. J., Pinardi, G., Volten, H., Braak, R., Richter, A., Schönhardt, A., van Roozendael, M., Fayt, C., Hermans, C., Dirksen, R. J., Vlemmix, T., Berkhout, A. J. C., Swart, D. P. J., Oetjen, H., Wittrock, F., Wagner, T., Ibrahim, O. W., de Leeuw, G., Moerman, M., Curier, R. L., Celarier, E. A., Cede, A., Knap, W. H., Veefkind, J. P., Eskes, H. J., Allaart, M., Rothe, R., Piters, A. J. M., and Levelt, P. F.: The 2005 and 2006 DANDELIONS NO2 and aerosol intercomparison campaigns, J. Geophys. Res., 113, D16S46, URL http://dx.doi.org/10.1029/2007JD008808, 2008.

Burrows, J., Vountas, M., Haug, H., Chance, K., Marquard, L., Muirhead, K., Platt, U., Richter, A., and Rozanov, V. V.: Study of the Ring Effect, Tech. rep., European Space Agency, Noordivijk, The Netherlands, 1996.

Bussemer, M.: Der Ring-Effekt: Ursachen und Einflußauf die spektroskopische Messung stratosphaerischer Spurenstoffe, Diploma thesis, University of Heidelberg, 1993.

Chance, K. V. and Spurr, R. J. D.: Ring effect studies: Rayleigh scattering, including molecular parameters for rotational Raman scattering, and the Fraunhofer spectrum, Appl. Opt., 36, 5224–5230, doi:10.1364/AO.36.005224, 1997.

Clémer, K., Van Roozendael, M., Fayt, C., Hendrick, F., Hermans, C., Pinardi, G., Spurr, R., Wang, P., and De Mazière, M.: Multiple wavelength retrieval of tropospheric aerosol optical properties from MAXDOAS measurements in Beijing, Atmos. Meas. Tech., 3, 863–878, doi:10.5194/amt-3-863-2010, URL http://www.atmos-meas-tech.net/3/863/2010/, 2010.

Collaud Coen, M., Weingartner, E., Apituley, A., Ceburnis, D., Fierz-Schmidhauser, R., Flentje, H., Henzing, J. S., Jennings, S. G., Moerman, M., Petzold, A., Schmid, O., and Baltensperger, U.: Minimizing light absorption measurement artifacts of the Aethalometer: evaluation of five correction algorithms, Atmospheric Measurement Techniques, 3, 457–474, doi:10.5194/amt-3-457-2010, URL http://www.atmos-meas-tech.net/3/457/2010/, 2010.

Deutschmann, T., Beirle, S., Frieß, U., Grzegorski, M., Kern, C., Kritten, L., Platt, U., Prados-Román, C., PukI¯te, J., Wagner, T., Werner, B., and Pfeilsticker, K.: The Monte Carlo atmospheric radiative transfer model McArtim: Introduction and validation of Jacobians and 3D features, Journal of Quantitative Spectroscopy and Radiative Transfer, 112, 1119 – 1137, doi:DOI:10.1016/j.jqsrt.2010.12.009, 2011.

Dix, B., Brenninkmeijer, C. A. M., Frieß, U., Wagner, T., and Platt, U.: Airborne multi-axis DOAS measurements of atmospheric trace gases on CARIBIC long-distance flights, Atmospheric Measurement Techniques, 2, 639–652, doi:10.5194/amt-2-639-2009, URL http://www.atmos-meas-tech.net/2/639/2009/, 2009.

Dubovik, O. and King, M.: A flexible inversion algorithm for retrieval of aerosol optical properties from Sun and sky radiance measurements, J. Geophys. Res.-Atmos., 105, 20 673–20 696, 2000.

Dubovik, O., Smirnov, A., Holben, B., King, M., Kaufman, Y., Eck, T., and Slutsker, I.: Accuracy assessments of aerosol optical properties retrieved from Aerosol Robotic Network (AERONET) Sun and sky radiance measurements, J. Geophys. Res.-Atmos., 105, 9791–9806, 2000.

Eck, T. F., Holben, B. N., Reid, J. S., Dubovik, O., Smirnov, A., O'Neill, N. T., Slutsker, I., and Kinne, S.: Wavelength dependence of the optical depth of biomass burning, urban, and desert dust aerosols, J. Geophys. Res., 104, 31 333–31 349, URL http://dx.doi.org/10.1029/1999JD900923, 1999.

Emeis, S., Schafer, K., and Munkel, C.: Observation of the structure of the urban boundary layer with different ceilometers and validation by RASS data, Meteorologische Zeitschrift, 18, 149–154, doi:10.1127/0941-2948/2009/0365, 2009.

Fayt, C. and Van Roozendael, M.: WINDOAS user manual, URL http://www.oma.be/BIRA-IASB/Molecules/BrO/WinDOAS-SUM-210b.pdf, 2001.

Fernald, F. G.: Analysis of atmospheric lidar observations: some comments, Appl. Optics, 23, 1984.

Fierz-Schmidhauser, R., Zieger, P., Wehrle, G., Jefferson, A., Ogren, J. A., Baltensperger, U., and Weingartner, E.: Measurement of relative humidity dependent light scattering of aerosols, Atmospheric Measurement Techniques, 3, 39–50, doi:10.5194/amt-3-39-2010, URL http://www.atmos-meas-tech.net/3/39/2010/, 2010.

Finlayson-Pitts, B. J. and Pitts jr., J. N.: Chemistry of the upper and lower atmosphere: Theory, experiments and applications, Academic Press, San Diego., 2000.

Fish, D. J. and Jones, R. L.: Rotational Raman scattering and the ring effect in zenith-sky spectra, Geophys. Res. Lett., 22, 811–814, URL http://dx.doi.org/10.1029/95GL00392, 1995.

Fishman, J. and Crutzen, P. J.: The origin of ozone in the troposphere, Nature, 274, 855–858, URL http://dx.doi.org/10.1038/274855a0, 1978.

Flentje, H., Heese, B., Reichardt, J., and Thomas, W.: Aerosol profiling using the ceilometer network of the German Meteorological Service, Atmospheric Measurement Techniques Discussions, 3, 3643–3673, doi:10.5194/amtd-3-3643-2010, URL http://www.atmos-meas-tech-discuss.net/3/3643/2010/, 2010.

Frankenberg, C., Meirink, J. F., van Weele, M., Platt, U., and Wagner, T.: Assessing Methane Emissions from Global Space-Borne Observations, Science, 308, 1010–1014, doi:10.1126/science.1106644, URL http://www.sciencemag.org/content/308/5724/1010.abstract, 2005.

Frieß, U., Monks, P. S., Remedios, J. J., Rozanov, A., Sinreich, R., Wagner, T., and Platt, U.: MAX-DOAS O4 measurements: A new technique to derive information on atmospheric aerosols: 2. Modeling studies, J. Geophys. Res.-Atmos., 111, doi:10.1029/2005JD006618, 2006.

Frieß, U., Deutschmann, T., Gilfedder, B. S., Weller, R., and Platt, U.: Iodine monoxide in the Antarctic snowpack, Atmospheric Chemistry and Physics, 10, 2439–2456, doi:10.5194/acp-10-2439-2010, URL http://www.atmos-chem-phys.net/10/2439/2010/, 2010.

Frieß, U., Sihler, H., Sander, R., Pöhler, D., Yilmaz, S., and Platt, U.: The vertical distribution of BrO and aerosols in the Arctic: Measurements by active and passive differential optical absorption spectroscopy, J. Geophys. Res., 116, D00R04–, URL http://dx.doi.org/10.1029/2011JD015938, 2011.

Galle, B., Johansson, M., Rivera, C., Zhang, Y., Kihlman, M., Kern, C., Lehmann, T., Platt, U., Arellano, S., and Hidalgo, S.: Network for Observation of Volcanic and Atmospheric Change (NOVAC)-A global network for volcanic gas monitoring: Network layout and instrument description, J. Geophys. Res.-Atmos., 115, doi:10.1029/2009JD011823, 2010.

Gomer, T., Brauers, T., Heintz, F., Stutz, J., and Platt, U.: MFC User Manual, Institut fuer Umweltphysik, Universitaet Heidelberg., vers. 1.98 edn., 1993.

Gür, B., Spietz, P., Orphal, J., and Burrows, J.: Absorption Spectra Measurements with the GOME-2 FMs using the IUP/IFE-UB´s Calibration Apparatus for Trace Gas Absorption Spectroscopy CATGAS, Final report, IUP University of Bremen, 2005.

Grainger, J. F. and Ring, J.: Anomalous Fraunhofer Line Profiles, Nature, 193, 762–762, URL http://dx.doi.org/10.1038/193762a0, 1962.

Greenblatt, G., Orlando, J., Burkholder, J., and Ravishankara, A.: Absorption Measurements of Oxygen Between 330 and 1140 nm, J. Geophys. Res., 95(D11), 18 577–18 582, 1990.

Gudmundsson, M., Pedersen, R., Vofjoerd, K., Thorbjarnardottir, B., Jakobsdottir, S., and Roberts, M.: Eruptions of Eyjafjallajökull Volcano, Iceland, Eos, 91, 2010.

Hasekamp, O. P. and Landgraf, J.: Ozone profile retrieval from backscattered ultraviolet radiances: The inverse problem solved by regularization, J. Geophys. Res., 106, 8077–8088, URL http://dx.doi.org/10.1029/2000JD900692, 2001.

Haug, H.: Raman-Streuung von Sonnenlicht in der Erdatmosphäre, Diploma thesis, Institut für Umweltphysik, Ruprecht-Karls-Universität Heidelberg, 1996.

Hausmann, M. and Platt, U.: Spectroscopic measurement of bromine oxide and ozone in the high Arctic during Polar Sunrise Experiment 1992, J. Geophys. Res., 99, 25 399–25 413, URL http://dx.doi.org/10.1029/94JD01314, 1994.

Heckel, A., Richter, A., Tarsu, T., Wittrock, F., Hak, C., Pundt, I., Junkermann, W., and Burrows, J. P.: MAX-DOAS measurements of formaldehyde in the Po-Valley, Atmospheric Chemistry and Physics, 5, 909–918, doi:10.5194/acp-5-909-2005, URL http://www.atmos-chem-phys.net/5/909/2005/, 2005.

Heese, B., Flentje, H., Althausen, D., Ansmann, A., and Frey, S.: Ceilometer lidar comparison: backscatter coefficient retrieval and signal-to-noise ratio determination, Atmospheric Measurement Techniques, 3, 1763–1770, doi:10.5194/amt-3-1763-2010, URL `http://www.atmos-meas-tech.net/3/1763/2010/`, 2010.

Henyey, L. and Greenstein, J.: Diffuse radiation in the Galaxy, Astrophys. J., 93, 70–83, 1941.

Hermans, C.: personal communication, For details see:, URL `http://spectrolab.aeronomie.be/o2_o4info.htm`, 2002.

Hess, M., Koepke, P., and Schult, I.: Optical Properties of Aerosols and Clouds: The Software Package OPAC, Bulletin of the American Meteorological Society, 79, 831–844, 1998.

Heue, K.-P.: Airborne Multi AXis DOAS instrument and measurements of two-dimensional tropospheric trace gas distributions, Ph.d. thesis, Combined Faculties for the Natural Sciences and for Mathematics, Universität Heidelberg, 2005.

Heue, K.-P., Wagner, T., Broccardo, S. P., Walter, D., Piketh, S. J., Ross, K. E., Beirle, S., and Platt, U.: Direct observation of two dimensional trace gas distributions with an airborne Imaging DOAS instrument, Atmospheric Chemistry and Physics, 8, 6707–6717, doi:10.5194/acp-8-6707-2008, URL `http://www.atmos-chem-phys.net/8/6707/2008/`, 2008.

Heue, K.-P., Brenninkmeijer, C. A. M., Wagner, T., Mies, K., Dix, B., Frieß, U., Martinsson, B. G., Slemr, F., and van Velthoven, P. F. J.: Observations of the 2008 Kasatochi volcanic SO_2 plume by CARIBIC aircraft DOAS and the GOME-2 satellite, Atmospheric Chemistry and Physics, 10, 4699–4713, doi:10.5194/acp-10-4699-2010, URL `http://www.atmos-chem-phys.net/10/4699/2010/`, 2010.

Hönninger, G.: Halogen Oxide Studies in the Boundary Layer by Multi Axis Differential Optical Absorption Spectroscopy and Active Longpath-DOAS, Ph. d. thesis, Combined Faculties for the Natural Sciences and for Mathematics, Universität Heidelberg, 2002.

Hönninger, G. and Platt, U.: Observations of BrO and its vertical distribution during surface ozone depletion at Alert, Atmospheric Environment, 36, 2481 – 2489, doi:10.1016/S1352-2310(02)00104-8, 2002.

Hönninger, G., von Friedeburg, C., and Platt, U.: Multi axis differential optical absorption spectroscopy (MAX-DOAS), Atmos. Chem. Phys., 4, 231–254, doi:10.5194/acp-4-231-2004, URL `http://www.atmos-chem-phys.net/4/231/2004/`, 2004.

Holben, B., Eck, T., Slutsker, I., Tanre, D., Buis, J., Setzer, A., Vermote, E., Reagan, J., Kaufman, Y., Nakajima, T., Lavenu, F., Jankowiak, I., and Smirnov, A.: AERONET - Federated Instrument Network and Data Archive

for Aerosol Characterization, Remote Sensing of Environment, 66, 1 – 16, doi: 10.1016/S0034-4257(98)00031-5, 1998.

Hoogen, R., Rozanov, V. V., and Burrows, J. P.: Ozone profiles from GOME satellite data: Algorithm description and first validation, J. Geophys. Res., 104, 8263–8280, URL http://dx.doi.org/10.1029/1998JD100093, 1999.

Ibrahim, O., Shaiganfar, R., Sinreich, R., Stein, T., Platt, U., and Wagner, T.: Car MAX-DOAS measurements around entire cities: quantification of NO_x emissions from the cities of Mannheim and Ludwigshafen (Germany), Atmospheric Measurement Techniques, 3, 709–721, doi:10.5194/amt-3-709-2010, URL http://www.atmos-meas-tech.net/3/709/2010/, 2010.

IPCC: Intergovernmental Panel on Climate Change: Summary for Policymakers. Climate Change 2007: The Fourth Assessment Report of the Intergovernmental Panel on Climate Change, Cambridge University Press, Cambridge, UK, pp. 7–22, 2007.

Irie, H., Kanaya, Y., Akimoto, H., Iwabuchi, H., Shimizu, A., and Aoki, K.: First retrieval of tropospheric aerosol profiles using MAX-DOAS and comparison with lidar and sky radiometer measurements, Atmospheric Chemistry and Physics, 8, 341–350, doi:10.5194/acp-8-341-2008, URL http://www.atmos-chem-phys.net/8/341/2008/, 2008.

Irie, H., Kanaya, Y., Akimoto, H., Iwabuchi, H., Shimizu, A., and Aoki, K.: Dual-wavelength aerosol vertical profile measurements by MAX-DOAS at Tsukuba, Japan, Atmos. Chem. Phys., 9, 2741–2749, doi:10.5194/acp-9-2741-2009, URL http://www.atmos-chem-phys.net/9/2741/2009/, 2009.

Irie, H., Takashima, H., Kanaya, Y., Boersma, K. F., Gast, L., Wittrock, F., Brunner, D., Zhou, Y., and Van Roozendael, M.: Eight-component retrievals from ground-based MAX-DOAS observations, Atmospheric Measurement Techniques, 4, 1027–1044, doi:10.5194/amt-4-1027-2011, URL http://www.atmos-meas-tech.net/4/1027/2011/, 2011.

Jaenicke, B.: Über die dynamik atmosphärischer aitkenteilchen, Ber. Bunsenges. Phys. Chem., 82, 1198–1202, 1978.

Jaenicke, R.: Aerosol-Cloud-Climate Interactions, chap. Tropospheric aerosols, pp. 1–31, Academic Press, San Diego, CA, 1993.

John, W., Wall, S. M., Ondo, J. L., and Winklmayr, W.: Modes in the size distributions of atmospheric inorganic aerosol, Atmospheric Environment. Part A. General Topics, 24, 2349 – 2359, doi:10.1016/0960-1686(90)90327-J, 1990.

Johnston, P.: Making uv/vis cross sections, reference fraunhofer and synthetic spectra, unpublished manuscript, 1996.

Kaufman, Y. J. and Koren, I.: Smoke and Pollution Aerosol Effect on Cloud Cover, Science, 313, 655–658, doi:10.1126/science.1126232, URL http://www.sciencemag.org/content/313/5787/655.abstract, 2006.

Kern, C.: Spectroscopic measurements of volcanic gas emissions in the ultra-violet wavelength region, Ph.D. thesis, Combined Faculties for the Natural Sciences and for Mathematics, Universität Heidelberg, 2009.

Kern, C., Sihler, H., Vogel, L., Rivera, C., Herrera, M., and Platt, U.: Halogen oxide measurements at Masaya volcano, Nicaragua using Active Long Path Differential Optical Absorption Spectroscopy, Bull. Volcanol., 71, 659–670, 2009.

Klett, J. D.: Stable analytical inversion solution for processing lidar returns, Appl. Optics, 22, 1981.

Kley, D. and McFarland, M.: Chemiluminescence detector for NO and NO2, Atmos. Technol., 12, 63–69, 1980.

Kritten, L., Butz, A., Dorf, M., Deutschmann, T., Kühl, S., Prados-Roman, C., Pukite, J., Rozanov, A., Schofield, R., and Pfeilsticker, K.: Time dependent profile retrieval of UV/vis absorbing radicals from balloon-borne limb measurements - a case study on NO_2 and O_3, Atmospheric Measurement Techniques, 3, 933–946, doi:10.5194/amt-3-933-2010, URL `http://www.atmos-meas-tech.net/3/933/2010/`, 2010.

Kuehl, S., Pukite, J., Deutschmann, T., Platt, U., and Wagner, T.: SCIAMACHY limb measurements of NO2, BrO and OClO. Retrieval of vertical profiles: Algorithm, first results, sensitivity and comparison studies, Advances in Space Research, 42, 1747 – 1764, doi:10.1016/j.asr.2007.10.022, 2008.

Kurucz, R. L., Furenlid, I., Brault, J., and Testerman, L.: Solar Flux Atlas from 296 to 1300 nm, Tech. rep., New Mexico, U.S.A.: National Solar Observatry, 1984.

Laj, P. and Philippin, S.: At the forefront of aerosol research throughout Europe, Science, Technology, and Innovation Projects, 10, 20–22, 2009.

Lee, D., Köhler, I., Grobler, E., Rohrer, F., Sausen, R., Gallardo-Klenner, L., Olivier, J., Dentener, F., and Bouwman, A.: Estimations of global no, emissions and their uncertainties, Atmospheric Environment, 31, 1735–1749, doi:10.1016/S1352-2310(96)00327-5, 1997.

Leighton, P. A.: Photochemistry of air pollution, Academic Press, New York., 1961.

Leser, H., Hönninger, G., and Platt, U.: MAX-DOAS measurements of BrO and NO2 in the marine boundary layer, Geophys. Res. Lett., 30, 1537–, URL `http://dx.doi.org/10.1029/2002GL015811`, 2003.

Levenberg, K.: A method for the solution of certain non-linear problems in least squares, Quart. Appl. Math., 2, 164–168, 1944.

Li, X., Brauers, T., Shao, M., Garland, R. M., Wagner, T., Deutschmann, T., and Wahner, A.: MAX-DOAS measurements in southern China: retrieval of aerosol extinctions and validation using ground-based in-situ data, Atmospheric Chemistry and Physics, 10, 2079–2089, doi:10.5194/acp-10-2079-2010, URL `http://www.atmos-chem-phys.net/10/2079/2010/`, 2010.

London, J.: Proceedings of the NATO Advanced Institute on the Atmospheric Ozone (Portugal), Faa - washington, d.c., usa, U.S. Dept. of Transportation., 1980.

Marquard, L., Wagner, T., and Platt, U.: Improved Air Mass Factor Concepts for Scattered Radiation Differential Optical Absorption Spectroscopy of Atmospheric Species, J. Geophys. Res., 105, 1315–1327., 2000.

Marquardt, D. W.: An Algorithm for Least-Squares Estimation of Nonlinear Parameters, Journal of the Society for Industrial and Applied Mathematics, 11, pp. 431–441, 1963.

Martin, M., Pöhler, D., Seitz, K., Sinreich, R., and Platt, U.: BrO measurements over the Eastern North-Atlantic, Atmospheric Chemistry and Physics, 9, 9545–9554, doi:10.5194/acp-9-9545-2009, URL http://www.atmos-chem-phys.net/9/9545/2009/, 2009.

Meller, R. and Moortgat, G. K.: Temperature dependence of the absorption cross sections of formaldehyde between 223 and 323 K in the wavelength range 225-375 nm, J. Geophys. Res., 105, 7089–7101, URL http://dx.doi.org/10.1029/1999JD901074, 2000.

Müller, T., Henzing, J. S., de Leeuw, G., Wiedensohler, A., Alastuey, A., Angelov, H., Bizjak, M., Collaud Coen, M., Engström, J. E., Gruening, C., Hillamo, R., Hoffer, A., Imre, K., Ivanow, P., Jennings, G., Sun, J. Y., Kalivitis, N., Karlsson, H., Komppula, M., Laj, P., Li, S.-M., Lunder, C., Marinoni, A., Martins dos Santos, S., Moerman, M., Nowak, A., Ogren, J. A., Petzold, A., Pichon, J. M., Rodriquez, S., Sharma, S., Sheridan, P. J., Teinilä, K., Tuch, T., Viana, M., Virkkula, A., Weingartner, E., Wilhelm, R., and Wang, Y. Q.: Characterization and intercomparison of aerosol absorption photometers: result of two intercomparison workshops, Atmospheric Measurement Techniques, 4, 245–268, doi:10.5194/amt-4-245-2011, URL http://www.atmos-meas-tech.net/4/245/2011/, 2011.

Morgan, W. T., Allan, J. D., Bower, K. N., Esselborn, M., Harris, B., Henzing, J. S., Highwood, E. J., Kiendler-Scharr, A., McMeeking, G. R., Mensah, A. A., Northway, M. J., Osborne, S., Williams, P. I., Krejci, R., and Coe, H.: Enhancement of the aerosol direct radiative effect by semi-volatile aerosol components: airborne measurements in North-Western Europe, Atmospheric Chemistry and Physics, 10, 8151–8171, doi:10.5194/acp-10-8151-2010, URL http://www.atmos-chem-phys.net/10/8151/2010/, 2010.

Munro, R., Siddans, R., Reburn, W. J., and Kerridge, B. J.: Direct measurement of tropospheric ozone distributions from space, Nature, 392, 168–171, URL http://dx.doi.org/10.1038/32392, 1998.

Noxon, J. F., Whipple, E. C., and Hyde, R. S.: Stratospheric NO2. 1. Observational Method and Behavior at Midlatitudes, J. Geophys. Res., 84, 5047–5076, 1979.

Pedersen, R. and Sigmundsson, F.: InSAR based sill model links spatially offset areas of deformation and seismicity for the 1994 unrest episode at Eyjafjallajokull volcano, Iceland, Geophys. Res. Lett., 31, doi:10.1029/2004GL020368, 2004.

Penndorf, R.: Tables of the refractive index for standard air and the rayleigh scattering coefficient for the spectral region between 0.2 and 200 μ and their application to atmospheric optics, J.Opt. Soc. Am., 47, 176–182, 1957.

Perner, D. and Platt, U.: Detection of nitrous acid in the atmosphere by differential optical absorption, Geophys. Res. Lett., 6(12), 917–920, 1979.

Perner, D. and Platt, U.: Absorption of light in the atmosphere by collision pairs of oxygen (O2)2, Geophys. Res. Lett., 7(12), 1053–1056, 1980.

Perner, D., Ehhalt, D. H., Pätz, H. W.and Platt, U., Röth, E. P., and Volz, A.: OH - Radicals in the lower troposphere, Geophys. Res. Lett., 3(8), 466–468, 1976.

Philippin, S. and Laj, P.: Networking the Unregulated Threat in the Air. Research Review, Research Review, 11, 32, 2009.

Philippin, S., Laj, P., Putaud, J.-P., Wiedensohler, A., de Leeuw, G., Fjaeraa, A., Platt, U., Baltensperger, U., and Fiebig, M.: EUSAAR - An Unprecedented Network of Aerosol Observation in Europe, Earozoru Kenkyu, 24, 78–83, 2009.

Phillips, P. .: A techniquef or the numericals olutiono f certaini ntegrale quationso f the first kind, J. Assoc. Comput. Mach., 9, 84–97, 1962.

Piters, A. J. M., Boersma, K. F., Kroon, M., Hains, J. C., Van Roozendael, M., Wittrock, F., Abuhassan, N., Adams, C., Akrami, M., Allaart, M. A. F., Apituley, A., Bergwerff, J. B., Berkhout, A. J. C., Brunner, D., Cede, A., Chong, J., Clémer, K., Fayt, C., Frieß, U., Gast, L. F. L., Gil-Ojeda, M., Goutail, F., Graves, R., Griesfeller, A., Großmann, K., Hemerijckx, G., Hendrick, F., Henzing, B., Herman, J., Hermans, C., Hoexum, M., van der Hoff, G. R., Irie, H., Johnston, P. V., Kanaya, Y., Kim, Y. J., Klein Baltink, H., Kreher, K., de Leeuw, G., Leigh, R., Merlaud, A., Moerman, M. M., Monks, P. S., Mount, G. H., Navarro-Comas, M., Oetjen, H., Pazmino, A., Perez-Camacho, M., Peters, E., du Piesanie, A., Pinardi, G., Puentadura, O., Richter, A., Roscoe, H. K., Schönhardt, A., Schwarzenbach, B., Shaiganfar, R., Sluis, W., Spinei, E., Stolk, A. P., Strong, K., Swart, D. P. J., Takashima, H., Vlemmix, T., Vrekoussis, M., Wagner, T., Whyte, C., Wilson, K. M., Yela, M., Yilmaz, S., Zieger, P., and Zhou, Y.: The Cabauw Intercomparison campaign for Nitrogen Dioxide measuring Instruments (CINDI): design, execution, and early results, Atmospheric Measurement Techniques Discussions, 4, 5935–6005, doi:10.5194/amtd-4-5935-2011, URL `http://www.atmos-meas-tech-discuss.net/4/5935/2011/`, 2011.

Platt, U.: The origin of nitrous and nitric acid in the atmosphere, pp. 299-319. W. Jaeschke, Springer Verlag, 1986.

Platt, U.: Air Monitoring by Spectroscopic Techniques, vol. 127, chap. Differential Optical Absorption Spectroscopy (DOAS), pp. 27–83, John Wiley, Hoboken, NY, 1994.

Platt, U. and Perner, D.: Direct Measurements of Atmospheric CH2O, HNO2, O3, NO2, and SO2 by Differential Optical Absorption in the Near UV, J. Geophys. Res., 85(C12), 7453–7458, 1980.

Platt, U. and Stutz, J.: Differential Optical Absorption Spectroscopy: Principles and Applications, Springer-Verlag, Berlin, 2008.

Platt, U., Perner, D., and Pätz, H.: Simultaneous Measurement of Atmospheric CH2O, O3, and NO2 by Differential Optical Absorption, J. Geophys. Res., 84(C10), 6329–6335, 1979.

Platt, U., Marquard, L., Wagner, T., and Perner, D.: Corrections for zenith scattered light DOAS, Geophys. Res. Lett., 24, 1759–1762, URL http://dx.doi.org/10.1029/97GL01693, 1997.

Platt, U., Meinen, J., Pöhler, D., and Leisner, T.: Broadband Cavity Enhanced Differential Optical Absorption Spectroscopy (CE-DOAS) - applicability and corrections, Atmospheric Measurement Techniques, 2, 713–723, doi:10.5194/amt-2-713-2009, URL http://www.atmos-meas-tech.net/2/713/2009/, 2009.

Platt, U., Meinen, J., Pöhler, D., and Leisner, T.: Corrigendum to "Broadband Cavity Enhanced Differential Optical Absorption Spectroscopy (CE-DOAS) - applicability and corrections" published in Atmos. Meas. Tech., 2, 713-723, 2009, Atmospheric Measurement Techniques, 3, 127–128, doi:10.5194/amt-3-127-2010, URL http://www.atmos-meas-tech.net/3/127/2010/, 2010.

Poehler, D., Vogel, L., Friess, U., and Platt, U.: Observation of halogen species in the Amundsen Gulf, Arctic, by active long-path differential optical absorption spectroscopy, Proceedings of the National Academy of Sciences, 107, 6582–6587, doi:10.1073/pnas.0912231107, 2010.

Prados-Roman, C., Butz, A., Deutschmann, T., Dorf, M., Kritten, L., Minikin, A., Platt, U., Schlager, H., Sihler, H., Theys, N., Van Roozendael, M., Wagner, T., and Pfeilsticker, K.: Airborne DOAS limb measurements of tropospheric trace gas profiles: case studies on the profile retrieval of O_4 and BrO, Atmospheric Measurement Techniques, 4, 1241–1260, doi:10.5194/amt-4-1241-2011, URL http://www.atmos-meas-tech.net/4/1241/2011/, 2011.

Press, W. H., Teukolsky, S. A., Vetterling, W. T., and Flannery, B. P.: Numerical Recipes 3rd Edition: The Art of Scientific Computing, Cambridge University Press, 3 edn., 2007.

Rödel, W.: Physik unserer Umwelt - Die Atmosphäre, (3. ed.). Berlin Heidelberg New York: Springer-Verlag, 2000.

Richter, A.: Absorptionsspektroskopische Messungen stratosphaerischer Spurengase ueber Bremen, 53°N, Ph. d. thesis, University of Bremen, Bremen, Germany, 1997.

Rodgers, C. D.: Retrieval of atmospheric temperature and composition from remote measurements of thermal radiation, Rev. Geophys., 14(4), 609–624, 1976.

Rodgers, C. D.: Characterization and Error Analysis of Profiles Retrieved From Remote Sounding Measurements, J. Geophys. Res., 95, 5587–5595, doi:10.1029/JD095iD05p05587, URL http://dx.doi.org/10.1029/JD095iD05p05587, 1990.

Rodgers, C. D.: Inverse Methods for Atmospheric Sounding: Theory and Practice, vol. 2 of *Atmos. Oceanic Planet. Phys.*, World Sci., Hackensack, NY, 2000.

Rodgers, C. D. and Connor, B. J.: Intercomparison of remote sounding instruments, J. Geophys. Res., 108, 4116–, URL http://dx.doi.org/10.1029/2002JD002299, 2003.

Roscoe, H. K., Van Roozendael, M., Fayt, C., du Piesanie, A., Abuhassan, N., Adams, C., Akrami, M., Cede, A., Chong, J., Clémer, K., Friess, U., Gil Ojeda, M., Goutail, F., Graves, R., Griesfeller, A., Grossmann, K., Hemerijckx, G., Hendrick, F., Herman, J., Hermans, C., Irie, H., Johnston, P. V., Kanaya, Y., Kreher, K., Leigh, R., Merlaud, A., Mount, G. H., Navarro, M., Oetjen, H., Pazmino, A., Perez-Camacho, M., Peters, E., Pinardi, G., Puentedura, O., Richter, A., Schönhardt, A., Shaiganfar, R., Spinei, E., Strong, K., Takashima, H., Vlemmix, T., Vrekoussis, M., Wagner, T., Wittrock, F., Yela, M., Yilmaz, S., Boersma, F., Hains, J., Kroon, M., Piters, A., and Kim, Y. J.: Intercomparison of slant column measurements of NO_2 and O_4 by MAX-DOAS and zenith-sky UV and visible spectrometers, Atmos. Meas. Tech., 3, 1629–1646, doi:10.5194/amt-3-1629-2010, URL http://www.atmos-meas-tech.net/3/1629/2010/, 2010.

Rothman, L. S., Gordon, I. E., Barbe, A., Benner, D. C., Bernath, P. E., Birk, M., Boudon, V., Brown, L. R., Campargue, A., Champion, J. P., Chance, K., Coudert, L. H., Dana, V., Devi, V. M., Fally, S., Flaud, J. M., Gamache, R. R., Goldman, A., Jacquemart, D., Kleiner, I., Lacome, N., Lafferty, W. J., Mandin, J. Y., Massie, S. T., Mikhailenko, S. N., Miller, C. E., Moazzen-Ahmadi, N., Naumenko, O. V., Nikitin, A. V., Orphal, J., Perevalov, V. I., Perrin, A., Predoi-Cross, A., Rinsland, C. P., Rotger, M., Simeckova, M., Smith, M. A. H., Sung, K., Tashkun, S. A., Tennyson, J., Toth, R. A., Vandaele, A. C., and Vander Auwera, J.: The HITRAN 2008 molecular spectroscopic database, J. Quant. Spectrosc. Ra., 110, 533–572, doi:10.1016/j.jqsrt.2009.02.013, 2009.

Rozanov, A., Rozanov, V., and Burrows, J. P.: A numerical radiative transfer model for a spherical planetary atmosphere: combined differential-integral approach involving the Picard iterative approximation, Journal of Quantitative Spectroscopy and Radiative Transfer, 69, 491 – 512, doi:DOI:10.1016/S0022-4073(00)00100-X, 2001.

Rozanov, A., Rozanov, V., Buchwitz, M., Kokhanovsky, A., and Burrows, J.: SCIATRAN 2.0 - A new radiative transfer model for geophysical applications in the 175-2400 nm spectral region, in: Atmospheric Remote Sensing: Earth's Surface, Troposphere, Stratosphere and Mesosphere - I, edited by Burrows, J. and Eichmann, K., vol. 36 of *ADVANCES IN SPACE RESEARCH*, pp. 1015–1019, doi:10.1016/j.asr.2005.03.012, 2005.

Rozanov, A. V., Rozanov, V. V., and Burrows, J. P.: Combined differential-integral approach for the radiation field computation in a spherical shell atmosphere: Nonlimb geometry, J. Geophys. Res., 105, 22 937–22 942, URL http://dx.doi.org/10.1029/2000JD900378, 2000.

Rozanov, V. V., Buchwitz, M., Eichmann, K. U., de Beek, R., and Burrows, J. P.: Sciatran - a new radiative transfer model for geophysical applications in the 240-2400 NM spectral region: the pseudo-spherical version, Advances in Space Research, 29, 1831 – 1835, doi:DOI:10.1016/S0273-1177(02)00095-9, 2002.

Sanders, R. W., Solomon, S., Carroll, M. A., and Schmeltekopf, A. L.: Ground-Based Measurements of O_3, NO_2, OClO and BrO During the 1987 Antarctic Ozone Depletion Event, in: Ozone in the Atmosphere, edited by Fabian, R. D. B. . P., pp. 65–+, 1989.

Sanghavi, S.: An effcient Mie theory implementation to investigate the influence of aerosols on radiative transfer, Diploma thesis, University of Heidelberg, 2003.

Sasano, Y., Browell, E. V., and Ismail, S.: Error caused by using a constant extinction/backscattering ratio in the lidar solution, Appl. Opt., 24, 3929–3932, doi:10.1364/AO.24.003929, 1985.

Schmid, O., Artaxo, P., Arnott, W. P., Chand, D., Gatti, L. V., Frank, G. P., Hoffer, A., Schnaiter, M., and Andreae, M. O.: Spectral light absorption by ambient aerosols influenced by biomass burning in the Amazon Basin. I: Comparison and field calibration of absorption measurement techniques, Atmospheric Chemistry and Physics, 6, 3443–3462, doi:10.5194/acp-6-3443-2006, URL http://www.atmos-chem-phys.net/6/3443/2006/, 2006.

Schroeder, W. H., Dobson, M., Kane, D. M., and Johnson, N. D.: Toxic trace elements associated with airborne particulate matter: A review, Journal of the Air Pollution Control Association, 37, 1267–1285, cited By (since 1996): 102, 1987.

Schumann, U., Weinzierl, B., Reitebuch, O., Schlager, H., Minikin, A., Forster, C., Baumann, R., Sailer, T., Graf, K., Mannstein, H., Voigt, C., Rahm, S., Simmet, R., Scheibe, M., Lichtenstern, M., Stock, P., Rüba, H., Schäuble, D., Tafferner, A., Rautenhaus, M., Gerz, T., Ziereis, H., Krautstrunk, M., Mallaun, C., Gayet, J.-F., Lieke, K., Kandler, K., Ebert, M., Weinbruch, S., Stohl, A., Gasteiger, J., Groß, S., Freudenthaler, V., Wiegner, M., Ansmann, A., Tesche, M., Olafsson, H., and Sturm, K.: Airborne observations of the Eyjafjalla volcano ash cloud over Europe during air space closure in April and May 2010, Atmospheric Chemistry and Physics, 11, 2245–2279, doi:10.5194/acp-11-2245-2011, URL http://www.atmos-chem-phys.net/11/2245/2011/, 2011.

Seidler, T.: PMAX-DOAS - Eine neue Methode zur Bestimmung von Aerosolproflen mittels polarisationsabhängiger MAX-DOAS Messungen, Master's thesis, Institute of Environmental Physics, University of Heidelbeg, 2008.

Seinfeld, J. H. and Pandis, S. N.: Atmospheric chemistry and physics, Wiley, Hoboken, NJ, 2. ed. edn., previous ed.: 1998, 2006.

Sheridan, P. J., Arnott, W. P., Ogren, J. A., Andrews, E., Atkinson, D. B., Covert, D. S., MoosmÃ¼ller, H., Petzold, A., Schmid, B., Strawa, A. W., Varma, R., and Virkkula, A.: The Reno Aerosol Optics Study: An Evaluation of Aerosol Absorption Measurement Methods, Aerosol Science and Technology, 39, 1–16, doi:10.1080/027868290901891, 2005.

Sigmundsson, F., Hreinsdottir, S., Hooper, A., Arnadottir, T., Pedersen, R., Roberts, M. J., Oskarsson, N., Auriac, A., Decriem, J., Einarsson, P., Geirsson, H., Hensch, M., Ofeigsson, B. G., Sturkell, E., Sveinbjornsson, H., and Feigl, K. L.: Intrusion triggering of the 2010 Eyjafjallajokull explosive eruption, Nature, 468, 426–U253, doi:10.1038/nature09558, 2010.

Sihler, H., Kern, C., Pöhler, D., and Platt, U.: Applying light-emitting diodes with narrowband emission features in differential spectroscopy, Opt. Lett., 34, 3716–3718, doi:10.1364/OL.34.003716, 2009.

Sinreich, R.: Multi-Axis Differential Optical Absorption Spectroscopy Measurements in Polluted Environments, Ph.d. thesis, Combined Faculties for the Natural Sciences and for Mathematics, Universität Heidelberg, 2008.

Sinreich, R., Friess, U., Wagner, T., and Platt, U.: Multi axis differential optical absorption spectroscopy (MAX-DOAS) of gas and aerosol distributions, Faraday Discuss., 130, 153–164, doi:10.1039/B419274P, 2005.

Sinreich, R., Filsinger, F., Friess, U., Platt, U., Sebastian, O., Wagner, T., Volkamer, R., and Kern, C.: MAX-DOAS detection of glyoxal during ICARTT 2004, Atmos. Chem. Phys., 7, 1293–1303, 2007.

Sinreich, R., Coburn, S., Dix, B., and Volkamer, R.: Ship-based detection of glyoxal over the remote tropical Pacific Ocean, Atmos. Chem. Phys., 10, 11 359–11 371, doi:10.5194/acp-10-11359-2010, URL `http://www.atmos-chem-phys.net/10/11359/2010/`, 2010.

Sioris, C. E. and Evans, W. F. J.: Filling in of Fraunhofer and gas-absorption lines in sky spectra as caused by rotational Raman scattering, Appl. Opt., 38, 2706–2713, 1999.

Solomon, S., Schmeltekopf, A. L., and Sanders, R. W.: On the interpretation of zenith sky absorption measurements, J. Geophys. Res., 92, 8311–8319., 1987.

Solomon, S., Portmann, R. W., Sanders, R. W., and Daniel, J. S.: Absorption of solar radiation by water vapor, oxygen, and related collision pairs in the Earth's atmosphere, J. Geophys. Res., 103, 3847–3858, URL `http://dx.doi.org/10.1029/97JD03285`, 1998.

Solomon, S., Qin, D., Manning, M., Chen, Z., Marquis, M., Averyt, K., Tignor, M., and Miller, H.: IPCC, 2007: Climate Change 2007: The Physical Science

Basis. Contribution of Working Group I to the Fourth Assessment Report of the Intergovernmental Panel on Climate Change, Cambridge, United Kingdom and New York, NY, USA.: Cambridge University Press., 2007.

Stamnes, K., Tsay, S.-C., Wiscombe, W., and Jayaweera, K.: Numerically stable algorithm for discrete-ordinate-method radiative transfer in multiple scattering and emitting layered media, Appl. Opt., 27, 2502–2509, 1988.

Steck, T.: Methods for Determining Regularization for Atmospheric Retrieval Problems, Appl. Opt., 41, 1788–1797, doi:10.1364/AO.41.001788, 2002.

Stockwell, W. and Calvert, J.: The Mechanism of the HO-SO2 Reaction, Atmos. Environ., 17, 2231–2235, 1983.

Stohl, A., Forster, C., Frank, A., Seibert, P., and Wotawa, G.: Technical note: The Lagrangian particle dispersion model FLEXPART version 6.2, Atmos. Chem. Phys., 5, 2461–2474, doi:10.5194/acp-5-2461-2005, URL http://www.atmos-chem-phys.net/5/2461/2005/, 2005.

Stohl, A., Prata, A. J., Eckhardt, S., Clarisse, L., Durant, A., Henne, S., Kristiansen, N. I., Minikin, A., Schumann, U., Seibert, P., Stebel, K., Thomas, H. E., Thorsteinsson, T., Tørseth, K., and Weinzierl, B.: Determination of time- and height-resolved volcanic ash emissions and their use for quantitative ash dispersion modeling: the 2010 Eyjafjallajökull eruption, Atmospheric Chemistry and Physics, 11, 4333–4351, doi:10.5194/acp-11-4333-2011, URL http://www.atmos-chem-phys.net/11/4333/2011/, 2011.

Stull, R. B.: An Introduction to Boundary Layer Meteorology, Dordrecht, Boston, London:Kluwer Academic Publishers. ISBN 90 277 27686, 1988.

Stutz, J. and Platt, U.: Numerical analysis and estimation of the statistical error of differential optical absorption spectroscopy measurements with least-squares methods, Appl. Optics, 35, 6041–6053, 1996.

Stutz, J., Kim, E. S., Platt, U., Bruno, P., Perrino, C., and Febo, A.: UV-visible absorption cross sections of nitrous acid, J. Geophys. Res., 105, 14 585–14 592, URL http://dx.doi.org/10.1029/2000JD900003, 2000.

Textor, C., Graf, H.-F., Timmreck, C., and Robock, A.: Emissions of Atmospheric Trace Compounds, chap. Emissions from volcanoes, pp. 269–303, Klewer, Dordrecht, Netherlands, 2004.

Tikhonov, A. .: On the solution of incorrectly stated problems and a method of regularization 1963., Dokl. Akad. Nauk SSSR, 151, 501–504, 1963.

Ulshöfer, V.: Photochemische Produktion von Carbonylsulfid im Oberflächenwasser der Ozeane und Gasaustausch mit der Atmosphäre, Ph.D. thesis, University of Heidelberg, 1995.

Ulshöfer, V. and Andreae, M.: Carbonyl Sulfide (COS) in the Surface Ocean and the Atmospheric COS Budget, Aquatic Geochemistry, 3, 283–303, 10.1023/A:1009668400667, 1997.

v. Friedeburg, C., Pundt, I., Mettendorf, K.-U., Wagner, T., and Platt, U.: Multi-axis-DOAS measurements of NO2 during the BAB II motorway emission campaign, Atmospheric Environment, 39, 977 – 985, doi:10.1016/j.atmosenv.2004.06.046, 2005.

Van de Hulst, H.: Light scattering by small particles, New York: Dover publication, 1981.

van Roozendael, M., Fayt, C., Post, P., Hermans, C., and J.-C., L.: Sounding the troposphere from space: a new era for atmospheric chemistry, chap. Retrieval of BrO and NO2 from UV-Visible Observations, Springer-Verlag, ISBN 3-540-40873-8, 2003.

Van Roozendael, M., Loyola, D., Spurr, R., Balis, D., Lambert, J. C., Livschitz, Y., Valks, P., Ruppert, T., Kenter, P., Fayt, C., and Zehner, C.: Ten years of GOME/ERS-2 total ozone data - The new GOME data processor (GDP) version 4: 1. Algorithm description, J. Geophys. Res.-Atmos., 111, doi:10.1029/2005JD006375, 2006.

Vandaele, A. C., Hermans, C., Simon, P. C., Carleer, M., Colin, R., Fally, S., Mérienne, M. F., Jenouvrier, A., and Coquart, B.: Measurements of the NO2 absorption cross-section from 42 000 cm-1 to 10 000 cm-1 (238-1000 nm) at 220 K and 294 K, Journal of Quantitative Spectroscopy and Radiative Transfer, 59, 171 – 184, doi:10.1016/S0022-4073(97)00168-4, atmospheric Spectroscopy Applications 96, 1998.

Vigouroux, C., Hendrick, F., Stavrakou, T., Dils, B., De Smedt, I., Hermans, C., Merlaud, A., Scolas, F., Senten, C., Vanhaelewyn, G., Fally, S., Carleer, M., Metzger, J.-M., Müller, J.-F., Van Roozendael, M., and De Mazière, M.: Ground-based FTIR and MAX-DOAS observations of formaldehyde at Réunion Island and comparisons with satellite and model data, Atmospheric Chemistry and Physics, 9, 9523–9544, doi:10.5194/acp-9-9523-2009, URL `http://www.atmos-chem-phys.net/9/9523/2009/`, 2009.

Virkkula, A., Mäkelä, T., Hillamo, R., Yli-Tuomi, T., Hirsikko, A., Hämeri, K., and Koponen, I. K.: A Simple Procedure for Correcting Loading Effects of Aethalometer Data., Journal of the Air & Waste Management Association, 57, 1214 – 1222, 2007.

Vogel, L.: Volcanic plumes: Spectral evaluation of measurements, early detection and bromine chemistry, Ph.D. thesis, Combined Faculties for the Natural Sciences and for Mathematics, Universität Heidelberg, 2011.

Volkamer, R., Molina, L. T., Molina, M. J., Shirley, T., and Brune, W. H.: DOAS measurement of glyoxal as an indicator for fast VOC chemistry in urban air, Geophys. Res. Lett., 32, L08 806–, URL http://dx.doi.org/10.1029/2005GL022616, 2005a.

Volkamer, R., Spietz, P., Burrows, J., and Platt, U.: High-resolution absorption cross-section of glyoxal in the UV-vis and IR spectral ranges, Journal of Photochemistry and Photobiology A: Chemistry, 172, 35 – 46, doi:10.1016/j.jphotochem.2004.11.011, 2005b.

Volkamer, R., Sheehy, P., Molina, L. T., and Molina, M. J.: Oxidative capacity of the Mexico City atmosphere - Part 1: A radical source perspective, Atmospheric Chemistry and Physics, 10, 6969–6991, doi:10.5194/acp-10-6969-2010, URL http://www.atmos-chem-phys.net/10/6969/2010/, 2010.

von Friedeburg, C.: Derivation of Trace Gas Information combining Differential Optical Absorption Spectroscopy with Radiative Transfer Modelling, Ph.d. thesis, Combined Faculties for the Natural Sciences and for Mathematics, Universitaet Heidelberg., 2003.

Wagner, T.: Satellite observations of atmospheric halogen oxides, Ph.D. thesis, University of Heidelberg, Heidelberg, Germany., 1999.

Wagner, T.: Gerechter Blick von oben, Physik Journal, 5, 3, URL http://www.pro-physik.de/details/physikjournalIssue/1089719/Issue_5_2007.html, 2007.

Wagner, T., von Friedeburg, C., Wenig, M., Otten, C., and Platt, U.: UV-visible observations of atmospheric O4 absorptions using direct moonlight and zenith-scattered sunlight for clear-sky and cloudy sky conditions, J. Geophys. Res., 107, 4424, URL http://dx.doi.org/10.1029/2001JD001026, 2002.

Wagner, T., Dix, B., von Friedeburg, C., Friess, U., Sanghavi, S., Sinreich, R., and Platt, U.: MAX-DOAS O-4 measurements: A new technique to derive information on atmospheric aerosols - Principles and information content, J. Geophys. Res.-Atmos., 109, doi:10.1029/2004JD004904, 2004.

Wagner, T., Deutschmann, T., and Platt, U.: Determination of aerosol properties from MAX-DOAS observations of the Ring effect, Atmos. Meas. Tech., 2, 495–512, doi:10.5194/amt-2-495-2009, URL http://www.atmos-meas-tech.net/2/495/2009/, 2009.

Wagner, T., Ibrahim, O., Shaiganfar, R., and Platt, U.: Mobile MAX-DOAS observations of tropospheric trace gases, Atmospheric Measurement Techniques, 3, 129–140, doi:10.5194/amt-3-129-2010, URL http://www.atmos-meas-tech.net/3/129/2010/, 2010.

Wagner, T., Beirle, S., Brauers, T., Deutschmann, T., Frieß, U., Hak, C., Halla, J. D., Heue, K. P., Junkermann, W., Li, X., Platt, U., and Pundt-Gruber, I.:

Inversion of tropospheric profiles of aerosol extinction and HCHO and NO_2 mixing ratios from MAX-DOAS observations in Milano during the summer of 2003 and comparison with independent data sets, Atmospheric Measurement Techniques Discussions, 4, 3891–3964, doi:10.5194/amtd-4-3891-2011, URL `http://www.atmos-meas-tech-discuss.net/4/3891/2011/`, 2011.

Watts, S. F.: The mass budgets of carbonyl sulfide, dimethyl sulfide, carbon disulfide and hydrogen sulfide, Atmospheric Environment, 34, 761–779, doi:10.1016/S1352-2310(99)00342-8, 2000.

Weingartner, E., Saathoff, H., Schnaiter, M., Streit, N., Bitnar, B., and Baltensperger, U.: Absorption of light by soot particles: determination of the absorption coefficient by means of aethalometers, Journal of Aerosol Science, 34, 1445–1463, doi:10.1016/S0021-8502(03)00359-8, 2003.

Wiscombe, W. J.: Improved Mie scattering algorithms, Appl. Opt., 19, 1505–1509, doi:10.1364/AO.19.001505, 1980.

Wittrock, F., Oetjen, H., Richter, A., Fietkau, S., Medeke, T., Rozanov, A., and Burrows, J. P.: MAX-DOAS measurements of atmospheric trace gases in Ny-Alesund - Radiative transfer studies and their application, Atmospheric Chemistry and Physics, 4, 955–966, doi:10.5194/acp-4-955-2004, URL `http://www.atmos-chem-phys.net/4/955/2004/`, 2004.

WMO/GAW: Aerosol Measurement Procedures Guidelines and Recommendations, GAW Report No. 153, World Meteorological Organization Global Atmosphere Watch, Geneva, Switzerland, 2003.

Zieger, P., Fierz-Schmidhauser, R., Gysel, M., Ström, J., Henne, S., Yttri, K. E., Baltensperger, U., and Weingartner, E.: Effects of relative humidity on aerosol light scattering in the Arctic, Atmospheric Chemistry and Physics, 10, 3875–3890, doi:10.5194/acp-10-3875-2010, URL `http://www.atmos-chem-phys.net/10/3875/2010/`, 2010.

Zieger, P., Weingartner, E., Henzing, J., Moerman, M., de Leeuw, G., Mikkilä, J., Ehn, M., Petäjä, T., Clémer, K., van Roozendael, M., Yilmaz, S., Frieß, U., Irie, H., Wagner, T., Shaiganfar, R., Beirle, S., Apituley, A., Wilson, K., and Baltensperger, U.: Comparison of ambient aerosol extinction coefficients obtained from in-situ, MAX-DOAS and LIDAR measurements at Cabauw, Atmospheric Chemistry and Physics, 11, 2603–2624, doi:10.5194/acp-11-2603-2011, URL `http://www.atmos-chem-phys.net/11/2603/2011/`, 2011.

Acknowledgements

Ganz besonders und an erster Stelle möchte ich mich bei Prof. Dr. Ulrich Platt bedanken, der diese interessante Arbeit ermöglicht hat.

Ein herzliches Dankeschön an Dr. Udo Frieß, der mir immer mit Rat und Tat zur Seite stand und diese Arbeit mit vielen Anregungen betreut hat. Vielen Dank auch für die vielen Hilfestellungen beim Bau des Instrumentes und Programmieren.

Vielen Dank auch an Prof. Dr. Thomas Wagner, der das zweite Gutachten dieser Arbeit übernommen und viele gute Ratschläge gegeben hat.

Ich danke der ganzen Arbeitsgruppe, für die freundschaftliche Atmosphäre und tolle Zusammenarbeit.

Mein besonderer Dank gilt Holger, Joelle, Leif und Robert für das Korrektur lesen. Vielen Dank an Christoph K., Denis und Jens für die vielen Tipps beim Bau des Instrumentes. Danke an Nicole und Christoph H. für die Ratschläge bezüglich der Vulkan Messungen. Ich danke auch Tim für die vielen Diskussionen über den Strahlungstransport.

Elke, Jessica, Robert und Sanam sei gedankt, dass sie mit mir das Büro geteilt haben und für die gute Atmosphäre.

Den ehemaligen IUPlern Barbara und Roman gilt mein Dank für die Tipps in den Anfangszeiten meiner Arbeit.

Ich danke dem gesamten Werkstatt Team um Ralph Pfeifer für die schnelle Bearbeitung und die guten Ratschläge rund um den Bau des Instrumentes.

Danke auch an Sekretariat und Verwaltung für eine stets freundliche und unkomplizierte Zusammenarbeit.

I would also like to thank all the people who have supported me during the several campaigns and provided the comparison data set:

- Cabauw: Arnould Apituley, Henk Klein Baltink, Bas Henzing, Gerrit de Leeuw, Ankie Piters, Roland van der A, and Paul Zieger
- Ispra: Mariana Adam, Alessandro Dell'Acqua, Carsten Grüning, and Jean-Philippe Putaud
- Leipzig/Melpitz: Dietrich Althausen, Holger Baars, and Birgit Heese

Ein herzliches Dankeschön gilt meiner Familie und besonders meinen Eltern, die mich in meinem Studium und meinen Entscheidungen stets unterstützten.

Der größte Dank aber gehört meiner Line, die mich zu jeder Zeit voll unterstützte.